acta physica slovaca vol. 57 No. 2, 177 – 406 **April 2007**

THE FINITE-DIFFERENCE AND FINITE-ELEMENT MODELING OF SEISMIC WAVE PROPAGATION AND EARTHQUAKE MOTION

P. Moczo[1,a,b], **J. Kristek**[a,b], **M. Galis**[b], **P. Pazak**[a], **M. Balazovjech**[a]
[a] *Faculty of Mathematics, Physics and Informatics, Comenius University*
Mlynská dolina F1, SK-842 48 Bratislava, Slovakia
[b] *Geophysical Institute, Slovak Academy of Sciences*
Dúbravská cesta 9, SK-845 28 Bratislava, Slovakia

Received 21 February 2007, accepted 28 February 2007

Numerical modeling of seismic wave propagation and earthquake motion is an irreplaceable tool in investigation of the Earth's structure, processes in the Earth, and particularly earthquake phenomena. Among various numerical methods, the finite-difference method is the dominant method in the modeling of earthquake motion. Moreover, it is becoming more important in the seismic exploration and structural modeling. At the same time we are convinced that the best time of the finite-difference method in seismology is in the future.

This monograph provides tutorial and detailed introduction to the application of the finite-difference (FD), finite-element (FE), and hybrid FD-FE methods to the modeling of seismic wave propagation and earthquake motion. The text does not cover all topics and aspects of the methods. We focus on those to which we have contributed.

We present alternative formulations of equation of motion for a smooth elastic continuum. We then develop alternative formulations for a canonical problem with a welded material interface and free surface. We continue with a model of an earthquake source. We complete the general theoretical introduction by a chapter on the constitutive laws for elastic and viscoelastic media, and brief review of strong formulations of the equation of motion. What follows is a block of chapters on the finite-difference and finite-element methods. We develop FD targets for the free surface and welded material interface. We then present various FD schemes for a smooth continuum, free surface, and welded interface. We focus on the staggered-grid and mainly optimally-accurate FD schemes. We also present alternative formulations of the FE method. We include the FD and FE implementations of the traction-at-split-nodes method for simulation of dynamic rupture propagation. The FD modeling is applied to the model of the deep sedimentary Grenoble basin, France. The FD and FE methods are combined in the hybrid FD-FE method. The hybrid method is then applied to two earthquake scenarios for the Grenoble basin.

Except chapters 1, 3, 5, and 12, all chapters include new, previously unpublished material and results.

PACS: 02.50.+s, 05.60.+w, 72.15.-v

KEYWORDS: Seismic wave propagation, Earthquake motion, Numerical modeling, Hybrid numerical modeling, Viscoelasticity, Earthquake source dynamics

[1] E-mail address: moczo@fmph.uniba.sk

Contents

Introduction

The invitation by Vladimír Bužek to write a text that would present a topic of our research was for us a strong motivating challenge and nice opportunity at the same time: we could and we should comprise a tutorial introduction, state-of-the-art review, and our recent results. We also present several new unpublished results.

Numerical modeling of seismic wave propagation and earthquake motion is an important and irreplaceable tool in investigation of the Earth's structure, processes in the Earth, and particularly earthquake phenomena.

An earthquake is a unique and interesting natural phenomenon. It is a powerful challenge for seismologists who, after a century of modern seismological research, still do not have answers to important questions regarding the process of preparation and initialization of earthquakes. Consequently, seismologists still cannot predict time, place and size of future earthquakes. In fact, it is even more interesting. Seismologists still do not know whether such prediction is possible in principle and will be possible technically.

An earthquake can cause death and huge material losses. An earthquake that kills and causes damage is not necessarily a big event in terms of relaxed energy. As it is clear in California and Japan, even relatively weak earthquakes can cause record economic losses. Apparently surprisingly, this is because the earthquake prone areas often are the most populated areas. Large populated areas may be close to active seismogenic faults and/or local geologic conditions can cause anomalous earthquake motion. An anomalous motion most often occurs at the surface of soft or unconsolidated sediments due to resonant phenomena in sedimentary bodies. Largest damages on buildings and constructions are often due to mutual resonance between the geologic and building structures. Given the fact that most of large cities are located at the surface of sediment-filled basins and valleys, it is not surprising that almost each recent moderate or big earthquake that hits the populated area causes tremendous damage and also kills people.

Seismologists must study earthquakes, investigate possibilities to predict time, place and size of the next earthquake. No matter whether they can predict occurrence of an earthquake itself, they have to predict earthquake ground motion during future earthquakes. Prediction of the earthquake motion at a site of interest is extremely important for planning and building new, and reinforcing existing buildings, as well as for undertaking actions that could help mitigate losses during future earthquakes.

Energetically important earthquakes are tectonic earthquakes. Most of tectonic earthquakes occur on active seismogenic faults. A fault is a relatively weak zone separating two blocks of the Earth's crust or lithosphere. While each of the two blocks as a whole moves with respect to the other block due to global tectonic processes, some area of their contact along the fault may be at rest due to friction. Because the two blocks (except the locked area) move, the shear (tangential) traction at the locked area of the fault grows. Should the shear traction at a point of the fault exceed the frictional strength, a slip (relative displacement of the two fault faces) occurs. As sliding at a point of the fault commences, the traction varies following a friction law. At the same time the rupture propagates from the point of initiation over the fault. Due to the rupture propagation, seismic (also called elastic) waves are radiated from the fault.

Seismic waves radiated from the fault cause earthquake ground motion (that is, a mechanical vibratory motion) at the Earth's surface.

Because the rupture process typically occurs in depths of several tens of kilometers, that is, in the Earth's crust and upper mantle, and ruptured area spreads over tens or hundreds of square kilometers, a direct controlled physical experiment, that would aim to model the process, is impossible. Direct seismological measurements are, in fact, restricted to the Earth's surface, and almost all the information about the rupture process and structure of the Earth's interior is encoded in instrument records of the seismic motion (seismograms) during earthquakes. Our knowledge of the earthquake source and the Earth's interior has to be confronted with the seismograms. It is therefore very clear that the numerical modeling of the rupture process on the fault and the seismic wave propagation in the Earth's interior really is an irreplaceable tool in the seismological research.

Though we focused on earthquakes we have to stress that we would have to develop computational and, particularly, numerical-modeling methods for seismic wave propagation even if we lived on a hypothetical planet without earthquakes. In such a case artificially generated seismic waves would be still the best tool to investigate the planet's interior.

The reason why we speak directly about the numerical-modeling methods is very clear. The Earth's interior is structurally complex medium with non-planar material discontinuities and gradients of seismic wave speeds, density, and quality factors. The Earth's surface has to be modeled in many problems with its complicated regional or local topography. The lithosphere is for seismic waves, in general, anisotropic. Analytical computational methods do not provide solutions for reasonable (that is, structurally sufficiently complex) models of the Earth's interior. Approximate methods have to be applied. Apart from the asymptotic methods for the high-frequency seismic wave propagation, the numerical methods play the key role. Among them still the finite-difference method is the dominant method in the modeling of earthquake motion. Moreover, it is becoming more important in the seismic exploration and structural modeling.

The finite-difference method, as any other method, has its own problems and limitations. It can be, however, advantageously combined with other method(s) in hybrid approaches that overcome limitations of the individual methods. An example is a combination of the finite-difference and finite-element methods.

Our monograph is focused on the application of the finite-difference, finite-element, and hybrid finite-difference – finite-element methods to seismic wave propagation and earthquake motion.

We start with alternative formulations of equation of motion for a smooth elastic continuum. We then develop alternative formulations for a canonical problem with a welded material interface and free surface. We continue with a simple model of an earthquake source. We complete the general theoretical introduction by a chapter on the constitutive laws for elastic and viscoelastic media, and brief review of strong formulations of the equation of motion. What follows is a block of chapters on the finite-difference and finite-element methods. Major part of the material is related to the finite-difference method.

Except chapters 1, 3, 5, and 12, all chapters include new, previously unpublished material and results.

We do not cover all topics and aspects of the finite-difference and finite-element methods. We have not included anisotropy and non-reflecting boundaries. The main reason is that we have not contributed to these topics. We have not included the incorporation of the free-surface topogra-

phy in the finite-difference method – we solve this in our hybrid finite-difference – finite element method. For the three topics in the finite-difference method we refer to a recent review article on the finite-difference modeling in seismology by Moczo et al. (2007). Neither we included explicit material on the computational efficiency. The review by Moczo et al. (2007) addresses also this key aspect of the modeling. The application of the finite-difference method to the seismic wave propagation and earthquake motion modeling is a subject of other reviews and textbooks as well, see Boore (1972), Levander (1989), Moczo (1998), Carcione et al. (2002), and Moczo et al. (2004b).

We also recommend general mathematical textbooks and monographs on the finite-difference method – Forsythe and Wasow (1960), Isaacson and Keller (1966), Richtmyer and Morton (1967), Mitchell (1969), Marchuk (1982), Anderson et al. (1984), Mitchell and Griffiths (1994), Morton and Mayers (1994), Durran (1999), and Cohen (2002). The application of the finite-difference method to the computational electrodynamics can be found in the impressive book by Taflove and Hagness (2005).

Textbooks and monographs on the finite-element method include Strang and Fix (1973), Akin (1986), Strang and Fix (1988), Zienkiewicz and Taylor (1989), Ottosen and Petersson (1992), Hughes (2000), Belytschko et al. (2000), and Reddy (2006). Very good recent examples of the application of the finite-element method to the seismic wave propagation and earthquake motion modeling are articles by Bielak et al. (2003) and Yoshimura et al. (2003).

We do not explain basics of the continuum mechanics (except necessary details on rheology of the elastic and viscoelastic media). The reader is referred to very good introductions to the continuum mechanics for seismologists in books by Aki and Richards (1980, 2002), and Pujol (2003). Neither we explain basics of the theory of seismic wave propagation and seismology. Textbook and monographs on theoretical seismology and seismic wave propagation include those by Aki and Richards (1980), Ben-Menahem and Singh (1981), Dahlen and Tromp (1998), Shearer (1999), Udías (1999), Červený (2001), Carcione (2001), Kennett (2001, 2002), Aki and Richards (2002), and Pujol (2003).

The finite-difference and finite-element method clearly are not the only numerical methods in seismology. We have to mention at least the boundary integral equation and boundary element methods (BIEM and BEM), for example Bouchon and Sánchez-Sesma (2007), spectral-element method (SPEM), for example Komatitsch et al. (2004) and Chaljub et al. (2007), and the arbitrary high-order derivative – discontinuous Galerkin method (ADER-DG), for example Käser and Dumbser (2006). These methods differ in accuracy with respect to different structural features of the complex heterogeneous models and considerably in the computational efficiency. They in several aspects represent alternatives to the finite-difference and finite-element methods. For comparison of several modeling methods we refer to the review paper by Takenaka et al. (1998). The most recent review of the computational and numerical-modeling methods can be found in the book edited by Wu and Maupin (2007).

Acknowledgements

First of all we thank Vladimír Bužek for his generous invitation to write this text. We greatly appreciate discussions with Robert J. Geller, Steven M. Day, Michel Bouchon and Pierre-Yves Bard on particular topics. We thank Emmanuel Chaljub who kindly provided his SPEM simulation for the ESG2006 Grenoble basin benchmark. Special thanks go to our teammates Peter

Franek and Miriam Kristekova for their kind help and support. This work was supported in part by the Marie Curie Research Training Network SPICE Contract No. MRTN-CT-2003-504267, VEGA Project 1/4032/07, and ESF Project JPD 3 2005/1-034.

List of Selected Abbreviations and Mathematical Symbols

DSF	discontinuous strong formulation, sec. 2.5
DW(M)	discrete wavenumber (method), Fig. 12.7
FD(M)	finite-difference (method)
FE(M)	finite-element (method)
GMB-EK	generalized Maxwell body, definition by Emmerich and Korn (1987), Fig. 4.11
GZB	generalized Zener body, Fig. 4.10
HB	Hooke body, Fig. 4.1
ISF	integral strong formulation, sec. 1.4
KVB	Kelvin-Voigt body, Fig. 4.5
MB	Maxwell body, Fig. 4.5
NB	nonreflecting boundary, Fig. 12.7
PDE, FDE	partial differential equation, finite-difference equation
R&S	rate- and state- dependent friction law, eqs. (3.13), (3.14)
SB	Stokes body, Fig. 4.3
SF	strong formulation, sec. 1.2
SW	slip weakening friction law, sec. 3.3.1
TSN	traction-at-split-nodes method, sec. 3.4
WF	weak formulation, sec. 1.3
ZB	Zener body, Fig. 4.5
$\alpha,\ \beta$	P-wave velocity, S-wave velocity
$\Gamma,\ \Gamma_D,\ \Gamma_N$	boundary of the computational domain, Dirichlet and Neumann boundaries, sec. 6.3
$\Delta\vec{T}(\vec{n};x_i)$	traction variation, eq. (3.3)
Δt	time step, eq. (6.1)
$\Delta x,\ \Delta y,\ \Delta z$	grid spacing, spatial step, eq. (6.1)
δC	relaxation of compliance, eq. (4.53)
δd_p	normal mode expansion coefficients, eq. (7.68)
δM	modulus defect, relaxation of modulus, eq. (4.41)
$\delta T,\ \delta H,\ \delta\vec{c}$	errors of the numerical operators and solution, eq. (7.61)
$\delta\mathbf{U}_I^m$	matrix of corrections to displacement values, eq. (7.101)
$\delta u,\ \delta\varepsilon_{ij}$	virtual displacement and virtual strain tensor, eq. (1.8)
$\delta(\xi),\ \delta(t)$	Dirac delta function
δ_{ij}	Kronecker delta, eq. (4.11)
δ_h	approximation to Dirac delta function, eq. (8.19)
$\varepsilon,\dot{\varepsilon}$	strain, strain rate, eqs. (4.1), (4.13)
$\varepsilon(\omega),\ \sigma(\omega)$	frequency-dependent Fourier transforms of one-dimensional strain and stress, eq. (4.4)

$\zeta_l(t)$	anelastic function, eq. (4.143)
$\zeta_l^{ij}(t)$	tensor of anelastic functions, eq. (4.166)
η	viscosity, eq. (4.13)
$\kappa,\ \lambda,\ \mu$	(unrelaxed) elastic moduli, eqs. (4.10), (4.12)
$\kappa^H,\ \mu^H,\ \rho^A$	harmonic and arithmetic averages of material parameters, eqs. (7.37) – (7.39)
λ_{min}	minimum wavelength, eq. (10.37)
μ_f	coefficient of friction, eq. (3.5)
$\mu_s,\ \mu_d$	static and dynamic coeficients of friction, eq. (3.11)
$\nu_i,\ \vec{\nu}$	normal vector, Fig. 1.1
$\xi,\ \eta,\ \zeta$	local coordinates, eq. (6.17)
ξ^{ij}	discrete approximations to the components of tensor of anelastic functions, Fig. 7.2
$\xi_l(t)$	anelastic function, eq. (4.148)
$\xi_l^{ij}(t)$	tensor of anelastic functions, eq. (4.168)
ρ	density, eq. (1.1)
$\bar{\rho}$	average density, eq. (8.48)
$\rho^{I\delta_h A}(a)$	integral arithmetic average of density, eq. (8.22)
$\rho^{I\delta_h AFS}(a)$	integral arithmetic average of density at the free surface, eq. (8.80)
$\rho^{IA}(a)$	integral arithmetic average of density, eq. (8.11)
$\rho^{IAFS}(a)$	integral arithmetic average of density at the free surface, eq. (8.78)
$\rho^{PA}(a)$	point arithmetic average of density, eq. (8.6)
Σ	surface, Fig. 1.1
σ	Poisson's ratio, eq. (7.27)
$\sigma,\ \sigma_{ij}$	one-dimensional stress, the stress tensor, eqs. (4.1), (4.7)
$\dot{\sigma}$	one-dimensional stress rate
$\sigma_{ij}^E,\ \sigma_{ij}^{A\,l}$	components of the elastic and viscoelastic stress tensor, eq. (6.48)
$\vec{\vec{\sigma}}$	stress tensor, eq. (6.8)
$\tau_\sigma,\ \tau_\varepsilon$	stress relaxation time, eq. (4.70), strain relaxation time, eq. (4.99)
$\Phi_S,\ \delta,\ \lambda$	strike, dip, rake, Fig. 3.3
$\phi(x_k) = 0,\ \psi(x_k) = 0$	parametric equation of the surface, eqs. (2.14), (2.15)
$\chi(t),\ \chi_{ijkl}$	creep function, eq. (4.43), tensor of creep functions, eq. (4.16)
Ψ	state variable in the R&S friction law, eq. (3.13)
$\psi(t),\ \psi_{ijkl}(t)$	stress relaxation function (4.19), tensor of stress relaxation functions, eq. (4.15)
Ω	volume, Fig. 1.1, interior of the computational domain, sec. 6.3
$\bar{\Omega}$	computational domain, sec. 6.3
Ω^e	sub-domain (element), sec. 6.3
ω	angular frequency, eq. (4.2)
ω_p	eigenfrequencies, eq. (7.62)
$\omega_r,\ \omega_l$	relaxation frequency, eq. (4.64)
$\tilde{\omega}_k$	frequencies, at which Q is known, eq. (4.154)
$\partial^{(m,n)}u,\ u^{(m,n)}$	denotes partial derivative $\partial^{m+n}u/\partial t^m\,\partial z^n$, eq. (7.83)

$+/-$	indications of the $+/-$ sides of an interface or fault
$+/-$	related to the partial node $p.n.^{+}/p.n.^{-}$, respectively, Fig. 3.2
A	area of the fault plane associated with a partial node, eq. (3.16)
$\mathbf{A}_I^m$	optimally-accurate time derivative operator, eq. (7.88)
AI	Arias intensity, eq. (14.6)
$a,\ b,\ L$	constitutive parameters for the R&S friction law, eq. (3.14)
$a,\ b$	finite-difference coefficients for the 4^{th}-order, eq. (6.5)
a_l	weight coefficient, eq. (4.120)
$\vec{a}^{\pm}$	acceleration at partial node, eq. (3.15)
C	elastic modulus, eq. (7.80)
$C,\ C(\omega)$	compliance, creep compliance, eq. (4.6)
$C_R,\ C_U$	relaxed and unrelaxed compliance, eq. (4.52)
$\overline{C}$	average elastic modulus, eq. (8.48)
CAV	cummulative absolute velocity, eq. (14.7)
$\vec{c},\ \vec{c}^{\,e}$	numerical, exact solution, eqs. (7.59), (7.60)
$\vec{c}_p$	eigenvector, eq. (7.62)
$coef\text{TE\_}u$	coefficient at u in the Taylor expansion, eq. (9.21)
$\mathbf{convA}_I^m$	conventional time derivative operator, eq. (7.96)
$\mathbf{convK}_I^m$	conventional spatial derivative operator, eq. (7.97)
d	depth, eq. (13.1)
d_p^e	normal mode expansion coefficients, eq. (7.65)
$D\vec{u}(x_i,t)$	slip, eq. (3.1)
$D\vec{v}(x_i,t)$	slip rate, eq. (3.2)
D_c	characteristic (critical) distance in the SW friction law, eq. (3.11)
$D_z^{(4)},\ D_z^{(2)}$	spatial operator, eqs. (11.1), (11.2)
dt	time step, eq. (3.21)
e	sequential number of element, sec. 6.3
$E(z),\ E^{\pm}(z)$	1D equation of motion, eqs. (7.80), (8.1)
E_i	components of the 3D equation of motion, eq. (7.105)
$\mathcal{F}\{x(t)\},\ \mathcal{F}^{-1}\{x(t)\}$	Fourier and inverse Fourier transforms, eqs. (4.2), (4.3)
f	frequency, Fig. 4.8
$\mathbb{f}$	global load force vector, eq. (6.36)
$\vec{F}^{\pm}$	force at a partial node, eq. (3.15)
$\vec{F}^{c,\pm}$	constraint force, eq. (3.16)
$f^{I\delta_h A}(a)$	integral arithmetic average of body force, eq. (8.23)
$f^{I\delta_h AFS}(a)$	integral arithmetic average of body force at the free surface, eq. (8.80)
$f^{IA}(a)$	integral arithmetic average of body force, eq. (8.12)
$f^{IAFS}(a)$	integral arithmetic average of body force at the free surface, eq. (8.78)
$f^{PA}(a)$	point arithmetic average of body force, eq. (8.7)
$f_i,\ \vec{f}$	body force, Fig. 1.1
G_{pq}	Green's function, eq. (3.37)
$H(\xi),\ H(t)$	Heaviside unit step function, eq. (2.18)
h	grid spacing, spatial step, eq. (6.1)

H	stiffness matrix, eq. (7.58)
H^e	exact spatial derivative operator, eq. (7.60)
$I,\ J,\ K$	grid indices, eq. (6.1)
$\mathbf{J}$	Jacobian, eq. (6.29)
$\mathbb{K}$	global stiffness matrix, eq. (6.36)
$\mathbf{K}^e$	local stiffness matrix, eq. (6.23)
$\mathbf{K}_I^m$	optimally-accurate spatial derivative operator, eq. (7.89)
l	slip path length, eq. (3.10)
$M,\ M(\omega)$	elastic modulus, frequency-dependent complex viscoelastic modulus, eqs. (4.22), (4.24)
$M^{\pm}$	mass of a partial node, eq. (3.15)
$\mathbb{M}$	global mass matrix, eq. (6.36)
$m_{pq},\ M_{pq}$	moment density tensor, eq. (3.38), moment tensor, eq. (3.40)
M_0	scalar seismic moment, eq. (3.49)
$\mathbf{M}^e$	local mass matrix, eq. (6.24)
$M_R,\ M_U$	relaxed and unrelaxed moduli, eqs. (4.39), (4.40)
M_w	moment magnitude, sec. 13.1
$MX,\ MY,\ MZ$	number of grid cells in the x-, y-, z-directions, respectively
$n,\ sh$	normal and shear components of vector quantities, sec. 3
N	number of grid spacing per λ_{min}, eq. (10.38)
N^e	total number of elements in a mesh, sec. 6.3
N^n	total number of nodes in a mesh, sec. 6.3
$n_i,\ \vec{n}$	normal vector, Fig. 1.1
n_n	number of nodes in an element, sec. 6.3
$O(h^n)$	order of a remainder, eq. (6.3)
PHA	peak horizontal acceleration
p	stability ratio, eq. (10.40)
$p.n.^{\pm}$	partial nodes, Fig. 3.2
$p_i,\ \vec{p}$	traction vector, eqs. (1.3), (1.7)
$p_x,\ p_y,\ p_z$	components of traction vector at Γ_N, eq. (6.15)
$Q(\omega)$	quality factor, eq. (4.42)
$Q_\alpha,\ Q_\beta$	quality factors for P- and S-waves , eq. (4.162)
$\vec{\mathcal{R}}$	residual, eq. (6.12)
$\vec{r}$	density of the restoring force, eq. (6.9)
$\mathbb{r}$	global restoring force, eq. (6.44)
$\mathbf{r}^e,\ \mathbf{r}$	local restoring force, eq. (6.38)
$\mathbf{r}_x,\ \mathbf{r}_y,\ \mathbf{r}_z$	subvectors of the local restoring force, eq. (6.38)
S	surface, Fig. 1.1
$S,\ S(t)$	frictional strength, eq. (3.5)
s	spatial sampling ratio
$\mathbf{s}^{(inv)}$	vector of the new (e-invariant) shape functions, eq. (6.79)
$\vec{s}$	displacement produced by source, eq. (12.18)
$s(t)$	source time function
s_i	shape functions, eq. (6.11)
$\mathbf{s}$	vector of the shape functions, eq. (6.18)

T', H'	modified mass and stiffness matrix, eq. (7.72)
T, T^e	mass matrix, exact time derivative operator, eqs. (7.58), (7.60)
$\mathbf{T}$	transformation matrix, eq. (6.80)
T^{ij}	discrete approximations to the components of stress tensor, Fig. 6.1
T_i, $\vec{T}$	traction vector – equivalent to p_i, eq. (1.3)
$\vec{T}(\vec{n}; x_i, t)$	total traction, eq. (3.3)
$\vec{T}^{\,0}(\vec{n}; x_i)$, $\vec{T}^{\,0}(\vec{n})$	initial traction, eq. (3.3)
$\vec{T}^f(D\vec{u}, D\vec{v}, \theta)$, $\vec{T}^f(t)$	frictional traction, eq. (3.4)
$\vec{T}^d$	kinematic (dynamic) frictional traction, eq. (3.12)
$\vec{T}^s$	static (yield) frictional traction, eq. (3.12)
$\vec{T}^c$, $\vec{T}^c(\vec{n})$	constraint traction, eq. (3.16)
$\vec{T}^{ct}$, $\vec{T}^{ct}(t)$	trial traction, eq. (3.25)
$U^m_{I,J,K}$	discrete approximation to the x-component of displacement or particle-velocity
$\mathbf{U}^m_I$	matrix of discrete displacement values, eq. (7.100)
$u_{,z}$	partial spatial derivative
$\mathbf{u}^m_I$	matrix of displacement values, eq. (7.87)
$\mathbf{u}_x$, $\mathbf{u}_y$, $\mathbf{u}_z$	vectors of discrete displacements, eq. (6.22)
u_{xi}, u_{yi}, u_{zi}	components of discrete displacements at nodes, eq. (6.11)
u_i, u_x, u_y, u_z, $\vec{u}$	displacement, eq. (1.1)
u_p	normal modes, eq. (7.77)
$u_x^{(0)}$, $u_x^{(1)}$, $u_x^{(2)}$, $u_x^{(12)}$	e-invariants of displacements in the x -direction, eq. (6.83)
$u_y^{(0)}$, $u_y^{(1)}$, $u_y^{(2)}$, $u_y^{(12)}$	e-invariants of displacements in the y -direction, eq. (6.83)
$\vec{u}_K$	recorded wavefield, eq. (12.21)
$\vec{u}_R$	residual wavefield, eq. (12.18)
$\dot{u}$	partial time derivative
$\dot{u}_i$, $\dot{u}_x$, $\dot{u}_y$, $\dot{u}_z$, $\dot{\vec{u}}$	particle velocity
$\ddot{u}_i$, $\ddot{u}_x$, $\ddot{u}_y$, $\ddot{u}_z$, $\ddot{\vec{u}}$	particle acceleration
V	volume, Fig. 1.1
$V^m_{I,J,K}$	discrete approximation to the y-component of displacement or particle-velocity
W	weight coefficient, eq. (8.20)
$W^m_{I,J,K}$	discrete approximation to the z-component of displacement or particle-velocity
$\mathbf{x}$, $\mathbf{y}$, $\mathbf{z}$	vectors of the global nodal coordinates, eq. (6.20)
$x^{(0)}$, $x^{(1)}$, $x^{(2)}$, $x^{(12)}$	e-invariants of the spatial coordinates x, eqs. (6.63), (6.65), (6.71)
x_i, x, y, z, $\vec{x}$	cartesian coordinates, global coordinates, sec. 6.3
x^e_k, y^e_k, z^e_k	nodal coordinates, eq. (6.16)
$y^{(0)}$, $y^{(1)}$, $y^{(2)}$, $y^{(12)}$	e-invariants of the spatial coordinates y, eqs. (6.63), (6.65), (6.71)
Y_l, Y_l^α, Y_l^β, Y_l^κ, Y_l^μ	anelastic coefficients, eqs. (4.149), (4.162), (4.164), (4.165)

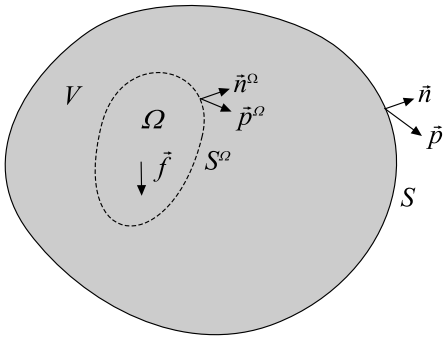

Fig. 1.1. Material volume V of a smooth continuum bounded by surface S. External traction $\vec{p}$ acts at surface S, body force $\vec{f}$ acts in volume V. Volume Ω with surface S^{Ω} is a testing volume considered in derivation of the equation of motion.

1 Equation of Motion for a Smooth Continuum

1.1 Problem Configuration

Consider a material volume V of continuum with surface S in which material parameters are continuous. Inside of V consider an arbitrary volume Ω with surface S^{Ω}. Let $\vec{n}^{\,\Omega}$ be a normal vector to surface S^{Ω} pointing from interior of volume Ω outward. Consider body force $\vec{f}(x_k, t)$ acting in volume Ω and traction $\vec{p}^{\,\Omega}(x_k, t)$ acting at surface S^{Ω}. Here $x_k \; ; \; k \in 1, 2, 3$ are Cartesian coordinates and t is time. The configuration is shown in Fig. 1.1.

1.2 Application of the Newton's Second Law - Strong Form

An application of Newton's second law to volume Ω gives

$$\frac{\mathrm{d}}{\mathrm{d}t} \int_{\Omega} \rho \frac{\partial u_i}{\partial t} \, \mathrm{d}V \; = \; \int_{S^{\Omega}} p_i^{\Omega} \mathrm{d}S \; + \int_{\Omega} f_i \mathrm{d}V \, . \tag{1.1}$$

Throughout the text $\mathrm{d}V$ and $\mathrm{d}S$ will be used for volume and surface elements, respectively. Because Ω and S^{Ω} move with particles, the particle mass $\rho \mathrm{d}\Omega$ does not change with time. The equation can be written as

$$\int_{\Omega} \rho \ddot{u}_i \mathrm{d}V \; = \; \int_{S^{\Omega}} p_i^{\Omega} \mathrm{d}S \; + \int_{\Omega} f_i \mathrm{d}V \, . \tag{1.2}$$

At surface S^{Ω}, traction $\vec{p}^{\,\Omega}$ is related to the stress tensor σ_{ij}:

$$p_i^{\Omega} \; = \; \sigma_{ij} \, n_j^{\Omega} \, . \tag{1.3}$$

In eq. (1.3) and hereafter we assume Einstein summation convention for repeated indices. Assuming continuity of the stress tensor throughout volume Ω, Gauss's divergence theorem can be

applied to the surface integral:

$$\int_{S^\Omega} p_i^\Omega \mathrm{d}S \;=\; \int_{S^\Omega} \sigma_{ij}\, n_j^\Omega \mathrm{d}S \;=\; \int_\Omega \sigma_{ij,j}\, \mathrm{d}V\,. \tag{1.4}$$

Equation (1.2) can be then written as

$$\int_\Omega (\rho\ddot{u}_i - \sigma_{ij,j} - f_i)\mathrm{d}V = 0\,. \tag{1.5}$$

Equation (1.5) is valid for any volume Ω inside V. We want to show that then the integrand itself is equal to zero: $\rho\ddot{u}_i - \sigma_{ij,j} - f_i = 0$. Assume that $\rho\ddot{u}_i - \sigma_{ij,j} - f_i > 0$ at some point inside V. Because the integrand is continuous throughout V, it is possible to find such volume Ω (containing that point) for which $\rho\ddot{u}_i - \sigma_{ij,j} - f_i > 0$ and thus also $\int_\Omega (\rho\ddot{u}_i - \sigma_{ij,j} - f_i)\mathrm{d}V > 0$. This, however, would be in contradiction with eq. (1.5). Thus,

$$\rho\ddot{u}_i - \sigma_{ij,j} - f_i = 0 \tag{1.6}$$

everywhere in V. Equation (1.6) together with boundary condition at surface S,

$$p_i = \sigma_{ij}\, n_j\,, \tag{1.7}$$

make a strong formulation for the considered problem.

1.3 Application of the Principle of Virtual Work - Weak Form

Alternatively to the application of Newton's second law to the material volume V we can apply the principle of virtual work. Consider a fixed state of continuum at some time and its virtual (arbitrary, infinitesimal) deformation. Let δu_i be the corresponding virtual displacements. Then the virtual deformation is characterized by the virtual strain tensor $\delta\varepsilon_{ij}$:

$$\delta\varepsilon_{ij} = \tfrac{1}{2}\,[\,(\delta u_i)_{,j} + (\delta u_j)_{,i}\,]\,. \tag{1.8}$$

Because virtual displacements are assumed in a fixed state of continuum, they do not affect displacements and accelerations of continuum particles in this state. The principle states that during the virtual deformation the work done by external forces has to be equal to a sum of an increment of energy of deformation and a work of inertial forces:

$$\int_S p_i \delta u_i \mathrm{d}S + \int_V f_i \delta u_i \mathrm{d}V \;=\; \int_V \sigma_{ij}\delta\varepsilon_{ij}\mathrm{d}V + \int_V \rho\ddot{u}_i \delta u_i \mathrm{d}V\,. \tag{1.9}$$

Functions δu_i are arbitrary, they are equivalent to weight functions. Therefore we replace δu_i by w_i in eqs. (1.8) and (1.9). Then, due to symmetry of the stress tensor,

$$\sigma_{ij}\,\delta\varepsilon_{ij} \;=\; \tfrac{1}{2}\,(\sigma_{ij}\,w_{i,j} + \sigma_{ij}\,w_{j,i}\,) \;=\; \sigma_{ij}\,w_{i,j}\;. \tag{1.10}$$

Equation (1.9) can be written as

$$\int_V (\rho\ddot{u}_i - f_i) w_i \mathrm{d}V + \int_V \sigma_{ij} w_{i,j}\,\mathrm{d}V \;=\; \int_S p_i w_i \mathrm{d}S\,. \tag{1.11}$$

If eq. (1.11) is satisfied for all possible choices of weight functions w_i then it is equivalent to the strong form of the equation of motion and is called the weak form of the equation of motion. 'Weak' here means a requirement of continuity of displacement (that is weaker than the requirement of continuity of its first spatial derivatives in the strong form), and the same requirement with respect to the weight functions.

1.4 Integral Strong Form

Integration by parts of the last term on the l.h.s. of eq. (1.11) yields

$$\int_V (\rho\ddot{u}_i - f_i)w_i \mathrm{d}V + \int_V (\sigma_{ij}\, w_i)_{,j}\ \mathrm{d}V - \int_V \sigma_{ij,j}\ w_i\, \mathrm{d}V\ =\ \int_S p_i\, w_i\, \mathrm{d}S \tag{1.12}$$

and, using Gauss's divergence theorem,

$$\int_V (\rho\ddot{u}_i - f_i)w_i \mathrm{d}V + \int_S \sigma_{ij}\, n_j\, w_i\, \mathrm{d}S - \int_V \sigma_{ij,j}\ w_i\, \mathrm{d}V\ =\ \int_S p_i\, w_i\, \mathrm{d}S\,. \tag{1.13}$$

Assembling the volume and surface integrals together gives

$$\int_V (\rho\, \ddot{u}_i - \sigma_{ij,j} - f_i)\, w_i\, \mathrm{d}V = \int_S (p_i - \sigma_{ij}\, n_j)\, w_i\, \mathrm{d}S\,. \tag{1.14}$$

We can call eq. (1.14) the integral strong form of the equation of motion. It requires continuity of the first derivative of displacement. In eq. (1.14) we can specify boundary condition for traction at surface S by specifying values of p_i. Note that term 'integral strong form' was used by Robert J. Geller in our personal communication. We adopted this term for clear distinction of this formulation from the (differential) strong formulation and weak formulation.

2 Canonical Problem With a Material Interface

2.1 Problem Configuration

Modify the problem configuration shown in Fig. 1.1 by considering volume V split into two material volumes, $V = V^+ \cup V^-$, $S = S^+ \cup S^-$, separated by a smooth welded material interface (material discontinuity) Σ with a unit normal vector $\vec{\nu}$ pointing from volume V^- to volume V^+. The configuration is shown in Fig. 2.1.

Boundary conditions at the welded interface are

$$u_i^+\ =\ u_i^- \qquad \text{at } \Sigma \tag{2.1}$$

and

$$\sigma_{ij}^+\, \nu_j\ =\ \sigma_{ij}^-\, \nu_j \quad \text{at } \Sigma\,. \tag{2.2}$$

Boundary conditions at surface S can be written as

$$p_i^\pm\ =\ \sigma_{ij}^\pm\, n_j \quad \text{at } S^\pm \qquad \text{or} \qquad p_i\ =\ \sigma_{ij}\, n_j \quad \text{at } S\,. \tag{2.3}$$

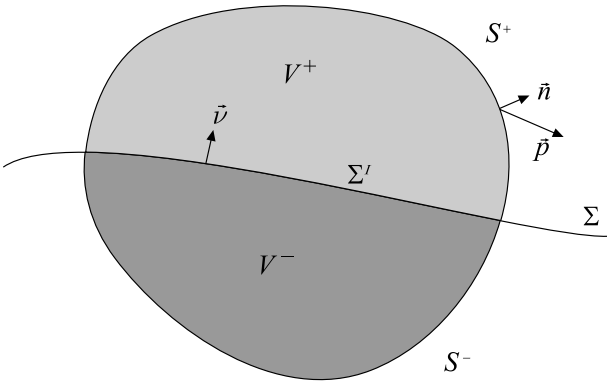

Fig. 2.1. Geometrical configuration of the canonical problem with a welded material interface Σ between media '$-$' and '$+$'.

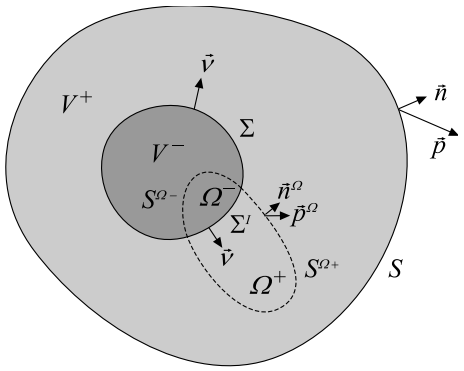

Fig. 2.2. Alternative geometrical configuration, say, the 'Earth-like configuration', of the canonical problem with a welded material interface Σ between media '$-$' and '$+$'. For this configuration we will give only the final formulations at the end of the chapter.

Alternatively we could modify the problem configuration shown in Fig. 1.1 by considering a 'core' inside volume V as shown in Fig. 2.2. Compared to configuration in Fig. 2.1 this one could be called the 'Earth-like configuration'. Because we are primarily interested in the numerical modeling of seismic wave propagation and earthquake motion in local near-surface structures, we will develop alternative formulations for the 'local configuration' in Fig. 2.1. At the end of this chapter, however, we will give a summary of formulations also for the 'Earth-like configuration'.

2.2 Strong Formulation (SF)

Applying eq. (1.6) to each of volumes V^- and V^+ we have

$$\rho^- \ddot{u}_i^- - \sigma_{ij}^-{}_{,j} - f_i^- \;=\; 0 \qquad \text{in the lower halfspace} \tag{2.4}$$

and

$$\rho^+ \ddot{u}_i^+ - \sigma_{ij}^+{}_{,j} - f_i^+ \;=\; 0 \qquad \text{in the upper halfspace}\,. \tag{2.5}$$

Equations (2.4) and (2.5) together with boundary conditions (2.1) - (2.3) make the strong formulation for our canonical problem with the welded material interface.

2.3 Weak Formulation (WF)

Considering our canonical problem with the welded material interface Σ we can apply eq. (1.11) to the whole volume $V = V^- \cup V^+$ or start with applications to each of the two volumes separately and continue with combination of the respective equations together with the welded-interface condition. We follow the latter approach in order to better show a structure of a final equation. The application of eq. (1.11) to volumes V^- and V^+ gives

$$\int_{V^-} (\rho^- \ddot{u}_i^- - f_i^-) w_i \mathrm{d}V + \int_{V^-} \sigma_{ij}^- w_{i,j}\,\mathrm{d}V \;=\; \int_{\partial V^-} p_i^- w_i \mathrm{d}S \tag{2.6}$$

and

$$\int_{V^+} (\rho^+ \ddot{u}_i^+ - f_i^+) w_i \mathrm{d}V + \int_{V^+} \sigma_{ij}^+ w_{i,j}\,\mathrm{d}V \;=\; \int_{\partial V^+} p_i^+ w_i \mathrm{d}S\,, \tag{2.7}$$

where

$$\partial V^\mp \;=\; S^\mp \cup \Sigma^I\,. \tag{2.8}$$

The surface integrals in eqs. (2.6) and (2.7) can be split:

$$\int_{\partial V^\mp} p_i^\mp w_i \mathrm{d}S \;=\; \int_{S^\mp} p_i^\mp w_i \mathrm{d}S + \int_{\Sigma^I} p_i^\mp w_i \mathrm{d}S\,. \tag{2.9}$$

Combining eqs. (2.6), (2.7) and (2.9) together with the welded-interface boundary condition,

$$p_i^-(\nu_j) \;=\; -\,p_i^+(-\nu_j) \qquad \text{at } \Sigma^I\,, \tag{2.10}$$

yields

$$\begin{aligned}\int_{V^-} (\rho^- \ddot{u}_i^- - f_i^-) w_i \mathrm{d}V \;+\; \int_{V^+} (\rho^+ \ddot{u}_i^+ - f_i^+) w_i \mathrm{d}V \;+ \\ + \int_{V^-} \sigma_{ij}^- w_{i,j}\,\mathrm{d}V \;+\; \int_{V^+} \sigma_{ij}^+ w_{i,j}\,\mathrm{d}V \;=\; \int_{S^-} p_i^- w_i \mathrm{d}S + \int_{S^+} p_i^+ w_i \mathrm{d}S\,.\end{aligned} \tag{2.11}$$

Equation (2.11) together with boundary condition (2.1) make a weak formulation for our canonical problem with the welded material interface.

2.4 Integral Strong Formulation (ISF)

Integration by parts of the third and fourth integrals on the l.h.s. of eq. (2.11) and subsequent application of Gauss's divergence theorem yields

$$\begin{aligned}\int_{V^-} \sigma_{ij}^- \, w_{i,j} \, \mathrm{d}V \, + \int_{V^+} \sigma_{ij}^+ \, w_{i,j} \, \mathrm{d}V = \qquad (2.12)\\ = \int_{\Sigma^I} \sigma_{ij}^- \, w_i \, \nu_j \, \mathrm{d}S \quad + \int_{S^-} \sigma_{ij}^- \, w_i \, n_j \, \mathrm{d}S - \int_{V^-} \sigma_{ij,j}^- \, w_i \, \mathrm{d}V + \\ + \int_{\Sigma^I} \sigma_{ij}^+ \, w_i \, (-\nu_j) \, \mathrm{d}S + \int_{S^+} \sigma_{ij}^+ \, w_i \, n_j \, \mathrm{d}S - \int_{V^+} \sigma_{ij,j}^+ \, w_i \, \mathrm{d}V.\end{aligned}$$

Substituting eq. (2.12) into eq. (2.11) yields

$$\begin{aligned}\int_{V^-} (\rho^- \ddot{u}_i^- - \sigma_{ij,j}^- - f_i^-) \, w_i \, \mathrm{d}V + \int_{V^+} (\rho^+ \ddot{u}_i^+ - \sigma_{ij,j}^+ - f_i^+) \, w_i \, \mathrm{d}V = \qquad (2.13)\\ = \int_{\Sigma^I} (\sigma_{ij}^+ - \sigma_{ij}^-) \, \nu_j \, w_i \, \mathrm{d}S + \int_{S^-} (p_i^- - \sigma_{ij}^- n_j) \, w_i \, \mathrm{d}S + \int_{S^+} (p_i^+ - \sigma_{ij}^+ n_j) \, w_i \, \mathrm{d}S \, .\end{aligned}$$

Compared to eq. (2.11), eq. (2.13) requires continuity of the first spatial derivatives of displacement (due to presence of the divergence of the stress tensor) while the requirement of continuity of the weight function is removed (due to performed integration by parts). Thus eq. (2.13) together with boundary condition (2.1) can be called an integral strong formulation for our canonical problem with the welded material interface.

2.5 Discontinuous Strong Formulation (DSF)

Let surface S (possibly a free – that is traction-free – surface or just a thought surface in the medium), material interface Σ, and volumes V^- and V^+ in our canonical problem be defined as

$$\begin{aligned}&\psi(x_k) < 0 \; ; \quad x_k \in \text{the lower halfspace except for } \Sigma,\\ &\psi(x_k) = 0 \; ; \quad x_k \in \Sigma, \qquad (2.14)\\ &\psi(x_k) > 0 \; ; \quad x_k \in \text{the upper halfspace except for } \Sigma,\end{aligned}$$

$$\begin{aligned}&\phi(x_k) < 0 \; ; \quad x_k \in V^- \cup V^+ \text{ except for } S,\\ &\phi(x_k) = 0 \; ; \quad x_k \in S, \qquad (2.15)\\ &\phi(x_k) > 0 \; ; \quad x_k \notin V^- \cup V^+,\end{aligned}$$

where ψ and ϕ are smooth functions of spatial coordinates. Then the normals to the surfaces Σ and S are

$$\nu_j = \psi_{,j} \qquad (2.16)$$

and

$$n_j = \phi_{,j} \; . \qquad (2.17)$$

Consider Heaviside unit step function

$$H(\xi) = \begin{cases} 0 & \xi < 0 \\ 1/2 \quad ; & \xi = 0 \\ 1 & \xi > 0\,. \end{cases} \tag{2.18}$$

Using definitions of surfaces Σ and S, eqs. (2.14) and (2.15), and Heaviside function we can express spatial distribution of quantities appearing in the equation of motion for our canonical problem in the following way:

$$\rho\,\ddot{u}_i = [\,\rho^-\ddot{u}_i^-\,H(-\psi) + \rho^+\ddot{u}_i^+\,H(\psi)\,]\;[\,H(-\phi) + K\,H(\phi)\,]\,, \tag{2.19}$$

$$\sigma_{ij} = [\quad \sigma_{ij}^-H(-\psi) + \quad \sigma_{ij}^+H(\psi)\,]\;[\,H(-\phi) + K\,H(\phi)\,]\,, \tag{2.20}$$

$$f_i = [\quad f_i^-\,H(-\psi) + \quad f_i^+H(\psi)\,]\;[\,H(-\phi) + K\,H(\phi)\,]\,. \tag{2.21}$$

Parameter K indicates presence/absence of material outside volume V. If $K = 1$, S is just a thought surface in the medium. If $K = 0$, S is a free surface.

Substituting eqs. (2.19) – (2.21) into the strong-form equation of motion (1.6) we obtain

$$[\,(\rho^-\ddot{u}_i^- - f_i^-)H(-\psi) + (\rho^+\ddot{u}_i^+ - f_i^+)H(\psi)\,]\;[\,H(-\phi) + K\,H(\phi)\,] \quad + \\ +\{\,[\,\sigma_{ij}^-H(-\psi) + \sigma_{ij}^+H(\psi)\,]\;[\,H(-\phi) + K\,H(\phi)\,]\}_{,j} = 0\,. \tag{2.22}$$

Considering

$$\{H(\pm\psi)\}_{,j} \;=\; \delta(\pm\psi)(\pm\psi_{,j}\,) \;=\; \pm\,\nu_j\,\delta(\psi)\,, \tag{2.23}$$

$$\{H(\pm\phi)\}_{,j} \;=\; \delta(\pm\phi)(\pm\phi_{,j}\,) \;=\; \pm\,n_j\,\delta(\phi)\,, \tag{2.24}$$

and differentiating the expression in braces in eq. (2.22), we obtain

$$\begin{aligned} &\{[\,\sigma_{ij}^-H(-\psi) + \sigma_{ij}^+H(\psi)\,]\,[\,H(-\phi) + K\,H(\phi)\,]\}_{,j} = \\ &\quad= [\,\sigma_{ij}^-H(-\psi) + \sigma_{ij}^+H(\psi)\,]\,[\,-n_j\,\delta(\phi) + K\,n_j\,\delta(\phi)\,] + \\ &\qquad + [\,\sigma_{ij}^-\,(-\nu_j)\,\delta(\psi) + \sigma_{ij}^+\,\nu_j\,\delta(\psi)\,]\,[\,H(-\phi) + K\,H(\phi)\,] + \\ &\qquad + [\,\sigma_{ij}^-{}_{,j}\,H(-\psi) + \sigma_{ij}^+{}_{,j}\,H(\psi)\,]\,[\,H(-\phi) + K\,H(\phi)\,] \\ &\quad= (K-1)\,\sigma_{ij}^-\,n_jH(-\psi)\,\delta(\phi) + (K-1)\,\sigma_{ij}^+\,n_jH(\psi)\,\delta(\phi) + \\ &\qquad + (\,\sigma_{ij}^+ - \sigma_{ij}^-\,)\,\nu_j\,\delta(\psi) + \\ &\qquad + [\,\sigma_{ij}^-{}_{,j}\,H(-\psi) + \sigma_{ij}^+{}_{,j}\,H(\psi)\,]\,[\,H(-\phi) + K\,H(\phi)\,]\,. \end{aligned} \tag{2.25}$$

Substituting eq. (2.25) into eq. (2.22) yields

$$\begin{aligned} &[\,(\rho^-\ddot{u}_i^- - \sigma_{ij}^-{}_{,j} - f_i^-)H(-\psi) \\ &+ (\rho^+\ddot{u}_i^+ - \sigma_{ij}^+{}_{,j} - f_i^+)H(\psi)\,]\,[\,H(-\phi) + K\,H(\phi)\,] = \\ &= (\,\sigma_{ij}^+ - \sigma_{ij}^-\,)\,\nu_j\,\delta(\psi) + \\ &+(K-1)\,\sigma_{ij}^-\,n_j\,H(-\psi)\,\delta(\phi) + (K-1)\,\sigma_{ij}^+\,n_j\,H(\psi)\,\delta(\phi)\,. \end{aligned} \tag{2.26}$$

The last two terms can be unified in one term

$$(K-1)\,\sigma_{ij}\,n_j\,\delta(\phi)\,. \tag{2.27}$$

Then

$$\begin{aligned}
&[\,(\,\rho^-\ddot{u}_i^- - \sigma_{ij}^-{}_{,j} - f_i^-\,)\,H(-\psi) \\
&+\,(\quad \rho^+\ddot{u}_i^+ - \sigma_{ij}^+{}_{,j} - f_i^+\,)\,H(\psi)\,]\,[\,H(-\phi) + K\,H(\phi)\,] = \\
&=\,(\,\sigma_{ij}^+ - \sigma_{ij}^-\,)\,\nu_j\,\delta(\psi) + (K-1)\,\sigma_{ij}\,n_j\,\delta(\phi)\,.
\end{aligned} \tag{2.28}$$

If surface S is just a thought surface in the medium, that is, $K = 1$, eq. (2.28) reduces to

$$\begin{aligned}
&(\,\rho^-\ddot{u}_i^- - \sigma_{ij}^-{}_{,j} - f_i^-\,)H(-\psi) \;+\; (\,\rho^+\ddot{u}_i^+ - \sigma_{ij}^+{}_{,j} - f_i^+\,)H(\psi) = \\
&\qquad\qquad = (\,\sigma_{ij}^+ - \sigma_{ij}^-\,)\,\nu_j\,\delta(\psi)\,.
\end{aligned} \tag{2.29}$$

If surface S is a free surface, that is, $K = 0$, eq. (2.28) becomes

$$\begin{aligned}
&[\,(\,\rho^-\ddot{u}_i^- - \sigma_{ij}^-{}_{,j} - f_i^-\,)H(-\psi) \;+\; (\,\rho^+\ddot{u}_i^+ - \sigma_{ij}^+{}_{,j} - f_i^+\,)H(\psi)\,]\,H(-\phi) = \\
&\qquad\qquad = (\,\sigma_{ij}^+ - \sigma_{ij}^-\,)\,\nu_j\,\delta(\psi) + (\,0 - \sigma_{ij}\,n_j\,)\,\delta(\phi)\,.
\end{aligned} \tag{2.30}$$

We wrote the last term on the r.h.s. of eq. (2.30) in a form of the last two terms on the r.h.s. of the integral strong-form equation (2.13) in order to point out the meaning of the term. We call eq. (2.28) or eqs. (2.29) and (2.30) together with boundary condition (2.1) a discontinuous strong formulation for our canonical problem. The developed representation was motivated by the idea of Zahradník and Priolo (1995) who used Heaviside step function to represent planar material interface.

2.6 Comparison of Formulations

The strong formulation, SF, eqs. (2.1) - (2.5), weak formulation, WF, eq. (2.11), integral strong formulation, ISF, eq. (2.13), and discontinuous strong formulation, DSF, eq. (2.28) are four alternative formulations we are able to find for our canonical problem with the welded material interface (Fig. 2.1). The formulations are given in Tab. 2.1 for a convenient visual comparison.

In addition to the basic differences explained in the chapter on the equation of motion for a smooth continuum we clearly see that the formulations differ in a way how they incorporate boundary conditions at interface Σ and surface S.

For completeness we also give summary of the alternative formulations for the 'Earth-like configuration' shown in Fig. 2.2 in Tab. 2.2.

There are three principal situations for a point of continuum for which one may try to find appropriate FD targets: a point in a smooth medium, point at a welded interface, and point at a free surface. A point in a continuous medium is easier to treat compared to the two latter situations. Later we will apply the above general formulations (SF, ISF and DSF) to the welded interface and free surface.

Tab. 2.1. Summary of formulations for the 3D canonical problem with the welded material interface (Fig. 2.1). WF - weak formulation, SF - strong formulation, ISF - integral strong formulation, DSF - discontinuous strong formulation.

	in volume V^- (also outside V^- in DSF)	in volume V^+ (also outside V^+ in DSF)	at interface Σ	at S
WF	$\int_{V^-}[(\rho^-\ddot{u}_i^- - f_i^-)w_i + \sigma_{ij}^- w_{i,j}]\,\mathrm{d}V$	$+\int_{V^+}[(\rho^+\ddot{u}_i^+ - f_i^+)w_i + \sigma_{ij}^+ w_{i,j}]\,\mathrm{d}V$		$= \int_S p_i w_i \mathrm{d}S$
			$u_i^- = u_i^+$	
SF	$\rho^-\ddot{u}_i^- - \sigma_{ij,j}^- - f_i^- = 0$	$\rho^+\ddot{u}_i^+ - \sigma_{ij,j}^+ - f_i^+ = 0$	$\sigma_{ij}^-\nu_j = \sigma_{ij}^+\nu_j$	$p_i = \sigma_{ij}n_j$
			$u_i^- = u_i^+$	
ISF	$\int_{V^-}(\rho^-\ddot{u}_i^- - \sigma_{ij,j}^- - f_i^-)w_i\mathrm{d}V$	$+\int_{V^+}(\rho^+\ddot{u}_i^+ - \sigma_{ij,j}^+ - f_i^+)w_i\mathrm{d}V$	$= \int_\Sigma(\sigma_{ij}^+ - \sigma_{ij}^-)\nu_j w_i \mathrm{d}S$	$+\int_S(p_i - \sigma_{ij}n_j)w_i\mathrm{d}S$
			$u_i^- = u_i^+$	
DSF	$(\rho^-\ddot{u}_i^- - \sigma_{ij,j}^- - f_i^-)\,H(-\psi)H(-\phi)$	$+(\rho^+\ddot{u}_i^+ - \sigma_{ij,j}^+ - f_i^+)\,H(\psi)H(-\phi)$		
	$(\rho^-\ddot{u}_i^- - \sigma_{ij,j}^- - f_i^-)\,H(-\psi)K\,H(\phi)$	$+(\rho^+\ddot{u}_i^+ - \sigma_{ij,j}^+ - f_i^+)\,H(\psi)K\,H(\phi)$	$= (\sigma_{ij}^+ - \sigma_{ij}^-)\nu_j\delta(\psi)$	$+(K-1)\sigma_{ij}n_j\delta(\phi)$
			$u_i^- = u_i^+$	
	$K = 0$: S is a free surface	$K = 1$: S is a thought surface		

Tab. 2.2. Summary of formulations for the alternative 'Earth-like configuration' shown in Fig. 2.2. WF - weak formulation, SF - strong formulation, ISF - integral strong formulation, DSF - discontinuous strong formulation.

	in volume V^-	in volume V^+ (also outside V^+ in DSF)	at interface Σ	at S
WF	$\int_{V^-}[(\rho^-\ddot{u}_i^- - f_i^-)w_i + \sigma_{ij}^- w_{i,j}]\,\mathrm{d}V$	$+\int_{V^+}[(\rho^+\ddot{u}_i^+ - f_i^+)w_i + \sigma_{ij}^+ w_{i,j}]\,\mathrm{d}V$		$= \int_S p_i w_i \mathrm{d}S$
			$u_i^- = u_i^+$	
SF	$\rho^-\ddot{u}_i^- - \sigma_{ij,j}^- - f_i^- = 0$	$\rho^+\ddot{u}_i^+ - \sigma_{ij,j}^+ - f_i^+ = 0$	$\sigma_{ij}^-\nu_j = \sigma_{ij}^+\nu_j$	$p_i = \sigma_{ij}^+ n_j$
			$u_i^- = u_i^+$	
ISF	$\int_{V^-}(\rho^-\ddot{u}_i^- - \sigma_{ij,j}^- - f_i^-)w_i\mathrm{d}V$	$+\int_{V^+}(\rho^+\ddot{u}_i^+ - \sigma_{ij,j}^+ - f_i^+)w_i\mathrm{d}V$	$= \int_\Sigma(\sigma_{ij}^+ - \sigma_{ij}^-)\nu_j w_i \mathrm{d}S$	$+\int_S(p_i - \sigma_{ij}^+ n_j)w_i\mathrm{d}S$
			$u_i^- = u_i^+$	
DSF	$(\rho^-\ddot{u}_i^- - \sigma_{ij,j}^- - f_i^-)\,H(-\psi)$	$+(\rho^+\ddot{u}_i^+ - \sigma_{ij,j}^+ - f_i^+)\,H(\psi)H(-\phi)$		
		$+(\rho^+\ddot{u}_i^+ - \sigma_{ij,j}^+ - f_i^+)\,H(\psi)K\,H(\phi)$	$= (\sigma_{ij}^+ - \sigma_{ij}^-)\nu_j\delta(\psi)$	$+(K-1)\sigma_{ij}^+ n_j\delta(\phi)$
			$u_i^- = u_i^+$	
	$K = 0$: S is a free surface	$K = 1$: S is a thought surface		

Tab. 2.3. Summary of formulations for the 1D canonical problem with the welded material interface (Fig. 2.3). WF - weak formulation, SF - strong formulation, ISF - integral strong formulation, DSF - discontinuous strong formulation.

	in '$-$' medium	in '$+$' medium	at interface $z=a$	at 0 at b
WF	$\int_0^a [(\rho^- \ddot{u}^- - f^-)w + \sigma^- w_{,z}]\,\mathrm{d}z$	$+\int_a^b [(\rho^+ \ddot{u}^+ - f^+)w + \sigma^+ w_{,z}]\,\mathrm{d}z$		$= p^-(0)w(0)$ $+ p^+(b)w(b)$
			$u^-(a) = u^+(a)$	
SF	$\rho^- \ddot{u}^- - \sigma^-_{,z} - f^- = 0$	$\rho^+ \ddot{u}^+ - \sigma^+_{,z} - f^+ = 0$	$\sigma^-(a) = \sigma^+(a)$	$p^-(0) = -\sigma^-(0)$ $p^+(b) = \sigma^+(b)$
			$u^-(a) = u^+(a)$	
ISF	$\int_0^a (\rho^- \ddot{u}^- - \sigma^-_{,z} - f^-)w\,\mathrm{d}z$	$+\int_a^b (\rho^+ \ddot{u}^+ - \sigma^+_{,z} - f^+)w\,\mathrm{d}z$	$= [\sigma^+(a) - \sigma^-(a)]w(a)$	$+ [p^-(0) - \sigma^-(0)]w(0)$ $+ [p^+(b) - \sigma^+(b)]w(b)$
			$u^-(a) = u^+(a)$	
DSF	$(\rho^- \ddot{u}^- - \sigma^-_{,z} - f^-)\, H(z) H(a-z)$	$+(\rho^+ \ddot{u}^+ - \sigma^+_{,z} - f^+)\, H(z-a) H(b-z)$		
	$(\rho^- \ddot{u}^- - \sigma^-_{,z} - f^-)\, K_0 H(-z)$	$+(\rho^+ \ddot{u}^+ - \sigma^+_{,z} - f^+)\, K_b H(z-b)$	$= (\sigma^+ - \sigma^-)\delta(z-a)$	$- (K_0 - 1)\sigma^-\delta(z)$ $+ (K_b - 1)\sigma^+\delta(z-b)$
			$u^-(a) = u^+(a)$	
	$K_0 = 1 : S_0$ is an integration surface	$K_b = 1 : S_b$ is an integration surface		
	$K_0 = 0 : S_0$ is a free surface	$K_b = 0 : S_b$ is a free surface		

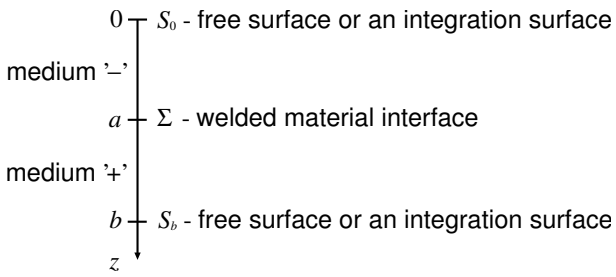

Fig. 2.3. Geometrical configuration of the 1D canonical problem with a welded material interface Σ between media '$-$' and '$+$'.

2.7 Formulations for a 1D Canonical Problem With a Material Interface

Here we apply the above formulations to a 1D problem. Although the 1D problem is relatively far from problems for realistic models of real structures in nature, it is obvious that it is methodologically basic and thus important. It is also convenient for introducing basic approaches.

2.7.1 Problem Configuration

The geometrical configuration of the 1D canonical problem with the welded material interface is shown in Fig. 2.3 The model is a 1D version of the 3D model shown in Fig. 2.1

2.7.2 The SF, WF, ISF and DSF Formulations

Considering the configuration of the 1D problem in Fig. 2.3 and normal vectors at surfaces S_0, Σ and S_b,

$$\vec{n}\,(S_0) \;=\; (\,0,\;0,-1\,), \tag{2.31}$$

$$\vec{\nu}\,(\Sigma) \;=\; (\,0,\;0,\quad 1\,), \tag{2.32}$$

$$\vec{n}\,(S_b) \;=\; (\,0,\;0,\quad 1\,), \tag{2.33}$$

it is straightforward to obtain formulations for the 1D problem from those given in Tab. 2.1 for the 3D problem. For a convenient visual comparison, the formulations are given in Tab. 2.3.

3 Canonical Problem with a Faulting Surface

3.1 Simple Model of an Earthquake Source

In many seismological problems an earthquake fault may be represented by a surface embedded in heterogeneous elastic or viscoelastic pre-stressed medium. A non-zero initial equilibrium stress is due to tectonic loading and residual stress after previous earthquakes on the fault. An earthquake itself may be modeled as spontaneous rupture propagation along the fault. The rupture generates seismic waves which then propagate from the fault into the embedding medium.

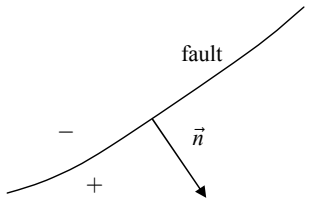

Fig. 3.1. Fault surface and the normal vector $\vec{n}$.

In general, several ruptures can propagate along the fault at one time. Inside the rupture displacement and particle-velocity vectors are discontinuous across the fault. At the same time traction is continuous. Let $\vec{n}\,(x_i)$ be a unit normal vector to the fault surface pointing from the '$-$' to '$+$' side of the surface (Fig. 3.1). Then slip, that is, discontinuity in displacement vector across the fault, can be defined as

$$D\vec{u}(x_i,t) \;=\; \vec{u}^{\,+}(x_i^+,t) \;-\; \vec{u}^{\,-}(x_i^-,t)\;. \tag{3.1}$$

Its time derivative, slip rate, that is, discontinuity in the particle-velocity vector across the fault, is then

$$D\vec{v}(x_i,t) \;=\; \vec{v}^{\,+}(x_i^+,t) \;-\; \vec{v}^{\,-}(x_i^-,t)\;. \tag{3.2}$$

The total traction on the fault is

$$\vec{T}(\vec{n};x_i,t) \;=\; \vec{T}^0(\vec{n};x_i) \;+\; \Delta\vec{T}(\vec{n};x_i,t)\;, \tag{3.3}$$

where $\vec{T}^0\,(\vec{n};x_i)$ is the initial traction and $\Delta\vec{T}\,(\vec{n};x_i,t)$ traction variation. The latter is due to the rupture propagation. Inside the rupture the total traction is related to slip at the same point of the fault through the friction law

$$\vec{T} \;=\; \vec{T}^f\,(D\vec{u},D\vec{v},\theta) \tag{3.4}$$

where $\vec{T}^f$ is frictional traction and θ represents a set of state variables. Equation (3.4), a fault constitutive law, means that the total dynamic traction on the fault is determined by the friction. Given the initial traction and material parameters of the fault, it is the friction law which controls initialization, propagation and healing (arrest) of the rupture.

3.2 Equations and Boundary Conditions for a Dynamic Shear Faulting

Consider further only shear faulting. This means that there is no opening of the fault and no interpenetrating of the fault materials. Define frictional strength or fault friction as

$$S \;=\; \mu_f\,\left|\,\vec{T}_n\right|\,, \tag{3.5}$$

where μ_f and $\vec{T}_n$ are coefficient of friction and fault-normal component of traction on the fault, respectively. First, assume a locked fault. If, at a point of the fault surface, the magnitude of

the shear traction (that is, traction tangential to the fault surface) is smaller than the frictional strength the fault remains locked and slip rate zero at the point. Should the shear traction exceed the frictional strength, slip occurs. The shear traction then varies following the friction law and eventually falls down to the dynamic frictional level. The slipping is opposed by the friction.

Let subscripts sh and n denote the shear and normal components with respect to the fault surface. The boundary conditions on the fault can be formulated, Day (1982), Day et al. (2005), as follows.

Shear faulting:

$$D\vec{u}_n \;=\; 0, \quad D\vec{v}_n \;=\; 0, \quad D\vec{u}_{sh} \;\neq\; 0, \quad D\vec{v}_{sh} \;\neq\; 0\;. \tag{3.6}$$

Shear traction bounded by the frictional strength:

$$\left|\,\vec{T}_{sh}\,\right| \;\leq\; S\;. \tag{3.7}$$

Colinearity of the shear traction and slip rate:

$$S\;D\vec{v}_{sh} \;-\; \vec{T}_{sh}\,(\vec{n})\;\left|D\vec{v}_{sh}\right| \;=\; 0\;. \tag{3.8}$$

The fact that the frictional traction opposes the slipping is consistent with the colinearity requirement because we consider vector $\vec{n}$ oriented in the direction from the '$-$' to '$+$' side of the fault and slip as the relative motion of the '$+$' side with respect to the '$-$' side of the fault: both $\vec{T}\,(\vec{n})$ and $D\vec{v}$ are viewed from the same side of the fault. If slip was defined as the relative motion of the '$-$' side with respect to the '$+$' side of the fault, requirement of the antiparallelism with the '$+$' sign in eq. (3.8) would be consistent with the frictional traction opposing the relative motion of the fault faces.

3.3 Friction Law

When a rupture front reaches a point of the fault and slip starts at that point (that is, the two originally neighboring points, one at the '$-$' and the other at the '$+$' side of the fault, start slipping), the total dynamic traction varies following the friction law and eventually falls down to the dynamic frictional level. Obviously, before the traction at the point reaches the dynamic frictional level, points of the fault in front of the considered point start slipping. Thus, the process of the traction degradation obviously occurs within a finite zone behind the so-called crack tip. This zone is termed cohesive zone or breakdown zone. The friction law determines processes and phenomena in the cohesive zone.

Following Bizzarri and Cocco (2005), the coefficient of friction can be function of several quantities,

$$\mu_f \;=\; \mu_f\left(\, l, |D\vec{v}|\,, \Psi_1, ..., \Psi_N, T, H, \lambda_c, h_m, g, C_e\,\right)\;, \tag{3.9}$$

where l is the slip path length

$$l = \int_0^t |D\vec{v}|(t')\,\mathrm{d}t'\;, \tag{3.10}$$

$|D\vec{v}|$ is modulus of the slip rate, $\Psi_1, ..., \Psi_N$ state variables, T temperature accounting for ductility, plastic flow, rock melting and vaporization, H humidity, λ_c characteristic length of the fault surface accounting for roughness and topography of asperity contacts and possibly responsible for mechanical lubrication, h_m material hardness, g gouge parameter accounting for surface consumption and gouge formation during sliding episodes, C_e chemical environment parameter. In general, fault-normal traction in eq. (3.5) should stand for a time-dependent effective normal traction accounting for a pore fluid pressure (which reduces the normal traction).

Equation (3.9) is in its full generality a very complicated constitutive law and one can expect that its incorporation in the numerical simulation of rupture propagation is far from trivial one for at least two reasons – methodological complexity and determination of values of all parameters.

According Cocco and Bizzarri (2002) and Bizzarri and Cocco (2003), two main groups of the friction laws were proposed – slip-dependent (Barenblatt, 1959; Ida, 1972; Palmer and Rice, 1973; Andrews, 1976a,b; Ohnaka and Yamashita, 1989) and rate- and state-dependent (Dieterich, 1979, 1986; Ruina, 1980, 1983; Okubo and Dieterich, 1984; Okubo, 1989; Beeler et al., 1994, other authors).

Here we restrict to the linear slip-weakening (SW) friction law as formulated by Ida (1972) and Andrews (1976a,b), and the rate- and state-dependent (R&S) friction law as formulated by Beeler et al. (1994).

3.3.1 Linear Slip-weakening (SW) Friction Law

Value of the coefficient of friction in the linear SW friction law decreases linearly from the value of the coefficient of static friction, μ_s, down to the value of the coefficient of kinematic (also called dynamic) friction, μ_d, over a characteristic (also called critical) distance D_c :

$$\begin{aligned} \mu_f &= \mu_s - \frac{\mu_s - \mu_d}{D_c}\, l \qquad ; \quad l < D_c\,, \\ \mu_f &= \mu_d \qquad\qquad\qquad\quad ; \quad l \geq D_c\,. \end{aligned} \tag{3.11}$$

Equivalently, the SW friction law can be expressed in terms of the corresponding shear tractions:

$$\begin{aligned} |\vec{T}^f_{sh}| &= |\vec{T}^s_{sh}| - \frac{|\vec{T}^s_{sh}| - |\vec{T}^d_{sh}|}{D_c}\, l \;\; ; \quad l < D_c\,, \\ |\vec{T}^f_{sh}| &= |\vec{T}^d_{sh}| \qquad\qquad\qquad\quad ; \quad l \geq D_c\,. \end{aligned} \tag{3.12}$$

Here $|\vec{T}^s_{sh}|$ and $|\vec{T}^d_{sh}|$ are the static (also called yield) and kinematic frictional shear tractions, respectively. In other words, the frictional strength depends only on a cumulative slip path length. Considering the SW friction law means that the evolution of the traction on the fault is 'prescribed' a priori. Though the SW friction law is relatively very simple, in practical applications it is, in fact, very difficult to estimate or determine reasonable values of coefficients of the static and kinematic frictions, and value of the critical distance.

3.3.2 Rate- and State-dependent (R&S) Friction Law

Value of the coefficient of friction in the R&S friction law depends on modulus of the slip rate, $|D\vec{v}_{sh}|$, and one state variable, Ψ :

$$\begin{aligned} \mu_f &= \mu\left(\,|D\vec{v}_{sh}|\,,\Psi\,\right)\,, \\ \frac{\mathrm{d}\Psi}{\mathrm{d}t} &= g\left(\,|D\vec{v}_{sh}|\,,\Psi\,\right)\,. \end{aligned} \tag{3.13}$$

Depending on the functional form for μ and g, there are several constitutive relations, see, for example, Beeler et al. (1994). The most commonly used R&S friction law is the law presented by Dieterich (1986):

$$\begin{aligned} \mu_f &= \mu_r \,-\, a\,\ln\frac{v_r}{|D\vec{v}_{sh}|} \,+\, b\,\ln\frac{\Psi\, v_r}{L}\,, \\ \frac{\mathrm{d}\Psi}{\mathrm{d}t} &= 1 \,-\, \frac{\Psi\;|D\vec{v}_{sh}|}{L}\,. \end{aligned} \tag{3.14}$$

Here a, b and L are constitutive parameters, μ_r and v_r reference values. The second equations in (3.13) and (3.14) describe evolution of the state variable. Unlike the SW friction law, the yield and kinematic frictional tractions are not prescribed a priori, they depend on the slip rate and state variable. Though the R&S friction law as formulated by eq. (3.14) does not explicitly include dependence on the slip path length, the law yields the slip-weakening Cocco and Bizzarri (2002). Cocco and Bizzarri (2002) and Bizzarri and Cocco (2003, 2005) compared the two friction laws in detail.

It is obvious that the implementation of the R&S friction law in the numerical-simulation methods is more complicated compared to the SW friction law.

3.4 Traction-at-Split-Nodes (TSN) Method

The discontinuity of displacement vector and particle-velocity vector together with the friction law pose a nontrivial boundary condition. While semi-analytical boundary integral equation (BIE) method is perhaps the most accurate method to account for the fault boundary conditions, especially on non-planar faults (e.g., Aochi and Fukuyama, 2002), its application is limited because it cannot include heterogeneity of the medium. Because the grid methods as the finite-difference, finite-element or spectral-element methods are computationally more efficient in accounting for material heterogeneity, they have been extensively applied to study source dynamics. Having in mind the grid numerical methods we explain here probably the most efficient method of incorporation of the fault boundary conditions for computation of rupture propagation and wave radiation, the traction-at-split-nodes (TSN) method. The TSN method has been developed independently by Andrews (1973, 1976a,b, 1999) and Day (1977, 1982); see also Day et al. (2005). For a brief review of other approaches in the grid methods see Moczo et al. (2007).

In the split-node approach the fault is represented by a grid surface of split (partial) nodes. Here, the grid simply means a set of discrete points properly distributed on the fault surface. At a grid point, each of the two partial nodes belongs to only one side of the fault and the two nodes may experience a relative motion (slip) along the fault.

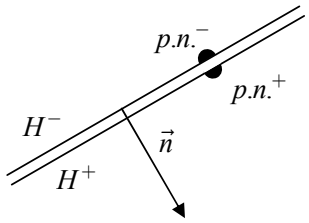

Fig. 3.2. Halfspaces H^- and H^+, partial nodes $p.n.^-$ and $p.n.^+$, and the normal vector $\vec{n}$.

Consider a halfspace H^- covered by a grid and a partial node $p.n.^-$ on the free surface of the halfspace. Similarly, consider halfspace H^+ and a partial node $p.n.^+$ on its free surface (Fig. 3.2). Correspondingly, the partial nodes at one position differ in the 'halfspace' properties/quantities (for example, mass, displacement, particle-velocity, forces, material parameters). However, they share the same grid position and the 'fault' properties/quantities (for example, slip, slip-rate, friction, coefficients of friction).

Define an outer normal vector $\vec{n}$ to the surface of the halfspace H^- pointing to the halfspace H^+ (i.e., $\vec{n}$ is in the '$p.n.^- \rightarrow p.n.^+$' direction). Let M^- and M^+ be masses of the two partial nodes. The partial node $p.n.^-$ is accelerated by a force $\vec{F}^-$ which is due to deformation in the halfspace H^- and, possibly, by body forces acting in the halfspace. Similarly, the partial node $p.n.^+$ is accelerated by a force $\vec{F}^+$. Thus, the accelerations are

$$\vec{a}^{\,\pm} \;=\; \frac{\vec{F}^{\pm}}{M^{\pm}} \,. \tag{3.15}$$

In order to simulate a fault, halfspaces H^- and H^+ can be coupled along their surfaces. The coupling can be accomplished by a constraint surface traction acting at the contact. Consider a traction $\vec{T}^c(\vec{n})$ quantifying a contact force with which material in H^+ acts upon material in H^-. Let A be an area of the fault surface associated with each partial node. The acceleration $\vec{a}^-$ of the partial node $p.n.^-$ is contributed by force $\vec{F}^-$ due to deformation in halfspace H^- and by the constraint force

$$\vec{F}^{c,-} \;=\; \vec{F}^c \;=\; A \cdot \vec{T}^c(\vec{n}) \tag{3.16}$$

due to the action of halfspace H^+. Then the acceleration is

$$\vec{a}^- \;=\; \frac{1}{M^-}\left(\vec{F}^- + \vec{F}^{c,-}\right) \;=\; \frac{1}{M^-}\left(\vec{F}^- + A \cdot \vec{T}^c\right). \tag{3.17}$$

Similarly, the acceleration $\vec{a}^+$ of the partial node $p.n.^+$ is contributed by force $\vec{F}^+$ due to deformation in halfspace H^+ and by the constraint force

$$\vec{F}^{c,+} \;=\; -\vec{F}^c \;=\; -A \cdot \vec{T}^c(\vec{n}) \tag{3.18}$$

due to the action of halfspace H^-. The acceleration of the partial node $p.n.^+$ is then

$$\vec{a}^+ \;=\; \frac{1}{M^+}\left(\vec{F}^+ + \vec{F}^{c,+}\right) \;=\; \frac{1}{M^+}\left(\vec{F}^+ - A \cdot \vec{T}^c\right). \tag{3.19}$$

Consider some initial equilibrium state described by initial traction $\vec{T}^0(\vec{n})$. The traction does not contribute to the acceleration of the partial node $p.n.^-$. If $\vec{T}^c$ is the total traction, only the difference $\vec{T}^c - \vec{T}^0$ contributes to the acceleration. Then accelerations at time t are

$$\vec{a}^{\pm}(t) \;=\; \frac{1}{M^{\pm}} \left\{ \vec{F}^{\pm}(t) \;\mp\; A \cdot \left[\vec{T}^c(t) - \vec{T}^0 \right] \right\}. \tag{3.20}$$

Though the initial traction is nonzero, the initial strain is considered zero. Then forces $\vec{F}^{\pm}$ correspond to deformations caused only by the dynamic changes due to rupture. The particle velocities and displacements of the partial nodes in the 2^{nd}-order approximation are then

$$\vec{v}^{\pm}\left(t + \frac{\mathrm{d}t}{2}\right) \;=\; \vec{v}^{\pm}\left(t - \frac{\mathrm{d}t}{2}\right) \;+\; \frac{\mathrm{d}t}{M^{\pm}} \left\{ \vec{F}^{\pm}(t) \;\mp\; A \cdot \left[\vec{T}^c(t) \;-\; \vec{T}^0 \right] \right\} \tag{3.21}$$

and

$$\vec{u}^{\pm}(t + \mathrm{d}t) \;=\; \vec{u}^{\pm}(t) \;+\; \mathrm{d}t \cdot \vec{v}^{\pm}\left(t + \frac{\mathrm{d}t}{2}\right). \tag{3.22}$$

For the slip rate we obtain from eq. (3.21)

$$\begin{aligned} D\vec{v}\left(t + \frac{\mathrm{d}t}{2}\right) \doteq \\ D\vec{v}\left(t - \frac{\mathrm{d}t}{2}\right) \;+\; \mathrm{d}t\; B \left\{ \frac{M^- \vec{F}^+(t) \;- M^+ \vec{F}^-(t)}{A \cdot (M^- + M^+)} \;-\; \left[\vec{T}^c(t) \;+\; \vec{T}^0 \right] \right\}, \end{aligned} \tag{3.23}$$

where

$$B \;=\; A\, \frac{M^- + M^+}{M^- M^+}. \tag{3.24}$$

Find a constraint traction $\vec{T}^c(t) = \vec{T}^{ct}(t)$ that assures zero slip rate before two partial nodes start slipping as well as vanishing slip rate when the slipping ceases. Because $\vec{T}^{ct}(t)$ has to be evaluated at each time level at each grid point on the fault and compared with the frictional strength, it is called trial traction. The question is how to time condition $D\vec{v} = 0$. If $D\vec{v}(t) = 0$ is required, the trial traction acts for the interval from $t - \mathrm{d}t/2$ to $t + \mathrm{d}t/2$ and can reverse the slipping (that is, produce back-slip) by the time it is integrated all the way up to $t + \mathrm{d}t/2$. This results in the traction driving slip rather than opposing it and thus in violating conservation of energy (Day, 2005, personal communication). Therefore, $D\vec{v}\,(t + \mathrm{d}t/2) = 0$ has to be required. Assuming $D\vec{v}\,(t + \mathrm{d}t/2) = 0$ in eq. (3.23) we obtain the trial traction

$$\vec{T}^{ct}(t) \;\doteq\; \vec{T}^{\,0} \;+\; \frac{\mathrm{d}t^{-1} M^- M^+ D\vec{v}\left(t - \frac{\mathrm{d}t}{2}\right) \;+\; M^- \vec{F}^+(t) - M^+ \vec{F}^-(t)}{A \cdot (M^- + M^+)}. \tag{3.25}$$

We also have to find a constraint traction during the slip, that is, frictional traction $\vec{T}^c_{sh}(t) = \vec{T}^f_{sh}(t)$ such that $D\vec{v}\,(t + \mathrm{d}t/2) \neq 0$. Assuming first $D\vec{v}\,(t + \mathrm{d}t/2) \neq 0$ for $\vec{T}^c_{sh}(t) = \vec{T}^f_{sh}(t)$ in eq. (3.23), and then $D\vec{v}\,(t + \mathrm{d}t/2) = 0$ for $\vec{T}^c(t) = \vec{T}^{ct}(t)$ leads to

$$D\vec{v}_{sh}\left(t + \frac{\mathrm{d}t}{2}\right) \doteq \mathrm{d}t\; B \left[\vec{T}^{ct}_{sh}(t) \;-\; \vec{T}^f_{sh}(t) \right]. \tag{3.26}$$

Recall the colinearity condition (3.8):

$$S(t)\, D\vec{v}_{sh}(t) \;-\; \vec{T}^{f}_{sh}(t)\; |\, D\vec{v}_{sh}(t)\,| \;=\; 0\;. \tag{3.27}$$

Using approximation

$$D\vec{v}_{sh}(t) \;\doteq\; \tfrac{1}{2}\left[\; D\vec{v}_{sh}\left(t-\frac{\mathrm{d}t}{2}\right) \;+\; D\vec{v}_{sh}\left(t+\frac{\mathrm{d}t}{2}\right)\;\right] \tag{3.28}$$

and eq. (3.26) we obtain from the colinearity (3.27)

$$\left[\;|D\vec{v}_{sh}(t)| \;+\; S(t)\,\frac{\mathrm{d}t}{2}\,B\;\right]\;\vec{T}^{f}_{sh}(t) \doteq \frac{S(t)}{2}\;\left[\; D\vec{v}_{sh}\left(t-\frac{\mathrm{d}t}{2}\right) \;+\; \mathrm{d}t\; B\;\vec{T}^{ct}_{sh}(t)\;\right]. \tag{3.29}$$

Define an auxiliary vector $\vec{\gamma}$

$$\vec{\gamma} \;=\; D\vec{v}_{sh}\left(t-\frac{\mathrm{d}t}{2}\right) \;+\; \mathrm{d}t\, B\,\vec{T}^{ct}_{sh}(t)\;. \tag{3.30}$$

Equations (3.29) and (3.30) imply that $\vec{T}^{f}_{sh}(t)$ has the direction of vector $\vec{\Upsilon} \;=\; \vec{\gamma}\,/\,|\vec{\gamma}|$. Therefore, the enforcement of the boundary conditions on the fault can be formulated as follows:

$$\text{If}\quad \left|\vec{T}^{ct}_{sh}(t)\right| \;\le\; S(t)\quad \text{then}\quad \vec{T}^{c}(t) \;=\; \vec{T}^{ct}(t)\;. \tag{3.31}$$

$$\text{If}\quad \left|\vec{T}^{ct}_{sh}(t)\right| \;>\; S(t)\quad \text{then}\quad \vec{T}^{c}_{sh}(t) \;=\; S(t)\,\vec{\Upsilon}\;,\quad \vec{T}^{c}_{n}(t) \;=\; \vec{T}^{ct}_{n}(t)\;. \tag{3.32}$$

The above approach, based on finding trial traction $\vec{T}^{ct}(t)$ ensuring $D\vec{v}\,(t+\mathrm{d}t/2) \;=\; 0$, and colinearity requirement at time t, can cause in some rare cases large oscillations of rake direction just around the time of rupture arrest (Day, 2005, personal communication). Day avoids the problem by modifying the colinearity condition:

$$S(t)\, D\vec{v}_{sh}\left(t+\frac{\mathrm{d}t}{2}\right) \;-\; \vec{T}^{f}_{sh}(t)\;\left|\, D\vec{v}_{sh}\left(t+\frac{\mathrm{d}t}{2}\right)\,\right| \;\doteq\; 0\;. \tag{3.33}$$

Substitution of eq. (3.26) into eq. (3.33) yields

$$\left[\; S(t) + \left|\,\vec{T}^{ct}_{sh}(t) \;-\; \vec{T}^{f}_{sh}(t)\right|\;\right]\;\vec{T}^{f}_{sh}(t) \;\doteq\; S(t)\,\vec{T}^{ct}_{sh}(t). \tag{3.34}$$

Equation (3.34) means that $\vec{T}^{f}_{sh}(t)$ has the same direction as $\vec{T}^{ct}(t)$. Then condition (3.32) is replaced by the following condition:

$$\begin{aligned}\text{If}\quad \left|\,\vec{T}^{ct}_{sh}(t)\right| \;>\; S(t)\quad \text{then}\quad \vec{T}^{c}_{sh}(t) \;&=\; S(t)\,\frac{\vec{T}^{ct}_{sh}(t)}{\left|\,\vec{T}^{ct}_{sh}(t)\right|}\;,\\ \vec{T}^{c}_{n}\;(t) \;&=\; \vec{T}^{ct}_{n}(t)\,.\end{aligned} \tag{3.35}$$

The modified approach behaves always well (Day, 2005, personal communication).

The slip rate is then

$$D\vec{v}_{sh}\left(t+\frac{\mathrm{d}t}{2}\right) \doteq \mathrm{d}t\ B\ \left[\ \vec{T}^{ct}_{sh}(t)\ -\ \vec{T}^{c}_{sh}(t)\ \right]\ , \tag{3.36}$$

where $\vec{T}^{c}_{sh}(t)$ is given by eq. (3.31) or eq. (3.35).

Note that an assumption of the small displacements is necessary for the TSN method. The assumption means that the accumulating slip does not change the configuration of the partial nodes adjacent to each other. This means that $h \gg |D\vec{u}_{sh}|$, where h is a spatial grid spacing. Another necessary condition is that the time-stepping algorithm is explicit and a force at a node accelerates only that node.

Accuracy of the TSN implementation heavily depends on the accuracy of calculation of the body forces $\vec{F}^{\pm}$ due to deformations in the halfspaces. Formally, at each time the surfaces of the halfspaces are the free surfaces.

3.5 Kinematic Model of an Earthquake Source

In many applications kinematic models of the earthquake source are used instead of the dynamic models. In the kinematic models rupture propagation is simulated using a set of point sources distributed along the fault surface. Each point source acts independently of other point sources. Each point source is a body-force equivalent (acting in a continuous medium) to a point with a nonzero slip (displacement discontinuity) – both produce the same displacement field. Timing of the point sources along the fault surface and their source-time functions (a source-time function corresponds to a time history of slip at a point) are determined prior a numerical simulation itself by a so-called kinematic inversion of the earthquake source. The kinematic inversion is a procedure aiming to fit records of earthquake motion at different observation points around the ruptured fault. It is clear that in the kinematic modeling the point sources do not physically interact with the medium.

In some applications it is sufficient to consider only an effective point-source approximation to a true finite faulting surface.

The corresponding theory is well explained in many textbooks and monographs, e.g., Aki and Richards (1980, 2002), Kostrov and Das (1988), Gubbins (1990), Kennett (2001), Pujol (2003). Here we restrict to a very brief review of basic relations necessary for later explanation of the simulation of the kinematic sources in the grid numerical methods.

The displacement at $\vec{x}$ and time t due to faulting surface Σ can be expressed by the representation theorem

$$u_n(\vec{x},t) \ =\ \int_{\Sigma} m_{pq} * G_{np,q}\ \mathrm{d}\Sigma\ . \tag{3.37}$$

Here m_{pq} is the moment-density tensor

$$m_{pq}\,(\vec{\xi},t) \ =\ c_{pqrs}\,(\vec{\xi})\ Du_r(\vec{\xi},t)\ n_s(\vec{\xi})\,, \tag{3.38}$$

where $\vec{\xi}$ specifies a position on a fault surface Σ, c_{pqrs} is a tensor of elastic moduli, $D\vec{u}$ is a slip vector and $\vec{n}$ is a fault normal. $G_{np,q}$ is a derivative of the Green's tensor. $G_{np,q}$ is

physically an equivalent of having a single couple with an arm in the q-direction and forces in the p-direction on a fault surface Σ at $\vec{\xi}$. Convolution $m_{pq} * G_{np,q}$ is a displacement at $\vec{x}$ due to couples at $\vec{\xi}$, and m_{pq} is the strength of the $(p,\ q)$ couple.

In the point-source approximation surface Σ can be considered as a system of couples located at a point:

$$u_n(\vec{x},t) \ = \ \left(\int_\Sigma m_{pq}\ d\Sigma \right) * G_{np,q} \ . \tag{3.39}$$

The moment tensor M_{pq} is defined as

$$M_{pq} \ = \ \int_\Sigma m_{pq}\ \mathrm{d}\Sigma \ . \tag{3.40}$$

Then displacement is given by

$$u_n(\vec{x},t) \ = \ M_{pq} * G_{np,q} \ , \tag{3.41}$$

where M_{pq} is the strength of the resulting $(p,\ q)$ couple at the point.

In the case of a tangential slip, $\vec{n} \cdot \vec{\nu} \ = \ 0$; $D\vec{u} \ = \ Du \cdot \vec{\nu}$ (see Fig. 3.3) in an isotropic medium, the moment-density tensor takes a simple form

$$m_{pq} \ = \ \mu \ (\ n_p \ Du_q \ + \ n_q \ Du_p \ ) \tag{3.42}$$

or

$$m_{pq} \ = \ \mu \ Du \ (\ n_p \ \nu_q \ + \ n_q \ \nu_p \ ) \ . \tag{3.43}$$

Then the moment tensor is

$$M_{pq} \ = \ \int_\Sigma \mu \ Du \ (\ n_p \ \nu_q \ + \ n_q \ \nu_p \ ) \ \mathrm{d}\Sigma \ . \tag{3.44}$$

Assuming a homogeneous medium in the source region or average μ we get

$$M_{pq} \ = \ \mu \ (\ n_p \ \nu_q \ + \ n_q \ \nu_p \ ) \int_\Sigma Du\,(\vec{\xi},t) \ \mathrm{d}\Sigma \ . \tag{3.45}$$

The integral can be approximated:

$$\int_\Sigma Du\,(\vec{\xi},t) \ \mathrm{d}\Sigma \ \doteq \ \overline{Du}\,(t) \int_\Sigma \mathrm{d}\Sigma \ \doteq \ \overline{Du}\,(t) \ A \ \doteq \ \overline{Du} \ s(t) \ A \ , \tag{3.46}$$

where

$$s\,(t) \ = \ \frac{\overline{Du}\,(t)}{\overline{Du}} \ ; \quad \overline{Du} \ = \ \overline{Du}\,(t \to \infty) \ . \tag{3.47}$$

Then the moment tensor takes a simple form

$$M_{pq} \ = \ \mu \ A \ \overline{Du} \ s\,(t) \ (\ n_p \ \nu_q \ + \ n_q \ \nu_p \ ) \, . \tag{3.48}$$

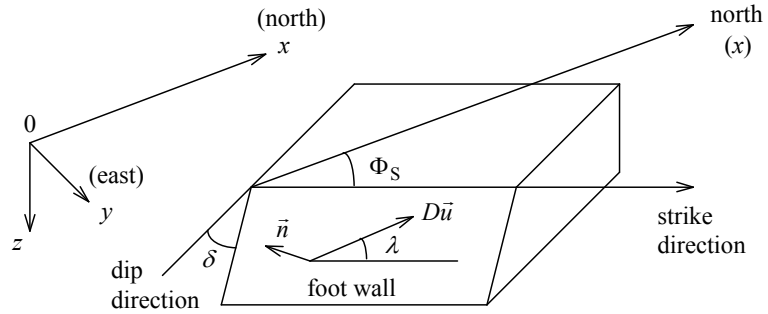

Fig. 3.3. Definition of the fault-orientation parameters and the coordinate system: Φ_S is strike, δ dip, λ rake, $\vec{n}$ fault normal, $D\vec{u} = Du \cdot \vec{\nu}$, and slip $D\vec{u}$ is taken as the movement of the hanging wall relative to the foot wall.

The scalar seismic moment M_0 is defined as

$$M_0 \;=\; \mu\, A\, \overline{Du}\;. \tag{3.49}$$

Eventually we obtain for the tangential slip

$$M_{pq} \;=\; M_0\;(\;n_p\,\nu_q \;+\; n_q\,\nu_p\;)\;\;s\,(t)\;. \tag{3.50}$$

In the coordinate system shown in Fig. 3.3 the components of vector $\vec{\nu}$ and the fault normal vector $\vec{n}$ are:

$$\begin{aligned}
\nu_x \;&=\;\;\;\cos\lambda\;\cos\Phi_S \;+\; \cos\delta\;\sin\lambda\;\sin\Phi_S\;,\\
\nu_y \;&=\;\;\;\cos\lambda\;\sin\Phi_S \;-\; \cos\delta\;\sin\lambda\;\cos\Phi_S\;,\\
\nu_z \;&=\;-\sin\lambda\;\;\sin\delta\;,
\end{aligned} \tag{3.51}$$

and

$$\begin{aligned}
n_x \;&=\;-\sin\delta\;\sin\Phi_S\;,\\
n_y \;&=\;\;\;\sin\delta\;\cos\Phi_S\;,\\
n_z \;&=\;-\cos\delta\;.
\end{aligned} \tag{3.52}$$

From eqs. (3.50) – (3.52) we can obtain

$$\begin{aligned}
M_{xy}(t) \;&=\;\;\;M_0\;(\sin\delta\;\cos\lambda\;\cos 2\Phi_S \;+\tfrac{1}{2}\;\sin 2\delta\;\sin\lambda\;\sin 2\Phi_S\;)\;s(t)\;,\\
M_{yz}(t) \;&=\;-\;M_0\;(\cos\delta\;\cos\lambda\;\sin\Phi_S \;-\;\;\cos 2\delta\;\sin\lambda\;\cos\Phi_S\;)\;s(t)\;,\\
M_{zx}(t) \;&=\;-\;M_0\;(\cos\delta\;\cos\lambda\;\cos\Phi_S \;+\;\;\cos 2\delta\;\sin\lambda\;\sin\Phi_S\;)\;s(t)\;,\\
M_{xx}(t) \;&=\;-\;M_0\;(\sin\delta\;\cos\lambda\;\sin 2\Phi_S \;+\;\;\sin 2\delta\;\sin\lambda\;\sin^2\Phi_S\;)\;s(t)\;,\\
M_{yy}(t) \;&=\;\;\;M_0\;(\sin\delta\;\cos\lambda\;\sin 2\Phi_S \;-\;\;\sin 2\delta\;\sin\lambda\;\cos^2\Phi_S\;)\;s(t)\;,\\
M_{zz}(t) \;&=\;\;\;M_0\;\sin 2\delta\;\sin\lambda\;\;s(t)\;.
\end{aligned} \tag{3.53}$$

The moment tensor is symmetric:

$$M_{xy} \;=\; M_{yx}\;,\; M_{yz} \;=\; M_{zy}\;,\; M_{zx} \;=\; M_{xz}\;. \tag{3.54}$$

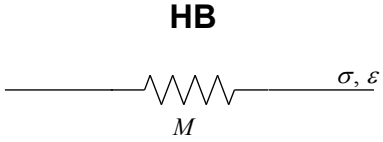

Fig. 4.1. Hooke body

4 Constitutive Law, Rheological Models of Continuum

Equation of motion is a general governing equation for a continuous medium. If we want to apply the equation to a specific type of continuum we have to specify how stress relates to strain for that type of medium (material). Such a relation is called a constitutive law. An application of the same stress to two different material bodies under the same conditions yields different deformations. On the other hand, one and the same material body can respond differently to different loads – depending on the magnitude of stress, duration of its application, and also other factors as, e.g., temperature. A variety of rheological models of continuum reflects a variety of material behaviors.

We will focus on those models that approximate behavior of the Earth's material when it responds to sudden stress variations due to seismic sources, as earthquakes or explosions. Seismic waves and motion produced by seismic sources are attenuated. Observations, e.g. Mc Donal et al. (1958), Liu et al. (1976), Spencer (1981), Murphy (1982), show that the internal friction (a measure of attenuation) in the Earth, Q^{-1}, is nearly constant over the seismic frequency range (from the seismic body waves to the Earth's free oscillations, that is for periods from approximately 0.01 s up to 1 hour). This is a consequence of the fact that the Earth's material is composed of different minerals and the attenuation in each of them is contributed by several processes.

We start with two extreme models – perfectly elastic and viscous media. Realizing their extremely different idealized behaviors we will obtain a reasonable indication for a more realistic model of the real material – viscoelastic medium.

4.1 Linear Elastic Body

4.1.1 Simple Mechanical Model – Hooke Body

Linear elastic body, Hooke body (Hooke model, Hooke element, elastic spring), represents behavior of a perfectly elastic (lossless) solid material. Stress is proportional to strain:

$$\sigma(t) = M \cdot \varepsilon(t) . \tag{4.1}$$

Here $\sigma(t)$ is the stress as a function of time t, $\varepsilon(t)$ strain, and M the time-independent elastic modulus. An application of a load yields an instantaneous deformation. A removal of the load yields instantaneous and total recovery. Hooke body does not have a memory: stress at a given time only depends on the deformation at the same time. Model of the Hooke body is illustrated in Fig. 4.1. The strain-time diagram for a constant stress applied at time t_0 and removed at time t_1 is shown in Fig. 4.2, left, the stress-strain diagram in Fig. 4.2, right.

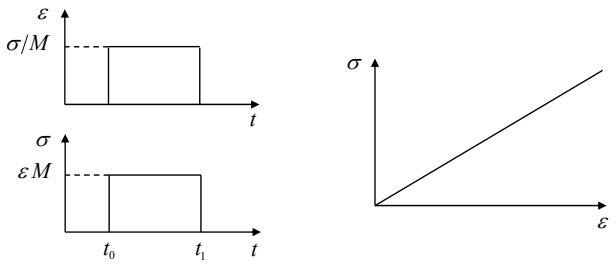

Fig. 4.2. Left: The strain-time diagram for a constant stress applied at time t_0 and removed at time t_1. Right: The stress-strain diagram.

Hereafter we will use symbol $\mathcal{F}$ for the direct and $\mathcal{F}^{-1}$ for the inverse Fourier transforms

$$\mathcal{F}\{x(t)\} \;=\; \int_{-\infty}^{\infty} x(t)\;\exp(-\,\mathrm{i}\omega\, t)\,\mathrm{d}t\;, \tag{4.2}$$

$$\mathcal{F}^{-1}\{X(\omega)\} \;=\; \frac{1}{2\pi}\int_{-\infty}^{\infty} X\,(\omega)\;\exp(\mathrm{i}\omega t)\,\mathrm{d}\omega\;. \tag{4.3}$$

Here ω is the angular frequency. An application of the Fourier transform to eq. (4.1) gives

$$\sigma\,(\omega) \;=\; M\cdot\varepsilon\,(\omega)\;. \tag{4.4}$$

An equivalent to eq. (4.1) is

$$\varepsilon\,(t) \;=\; C\cdot\sigma\,(t)\;, \tag{4.5}$$

where

$$C \;=\; \frac{1}{M} \tag{4.6}$$

is the compliance.

4.1.2 Stress-Strain Relation in Linear Elastic Continuum

Cauchy's generalization of the original Hooke's law in tensor form reads

$$\sigma_{ij} \;=\; c_{ijkl}\,\varepsilon_{kl}\;, \tag{4.7}$$

where c_{ijkl} is a tensor of elastic constants (they are constant with respect to the strain-tensor components, not necessarily with respect to spatial position). Equation (4.7) assumes that each stress-tensor component is a linear combination of all components of the strain tensor. Symmetry of the stress and strain tensors implies symmetries

$$c_{ijkl} \;=\; c_{jikl}\;,\quad c_{ijkl} \;=\; c_{ijlk}\;, \tag{4.8}$$

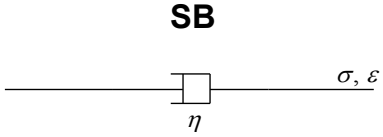

Fig. 4.3. Stokes body

respectively. Application of the first law of thermodynamics yields additional symmetry,

$$c_{ijkl} \;=\; c_{klij} \;. \tag{4.9}$$

Symmetries (4.8) - (4.9) reduce the number of independent elastic constants from 81 down to 21 that describe the most general anisotropic medium. The situation dramatically simplifies in the case of the isotropic medium. The behavior of the isotropic elastic medium is described by two independent elastic constants. The stress-strain relation can be written in the form

$$\sigma_{ij} = \;\kappa\,\varepsilon_{kk}\,\delta_{ij} \;+\; 2\mu\;\left(\,\varepsilon_{ij} - \;\tfrac{1}{3}\varepsilon_{kk}\,\delta_{ij}\right), \tag{4.10}$$

where κ and μ are bulk and shear moduli, respectively, and

$$\delta_{ij} \;=\; \begin{cases} 1 \;; & i = j \\ 0 \;; & i \neq j \end{cases} \tag{4.11}$$

defines the Kronecker delta. Equation (4.10) corresponds to decomposition of the stress tensor into dilatational and deviatoric components. Alternatively the stress-strain relation can be written using Lamé constants λ and μ in the form

$$\sigma_{ij} = \;\lambda\,\varepsilon_{kk}\delta_{ij} \;+\; 2\mu\,\varepsilon_{ij} \;. \tag{4.12}$$

4.2 Linear Viscous Body

Linear viscous body, Stokes body (Stokes model, Stokes element, Stokes dashpot; also Newton model, Newton element, viscous dashpot) represents the other extreme behavior in the variety of linear rheological bodies, the behavior of the viscous fluid. Stress is proportional to strain rate:

$$\sigma\,(t) \;=\; \eta\cdot\dot{\varepsilon}\,(t) \;. \tag{4.13}$$

Here η is the time-independent viscosity. An application of a load yields non-instantaneous linearly increasing deformation. A removal of the load does not yield removal of deformation – there is no recovery. Stokes body has extreme or absolute memory. Model of the Stokes body is illustrated in Fig. 4.3. The strain-time diagram for a constant stress applied at time t_0 and removed at time t_1 is shown in Fig. 4.4 (left), the stress – strain-rate diagram in Fig. 4.4 (right). An application of the Fourier transform to eq. (4.13) gives

$$\sigma\,(\omega) \;=\; \mathrm{i}\omega\,\eta\cdot\varepsilon\,(\omega) \;. \tag{4.14}$$

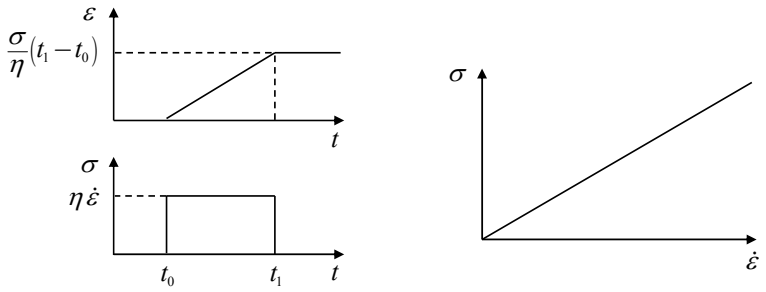

Fig. 4.4. Left: The strain-time diagram for a constant stress applied at time t_0 and removed at time t_1. Right: The stress - strain-rate diagram.

4.3 More Realistic Models of the Earth's Material

Let us summarize and compare the two types of material behaviors. Perfectly elastic material can store mechanical energy without loss; it cannot dissipate the energy. Viscous fluid can dissipate energy but not store it. Certainly, more realistic rheological models of real materials should have both properties.

Stress of a linear elastic body only depends on an instantaneous deformation. For example, a sudden application of a constant stress (unit step function of stress) to the elastic body causes instantaneous deformation which remains constant. If an additional constant stress is applied at some later time, the elastic body deforms instantaneously and proportionally only to the total stress applied at that time, no matter how long the previous stress was applied. In other words, the elastic body does not have memory – deformation does not depend on the previous history.

A sudden application of a constant stress to a viscous fluid does not cause instantaneous deformation. Instead, deformation starts growing steadily from zero value at the moment of the stress application. If an additional constant stress is applied at some later time, the deformation at that very moment depends only on the previous history – because the fluid is not capable to respond instantaneously with nonzero deformation to the additional stress load. We could say, in contrast to the elastic body, that the viscous fluid has an absolute memory.

Obviously, more realistic rheological models of real materials should have both properties – capability to respond immediately and memory of the previous stress-strain history. Viscoelastic models combine the very different properties of the elastic and viscous models.

For a basic detailed text on the rheology of the Earth we refer to monograph by Ranalli (1995).

4.4 Viscoelastic Continuum

4.4.1 Stress-Strain Relation in Viscoelastic Medium

The stress-strain relation in a viscoelastic medium can be defined as

$$\sigma_{ij}(t) \;=\; \int_{-\infty}^{t} \psi_{ijkl}(t-\tau)\; \dot{\varepsilon}_{kl}(\tau)\; \mathrm{d}\tau \;, \tag{4.15}$$

where ψ_{ijkl} is a tensor of relaxation functions describing behavior of the material. An alternative form of the stress-strain relation is the strain-stress relation

$$\varepsilon_{ij}(t) \;=\; \int_{-\infty}^{t} \chi_{ijkl}(t-\tau)\;\dot{\sigma}_{kl}(\tau)\;\mathrm{d}\tau\;, \tag{4.16}$$

where χ_{ijkl} is a tensor of creep functions which also describe behavior of the material.

For the isotropic medium the stress-strain relation can be written as

$$\begin{aligned}\sigma_{ij}(t) \;=\; & \delta_{ij} \int_{-\infty}^{t} \kappa(t-\tau)\;\dot{\varepsilon}_{kk}(\tau)\;\mathrm{d}\tau \\ & +\;\; 2 \int_{-\infty}^{t} \mu(t-\tau)\;\left[\;\dot{\varepsilon}_{ij}(\tau)\;-\;\tfrac{1}{3}\,\delta_{ij}\,\dot{\varepsilon}_{kk}(\tau)\;\right]\;\mathrm{d}\tau\;,\end{aligned} \tag{4.17}$$

where $\kappa(t)$ and $\mu(t)$ are relaxation functions; compare with time-independent bulk and shear moduli in eq. (4.10). Alternatively, eq. (4.17) can be rewritten as

$$\sigma_{ij}(t) \;=\; \delta_{ij} \int_{-\infty}^{t} \lambda(t-\tau)\;\dot{\varepsilon}_{kk}(\tau)\;\mathrm{d}\tau \;+\; 2 \int_{-\infty}^{t} \mu(t-\tau)\;\dot{\varepsilon}_{ij}(\tau)\;\mathrm{d}\tau\;. \tag{4.18}$$

Relations (4.15), (4.17) and (4.18) are formulations of the Boltzmann superposition and causality principle. For a complete and rigorous treatment we refer to Christensen (1971).

Later we will use formulation (4.17) to obtain equations for wave propagation in attenuating medium. Here, for simplicity, we continue with a 1D problem in order to clarify basic mathematical description and physics of viscoelastic continuum.

In a simple scalar notation Boltzmann superposition and causality principle takes the form

$$\sigma(t) \;=\; \int_{-\infty}^{t} \psi\,(t-\tau)\;\dot{\varepsilon}\,(\tau)\;\mathrm{d}\tau\;, \tag{4.19}$$

where $\sigma(t)$ is stress, $\dot{\varepsilon}(t)$ time derivative of strain, and $\psi(t)$ stress relaxation function - a stress response to Heaviside unit step function in strain. According to eq. (4.19), the stress at a given time t is determined by the entire history of the strain until time t. The upper integration limit ensures the causality. Mathematically, the integral in eq. (4.19), also called the hereditary integral, represents a time convolution of the relaxation function and strain rate. We can use symbol $*$ for the convolution. Equation (4.19) then can be written as

$$\sigma(t) \;=\; \psi(t) * \dot{\varepsilon}(t)\;. \tag{4.20}$$

Due to properties of convolution,

$$\sigma(t) \;=\; \dot{\psi}(t) * \varepsilon(t)\;. \tag{4.21}$$

Since $\psi(t)$ is the stress response to a unit step function in strain, its time derivative,

$$M(t) \;=\; \dot{\psi}(t)\;, \tag{4.22}$$

is the stress response to the Dirac δ-function in strain. Equation (4.21) can be written as

$$\sigma(t) \;=\; M(t) * \varepsilon(t) \;. \tag{4.23}$$

We can compare eq. (4.23) with eq. (4.1): whereas the stress-strain relation for the elastic body is a simple linear relation with a constant elastic modulus, the stress-strain relation for the viscoelastic body has a convolutory form as a consequence of the time-dependent modulus $M(t)$.

An application of the Fourier transform to eq. (4.23) gives

$$\sigma\left(\omega\right) \;=\; M\left(\omega\right) \cdot \varepsilon\left(\omega\right) \;, \tag{4.24}$$

where

$$M\left(\omega\right) \;=\; \mathcal{F}\left\{M(t)\right\} \;=\; \mathcal{F}\left\{\dot{\psi}(t)\right\} \tag{4.25}$$

is the complex, frequency-dependent viscoelastic modulus. An application of the inverse Fourier transform to eq. (4.25) gives

$$\dot{\psi}(t) \;=\; \mathcal{F}^{-1}\{M(\omega)\} \tag{4.26}$$

and, due to properties of the Fourier transform,

$$\psi(t) \;=\; \mathcal{F}^{-1}\left\{\frac{M(\omega)}{\mathrm{i}\omega}\right\} \;. \tag{4.27}$$

Equation (4.24), in comparison with eq. (4.19), clearly indicates that the incorporation of the linear viscoelasticity and consequently attenuation into the frequency-domain computations is much easier than those in the time-domain computations – real frequency-independent moduli are simply replaced by complex, frequency-dependent quantities (the correspondence principle in the linear theory of viscoelasticity).

The time derivative of the stress is, see eq. (4.21),

$$\dot{\sigma}(t) \;=\; \dot{\psi}(t) * \dot{\varepsilon}(t) \tag{4.28}$$

or, due to eq. (4.22),

$$\dot{\sigma}(t) \;=\; M(t) * \dot{\varepsilon}(t) \;. \tag{4.29}$$

Consider eq. (4.25):

$$M\left(\omega\right) \;=\; \mathcal{F}\left\{\dot{\psi}(t)\right\} \;=\; \int_{-\infty}^{\infty} \dot{\psi}(t)\; \exp(-\mathrm{i}\omega t)\; \mathrm{d}t \;. \tag{4.30}$$

Because $\psi(t)$ is the stress response to Heaviside unit step function in strain,

$$\psi(t) \;=\; \tilde{\psi}(t)\; H(t) \quad : \quad \tilde{\psi}(0) \;=\; \psi(0) \;, \quad \tilde{\psi}(t) \;=\; \psi(t) \;; \quad t > 0 \;. \tag{4.31}$$

Here and hereafter in this chapter, the Heaviside function is equal to 1 for zero argument. Equivalently, $\tilde{\psi}(t) \;=\; \psi(t)\,;\; t \geq 0$. Then

$$\dot{\psi}(t) \;=\; \dot{\tilde{\psi}}(t)\; H(t) \;+\; \tilde{\psi}(t)\, \delta(t) \tag{4.32}$$

and

$$\begin{aligned} M(\omega) \;&=\; \int_{-\infty}^{\infty} \Big[\, \dot{\tilde{\psi}}(t)\; H(t) \;+\; \tilde{\psi}(t)\; \delta(t) \Big]\; \exp(-\mathrm{i}\omega t)\; \mathrm{d}t \\ &=\; \psi(0) \;+\; \int_0^{\infty} \dot{\psi}(t)\; \exp(-\mathrm{i}\omega t)\; \mathrm{d}t \\ &=\; \psi(0) \;+\; \int_0^{\infty} \frac{\mathrm{d}}{\mathrm{d}t}[\psi(t) - \psi(\infty)]\; \exp(-\mathrm{i}\omega t)\; \mathrm{d}t \\ &=\; \psi(0) \;+\; [\psi(t) \;-\; \psi(\infty)]\; \exp(-\mathrm{i}\omega t)|_0^{\infty} \\ &\quad -\; \int_0^{\infty} [\psi(t) - \psi(\infty)]\; \frac{\mathrm{d}}{\mathrm{d}t}[\exp(-\mathrm{i}\omega t)]\; \mathrm{d}t \\ &=\; \psi(0) \;-\; [\psi(0) \;-\; \psi(\infty)] \;-\; \int_0^{\infty} [\psi(t) - \psi(\infty)]\; (-\mathrm{i}\omega) \exp(-\mathrm{i}\omega t)\; \mathrm{d}t \\ &=\; \psi(\infty) \;+\; \mathrm{i}\omega \int_0^{\infty} [\psi(t) \;-\; \psi(\infty)]\; \exp(-\mathrm{i}\omega t)\; \mathrm{d}t\;. \end{aligned} \tag{4.33}$$

We found that

$$M(\omega) \;=\; \psi(\infty) \;+\; \mathrm{i}\omega \int_0^{\infty} [\psi(t) \;-\; \psi(\infty)]\; \exp(-\mathrm{i}\omega t)\; \mathrm{d}t\;. \tag{4.34}$$

It follows from eq. (4.34) that

$$M(\omega = 0) \;=\; \psi(t = \infty)\;. \tag{4.35}$$

Alternatively to eq. (4.33) we can consider

$$\begin{aligned} M(\omega) \;&=\; \int_{-\infty}^{\infty} \Big[\, \dot{\tilde{\psi}}(t)\; H(t) \;+\; \tilde{\psi}(t)\; \delta(t) \Big]\; \exp(-\mathrm{i}\omega t)\; \mathrm{d}t \\ &=\; \psi(0) \;+\; \int_0^{\infty} \dot{\psi}(t)\; \exp(-\mathrm{i}\omega t)\; \mathrm{d}t \\ &=\; \psi(0) \;+\; \dot{\psi}(t)\; \frac{\exp(-\mathrm{i}\omega t)}{-\mathrm{i}\omega}\; \Big|_0^{\infty} \;-\; \int_0^{\infty} \ddot{\psi}(t)\; \frac{\exp(-\mathrm{i}\omega t)}{-\mathrm{i}\omega}\; \mathrm{d}t\,. \end{aligned} \tag{4.36}$$

Then

$$\begin{aligned} \lim_{\omega \to \infty} M(\omega) \;&=\; \psi(0) \;+\; \lim_{\omega \to \infty} \left[\dot{\psi}(t)\; \frac{\exp(-\mathrm{i}\omega t)}{-\mathrm{i}\omega}\; \Big|_0^{\infty} - \int_0^{\infty} \ddot{\psi}(t)\; \frac{\exp(-\mathrm{i}\omega t)}{-\mathrm{i}\omega}\; \mathrm{d}t \right] \\ &=\; \psi(0) \;+\; 0\,. \end{aligned} \tag{4.37}$$

Consequently,

$$M(\omega = \infty) \;=\; \psi(t = 0)\;. \tag{4.38}$$

Having found relations (4.35) and (4.38), we can define the following characteristics: An instantaneous elastic response of the viscoelastic material is given by the so-called unrelaxed modulus M_U, a long-term equilibrium response is given by the relaxed modulus M_R

$$M_U \;=\; \lim_{t\to 0} \psi(t) \qquad , \quad M_R \;=\; \lim_{t\to \infty} \psi(t)\;. \tag{4.39}$$

In the frequency domain

$$M_U \;=\; \lim_{\omega\to \infty} M\left(\omega\right)\;, \quad M_R \;=\; \lim_{\omega\to 0} M\left(\omega\right)\;. \tag{4.40}$$

The modulus defect or relaxation of modulus is

$$\delta M \;=\; M_U \;-\; M_R\;. \tag{4.41}$$

An application of a unit-step strain, $\varepsilon(t) = H(t)$, causes decrease of $\psi\left(t\right)$, that is, relaxation, from the unrelaxed state with $\psi(0) = M_U$ to the relaxed state with $\psi(\infty) = M_R\,.$

Given the viscoelastic modulus, the quality factor $Q(\omega)$ is

$$Q\left(\omega\right) \;=\; \frac{\mathrm{Re}\, M\left(\omega\right)}{\mathrm{Im}\, M\left(\omega\right)}\;. \tag{4.42}$$

It can be shown that $1/\,Q(\omega)$ is a measure of internal friction in a linear viscoelastic body.

As already indicated a numerical integration of the stress-strain relation (4.19) is practically intractable due to the large computer time and memory requirements. This led many modelers to incorporate only oversimplified $Q\left(\omega\right)$ laws in the time-domain computations.

An alternative to the stress-strain relation (4.19) is the strain-stress relation. The strain at a given time t is determined by the entire history of the stress until time t:

$$\varepsilon(t) \;=\; \int_{-\infty}^{t} \chi\left(t-\tau\right)\; \dot{\sigma}\left(\tau\right)\; \mathrm{d}\tau \tag{4.43}$$

or

$$\varepsilon(t) \;=\; \chi(t) * \dot{\sigma}(t)\;. \tag{4.44}$$

Here $\chi(t)$ is the creep function - a strain response to Heaviside unit step function in stress. Due to properties of the convolution, eq. (4.44) can be rewritten as

$$\varepsilon(t) \;=\; \dot{\chi}(t) * \sigma(t)\;. \tag{4.45}$$

Since $\chi(t)$ is the strain response to a unit step function in stress, its time derivative,

$$C(t) \;=\; \dot{\chi}(t)\,, \tag{4.46}$$

is the strain response to the Dirac δ-function in stress. Equation (4.45) can be written as

$$\varepsilon(t) \;=\; C(t) * \sigma(t)\;. \tag{4.47}$$

An application of the Fourier transform to eq. (4.47) yields

$$\varepsilon\,(\omega) \;=\; C\,(\omega)\cdot\sigma\,(\omega)\;\;, \tag{4.48}$$

where

$$C\,(\omega) \;=\; \mathcal{F}\,\{C(t)\,\} \;=\; \mathcal{F}\,\{\dot{\chi}(t)\,\} \tag{4.49}$$

is the complex, frequency-dependent creep compliance. An application of the inverse Fourier transform to eq. (4.49) gives

$$\dot{\chi}(t) \;=\; \mathcal{F}^{-1}\,\{C\,(\omega)\} \tag{4.50}$$

and, due to properties of the Fourier transform,

$$\chi(t) \;=\; \mathcal{F}^{-1}\left\{\frac{C\,(\omega)}{\mathrm{i}\omega}\right\}\;. \tag{4.51}$$

Relations

$$C_U \;=\; \lim_{t\to 0}\chi(t)\;,\quad C_R \;=\; \lim_{t\to\infty}\chi(t) \tag{4.52}$$

define the unrelaxed compliance C_U and relaxed compliance C_R. Relaxation of compliance is defined as

$$\delta C \;=\; C_R \;- C_U\;. \tag{4.53}$$

An application of a unit-step stress, $\sigma(t) = H(t)$, causes increase of $\chi(t)$, that is, creep, from the unrelaxed state with $\chi(0) \;=\; C_U$ to the relaxed state with $\chi(\infty) = C_R$. Using eqs. (4.21) and (4.45), and properties of convolution we can write

$$\begin{aligned}\sigma(t) \;&=\; \dot{\psi}(t) * \varepsilon(t)\\ &=\; \dot{\psi}(t) \;*\; [\;\dot{\chi}(t) * \sigma(t)\;]\\ &=\; [\;\dot{\psi}(t) * \dot{\chi}(t)\;] * \sigma(t)\;.\end{aligned} \tag{4.54}$$

It follows from eq. (4.54) that

$$\dot{\psi}(t) * \dot{\chi}(t) \;=\; \delta(t) \tag{4.55}$$

and, consequently,

$$M\,(\omega)\cdot C\,(\omega) \;=\; 1\;. \tag{4.56}$$

For the unrelaxed and relaxed states it follows that

$$C_U \;=\; \frac{1}{M_U}\;,\quad C_R \;=\; \frac{1}{M_R}\;. \tag{4.57}$$

Tab. 4.1. Time-domain and frequency-domain rules for linear rheological models

element	stress-strain relation
time domain	
Hooke (spring)	$\sigma(t) = M \cdot \varepsilon(t)$, M - elastic modulus
Stokes (dashpot)	$\sigma(t) = \eta \cdot \dot{\varepsilon}(t)$, η - viscosity
frequency domain	
Hooke (spring)	$\sigma(\omega) = M \cdot \varepsilon(\omega)$, M - elastic modulus
Stokes (dashpot)	$\sigma(\omega) = i\omega\eta \cdot \varepsilon(\omega)$, η - viscosity

connection	σ	ε
in series	equal	additive
in parallel	additive	equal

4.4.2 Time-domain and Frequency-domain Rules for Linear Viscoelastic Models

Models which quite well approximate rheological properties and behavior of the real Earth's material can be constructed by connecting the simplest rheological elements, Hooke and Stokes elements, in parallel or series. The properties of the models can be analyzed in the time and frequency domains. There are relatively simple rules in both domains that allow obtaining mathematical representations of the models. The time-domain and frequency-domain rules for linear rheological models are given in Table 4.1.

4.4.3 Simplest Linear Viscoelastic Models

Maxwell Body. One of the simplest viscoelastic models is Maxwell body (Fig. 4.5, top panel). We can easily derive the basic characteristics of this rheological model. An application of the frequency-domain rules leads to:

Hooke body:

$$\sigma_{HB}(\omega) = M\,\varepsilon_{HB}(\omega)\,. \tag{4.58}$$

Stokes body:

$$\sigma_{SB}(\omega) = \mathrm{i}\omega\eta\ \varepsilon_{SB}(\omega)\,. \tag{4.59}$$

Maxwell body $=$ Hooke body connected in series with Stokes body:

$$\sigma = \sigma_{HB} = \sigma_{SB}\,, \quad \varepsilon = \varepsilon_{HB} + \varepsilon_{SB}\,, \tag{4.60}$$

$$\varepsilon(\omega) = \frac{\sigma(\omega)}{M} + \frac{\sigma(\omega)}{\mathrm{i}\omega\eta}\,, \tag{4.61}$$

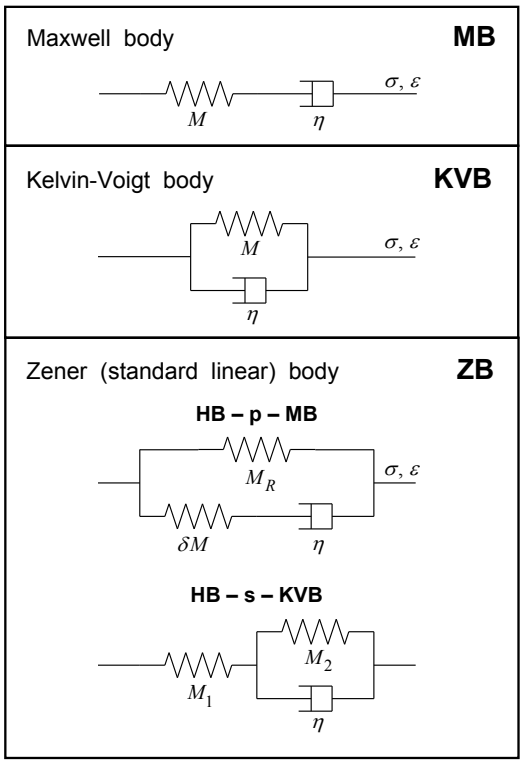

Fig. 4.5. The simplest rheological models of viscoelastic materials. HB denotes Hooke body, p means connection in parallel, and s means connection in series.

$$\sigma\,(\omega) \;=\; \left(\frac{\mathrm{i}\omega\eta\,M}{M+\mathrm{i}\,\omega\eta}\right)\varepsilon\,(\omega)\,, \tag{4.62}$$

$$\sigma\,(\omega) \;=\; M(\omega)\,\varepsilon\,(\omega) \;\;;\quad M(\omega) \;=\; \frac{\mathrm{i}\omega\,M}{\omega_r+\;\mathrm{i}\omega}\;. \tag{4.63}$$

Here,

$$\omega_r \;=\; \frac{M}{\eta}\;. \tag{4.64}$$

From the frequency-dependent modulus we easily obtain the relaxed and unrelaxed moduli

$$M_R \;=\; \lim_{\omega\to 0} M(\omega) \;=\; 0\,, \tag{4.65}$$

and

$$M_U \;=\; \lim_{\omega\to\infty} M(\omega) \;=\; M\;. \tag{4.66}$$

Relations (4.65) and (4.66) mean that Maxwell body under the application of a unit-step strain relaxes from value M_U (at the time of application of the unit-step strain) down to a zero stress. Because, eq. (4.57),

$$C_R \;=\; \frac{1}{M_R}\;, \tag{4.67}$$

Maxwell body creeps forever under the application of a unit-step stress.

Find now the stress relaxation function. Using eqs. (4.27) and (4.63) we have

$$\psi(t) \;=\; \mathcal{F}^{-1}\left\{\frac{M\,(\omega)}{\mathrm{i}\,\omega}\right\} \;=\; \mathcal{F}^{-1}\left\{\frac{M}{\omega_r + \,\mathrm{i}\omega}\right\} \tag{4.68}$$

and

$$\psi(t) \;=\; M\,\exp(-\omega_r\,t)\,H(t) \;=\; M\,\exp(-t/\tau_\sigma)\,H(t)\;. \tag{4.69}$$

Here,

$$\tau_\sigma \;=\; \frac{1}{\omega_r} \;=\; \frac{\eta}{M} \tag{4.70}$$

is the stress relaxation time (also Maxwell relaxation time). Then ω_r can be called the relaxation frequency. The relaxation time τ_σ characterizes time during which stress falls down by a characteristic value. Using eq. (4.22) we can also find the time-dependent modulus

$$M(t) \;=\; \dot{\psi}(t) \;=\; M\,\exp(-\omega_r\,t)\;\left[\,\delta(t) \,-\, \omega_r\,H(t)\,\right]\;. \tag{4.71}$$

An application of the time-domain rules leads to:

Hooke body:

$$\sigma_{HB}\,(t) \;=\; M\,\varepsilon_{HB}\,(t)\,. \tag{4.72}$$

Stokes body:

$$\sigma_{SB}\,(t) \;=\; \eta\,\dot{\varepsilon}_{SB}\,(t)\,. \tag{4.73}$$

Maxwell body $=$ Hooke body connected in series with Stokes body:

$$\sigma \;=\; \sigma_{HB} \;=\; \sigma_{SB}\;, \quad \varepsilon \;=\; \varepsilon_{HB} + \varepsilon_{SB}\;, \tag{4.74}$$

$$\dot{\varepsilon}\,(t) \;=\; \frac{\dot{\sigma}\,(t)}{M} \;+\; \frac{\sigma\,(t)}{\eta}\,, \tag{4.75}$$

$$\sigma\,(t)\;+\;\tau_r\,\dot{\sigma}\,(t)\;=\;\tau_r\,M\,\dot{\varepsilon}\,(t)\,. \tag{4.76}$$

The use of eqs. (4.29) and (4.71) yields

$$\begin{aligned}\sigma(t)\;&=\;M(t)*\varepsilon(t)\\ &=\;\int_{-\infty}^{t} M\,\exp\left(-\omega_r(t-\tau)\right)\,\left[\,\delta(t-\tau)\;-\;\omega_r\,H(t-\tau)\,\right]\,\varepsilon\,(\tau)\;\mathrm{d}\tau\\ &=\;M\,\varepsilon(t)\;-\;\int_0^t M\,\exp\left(-\omega_r(t-\tau)\right)\,\omega_r\,\varepsilon\,(\tau)\;\mathrm{d}\tau\end{aligned} \tag{4.77}$$

and

$$\sigma(t)\;=\;M\,\varepsilon(t)\;-\;\omega_r\,M\int_0^t \exp\left(-\omega_r(t-\tau)\right)\,\varepsilon\,(\tau)\;\mathrm{d}\tau\;. \tag{4.78}$$

Assume $\sigma(t)\;=\;H(t)$ in eq. (4.75) and integrate the equation with respect to time in the interval $\langle\,0,\;\;t\,\rangle$:

$$\begin{aligned}\chi(t)\;&=\;\varepsilon(t)\;=\;\frac{1}{M}\int_0^t \delta\,(\xi)\;\mathrm{d}\xi\;+\;\frac{1}{\eta}\int_0^t H\,(\xi)\;\mathrm{d}\xi\\ &=\;\frac{1}{M}\;\left(1\;+\;\frac{M}{\eta}\,t\right)\;.\end{aligned} \tag{4.79}$$

Then, using definition (4.70),

$$\chi(t)\;=\;\frac{1}{M}\;\left(1\;+\;\frac{t}{\tau_\sigma}\right)\;;\quad t\;\geq\;0\,. \tag{4.80}$$

The first term on the right-hand side of eq. (4.80) represents the elastic deformation that appears instantaneously at the time of application of the unit-step stress. This deformation is instantaneously removed upon removal of the stress. The second term represents viscous deformation that grows with time and that will remain after the stress is removed. The behavior of Maxwell body is illustrated in Figs. 4.6 and 4.7.

Kelvin-Voigt Body. Another simplest viscoelastic models is Kelvin-Voigt body (Fig. 4.5, middle panel). We can easily derive the basic characteristics of this rheological model. An application of the frequency-domain rules leads to:

Hooke body:

$$\sigma_{HB}\,(\omega)\;=\;M\,\varepsilon_{HB}\,(\omega)\,. \tag{4.81}$$

Stokes body:

$$\sigma_{SB}\,(\omega)\;=\;\mathrm{i}\omega\,\eta\,\varepsilon_{SB}\,(\omega)\,. \tag{4.82}$$

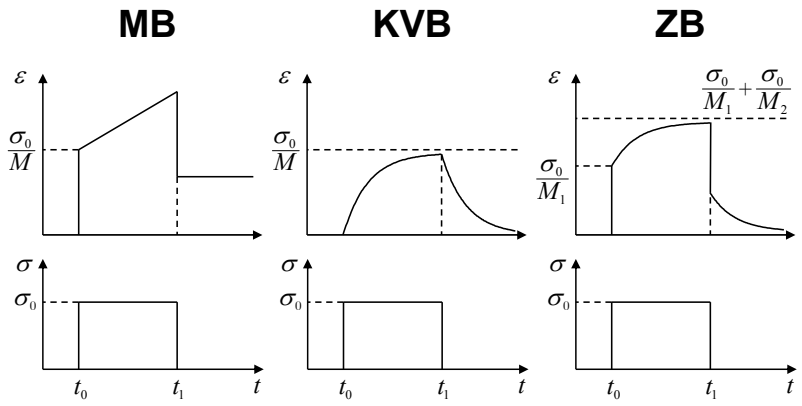

Fig. 4.6. Creep in Maxwell (MB), Kelvin-Voigt (KV) and Zener (standard linear) (ZB) bodies: strain-time diagrams for a constant stress applied at time t_0 and removed at time t_1.

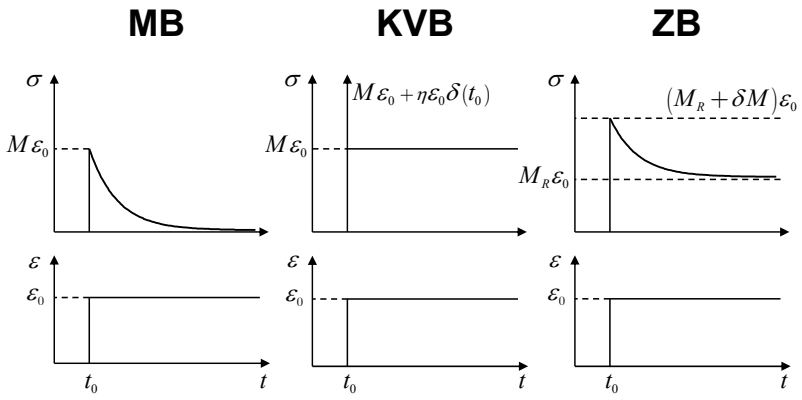

Fig. 4.7. Stress relaxation in Maxwell, Kelvin-Voigt and Zener (standard linear) bodies: stress-time diagrams for a constant strain applied at time t_0.

Kelvin-Voigt body $=$ Hooke body connected in parallel with Stokes body:

$$\sigma \;=\; \sigma_{HB} + \sigma_{SB}\;, \quad \varepsilon \;=\; \varepsilon_{HB} \;=\; \varepsilon_{SB}\;, \tag{4.83}$$

$$\sigma\,(\omega) \;=\; (\,M \;+\; \mathrm{i}\omega\eta\,)\;\varepsilon\,(\omega)\;, \tag{4.84}$$

$$\sigma\,(\omega) \;=\; M(\omega)\,\varepsilon\,(\omega) \;\;;\quad M(\omega) \;=\; M \;+\; \mathrm{i}\omega\eta\,, \tag{4.85}$$

$$M_R \;=\; \lim_{\omega\to 0} M\,(\omega) \;=\; M\,, \tag{4.86}$$

$$\dot{\psi}(t) \;=\; M(t) \;=\; \mathcal{F}^{-1}\left\{M\,(\omega)\right\} \;=\; \mathcal{F}^{-1}\left\{M \;+\; \mathrm{i}\omega\,\eta\right\}\,, \tag{4.87}$$

$$M(t) \;=\; M\,\delta(t) \;+\; \eta\,\dot{\delta}\,(t)\,, \tag{4.88}$$

$$\psi(t) \;=\; M\,H(t) \;+\; \eta\,\delta\,(t)\,, \tag{4.89}$$

$$M_U \;=\; \lim_{t\to 0} \psi\,(t) \;=\; M \;+\; \eta\,\delta(0)\,. \tag{4.90}$$

An application of the time-domain rules leads to:

Hooke body:

$$\sigma_{HB}\,(t) \;=\; M\,\varepsilon_{HB}\,(t)\,. \tag{4.91}$$

Stokes body:

$$\sigma_{SB}\,(t) \;=\; \eta\,\dot{\varepsilon}_{SB}\,(t)\,. \tag{4.92}$$

Kelvin-Voigt body $=$ Hooke body connected in parallel with Stokes body:

$$\sigma \;=\; \sigma_{HB} + \sigma_{SB}\,, \quad \varepsilon \;=\; \varepsilon_{HB} \;=\; \varepsilon_{SB}\,, \tag{4.93}$$

$$\sigma\,(t) \;=\; M\,\varepsilon\,(t) \;+\; \eta\,\dot{\varepsilon}\,(t)\,. \tag{4.94}$$

We would obtain eq. (4.94) also by using eqs. (4.23) and (4.88). It follows from eq. (4.56) that the compliance is

$$C\,(\omega) \;=\; \frac{1}{M + \mathrm{i}\omega\,\eta} \tag{4.95}$$

and from eq. (4.50) that the time derivative of the creep function is

$$\dot{\chi}(t) \;=\; \mathcal{F}^{-1}\left\{\;\frac{1}{M + \mathrm{i}\omega\,\eta}\;\right\} \;=\; \frac{1}{\eta}\;\exp\left(-M\,\frac{t}{\eta}\right)\;H(t)\,. \tag{4.96}$$

Then the creep function is obtained by the time integration

$$\chi(t) \;=\; \int_0^t \frac{1}{\eta}\;\exp\left(-M\,\frac{\vartheta}{\eta}\right)\;H(\vartheta)\,\mathrm{d}\vartheta \tag{4.97}$$

that gives

$$\chi(t) \;=\; \frac{1}{M}\;\left[1\;-\;\exp\left(-\frac{t}{\tau_\varepsilon}\right)\right]\;\;;\quad t\geq 0\,. \tag{4.98}$$

Here,

$$\tau_\varepsilon \;=\; \frac{\eta}{M} \tag{4.99}$$

is the strain relaxation time (also called retardation time). This terminology comes from the exponential character of increase of the creep function. It follows from eqs. (4.52) and (4.98) that

$$C_U \;=\; 0\,. \tag{4.100}$$

The latter result means that the Kelvin-Voigt body has zero creep (zero strain) at the time of the application of the unit-step stress. At the same time, as

$$M_U \;=\; \frac{1}{C_U} \;=\; \infty\,, \tag{4.101}$$

the instantaneous stress response at the time of the application of the unit-step strain is singular. The behavior of the Kelvin-Voigt body is illustrated in Figs. 4.6 and 4.7.

Zener Body (Standard Linear Body). A more general than Maxwell and Kelvin-Voigt bodies is still relatively simple viscoelastic Zener (also standard linear) body (Fig. 4.5, bottom panel). There are two equivalent models: HB – p – MB (Hooke body connected in parallel with Maxwell body) and HB – s – KVB (Hooke body connected in series with Kelvin-Voigt body). It is easier to see the meaning of the elastic moduli in the HB – p – MB model. At the time of the application of the unit-step strain, the instantaneous, that is, unrelaxed, stress will be given by the sum of moduli of the two elastic springs, $M_U = M_R + \delta M$. At the same time deformation of the dashpot will start to grow from zero. The growth of the viscous deformation will gradually release stress of the spring connected in series with the dashpot (that is, spring in Maxwell body). In the limit, the relaxed stress, M_R , will be only in the spring connected in parallel with Maxwell body. We can easily derive the basic characteristics of this rheological model. An application of the frequency-domain rules leads to:

Hooke body:

$$\sigma_{HB}\,(\omega) \;=\; M_R\,\varepsilon_{HB}\,(\omega)\,. \tag{4.102}$$

Maxwell body, eq. (4.62):

$$\sigma_{MB}\,(\omega) \;=\; \left(\frac{\mathrm{i}\omega\,\eta\,\delta M}{\delta M+\mathrm{i}\omega\,\eta}\right)\,\varepsilon_{MB}\,(\omega)\,. \tag{4.103}$$

Zener body $=$ Hooke body connected in parallel with Maxwell body:

$$\sigma \;=\; \sigma_{HB}+\sigma_{MB}\;,\quad \varepsilon \;=\; \varepsilon_{HB} \;=\; \varepsilon_{MB}, \tag{4.104}$$

$$\sigma(\omega) = M_R\,\varepsilon(\omega) + \frac{\mathrm{i}\omega\eta\,\delta M}{\delta M + \mathrm{i}\omega\eta}\,\varepsilon(\omega)$$

$$= M_R\,\frac{1 + \mathrm{i}\omega\dfrac{\eta}{\delta M}\dfrac{M_U}{M_R}}{1 + \mathrm{i}\omega\dfrac{\eta}{\delta M}}\,\varepsilon(\omega)\,. \tag{4.105}$$

Define stress and strain relaxation times, τ_σ and τ_ε,

$$\tau_\sigma = \frac{\eta}{\delta M}\,, \quad \tau_\varepsilon = \frac{\eta}{\delta M}\frac{M_U}{M_R}\,. \tag{4.106}$$

Note that stress relaxation time τ_σ is defined in the same way as that for the Maxwell body, eq. (4.70). Then

$$\sigma(\omega) = M(\omega)\,\varepsilon(\omega)\;; \quad M(\omega) = M_R\,\frac{1 + \mathrm{i}\omega\,\tau_\varepsilon}{1 + \mathrm{i}\omega\,\tau_\sigma}\,. \tag{4.107}$$

Taking limits of $M(\omega)$ we verify our interpretation of the meaning of the elastic moduli:

$$\lim_{\omega\to\infty} M(\omega) = M_U = M_R + \delta M\,, \quad \lim_{\omega\to 0} M(\omega) = M_R. \tag{4.108}$$

From eqs. (4.106) we have the simple relation between the unrelaxed and relaxed moduli:

$$M_U = M_R\,\frac{\tau_\varepsilon}{\tau_\sigma}. \tag{4.109}$$

We can now determine the stress relaxation function using eqs. (4.27) and (4.107):

$$\psi(t) = \mathcal{F}^{-1}\left\{\frac{M(\omega)}{\mathrm{i}\omega}\right\} = \mathcal{F}^{-1}\left\{M_R\,\left[-\frac{\mathrm{i}}{\omega} + \frac{\mathrm{i}\tau_\varepsilon}{\mathrm{i} - \tau_\sigma\,\omega} - \frac{\mathrm{i}\tau_\sigma}{\mathrm{i} - \tau_\sigma\,\omega}\right]\right\}\,. \tag{4.110}$$

It is now easy to find

$$\psi(t) = M_R\left[1 - \left(1 - \frac{\tau_\varepsilon}{\tau_\sigma}\right)\,\exp\left(-\frac{t}{\tau_\sigma}\right)\right]H(t)\,. \tag{4.111}$$

It is also easy to obtain the creep function of Zener body as

$$\chi(t) = \frac{1}{M_R}\left[1 - \left(1 - \frac{\tau_\sigma}{\tau_\varepsilon}\right)\,\exp\left(-\frac{t}{\tau_\varepsilon}\right)\right]H(t)\,. \tag{4.112}$$

The behavior of Zener body is illustrated in Figs. 4.6 and 4.7.

4.4.4 Attenuation in the Simplest Models

Viscoelastic modulus M and attenuation $1/Q$ for Maxwell and Kelvin-Voigt bodies are illustrated in Fig. 4.8. Recalling the observation that attenuation is nearly constant over the seismic frequency range it is obvious that neither Maxwell body nor Kelvin-Voigt body provide suitable

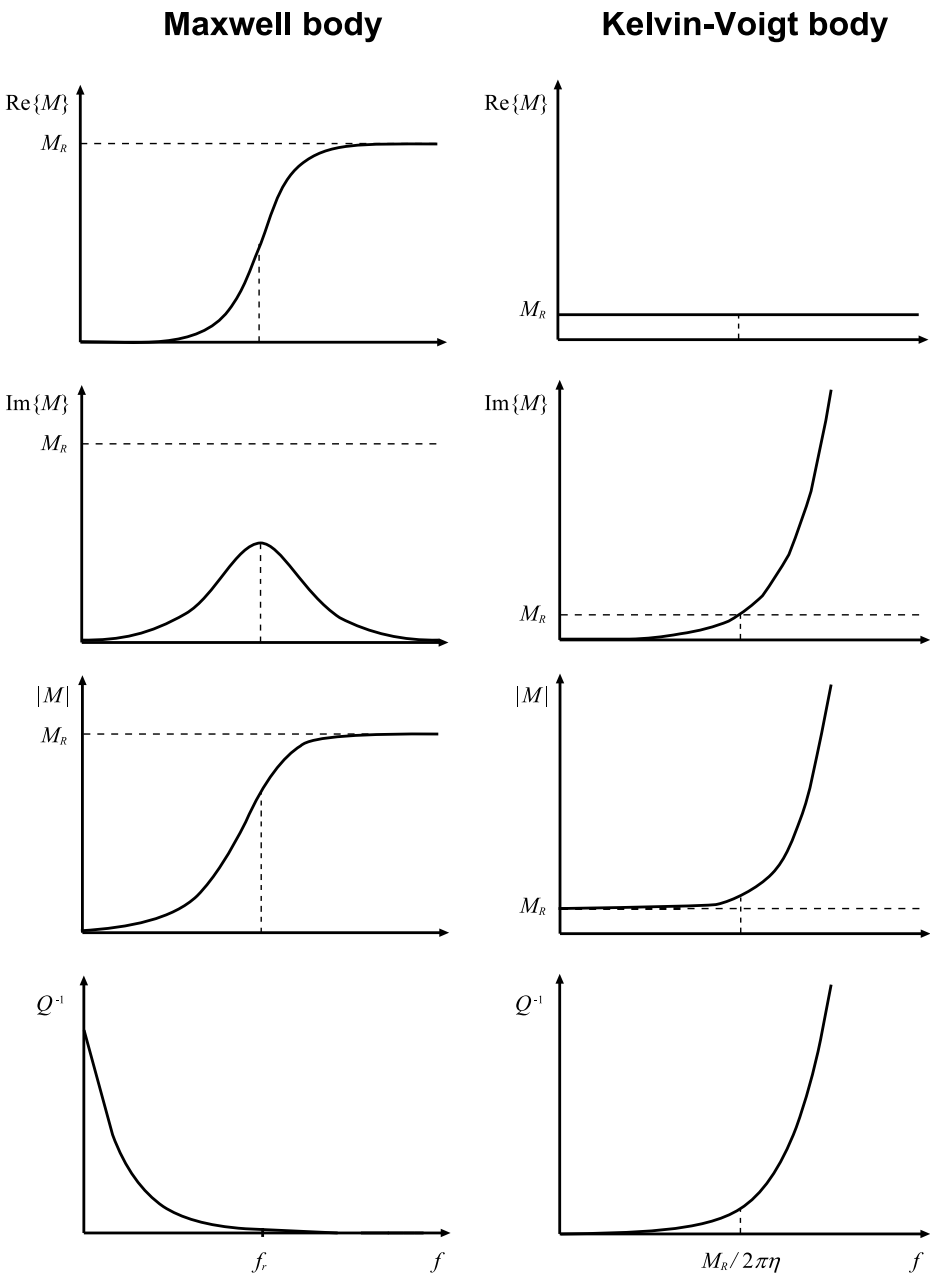

Fig. 4.8. Viscoelastic modulus M and attenuation $1/Q$ as functions of frequency f. The horizontal axis (frequency) is logarithmic, the vertical axis decadic. Modulus for Maxwell body is calculated using eq. (4.63), modulus for Kelvin-Voigt body using eq. (4.85). Frequency dependence of $1/Q$ is calculated using eq. (4.42).

rheology for implementation of realistic attenuation in the modeling of seismic wave propagation.

Figure 4.9 (the left column) shows viscoelastic modulus and attenuation $1/Q$ for Zener body. The attenuation curve suggests that a superposition of several Zener bodies with properly distributed relaxation frequencies could make a rheological viscoelastic model suitable for approximating nearly constant attenuation over modeled/desired frequency range. This was a basic idea of Liu et al. (1976) who introduced generalized Zener body (GZB, Fig. 4.10) in order to account for realistic attenuation of seismic waves.

Recall what we explained before. Incorporation of the linear viscoelasticity and consequently attenuation into the frequency-domain computations is relatively easy, see eq. (4.24): real frequency-independent moduli are simply replaced by complex, frequency-dependent quantities (the correspondence principle in the linear theory of viscoelasticity). On the other hand, in the time domain, the stress-strain relation has convolutory form, see eq. (4.19). Having in mind time-domain numerical methods for structurally complex heterogeneous media, for example grid methods as the finite-difference, finite-element or spectral-element methods, it is easy to understand that it is practically intractable to keep in memory the entire strain history at each grid point and evaluate convolution integral at each grid point at each time level. This is the key problem in incorporation of the realistic attenuation in the time-domain methods. The only solution is to convert the convolutory stress-strain relation into a differential form, that is, to find equivalent differential equations additional to the equation of motion and apply a chosen numerical method to the set of differential equations.

Thus, having the GZB model itself as a suitable viscoelastic model is not enough. We need to convert the convolutory stress-strain relation into a suitable differential form. We will follow a historic development in solving the problem.

4.4.5 Conversion of the Convolutory Stress-Strain Relation into a Differential Form

Consider $M(\omega)$ as a rational function

$$M(\omega) = \frac{P_m(\mathrm{i}\omega)}{Q_n(\mathrm{i}\omega)} \tag{4.113}$$

with

$$P_m(\mathrm{i}\omega) = \sum_{l=1}^{m} p_l (\mathrm{i}\omega)^l \quad , \quad Q_n(\mathrm{i}\omega) = \sum_{l=1}^{n} q_l (\mathrm{i}\omega)^l \, . \tag{4.114}$$

An application of the inverse Fourier transform to eq. (4.24) with $M(\omega)$ given by eq. (4.113) leads to

$$\sum_{l=1}^{n} q_l \, \frac{\mathrm{d}^l \sigma(t)}{\mathrm{d}t^l} = \sum_{l=1}^{m} p_l \, \frac{\mathrm{d}^l \varepsilon(t)}{\mathrm{d}t^l} \, , \tag{4.115}$$

the n^{th}-order differential equation for $\sigma(t)$, which can be eventually numerically solved much more easily than the convolution integral. In other words, the convolution integral in eq. (4.19) can be converted into a differential form if $M(\omega)$ is a rational function of $\mathrm{i}\omega$. Day and Minster

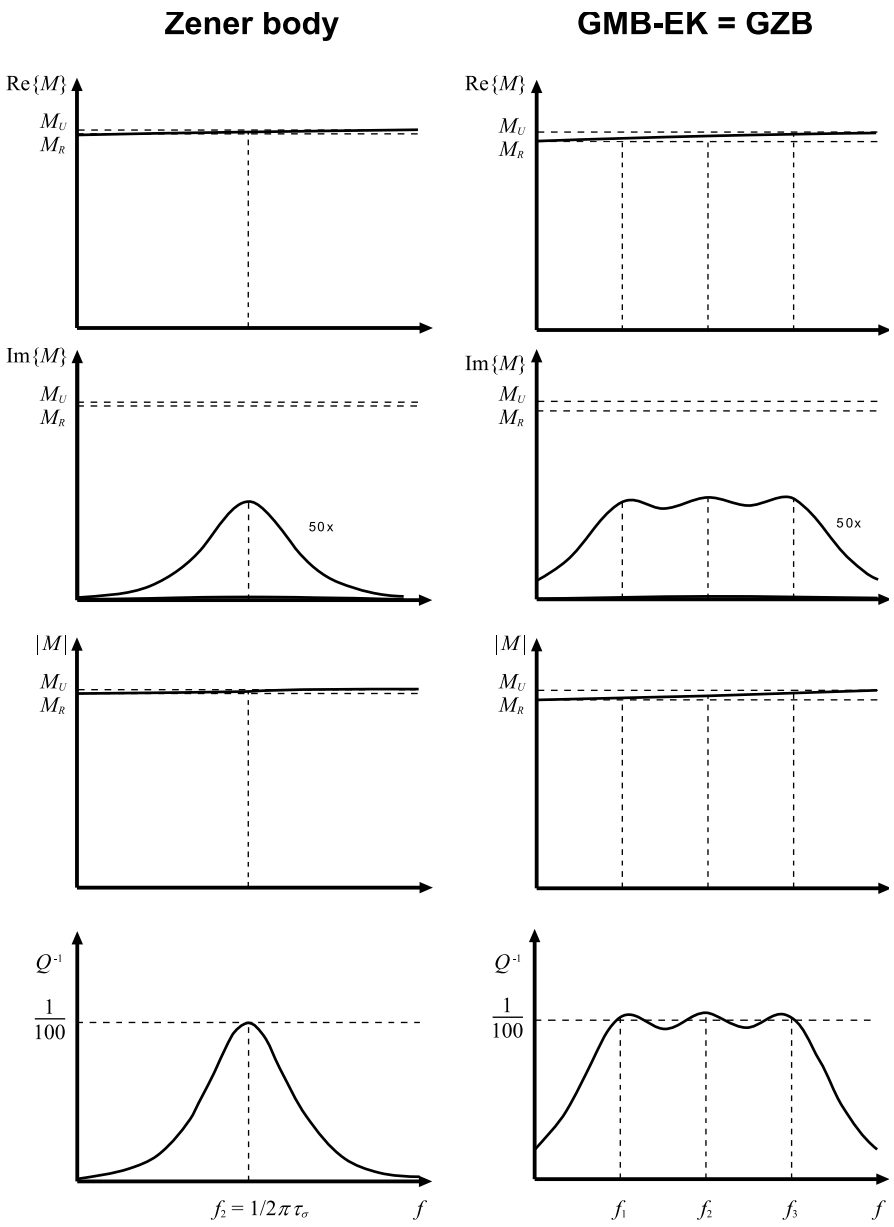

Fig. 4.9. Viscoelastic modulus M and attenuation $1/Q$ as functions of frequency f. The horizontal axis (frequency) is logarithmic, the vertical axis decadic. Modulus for Zener body is calculated using eq. (4.107) with relaxation times $\tau_\sigma = 1/2\pi$ and $\tau_\varepsilon = 101\,\tau_\sigma/99$ (the value for τ_ε is chosen in order to have $Q = 100$), modulus for GMB-EK body using eq. (4.121) with $n = 3$ and relaxation frequencies $f_1 = 0.1$ Hz, $f_2 = 1$ Hz, and $f_3 = 10$ Hz. The other parameters are chosen in order to have one and the same value for Q at relaxation frequencies. Frequency dependence of $1/Q$ is calculated using eq. (4.42).

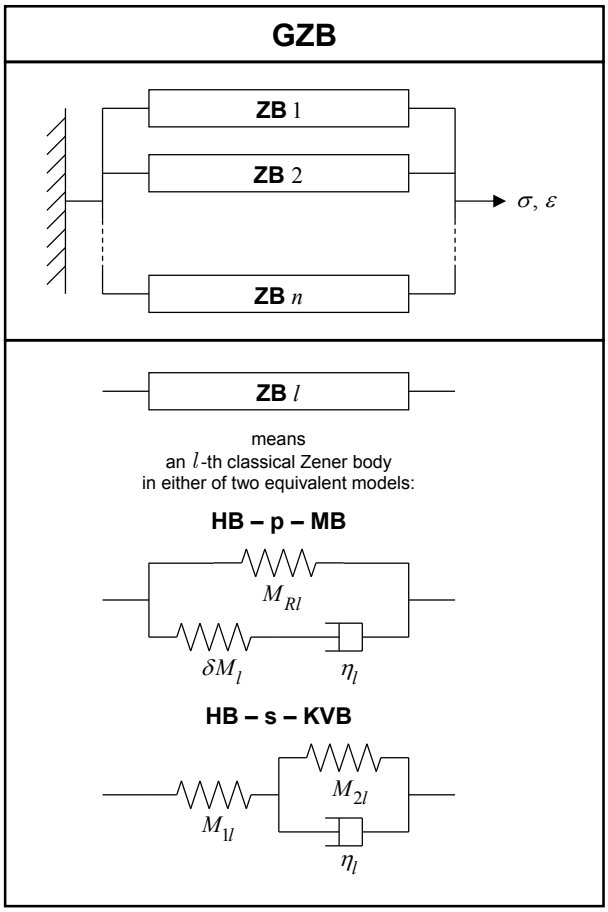

Fig. 4.10. Rheological model of the Generalized Zener Body (GZB). For a classical Zener body (standard linear body) there are two equivalent models: HB – p – MB, that is, Hooke element connected in parallel with Maxwell body, and HB – s – KVB, that is, Hooke element connected in series with Kelvin-Voigt body. In the HB – p – MB model it is easier to recognize the relaxed modulus M_{Rl} and modulus defect δM. M_{1l} and M_{2l} in the HB – s – KVB model denote elastic moduli. In both models η_l stands for viscosity.

(1984) assumed that, in general, the viscoelastic modulus is not a rational function. Therefore they suggested approximating a viscoelastic modulus by an n^{th}-order rational function and determining its coefficients by the Padé approximant method. They obtained n ordinary differential equations for n additional internal variables, which replace the convolution integral. The sum of the internal variables multiplied by the unrelaxed modulus gives an additional viscoelastic term to the elastic stress. The revolutionary work of Day and Minster not only developed one particular approach but, in fact, indirectly suggested the future evolution – a direct use of the rheological models whose $M(\omega)$ is a rational function of $\mathrm{i}\omega$.

Emmerich and Korn (1987) realized that an acceptable relaxation function corresponds to rheology of what they defined as the generalized Maxwell body – n Maxwell bodies and one Hooke element (elastic spring) connected in parallel; see Fig. 4.11. Note that the generalized Maxwell body in the literature on rheology is defined without the additional single Hooke element. Therefore, we denote the model considered by Emmerich and Korn (1987) by GMB-EK.

Because, in fact, any model consisting of linear springs and dashpots (Stokes elements) connected in series or parallel has its viscoelastic modulus in form of a rational function of $\mathrm{i}\omega$, the GMB-EK allowed replacing the convolution integral by a differential form. Emmerich and Korn (1987) obtained for the new variables similar differential equations as Day and Minster (1984). In order to fit an arbitrary $Q(\omega)$ law they chose the relaxation frequencies logarithmically equidistant over a desired frequency range and used the least-square method to determine weight factors of the relaxation mechanisms (classical Maxwell bodies). Emmerich and Korn (1987) demonstrated that their approach is better than the approach based on the Padé approximant method in both accuracy and computational efficiency.

Independently, Carcione et al. (1988a,b), in accordance with the approach of Liu et al. (1976), assumed the generalized Zener body (GZB) - n Zener bodies, that is, n standard linear bodies, connected in parallel; see Fig. 4.10. Carcione et al. developed a theory for the GZB and introduced term memory variables for the obtained additional variables.

We will briefly review the GMB-EK and GZB presented in papers by Emmerich and Korn (1987) and Carcione et al. (1988a,b), respectively.

4.4.6 Generalized Maxwell Body and Generalized Zener Body

Generalized Maxwell Body (GMB-EK). Using the frequency-domain rules for the linear viscoelastic models we easily find for the GMB-EK, shown in Fig. 4.11,

$$M(\omega) = M_H + \sum_{l=1}^{n} \frac{\mathrm{i} M_l \omega}{\omega_l + \mathrm{i}\omega} \tag{4.116}$$

with relaxation frequencies

$$\omega_l = \frac{M_l}{\eta_l} \; ; \quad l = 1, ..., n \; . \tag{4.117}$$

We find relaxed and unrelaxed moduli

$$M_R = \lim_{\omega \to 0} M(\omega) = M_H \quad , \quad M_U = \lim_{\omega \to \infty} M(\omega) = M_R + \sum_{l=1}^{n} M_l \; . \tag{4.118}$$

Since $M_U = M_R + \delta M$,

$$M_l = \delta M_l \; . \tag{4.119}$$

Without any simplification we can consider

$$\delta M_l = a_l \, \delta M \; ; \quad \sum_{l=1}^{n} a_l = 1 \; . \tag{4.120}$$

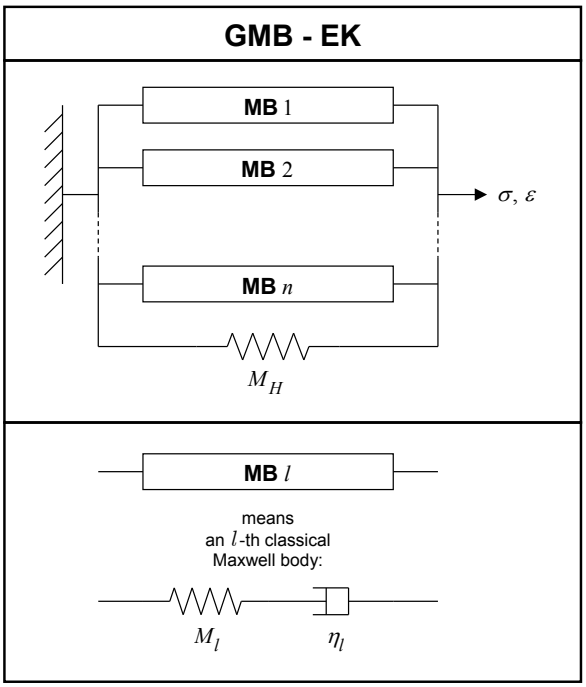

Fig. 4.11. Rheological model of the Generalized Maxwell Body (GMB-EK) defined by Emmerich and Korn (1987). MB denotes Maxwell body, M_H and M_l denote elastic moduli, η_l viscosity.

Then

$$M(\omega) = M_R + \delta M \sum_{l=1}^{n} \frac{\mathrm{i} a_l \omega}{\omega_l + \mathrm{i}\omega} . \tag{4.121}$$

Using relation (4.27) we easily obtain the relaxation function

$$\psi(t) = \left[M_R + \delta M \sum_{l=1}^{n} a_l e^{-\omega_l t} \right] \cdot H(t) , \tag{4.122}$$

where $H(t)$ is the Heaviside unit step function. The above formulas were presented by Emmerich and Korn (1987).

Generalized Zener Body (GZB). From the two equivalent models of the GZB (see Fig. 4.10) we choose the one in which a single ZB is of the HB-p-MB type (Hooke element in parallel with Maxwell body). This is because we can immediately see the meaning (M_{Rl}, δM_l) of the elastic moduli of both Hooke elements in each ZB. For the GZB we easily obtain a well-known

$$M(\omega) = \sum_{l=1}^{n} M_{Rl} \frac{1 + \mathrm{i}\tau_{\varepsilon l}\omega}{1 + \mathrm{i}\tau_{\sigma l}\omega} \tag{4.123}$$

with relaxation times

$$\tau_{\varepsilon l} \;=\; \frac{\eta_l}{\delta M_l}\frac{M_{U\,l}}{M_{R\,l}} \quad , \quad \tau_{\sigma l} \;=\; \frac{\eta_l}{\delta M_l} \quad , \quad \frac{\tau_{\varepsilon l}}{\tau_{\sigma l}} \;=\; \frac{M_{U\,l}}{M_{R\,l}} \tag{4.124}$$

and

$$M_{U\,l} \;=\; M_{R\,l} \;+\; \delta M_l \;. \tag{4.125}$$

The unrelaxed and relaxed moduli are

$$\begin{aligned} M_R \;&=\; \lim_{\omega\to 0} M\,(\omega) \;\;=\; \sum_{l=1}^{n} M_{R\,l} \;, \\ M_U \;&=\; \lim_{\omega\to \infty} M\,(\omega) \;=\; \sum_{l=1}^{n} M_{R\,l}\frac{\tau_{\varepsilon l}}{\tau_{\sigma l}} \;=\; M_R \;+\; \sum_{l=1}^{n} \delta M_l \;. \end{aligned} \tag{4.126}$$

Using relation (4.27) we easily obtain the relaxation function

$$\psi(t) \;=\; \left\{ \sum_{l=1}^{n} M_{R\,l} \left[\, 1 - \left(1 - \frac{\tau_{\varepsilon l}}{\tau_{\sigma l}}\right) \exp\left(-\frac{t}{\tau_{\sigma l}}\right)\right] \right\} \cdot H(t) \;. \tag{4.127}$$

Assuming simplification (Carcione, 2001)

$$M_{R\,l} \;=\; \frac{1}{n} M_R \tag{4.128}$$

we get

$$\begin{aligned} M\,(\omega) \;&=\; \frac{M_R}{n} \sum_{l=1}^{n} \frac{1 + \mathrm{i}\,\tau_{\varepsilon l}\,\omega}{1 + \mathrm{i}\,\tau_{\sigma l}\,\omega} \;, \\ \psi(t) \;\;&=\; M_R \left[\, 1 \;-\; \frac{1}{n} \sum_{l=1}^{n} \left(\, 1 \;-\; \frac{\tau_{\varepsilon l}}{\tau_{\sigma l}}\right) \exp\left(-\frac{t}{\tau_{\sigma l}}\right)\right] \cdot H(t) \;. \end{aligned} \tag{4.129}$$

Formulas (4.128) and (4.129) were presented by Carcione (2001). As far as we know, papers dealing with the incorporation of the attenuation based on the GZB, starting from (Liu et al., 1976), had the same error – the missing factor $1/n$ in the viscoelastic modulus and relaxation function ($1/L$ in most of the papers, L being the number of classical Zener bodies, that is, the number of relaxation mechanisms).

Equivalence of the GMB-EK and GZB. After papers by Emmerich and Korn (1987) and Carcione et al. (1988a,b) different authors decided either for the GMB-EK or GZB.

The GMB-EK formulas were used by Emmerich (1992), Fäh (1992), Moczo and Bard (1993), and in many other papers. Moczo et al. (1997) applied the approach also in the finite-element method and hybrid finite-difference – finite-element method. An important aspect was that in the papers one memory variable was defined for one displacement component. Later Xu and McMechan (1995) introduced term composite memory variables which, however, did not differ from the variables used from the very beginning in the above papers.

Robertsson et al. (1994) implemented the memory variables based on the GZB rheology into the staggered-grid velocity-stress finite-difference scheme. Their numerical results do not suffer from the missing factor $1/n$ because they were performed for $n = 1$. Blanch et al. (1995) suggested an approximate single-parameter method, τ-method, to approximate constant $Q(\omega)$ law. Xu and McMechan (1998) used simulated annealing for determining a best combination of relaxation mechanisms to approximate a desired $Q(\omega)$ law. In the two latter papers the factor $1/n$ was missing in the relaxation functions.

As far as we know, in many following papers the authors using the GZB did not comment on the rheology of the GMB-EK and the corresponding time-domain algorithms, and the authors using the GMB-EK did not comment those for the GZB. Thus, two parallel sets of papers and algorithms had been developed during years.

Moczo and Kristek (2005) analyzed the two models and showed that they are equivalent.

Here we follow the derivation by Moczo and Kristek (2005). Consider again the ZB (HB – p – MB) model. The application of the frequency-domain rules (Table 4.1) to the l-th ZB, that is to (HB – p – MB), gives

$$\sigma_l(\omega)\cdot\left(\frac{1}{\delta M_l}+\frac{1}{\mathrm{i}\eta_l\omega}\right)=\left(1+\frac{M_{Rl}}{\delta M_l}+\frac{M_{Rl}}{\mathrm{i}\eta_l\omega}\right)\cdot\varepsilon(\omega)\ . \tag{4.130}$$

Defining

$$\omega_l=\frac{\delta M_l}{\eta_l} \tag{4.131}$$

and rearranging eq. (4.130) we get

$$\sigma_l(\omega)=M_l(\omega)\cdot\varepsilon(\omega)\ ;\quad M_l(\omega)=M_{Rl}+\frac{\mathrm{i}\delta M_l\omega}{\omega_l+\mathrm{i}\omega}\ . \tag{4.132}$$

For n ZB (H – p – M) connected in parallel, that is, for the GZB (Fig. 4.10), the stress is

$$\sigma(\omega)=\sum_{l=1}^{n}\sigma_l(\omega)=\left[\sum_{l=1}^{n}M_l(\omega)\right]\cdot\varepsilon(\omega) \tag{4.133}$$

and thus

$$M(\omega)=\sum_{l=1}^{n}M_{Rl}+\sum_{l=1}^{n}\frac{\mathrm{i}\delta M_l\omega}{\omega_l+\mathrm{i}\omega}\ . \tag{4.134}$$

Because

$$M_R=\sum_{l=1}^{n}M_{Rl}\ ,\quad M_U=M_R+\sum_{l=1}^{n}\delta M_l\ ,\quad M_U=M_R+\delta M\ , \tag{4.135}$$

without loss of generality we can consider

$$\delta M_l=a_l\,\delta M\ ;\quad \sum_{l=1}^{n}a_l=1 \tag{4.136}$$

and get

$$M(\omega) = M_R + \delta M \sum_{l=1}^{n} \frac{\mathrm{i} a_l \omega}{\omega_l + \mathrm{i}\omega} . \tag{4.137}$$

We see that for the GZB (HB – p – MB), Fig. 4.10, we obtained exactly the same $M(\omega)$ as it has been obtained by Emmerich and Korn (1987) for their GMB-EK (Fig. 4.11). It is also easy to get the same for the GZB (HB – s – KVB) or to rewrite non-simplified $\psi(t)$ for the GZB, eq. (4.127), into the form of $\psi(t)$ for the GMB-EK, eq. (4.122), without any simplification. In other words, the rheology of the GMB-EK and GZB is one and the same. As a consequence, we can continue with the GMB-EK and its simpler-form relations compared to those developed in papers on the GZB with two relaxation times. Also note that there is no need for a simplification (4.128) in eqs. (4.129).

Viscoelastic modulus M and attenuation $1/Q$ as functions of frequency f are illustrated in the right column of Fig. 4.9.

4.4.7 Anelastic Functions (Memory Variables)

We will use term anelastic functions instead of memory variables. It is easy to rewrite the viscoelastic modulus (4.137) and relaxation function (4.122) using the unrelaxed modulus,

$$M(\omega) = M_U - \delta M \sum_{l=1}^{n} \frac{a_l \omega_l}{\omega_l + \mathrm{i}\omega} \tag{4.138}$$

and

$$\psi(t) = \left[M_U - \delta M \sum_{l=1}^{n} a_l \left(1 - e^{-\omega_l t}\right) \right] \cdot H(t) , \tag{4.139}$$

and obtain the time derivative of the relaxation function

$$\begin{aligned} M(t) &= \dot{\psi}(t) \\ &= -\delta M \sum_{l=1}^{n} a_l \omega_l e^{-\omega_l t} \cdot H(t) + \left[M_U - \delta M \sum_{l=1}^{n} a_l \left(1 - e^{-\omega_l t}\right) \right] \cdot \delta(t) . \end{aligned} \tag{4.140}$$

Inserting eq. (4.140) into eq. (4.23) gives

$$\begin{aligned} \sigma(t) = & -\int_{-\infty}^{t} \delta M \sum_{l=1}^{n} a_l \omega_l e^{-\omega_l (t-\tau)} \cdot H(t-\tau) \cdot \varepsilon(\tau) \, \mathrm{d}\tau \\ & + \int_{-\infty}^{t} M_U \cdot \delta(t-\tau) \cdot \varepsilon(\tau) \, \mathrm{d}\tau \\ & - \int_{-\infty}^{t} \delta M \sum_{l=1}^{n} a_l \left(1 - e^{-\omega_l (t-\tau)}\right) \cdot \delta(t-\tau) \cdot \varepsilon(\tau) \, \mathrm{d}\tau \end{aligned} \tag{4.141}$$

and

$$\sigma(t) \;=\; M_U \cdot \varepsilon(t) \;-\; \delta M \sum_{l=1}^{n} a_l\, \omega_l \int_{-\infty}^{t} \varepsilon\,(\tau) \;\cdot e^{-\omega_l (t-\tau)}\, \mathrm{d}\tau \;. \tag{4.142}$$

Now it is possible to replace the convolution integral by additional functions (anelastic functions, internal variables, new variables, memory variables). Day and Minster (1984), Emmerich and Korn (1987) and Carcione et al. (1988a,b) defined the additional functions as dependent also on the material properties.

For an important reason that will be explained later, Kristek and Moczo (2003) defined their anelastic functions as independent of the material properties. Here we follow derivation by Kristek and Moczo (2003). Defining an anelastic function

$$\zeta_l(t) \;=\; \omega_l \int_{-\infty}^{t} \varepsilon\,(\tau) \;\cdot e^{-\omega_l (t-\tau)}\, \mathrm{d}\tau \;, \quad l = 1, ..., n \tag{4.143}$$

we get the stress-strain relation in the form

$$\sigma(t) \;=\; M_U \cdot \varepsilon(t) - \sum_{l=1}^{n} \delta M\, a_l\, \zeta_l(t) \;. \tag{4.144}$$

Applying time derivative to eq. (4.143) we get

$$\begin{aligned} \dot{\zeta}_l(t) \;&=\; \omega_l \,\frac{\mathrm{d}}{\mathrm{d}t} \int_{-\infty}^{t} \varepsilon\,(\tau) \cdot e^{-\omega_l (t-\tau)}\, \mathrm{d}\tau \\ &=\; \omega_l \left[-\omega_l \int_{-\infty}^{t} \varepsilon\,(\tau) \;\cdot e^{-\omega_l (t-\tau)}\, \mathrm{d}\tau + \varepsilon(t) \right] \\ &=\; \omega_l \,[\, -\zeta_l(t) \;+\; \varepsilon(t)\,] \end{aligned} \tag{4.145}$$

and

$$\dot{\zeta}_l(t) \;+\; \omega_l\, \zeta_l(t) \;=\; \omega_l\, \varepsilon(t) \;; \quad l = 1, ..., n \;. \tag{4.146}$$

Equations (4.144) and (4.146) define the time-domain stress-strain relation for the viscoelastic medium whose rheology corresponds to rheology of the GMB-EK (and to its equivalent – the GZB).

In the so-called velocity-stress formulation (the next chapter) the time derivative of the stress is needed. In such a case, $M(t)$ given by eq. (4.140) is inserted into relation (4.29) and the above procedure of obtaining the anelastic functions and stress-strain relation can be followed with time derivatives of the stress and strain instead of the stress and strain themselves. An alternative procedure is to apply time derivatives to eqs. (4.144) and (4.146), and define the anelastic function as the time derivative of the anelastic function (4.143). In either case we obtain

$$\dot{\sigma}(t) \;=\; M_U \cdot \dot{\varepsilon}(t) \;-\; \sum_{l=1}^{n} \delta M\, a_l\, \xi_l(t) \tag{4.147}$$

and

$$\dot{\xi}_l(t) \;+\; \omega_l\, \xi_l(t) \;=\; \omega_l\, \dot{\varepsilon}(t)\;; \quad l = 1, ..., n\;. \tag{4.148}$$

It is useful to define anelastic coefficients

$$Y_l \;=\; a_l\, \frac{\delta M}{M_U}\;; \quad l = 1, ..., n\;. \tag{4.149}$$

Then the stress-strain relations (4.144) and (4.147) become

$$\sigma(t) \;=\; M_U \cdot \varepsilon(t) \;-\; \sum_{l=1}^{n} M_U\, Y_l\, \zeta_l(t) \tag{4.150}$$

and

$$\dot{\sigma}(t) \;=\; M_U \cdot \dot{\varepsilon}(t) \;-\; \sum_{l=1}^{n} M_U\, Y_l\, \xi_l(t)\;. \tag{4.151}$$

The related eqs. (4.146) and (4.148) are unchanged. It is clear that the stress or its time derivative can be calculated if the unrelaxed modulus and anelastic coefficients are known. The unrelaxed modulus is directly related to the elastic speed of wave propagation, the anelastic coefficients have to be determined from $Q(\omega)$-law.

Using the anelastic coefficient, the elastic modulus and viscosity in the l-th MB are $M_U\, Y_l$ and $\dfrac{1}{\omega_l}\, M_U\, Y_l$, respectively, the relaxed modulus is

$$M_R \;=\; M_U \left(1 - \sum_{l=1}^{n} Y_l \right),$$

and viscoelastic modulus

$$M\,(\omega) \;=\; M_U \left[1 - \sum_{l=1}^{n} Y_l \frac{\omega_l}{\omega_l + \;\mathrm{i}\omega} \right]. \tag{4.152}$$

(Note that Emmerich and Korn (1987), used slightly less numerically accurate $y_l = a_l\; \delta M / M_R$; $l = 1, ..., n$.) The quality factor (4.42) is

$$\frac{1}{Q\,(\omega)} \;=\; \frac{\sum\limits_{l=1}^{n} Y_l \dfrac{\omega_l\, \omega}{\omega_l^2 + \omega^2}}{1 \;-\; \sum\limits_{l=1}^{n} Y_l \dfrac{\omega_l^2}{\omega_l^2 + \omega^2}}\;. \tag{4.153}$$

From eq. (4.153) we can get

$$Q^{-1}\,(\omega) \;=\; \sum_{l=1}^{n} \frac{\omega_l\, \omega \;+\; \omega_l^2\, Q^{-1}\,(\omega)}{\omega_l^2 + \omega^2}\; Y_l\;. \tag{4.154}$$

Equation (4.154) can be used to numerically fit any $Q(\omega)$-law. Emmerich and Korn (1987) demonstrated that a sufficiently accurate approximation to nearly constant $Q(\omega)$ is obtained if the relaxation frequencies ω_l cover the frequency range under interest logarithmically equidistantly. If, for example, $Q(\omega)$ values are known at frequencies $\tilde{\omega}_k \; ; \; k = 1, ..., 2n-1$, with $\tilde{\omega}_1 = \omega_1, \; \tilde{\omega}_{2n-1} = \omega_n$, eq. (4.154) can be solved for the anelastic coefficients using the least square method.

A more detailed discussion of the frequency range and its sampling by frequencies $\tilde{\omega}_k$ can be found in the paper by Graves and Day (2003, equations 13 and 14).

In practice, a phase velocity at certain reference frequency ω_r , instead of the elastic velocity corresponding to the unrelaxed modulus, is known from measurements. The phase velocity $c(\omega)$ is given by

$$\frac{1}{c(\omega)} \; = \; \mathrm{Re}\left[\left(\frac{M(\omega)}{\rho}\right)^{-1/2}\right] . \tag{4.155}$$

From equations (4.152) and (4.155) we get (Moczo et al., 1997) for the phase velocity $c(\omega_r)$

$$M_U \; = \; \rho\, c^2(\omega_r) \; \frac{R + \Theta_1}{2R^2} \; , \tag{4.156}$$

where

$$\begin{aligned} R &= \left(\Theta_1^2 + \Theta_2^2\right)^{1/2} \; , \\ \Theta_1 &= 1 - \sum_{l=1}^{n} Y_l \frac{1}{1 + (\omega_r/\omega_l)^2} \; , \quad \Theta_2 = \sum_{l=1}^{n} Y_l \frac{\omega_r/\omega_l}{1 + (\omega_r/\omega_l)^2} \; . \end{aligned} \tag{4.157}$$

Thus, using equations (4.156) and (4.157), the unrelaxed modulus can be determined from the anelastic coefficients $Y_l \; ; \; l = 1, ..., n$, and phase velocity $c(\omega_r)$.

Before we continue with a 3D problem, for completeness we briefly mention formalism used specifically for the GZB model, that is, before the equivalence of the GZB and GMB rheologies was presented by Moczo and Kristek (2005). Using eqs. (4.127), (4.22), (4.29) and (4.126) we can obtain the following equations that are equivalent to those presented by Robertsson et al. (1994):

$$\dot{\sigma}(t) \; = \; M_U \cdot \dot{\varepsilon}(t) \; - \; \sum_{l=1}^{n} r_l(t) \; , \tag{4.158}$$

$$r_l(t) \; = \; \frac{M_{Rl}}{\tau_{\sigma l}} \left(1 - \frac{\tau_{\varepsilon l}}{\tau_{\sigma l}}\right) \int_{-\infty}^{t} \dot{\varepsilon}(\tau) \cdot \exp\left(-\frac{t - \tau}{\tau_{\sigma l}}\right) \mathrm{d}\tau \; , \quad l = 1, ..., n \; , \tag{4.159}$$

$$\dot{r}_l(t) \; + \; \frac{1}{\tau_{\sigma l}} \, r_l(t) \; = \; \frac{M_{Rl}}{\tau_{\sigma l}} \left(1 - \frac{\tau_{\varepsilon l}}{\tau_{\sigma l}}\right) \dot{\varepsilon}(t) \; , \quad l = 1, ..., n \; . \tag{4.160}$$

As already explained, the anelastic functions (memory variables) $r_l(t)$ in eqs. (4.158) - (4.160) depend on material.

Rheology of a 3D isotropic medium, see eq. (4.17), can be assumed as made of rheologies of two GMB-EK bodies. One is for time-dependent relaxation function $\kappa(t)$ or, equivalently, for the complex frequency-dependent bulk modulus $\kappa(\omega)$. The other is for time-dependent relaxation function $\mu(t)$ or, equivalently, for the complex frequency-dependent shear modulus $\mu(\omega)$.

Analogously to the 1D problem we can obtain the stress-strain relation corresponding to the assumed superposition of two GMB-EK (or, equivalently, two GZB) bodies for the 3D rheology Kristek and Moczo (2003):

$$\begin{aligned} \sigma_{ij} \;&=\; \kappa\,\varepsilon_{kk}\,\delta_{ij} \;+\; 2\mu\left(\varepsilon_{ij} - \tfrac{1}{3}\varepsilon_{kk}\,\delta_{ij}\right) \\ &-\; \sum_{l=1}^{n}\left[\,\kappa\,Y_l^{\kappa}\zeta_l^{kk}\delta_{ij} \;+\; 2\mu\,Y_l^{\mu}\left(\zeta_l^{ij} - \tfrac{1}{3}\zeta_l^{kk}\delta_{ij}\right)\right] \;. \end{aligned} \tag{4.161}$$

Here, $i,j,k \in \{1,2,3\}$, the equal-index summation convention applies to index k but does not apply to index l. $\kappa\,(x_1,\;x_2,\;x_3)$ and $\mu\,(x_1,\;x_2,\;x_3)$ are unrelaxed (elastic) bulk and shear moduli, and Y_l^{κ} and Y_l^{μ} are the corresponding anelastic coefficients. Assuming a measured or estimated $Q_\alpha\,(\omega)$ for the P- and $Q_\beta\,(\omega)$ for the S-waves, the corresponding anelastic coefficients Y_l^{α} and Y_l^{β} are obtained using, compare with eq. (4.154),

$$Q_\nu^{-1}\,(\tilde{\omega}_k) \;=\; \sum_{l=1}^{n}\frac{\omega_l\,\tilde{\omega}_k \;+\; \omega_l^2\,Q_\nu^{-1}\,(\tilde{\omega}_k)}{\omega_l^2 \;+\; \tilde{\omega}_k^2}\;Y_l^{\nu}\;;\quad k=1,...,2n-1\;;\quad \nu\in\{\alpha,\beta\}\,, \tag{4.162}$$

where

$$\alpha \;=\; \left(\frac{\kappa+\frac{4}{3}\mu}{\rho}\right)^{1/2}\;,\qquad \beta \;=\; \left(\frac{\mu}{\rho}\right)^{1/2} \tag{4.163}$$

are the elastic (that is, corresponding to unrelaxed moduli) P- and S-wave velocities. Then the anelastic coefficients Y_l^{κ} and Y_l^{μ} are given by

$$Y_l^{\kappa} \;=\; \left(\alpha^2\,Y_l^{\alpha} - \tfrac{4}{3}\,\beta^2\,Y_l^{\beta}\right)\Big/\left(\alpha^2 - \tfrac{4}{3}\beta^2\right)\;;\quad l=1,...,n\,, \tag{4.164}$$

and

$$Y_l^{\mu} \;=\; Y_l^{\beta}\;;\quad l=1,...,n\,, \tag{4.165}$$

respectively. For each of 6 independent strain-tensor components we have n material-independent anelastic functions ζ_l^{ij}. The anelastic functions satisfy equations

$$\dot{\zeta}_l^{ij} + \omega_l\,\zeta_l^{ij} \;=\; \omega_l\;\varepsilon_{ij}\;;\quad l=1,...,n\,. \tag{4.166}$$

Note that the equal-index summation convention does not apply to index l. Thus, the relation between the stress and strain tensors in the viscoelastic medium with rheology of the GMB-EK

is given by eqs. (4.161) and (4.166) with anelastic functions given by eqs. (4.164) and (4.165). As mentioned before, in the case of the velocity-stress formulation of the equation of motion, time derivative of the stress tensor is needed. It is easy to obtain from eqs. (4.161) and (4.166)

$$\begin{aligned} \dot{\sigma}_{ij} &= \kappa\, \dot{\varepsilon}_{kk}\, \delta_{ij} + 2\mu \left(\dot{\varepsilon}_{ij} - \tfrac{1}{3}\, \dot{\varepsilon}_{kk}\, \delta_{ij}\right) \\ &- \sum_{l=1}^{n} \left[\kappa\, Y_l^{\kappa} \xi_l^{kk}\, \delta_{ij} + 2\mu\, Y_l^{\mu} \left(\xi_l^{ij} - \tfrac{1}{3}\, \xi_l^{kk}\, \delta_{ij}\right) \right] \end{aligned} \tag{4.167}$$

and

$$\dot{\xi}_l^{ij} + \omega_l\, \xi_l^{ij} = \omega_l\, \dot{\varepsilon}_{ij} \;; \quad l = 1, ..., n\,. \tag{4.168}$$

Incorporation of attenuation for anisotropic media is a little bit more complicated; see, e.g., Carcione and Cavallini (1994) and Carcione (2001).

5 Displacement, Displacement-velocity-stress, Displacement-stress, and Velocity-stress Formulations of the Equation of Motion

Having the equation of motion and constitutive law we can introduce alternative formulations in terms of which field quantity is considered as an unknown function. Here we restrict to the strong formulation for elastic and isotropic medium. We can easily obtain four alternative formulations. Their names clearly indicate which quantities (that is, displacement vector, particle-velocity vector, stress tensor) are chosen as unknown functions. They are

displacement-stress

$$\begin{aligned} \rho\, \ddot{u}_i &= \sigma_{ij,j} + f_i \\ \sigma_{ij} &= \kappa\, \varepsilon_{kk}\, \delta_{ij} + 2\mu \left(\varepsilon_{ij} - \tfrac{1}{3}\varepsilon_{kk}\, \delta_{ij}\right) \\ &\text{or} \\ \sigma_{ij} &= \lambda\, \varepsilon_{kk}\, \delta_{ij} + 2\mu\, \varepsilon_{ij} \end{aligned} \tag{5.1}$$

displacement-velocity-stress

$$\begin{aligned} \rho\, \dot{v}_i &= \sigma_{ij,j} + f_i \\ v_i &= \dot{u}_i \\ \sigma_{ij} &= \kappa\, \varepsilon_{kk}\, \delta_{ij} + 2\mu \left(\varepsilon_{ij} - \tfrac{1}{3}\varepsilon_{kk}\, \delta_{ij}\right) \\ &\text{or} \\ \sigma_{ij} &= \lambda\, \varepsilon_{kk}\, \delta_{ij} + 2\mu\, \varepsilon_{ij} \end{aligned} \tag{5.2}$$

velocity-stress

$$\begin{aligned} \rho\,\dot{v}_i &= \sigma_{ij,j} + f_i \\ \dot{\sigma}_{ij} &= \kappa\,\dot{\varepsilon}_{kk}\,\delta_{ij} + 2\mu\,\left(\dot{\varepsilon}_{ij} - \tfrac{1}{3}\dot{\varepsilon}_{kk}\,\delta_{ij}\right) \\ &\text{or} \\ \dot{\sigma}_{ij} &= \lambda\,\dot{\varepsilon}_{kk}\,\delta_{ij} + 2\mu\,\dot{\varepsilon}_{ij} \end{aligned} \tag{5.3}$$

displacement

$$\begin{aligned} \rho\,\ddot{u}_i &= [(\kappa - \tfrac{2}{3}\mu)\,u_{k,k}]_{,i} + (\mu\,u_{i,j})_{,j} + (\mu\,u_{j,i})_{,j} + f_i \\ &\text{or} \\ \rho\,\ddot{u}_i &= [\lambda\,u_{k,k}]_{,i} + (\mu\,u_{i,j})_{,j} + (\mu\,u_{j,i})_{,j} + f_i\,. \end{aligned} \tag{5.4}$$

For brevity, the strain tensor

$$\varepsilon_{i\,j} = \tfrac{1}{2}\,(u_{i,j} + u_{j,i}) \tag{5.5}$$

and its time derivative

$$\dot{\varepsilon}_{i\,j} = \tfrac{1}{2}\,(v_{i,j} + v_{j,i}) \tag{5.6}$$

were used here in the first three formulations. The equations can be easily generalized for the case of viscoelastic, eq. (4.161) or (4.167), or anisotropic media, eqs. (4.7).

6 Numerical Methods

6.1 Introduction

Analytical mathematical methods do not provide solutions to problems for structurally complex models. Such models are, however, necessary if they should reasonably approximate real structures in the Earth. Approximate methods have to be applied. Numerical methods transform an original differential or integral formulation of a problem into a system of algebraic equations. This is because algebraic operations can be efficiently performed using computers.

A continuous function has to be represented by a finite set of numbers. Numerical methods differ in how they solve this task. They also differ in a way how they approximate spatial and time derivatives of functions.

There are two other basic aspects of each numerical method: accuracy and computational efficiency (in terms of the computer memory and time). One can guess that these two aspects are in most cases contradictory and a practical decision-making has to consider a trade-off between the accuracy and computational efficiency.

If a computational domain is covered by a discrete space-time grid, that is, if continuous medium and continuous functions are somehow represented using a set of discrete space-time positions, we could speak of grid methods. Some authors (for example Durran, 1999), however, distinguish grid-point methods (such as the finite-difference or finite-volume methods) and

series-expansion methods (such as the spectral or finite-element methods) though all they use set of discrete points.

In general, grid-point methods are simpler and easier to implement in the computer codes, compared to the series-expansion methods. Likely because of this, they have been in use for a longer time than the series-expansion methods.

In the grid-point methods each function is represented by its values at grid points. The space-time distribution of grid points may be, in principle, arbitrary but it significantly affects properties of the resulting numerical approximation. In the finite-difference method usually no assumption is made about functional values in-between the grid points. A derivative of a function is approximated using a finite-difference formula which makes use of function values at a specified set of grid points.

In the finite-volume method some assumption is made about the functional values in-between the grid points. A value at a grid point is averaged over a grid cell. A derivative of a function obviously is determined by the assumed space-time structure of the approximate function. The finite-difference and finite-volume schemes are very close if the approximate function is smooth.

In the series-expansion methods an unknown function is usually represented by a linear combination of a finite number of continuous expansion functions (shape functions). Consequently, a finite set of coefficients of the expansion functions describe an approximate solution. Given the chosen expansion functions, a spatial derivative is determined analytically. The time derivatives are usually approximated using the finite-difference formulas.

In the spectral-element and finite-element methods a computational domain is covered by a mesh of elements (they nodal points form a grid of discrete points). In the spectral-element method the expansion functions form an orthogonal set. In the finite-element method the expansion functions are nonzero only in one element. If the expansion functions are chosen to be piece-wise linear functions, the resulting finite-element scheme may be similar to those obtained from the grid-point methods.

In the following we will focus on the finite-difference and finite-element methods.

6.2 The Finite-difference Method (FDM)

The application of the method to a particular differential problem includes a.) construction of a discrete FD model of the problem (coverage of the computational domain by a space-time grid, FD approximations to derivatives, functions, initial and/or boundary condition all at the grid points, construction of a system of the finite-difference, i.e., algebraic, equations), b.) analysis of the FD model (consistency and order of the approximation, stability, convergence), c.) numerical computations. The analysis of the FD model or numerical computations may lead to redefinition of the grid and FD approximations, if numerical behavior is not satisfactory.

6.2.1 Grids

Consider a Cartesian coordinate system $(x,\ y,\ z)$ and a computational domain in the four-dimensional space of variables $(x,\ y,\ z,\ t)$ with t meaning time. A set of discrete space-time points

(positions)

$$(x_I, y_J, z_K, t_m); \qquad \begin{aligned} x_I &= x_0 + I\ \Delta x\,, \\ y_J &= y_0 + J\ \Delta y\,, \\ z_K &= z_0 + K\,\Delta z\,, \\ t_m &= t_0 + m\,\Delta t\,, \end{aligned} \tag{6.1}$$

and I, J, K, $m \in \{0, 1, 2, ...\}$ define a space-time grid. The spatial increments Δx, Δy and Δz are usually called grid spacings, Δt is the time step. In many applications, the regular (uniform) rectangular grid with the grid spacings $\Delta x = \Delta y = \Delta z = h$ is a natural and reasonable choice. The value of a function u at a grid position $(x_I,\, y_J,\, z_K,\, t_m)$, that is $u\,(I, J, K, m)$ or $u^m_{I,J,K}$, is approximated by a grid function $U^m_{I,J,K} = U(x_I,\, y_J,\, z_K,\, t_m)$.

Other than Cartesian coordinate systems can be used to define a grid. A particular choice should be problem-dependent. Whereas, for example, spherical coordinates are convenient for the whole Earth's models, cylindrical coordinates are suitable for modeling boreholes. The choice of the grid determines the structure and properties of the FD approximations to derivatives and consequently the properties of the FD equations. In the following we will restrict to FD schemes constructed for grids corresponding to the Cartesian coordinate systems.

The use of a uniform grid usually yields algorithmically simplest FD schemes. This, however, may contradict the computational efficiency. In some problems it may be advantageous to define a non-uniform grid. Examples are grids with irregularly varying size of the grid spacing or discontinuous (combined) grids with a sudden change in size of the grid spacing. Such grids can better accommodate geometry of the model or reduce the total number of grid points covering the computational space.

If at a grid point the neighbor grid points are always known (for example, if they are defined using some mathematical rule) we speak about structured grids. If at a grid point some additional information is needed about the neighbor grid points we speak about unstructured grids. Obviously, structured grids usually yield computationally faster algorithms compared to those on unstructured grids.

In a conventional grid, all functions are approximated at the same grid positions. In a partly-staggered grid, displacement or particle-velocity components are located at one grid position whereas the stress-tensor components are located at another grid position. In a staggered grid, each displacement and/or particle-velocity component and each shear stress-tensor component has its own grid position. The normal stress-tensor components share another grid position. The staggered distribution of quantities in space is related (through the equation of motion) to the staggered distribution of quantities in time. In all types of grids, an effective density is assigned to a grid position of each displacement or particle-velocity component while an effective elastic modulus is assigned to each grid position of the stress-tensor components. The so-called grid cells of the conventional, partly-staggered and staggered grids are illustrated in Fig. 6.1.

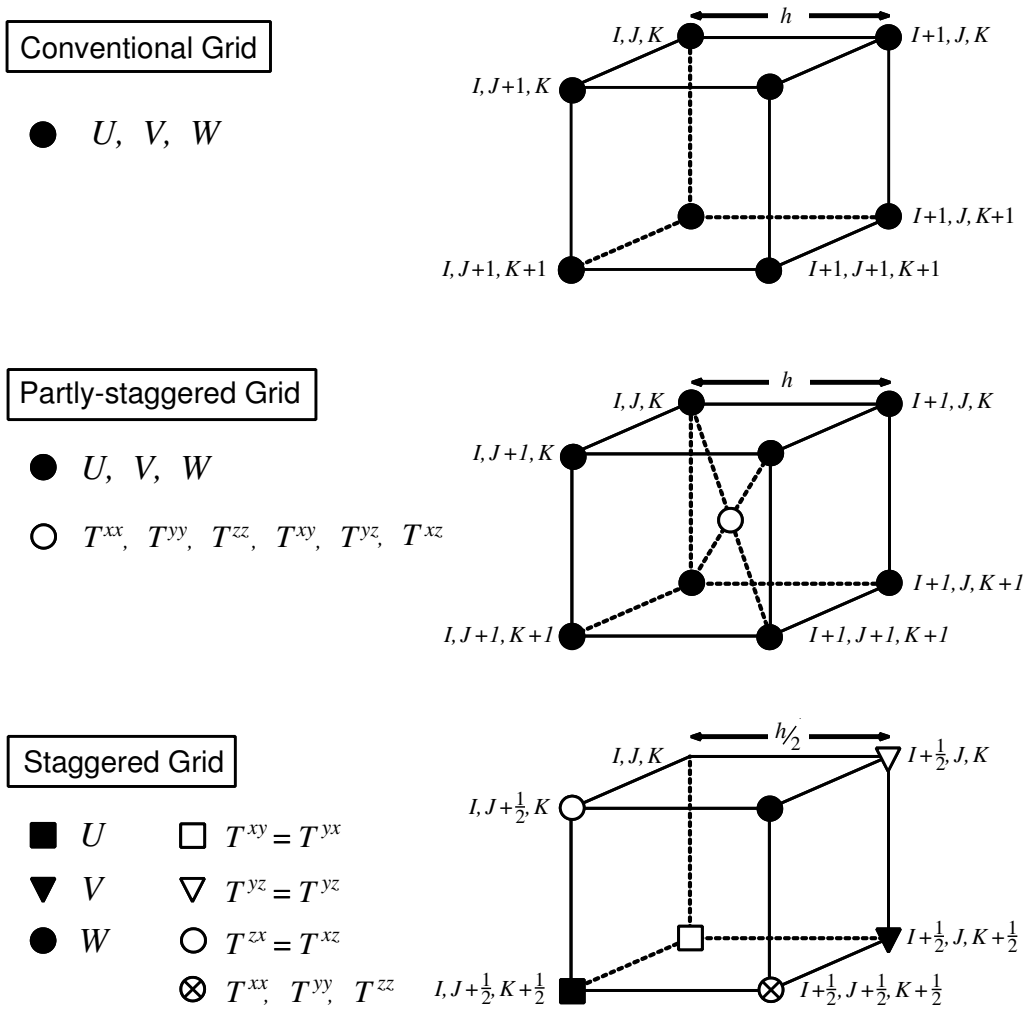

Fig. 6.1. Spatial grid cells in the conventional, partly-staggered and staggered grids. All displacement-vector components U, V and W are located at each grid position in the conventional grid. Either displacement or particle-velocity components U, V and W share the same grid positions whereas stress-tensor components T^{xx}, T^{yy}, T^{zz}, T^{xy}, T^{yz}, and T^{zx} share other grid positions in the partly-staggered grid. Displacement and/or particle-velocity components U, V and W are located at different grid positions as well as stress-tensor components T^{xx}, T^{yy}, T^{zz}, T^{xy}, T^{yz}, and T^{zx} are in the staggered grid. Because the normal stress-tensor components are determined by the same spatial derivatives of the displacement components, they share one grid position.

6.2.2 Finite-difference Approximations

For function $\phi(x)$ with a continuous first derivative, limits

$$\begin{aligned}
\frac{\mathrm{d}\phi}{\mathrm{d}x}(x_0) &= \lim_{h\to 0}\frac{\phi(x_0+h)-\phi(x_0)}{h}\,,\\
\frac{\mathrm{d}\phi}{\mathrm{d}x}(x_0) &= \lim_{h\to 0}\frac{\phi(x_0)\qquad -\phi(x_0-h)}{h}\,,\\
\frac{\mathrm{d}\phi}{\mathrm{d}x}(x_0) &= \lim_{h\to 0}\frac{\phi(x_0+h)-\phi(x_0-h)}{2h}
\end{aligned} \tag{6.2}$$

give one and the same result. Because, however, in the FD grid the size of h is bounded by the size of the grid spacing (distance between two neighboring grid points in the x-direction in this case), the limits cannot be evaluated. Instead, the so-called forward-difference, backward-difference and central-difference formulas,

$$\begin{aligned}
\frac{\mathrm{d}\phi}{\mathrm{d}x}(x_0) &= \frac{\phi(x_0+h)-\phi(x_0)}{h} &&+\ O(h^1)\,,\\
\frac{\mathrm{d}\phi}{\mathrm{d}x}(x_0) &= \frac{\phi(x_0)\qquad -\phi(x_0-h)}{h} &&+\ O(h^1)\,,\\
\frac{\mathrm{d}\phi}{\mathrm{d}x}(x_0) &= \frac{\phi(x_0+h)-\phi(x_0-h)}{2h} &&+\ O(h^2)\,,
\end{aligned} \tag{6.3}$$

approximate the first derivative. The leading term of the truncation error in the two first one-sided formulas is proportional to the grid spacing h - the approximations are just 1^{st}-order accurate. The central-difference formula gives approximation of the 2^{nd}-order. Obviously, in general, the three FD formulas will give different approximate values for the same derivative. Moreover, the use of a particular approximation leads to a particular FD (algebraic) equation.

A 2^{nd}-order FD approximation frequently used to approximate the second derivative in the conventional displacement FD schemes is

$$\frac{\mathrm{d}^2\phi}{\mathrm{d}x^2}(x_0) = \frac{\phi(x_0-h)-2\,\phi(x_0)+\phi(x_0+h)}{h^2} + O(h^2)\,. \tag{6.4}$$

The most frequently used 4^{th}-order approximation to the first derivative in the staggered-grid FD schemes reads

$$\begin{aligned}
\frac{\mathrm{d}\phi}{\mathrm{d}x}(x_0) = \frac{1}{h}\Big\{\ & a\ \left[\phi\left(x_0+\tfrac{3}{2}h\right)-\phi\left(x_0-\tfrac{3}{2}h\right)\right]\ +\\
&+\ b\ \left[\phi\left(x_0+\tfrac{1}{2}h\right)-\phi\left(x_0-\tfrac{1}{2}h\right)\right]\Big\}\ +\ O(h^4)\,.
\end{aligned} \tag{6.5}$$

Here $a = -1/24$ and $b = 9/8$. Using Taylor expansions it is very easy to find a desired approximation to a derivative. In solving a particular problem we may need to approximate a derivative at a given grid point using function values at a certain set of neighboring grid points and with a necessary/desired order of accuracy. Obviously, a reachable order of accuracy in general depends on the configuration of the set of grid positions. An approximated derivative is

expresses in a form of a linear combination of function values at chosen grid positions. All values are Taylor expanded. By equating coefficients for equal powers of the argument increment we then construct a set of algebraic equations for the unknown coefficients of the linear combination such that the linear combination approximates the desired derivative with a desired structure of the truncation error. In non-optimized approximations the only criterion applied to the truncation error is the order of the leading term of the truncation error. The procedure is applicable in the 1D, 2D and 3D as well as in the 4D space-time domain. In the following chapters we will derive several FD approximations of different properties. Here we finish the brief introduction with references to more detailed explanations or treatments: Anderson et al. (1984), Dablain (1986), Fornberg (1988), Geller and Takeuchi (1995, 1998), Klimeš (1996), and Cohen (2002), Moczo et al. (2004b).

6.2.3 Heterogeneous Schemes

If the medium is homogeneous or smoothly heterogeneous (material properties are described by smooth continuous functions of spatial coordinates) it is relatively easy to find a FD scheme. It usually is a suitable FD approximation of the strong form of the equation of motion. If functions describing material properties are discontinuous, that is, if material interfaces (material discontinuities) are present, situation gets considerably more complicated. Motion at points away from the interface is governed by the equation of motion. However, motion at points at the material interface is constrained by boundary conditions. As it is clear from the chapter on the canonical problem with a welded material interface a FD scheme should be a discrete approximation to one of the alternative formulations (we presented four formulations – SF, WF, ISF and DSF). Application of the SF most naturally leads to the so-called homogeneous approach – one scheme is used for points away from the interface, other scheme(s) is (are) used for points at the interface. It is quite obvious that this approach may pose a problem – a homogeneous FD scheme may be specific for a particular problem. Some other problem may require other FD scheme(s). Therefore its application to complex models with curved material discontinuities is, in general, relatively difficult and impractical. Moreover, finding a stable and sufficiently accurate FD approximation to the boundary conditions is not a trivial problem, see, e.g., Kummer and Behle (1982), Slawinski and Krebes (2002).

In the alternative heterogeneous approach only one FD scheme is used for all interior grid points (points not lying on boundaries of a grid) no matter what their positions are with respect to the material discontinuity. The presence of the material discontinuity is accounted for only by assigning appropriate values of elastic moduli and density. Therefore, except for treating the free surface, the heterogeneous approach has been much more popular since the beginning of the seventies. The problem is that in most cases heterogeneous FD schemes were obtained by approximating the equation of motion itself, that is, without proper incorporation of the boundary conditions. In other words, in most cases heterogeneous FD schemes were not consistent with the boundary conditions, mainly with the traction continuity.

6.2.4 Explicit and Implicit Schemes

In an implicit scheme, the motion at a given time level is calculated simultaneously at all spatial grid points from the motion values at previous time levels using the inverse of a matrix. In an

explicit scheme, the motion at any (one) spatial grid point can be updated for the next time level using an explicit FD formula which uses only values of motion at previous time levels. Clearly, the explicit schemes are computationally simpler. Therefore explicit FD schemes have been used in most earthquake ground motion modeling and exploration seismology studies. An interesting example is the numerical realization of the optimally-accurate schemes. The optimization yields an implicit FD scheme. In order to avoid solving large systems of algebraic equations, Geller and Takeuchi (1998) applied a predictor-corrector scheme. For the implicit schemes see, e.g., Emerman et al. (1982), Mufti (1985).

6.2.5 Properties of the FD Schemes

As we mentioned in the introduction to this chapter, a FD scheme should be analyzed for its properties before it is applied. A FD scheme should be consistent with the original problem, stable and convergent. Though intuitively these concepts seem quite clear and obvious, they have to be clearly defined and formulated. Here we closely follow Moczo et al. (2004b, 2007). Let PDE denote a partial differential equation and FDE a FD equation(s). (A FD scheme may be used instead of FDE.)

Consistency. A FDE is consistent with the PDE if the difference between the FDE and the PDE (the truncation error) vanishes as the sizes of the time step and spatial grid spacing go to zero independently, that is,

$$\lim_{h\to 0,\ \Delta t\to 0} |\mathrm{PDE} - \mathrm{FDE}| \ = \ 0 \ . \tag{6.6}$$

In most cases there is no relation between h and Δt required. If, however, condition (6.6) is true only when a certain relationship is satisfied between Δt and h, the FDE is conditionally consistent.

Stability. A FDE is stable if it produces a bounded solution when the exact solution is bounded, and is unstable if it produces an unbounded solution when the exact solution is bounded. If the solution of the FDE is bounded for all values of Δt and h, the FDE is unconditionally stable. If the solution of the FDE is bounded only for certain values of Δt and h, the FDE is conditionally stable. If the solution of the FDE is unbounded for all values of Δt and h, the FDE is unconditionally unstable.

The stability analysis can be performed only for linear PDE. A nonlinear PDE must be first linearized locally. The FDE of the linearized PDE can be analyzed for stability. The most commonly used method for the stability analysis is the von Neumann method. The basic idea of the von Neumann method is to represent a discrete solution at a time $m\Delta t$ and spatial point $I\,h$, that is at one grid point, by a finite Fourier series, and examine stability of the individual Fourier components. Thus, the method investigates the local stability. The discrete solution is stable if and only if each Fourier component is stable. Von Neumann analysis is applicable to linear FDE with constant coefficients. Though a spatial periodicity is assumed for the finite Fourier series, the analysis can give a useful result even if this is not the case.

Convergence. A FDE is convergent if the solution of the FDE approaches the exact solution of

the PDE as the sizes of the time step and spatial grid spacing go to zero. Denoting the solutions obtained by the PDE and FDE as $u^m_{I,J,K}$ and $U^m_{I,J,K}$, respectively, the convergence means

$$\lim_{h\to 0,\ \Delta t\to 0} \left(U^m_{I,J,K} - u^m_{I,J,K} \right) = 0 \ . \tag{6.7}$$

It is important to note that the consistency is the property of the FDE because it relates the FDE to the PDE. On the other hand, stability and convergence are properties of the numerical solution of the FDE.

Lax equivalence theorem. In general, while it is easy to analyze the consistency, proving convergence can be a very difficult mathematical problem. Therefore, it is very helpful that the convergence is related to the consistency and the stability: It follows from the Lax equivalence theorem that if the FDE is consistent and stable, it is also convergent.

Grid dispersion. Because FD solution is a discrete approximation to a true solution, the phase and group velocities in the grid differ from the true velocities in the medium. The grid velocities depend on the spatial sampling ratio $s = h/\lambda$, where λ is the wavelength that is to be propagated in the grid, and also on Courant number $c\Delta t/h$, where c is the true phase velocity. The grid dispersion is a very important grid phenomenon. It has a cumulative effect on the wave propagation – the longer the travel distance, the larger the effect of the difference between the grid and true velocity. Therefore, the grid dispersion has to be analyzed prior to the numerical calculations. Given the desired travel path one has to choose appropriate spatial sampling of the minimum wavelength to be propagated with a desired level of accuracy.

Because viscoelastic medium is intrinsically dispersive one has to face a possible superposition of two dispersion effects. Investigation of the grid dispersion in viscoelastic media is thus even more important than in the case of the elastic media; see, for example, Robertsson et al. (1994).

The grid-dispersion relation, that is, relation between grid velocity, spatial grid spacing, time step and material properties, can be obtained from the stability analysis. Such analysis may be complicated for heterogeneous media. In such cases effects of the grid dispersion should be examined by numerical experiments.

For a detailed analysis of stability, grid dispersion and accuracy of the FD schemes solving the equation of motion on the conventional and staggered-grid schemes in 2D and 3D problems in homogeneous media see, for example, papers by Marfurt (1984), Crase et al. (1992), Igel et al. (1995), Geller and Takeuchi (1995, 1998), Klimeš (1996), Takeuchi and Geller (2000), Mizutani et al. (2000), Moczo et al. (2000a, 2004b).

6.3 The Finite-Element Method (FEM)

In principle we could follow most of standard textbooks on the finite-element method (FEM), e.g., Strang and Fix (1988), Zienkiewicz and Taylor (1989), Hughes (2000), Felippa (2005), Reddy (2006), and develop a discrete approximation to the equation of motion in its weak formulation (1.11). Here we present an alternative approach based on the idea of Michlin (1970). We will directly derive the semi-discrete weak form of the equation of motion from the strong (differential) form of the equation of motion (1.6). The equation can be written in the vector

form:

$$\rho\,\ddot{\vec{u}} \;=\; \mathrm{div}\,\vec{\vec{\sigma}} \;+\; \vec{f}. \tag{6.8}$$

Equation (6.8) expresses the fact that three acting forces have to be in equilibrium:

1. Density of the inertial force $\rho\,\ddot{\vec{u}} = (\rho\,\ddot{u}_x,\ \rho\,\ddot{u}_y,\ \rho\,\ddot{u}_z)^T$.
2. Density of the restoring (elastic) force

$$\vec{r} = \begin{bmatrix} r_x \\ r_y \\ r_z \end{bmatrix} \;=\; \mathrm{div}\,\vec{\vec{\sigma}} \;=\; \begin{bmatrix} \sigma_{xx,x} + \sigma_{xy,y} + \sigma_{xz,z} \\ \sigma_{yx,x} + \sigma_{yy,y} + \sigma_{yz,z} \\ \sigma_{zx,x} + \sigma_{zy,y} + \sigma_{zz,z} \end{bmatrix}. \tag{6.9}$$

3. Density of the (external) loading force $\vec{f} = (f_x,\ f_y,\ f_z)^T$.

The stress-strain relation for an isotropic elastic medium, eq. (4.12), can be written in the matrix form:

$$\begin{bmatrix} \sigma_{xx} \\ \sigma_{yy} \\ \sigma_{zz} \\ \sigma_{xy} \\ \sigma_{yz} \\ \sigma_{xz} \end{bmatrix} = \begin{bmatrix} \lambda+2\mu & \lambda & \lambda & 0 & 0 & 0 \\ \lambda & \lambda+2\mu & \lambda & 0 & 0 & 0 \\ \lambda & \lambda & \lambda+2\mu & 0 & 0 & 0 \\ 0 & 0 & 0 & \mu & 0 & 0 \\ 0 & 0 & 0 & 0 & \mu & 0 \\ 0 & 0 & 0 & 0 & 0 & \mu \end{bmatrix} \begin{bmatrix} u_{x,x} \\ u_{y,y} \\ u_{z,z} \\ u_{x,y} + u_{y,x} \\ u_{y,z} + u_{z,y} \\ u_{x,z} + u_{z,x} \end{bmatrix}. \tag{6.10}$$

Consider spatial domain $\bar{\Omega} \;=\; \Omega \cup \Gamma$, where Ω is the interior and Γ is the boundary of the domain. In general, assume Dirichlet boundary condition at part Γ_D of boundary Γ, and Neumann boundary condition at part Γ_N of boundary Γ, respectively, where $\Gamma \;=\; \Gamma_D \cup \Gamma_N$. We also assume initial values of displacements and particle velocities in $\bar{\Omega}$.

The application of the FE method to the specified differential problem can be summarized in the four basic steps:

1. Divide domain $\bar{\Omega}$ into sub-domains (elements) Ω^e such that $\bar{\Omega} \;= \cup \Omega^e$, where e is the sequential number of an element.
2. Discretize equation for each element Ω^e. The discretization yields a system of ordinary differential (in time) equations for each element - a local system of equations.
3. Assemble local systems of equations into one global system of equations.
4. Solve the global system of equations.

In the following we will explain the four steps in detail.

The element is a geometrical entity defined by positions of nodes. A shape of the element and the number of nodes will be discussed later. Domain $\bar{\Omega}$ has to be covered by elements without holes and overlapping.

Assume an approximate solution in one element in the form of linear combinations

$$u_x = \sum_{i=1}^{k} u_{xi}\, s_i\,, \quad u_y = \sum_{i=1}^{k} u_{yi}\, s_i\,, \quad u_z = \sum_{i=1}^{k} u_{zi}\, s_i\,, \tag{6.11}$$

where u_{xi}, u_{yi} and u_{zi} are time-dependent interpolation coefficients, and s_i are the interpolation functions (or shape functions). Substituting the assumed approximate solution (6.11) into eq. (6.8) we obtain residual

$$\vec{\mathcal{R}} \;=\; \rho\,\ddot{\vec{u}} \;-\; \vec{r} \;-\; \vec{f}. \tag{6.12}$$

Equation (6.8) is satisfied in the functional space generated by the base $s_i = (s_1, s_2, s_3, ..., s_k)^T$, if and only if $\vec{\mathcal{R}} \;=\; 0$. In other words, the residual must be orthogonal to the whole functional space in which a solution is assumed. Therefore

$$\int_{\Omega^e} \vec{\mathcal{R}}\, s_i \,\mathrm{d}\Omega = 0\,; \quad i \in \{1, 2, 3, ..., k\}\,. \tag{6.13}$$

The system of equations (6.13) can be written in the form

$$\begin{aligned}
\int_{\Omega^e} \rho\,\ddot{u}_x\, s_i \,\mathrm{d}\Omega \;&=\; \int_{\Omega^e} (\sigma_{xx,x} + \sigma_{xy,y} + \sigma_{xz,z})\, s_i \,\mathrm{d}\Omega \;+\; \int_{\Omega^e} f_x\, s_i \,\mathrm{d}\Omega\,, \\
\int_{\Omega^e} \rho\,\ddot{u}_y\, s_i \,\mathrm{d}\Omega \;&=\; \int_{\Omega^e} (\sigma_{yx,x} + \sigma_{yy,y} + \sigma_{yz,z})\, s_i \,\mathrm{d}\Omega \;+\; \int_{\Omega^e} f_y\, s_i \,\mathrm{d}\Omega\,, \\
\int_{\Omega^e} \rho\,\ddot{u}_z\, s_i \,\mathrm{d}\Omega \;&=\; \int_{\Omega^e} (\sigma_{zx,x} + \sigma_{zy,y} + \sigma_{zz,z})\, s_i \,\mathrm{d}\Omega \;+\; \int_{\Omega^e} f_z\, s_i \,\mathrm{d}\Omega\,, \\
&\qquad\qquad\qquad\qquad\qquad\qquad i \in \{1, 2, 3, ..., k\}\ .
\end{aligned} \tag{6.14}$$

Using integration by parts and Green's theorem we can 'move' the spatial derivative from stress tensor to basis functions:

$$\begin{aligned}
\int_{\Omega^e} \rho\,\ddot{u}_x\, s_i \,\mathrm{d}\Omega \;&=\; \int_{\Omega^e} (\,\sigma_{xx} s_{i,x} + \sigma_{xy} s_{i,y} + \sigma_{xz} s_{i,z}\,)\;\mathrm{d}\Omega \\
&\quad+\; \int_{\Gamma^e} p_x s_i \,\mathrm{d}\Gamma \;+\; \int_{\Omega^e} f_x s_i \,\mathrm{d}\Omega\,, \\
\int_{\Omega^e} \rho\,\ddot{u}_y\, s_i \,\mathrm{d}\Omega \;&=\; \int_{\Omega^e} (\,\sigma_{yx} s_{i,x} + \sigma_{yy} s_{i,y} + \sigma_{yz} s_{i,z}\,)\;\mathrm{d}\Omega \\
&\quad+\; \int_{\Gamma^e} p_y s_i \,\mathrm{d}\Gamma \;+\; \int_{\Omega^e} f_y s_i \,\mathrm{d}\Omega\,, \\
\int_{\Omega^e} \rho\,\ddot{u}_z\, s_i \,\mathrm{d}\Omega \;&=\; \int_{\Omega^e} (\,\sigma_{zx} s_{i,x} + \sigma_{zy} s_{i,y} + \sigma_{zz} s_{i,z}\,)\;\mathrm{d}\Omega \\
&\quad+\; \int_{\Gamma^e} p_z s_i \,\mathrm{d}\Gamma \;+\; \int_{\Omega^e} f_z s_i \,\mathrm{d}\Omega\,, \\
&\qquad\qquad i \in \{1, 2, 3, ..., k\}\ ,
\end{aligned} \tag{6.15}$$

where p_x, p_y and p_z are components of prescribed traction. Before this operation we required that solution u_x, u_y and u_z be twice differentiable and shape functions s_i integrable. After the operation we require that solution u_x, u_y and u_z as well as shape function s_i be once differentiable.

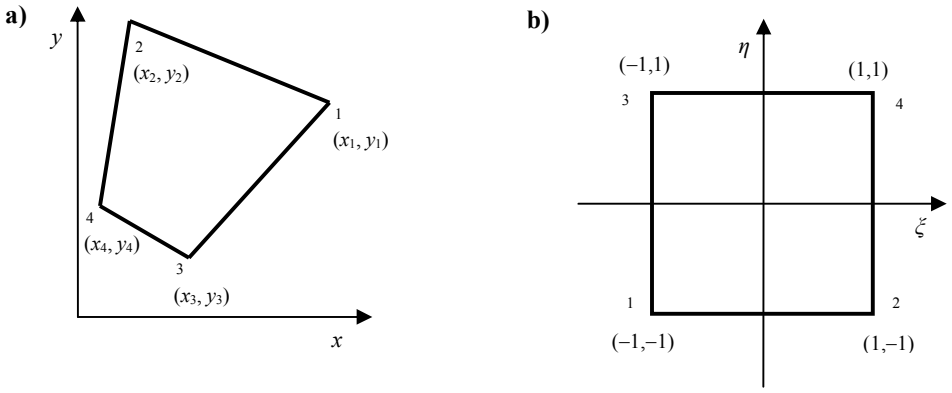

Fig. 6.2. The transformation of the quadrilateral element in the global coordinates (a) into the master element in the local coordinates (b).

6.3.1 The FEM Formulation with the Stiffness Matrix

We have to choose the shape functions s_i. The choice of the shape functions is an important step which will determine many aspects and properties of the approximate solution. Here we will use the Lagrange polynomials. In this case the interpolation coefficients u_{xi}, u_{yi} and u_{zi} are the discretized displacements at the nodes of element. As a consequence, the number of shape functions has to be equal to the number of the nodes. Let n_n be the number of the nodes in the element. Then the choice of the Lagrange polynomials as the shape functions means the following n_n conditions for each shape function:

$$s_i(x_k^e, y_k^e, z_k^e) \;=\; \delta_{ik} \;\;;\;\; i,k \in \{1,2,...,n_n\}\,, \tag{6.16}$$

where $(\,x_k^e,\, y_k^e,\, z_k^e\,)$ are the nodal coordinates. Given the number of the nodes, n_n, we choose such Lagrange polynomials for which the system has a unique solution. The number of the nodes is very closely related to the geometrical shape of the element and order of approximation. Examples in the 2D problem are 3-node linear triangle or 4-node bi-linear quadrilateral elements. Examples in the 3D problem are 4-node linear tetrahedra or 8-node tri-linear hexahedra elements.

Solving system (6.16) yields the shape functions for one element. Obviously, we have to find shape functions for all elements covering the computational domain. At the same time it is clear that the calculating, storing and working with different sets of the shape functions for different elements is very impractical. We can avoid such tedious treatment by the use of the so-called master element. The idea is simple: an element from the global coordinate system (x, y, z) can be transformed to a master element in the local coordinate system $(\,\xi, \eta, \zeta\,)$. This is illustrated in Fig. 6.2 for the case of the quadrilateral element. If we can find such a transformation it is then enough to find or define shape functions only for the master element.

Consider an 8-node hexahedra element (HEX8) with nodes in the corners of the hexahedron. The HEX8 master element has nodes with the local coordinates given by these vectors/sequences

$$\begin{aligned}
\xi_k &\in \{-1, \quad 1, -1, \quad 1, -1, \quad 1, -1, 1\}, \\
\eta_k &\in \{-1, -1, \quad 1, \quad 1, -1, -1, \quad 1, 1\}, \\
\zeta_k &\in \{-1, -1, -1, -1, \quad 1, \quad 1, \quad 1, 1\}.
\end{aligned} \tag{6.17}$$

The shape functions s_i for the HEX8 master element can be written in the form

$$\mathbf{s} = \begin{bmatrix} s_1 \\ s_2 \\ s_3 \\ s_4 \\ s_5 \\ s_6 \\ s_7 \\ s_8 \end{bmatrix} = \frac{1}{8} \begin{bmatrix} (1-\xi)(1-\eta)(1-\zeta) \\ (1+\xi)(1-\eta)(1-\zeta) \\ (1-\xi)(1+\eta)(1-\zeta) \\ (1+\xi)(1+\eta)(1-\zeta) \\ (1-\xi)(1-\eta)(1+\zeta) \\ (1+\xi)(1-\eta)(1+\zeta) \\ (1-\xi)(1+\eta)(1+\zeta) \\ (1+\xi)(1+\eta)(1+\zeta) \end{bmatrix}. \tag{6.18}$$

The transformation of coordinates can be expressed in the form

$$x = \mathbf{s}^T \mathbf{x}, \quad y = \mathbf{s}^T \mathbf{y}, \quad z = \mathbf{s}^T \mathbf{z}, \tag{6.19}$$

where $\mathbf{x}$, $\mathbf{y}$ and $\mathbf{z}$ are vectors of the global coordinates of the nodes in the element,

$$\begin{aligned}
\mathbf{x} &= (x_1, x_2, x_3, x_4, x_5, x_6, x_7, x_8)^T, \\
\mathbf{y} &= (y_1, y_2, y_3, y_4, y_5, y_6, y_7, y_8)^T, \\
\mathbf{z} &= (z_1, z_2, z_3, z_4, z_5, z_6, z_7, z_8)^T.
\end{aligned} \tag{6.20}$$

Using the vector notation we can also rewrite the approximate solution (6.11) in the form

$$u_x = \mathbf{s}^T \mathbf{u}_x, \quad u_y = \mathbf{s}^T \mathbf{u}_y, \quad u_z = \mathbf{s}^T \mathbf{u}_z, \tag{6.21}$$

where

$$\begin{aligned}
\mathbf{u}_x &= (u_{x1}, u_{x2}, u_{x3}, u_{x4}, u_{x5}, u_{x6}, u_{x7}, u_{x8})^T, \\
\mathbf{u}_y &= (u_{y1}, u_{y2}, u_{y3}, u_{y4}, u_{y5}, u_{y6}, u_{y7}, u_{y8})^T, \\
\mathbf{u}_z &= (u_{z1}, u_{z2}, u_{z3}, u_{z4}, u_{z5}, u_{z6}, u_{z7}, u_{z8})^T
\end{aligned} \tag{6.22}$$

are vectors of the discretized displacements at nodes.

Application of eqs. (6.18), (6.19) and (6.21) to eq. (6.15) yields a system of ordinary differential equations for one element e:

$$\mathbf{M}^e \ddot{\mathbf{u}}^e + \mathbf{K}^e \mathbf{u}^e = \mathbf{bc}^e + \mathbf{f}^e. \tag{6.23}$$

The equation can be written in the partly expanded form

$$\begin{bmatrix} \mathbf{M} & 0 & 0 \\ 0 & \mathbf{M} & 0 \\ 0 & 0 & \mathbf{M} \end{bmatrix} \begin{bmatrix} \ddot{\mathbf{u}}_x \\ \ddot{\mathbf{u}}_y \\ \ddot{\mathbf{u}}_z \end{bmatrix} + \begin{bmatrix} \mathbf{K}_{11} & \mathbf{K}_{12} & \mathbf{K}_{13} \\ \mathbf{K}_{12}^T & \mathbf{K}_{22} & \mathbf{K}_{23} \\ \mathbf{K}_{13}^T & \mathbf{K}_{23}^T & \mathbf{K}_{33} \end{bmatrix} \begin{bmatrix} \mathbf{u}_x \\ \mathbf{u}_y \\ \mathbf{u}_z \end{bmatrix} = \begin{bmatrix} \mathbf{bc}_x \\ \mathbf{bc}_y \\ \mathbf{bc}_z \end{bmatrix} + \begin{bmatrix} \mathbf{f}_x \\ \mathbf{f}_y \\ \mathbf{f}_z \end{bmatrix}, \tag{6.24}$$

where $\mathbf{f}_x$, $\mathbf{f}_y$ and $\mathbf{f}_z$ are the nodal forces due to body forces acting in the whole element,

$$\mathbf{f}_x = \int_{\Omega^e} f_x \mathbf{s}\,\mathrm{d}\Omega\,, \quad \mathbf{f}_y = \int_{\Omega^e} f_y \mathbf{s}\,\mathrm{d}\Omega\,, \quad \mathbf{f}_z = \int_{\Omega^e} f_z \mathbf{s}\,\mathrm{d}\Omega\,, \tag{6.25}$$

and $\mathbf{bc}_x$, $\mathbf{bc}_y$ and $\mathbf{bc}_z$ are the nodal forces due to tractions acting at the boundary of the element,

$$\mathbf{bc}_x = \int_{\Gamma^e} p_x \mathbf{s}\,\mathrm{d}\Gamma\,, \quad \mathbf{bc}_y = \int_{\Gamma^e} p_y \mathbf{s}\,\mathrm{d}\Gamma\,, \quad \mathbf{bc}_z = \int_{\Gamma^e} p_z \mathbf{s}\,\mathrm{d}\Gamma\,. \tag{6.26}$$

Matrix $\mathbf{M}^e$ is the local mass matrix

$$\mathbf{M}^e = \begin{bmatrix} \mathbf{M} & 0 & 0 \\ 0 & \mathbf{M} & 0 \\ 0 & 0 & \mathbf{M} \end{bmatrix} = \rho \begin{bmatrix} \mathbf{H} & 0 & 0 \\ 0 & \mathbf{H} & 0 \\ 0 & 0 & \mathbf{H} \end{bmatrix}, \tag{6.27}$$

where

$$\mathbf{H} = \int_{\Omega^M} \left(\mathbf{s}\,\mathbf{s}^T \det \mathbf{J}\right) \mathrm{d}\Omega\,. \tag{6.28}$$

Here, Ω^M relates to a volume of the master element, and the Jacobian of transformation (6.19), is

$$\mathbf{J} = \begin{bmatrix} x_{,\xi} & x_{,\eta} & x_{,\zeta} \\ y_{,\xi} & y_{,\eta} & y_{,\zeta} \\ z_{,\xi} & z_{,\eta} & z_{,\zeta} \end{bmatrix}. \tag{6.29}$$

Matrix $\mathbf{K}^e$ is the local stiffness matrix

$$\mathbf{K}^e = \begin{bmatrix} \mathbf{K}_{11} & \mathbf{K}_{12} & \mathbf{K}_{13} \\ \mathbf{K}_{12}^T & \mathbf{K}_{22} & \mathbf{K}_{23} \\ \mathbf{K}_{13}^T & \mathbf{K}_{23}^T & \mathbf{K}_{33} \end{bmatrix}. \tag{6.30}$$

The sub-matrices have the form

$$\begin{aligned}
\mathbf{K}_{11} &= (\lambda+2\mu)\,\mathbf{H}_{xx} + \mu\,\mathbf{H}_{yy} + \mu\,\mathbf{H}_{zz}\,, \\
\mathbf{K}_{22} &= \mu\,\mathbf{H}_{xx} + (\lambda+2\mu)\,\mathbf{H}_{yy} + \mu\,\mathbf{H}_{zz}\,, \\
\mathbf{K}_{33} &= \mu\,\mathbf{H}_{xx} + \mu\,\mathbf{H}_{yy} + (\lambda+2\mu)\,\mathbf{H}_{zz}\,, \\
\mathbf{K}_{12} &= \lambda\,\mathbf{H}_{xy} + \mu\,\mathbf{H}_{yx}\,, \\
\mathbf{K}_{13} &= \lambda\,\mathbf{H}_{xz} + \mu\,\mathbf{H}_{zx}\,, \\
\mathbf{K}_{23} &= \lambda\,\mathbf{H}_{yz} + \mu\,\mathbf{H}_{zy}\,,
\end{aligned} \tag{6.31}$$

where

$$\mathbf{H}_{ij} = \int_{\Omega^M} \left(\mathbf{s}_{,i}\,\mathbf{s}_{,j}^T \det \mathbf{J}\right) \mathrm{d}\Omega\,; \quad i,j \in \{x,y,z\}\,. \tag{6.32}$$

Integrals (6.28) and (6.32) are evaluated for the master element, that is, in the local coordinates. The shape function are defined in the local coordinates, see eq. (6.18). In eq. (6.32) we, however,

need derivatives of the shape functions with respect to the global coordinates. Using the chain rule we can write

$$\begin{aligned}
\mathbf{s},_x &= \mathbf{s},_\xi \, \xi,_x + \mathbf{s},_\eta \, \eta,_x + \mathbf{s},_\zeta \, \zeta,_x \ , \\
\mathbf{s},_y &= \mathbf{s},_\xi \, \xi,_y + \mathbf{s},_\eta \, \eta,_y + \mathbf{s},_\zeta \, \zeta,_y \ , \\
\mathbf{s},_z &= \mathbf{s},_\xi \, \xi,_z + \mathbf{s},_\eta \, \eta,_z + \mathbf{s},_\zeta \, \zeta,_z \ .
\end{aligned} \tag{6.33}$$

The derivatives of the local coordinates with respect to the global coordinates are the elements of the inverse Jacobian of transformation (6.19),

$$\mathbf{J}^{-1} = \begin{bmatrix} \xi,_x & \xi,_y & \xi,_z \\ \eta,_x & \eta,_y & \eta,_z \\ \zeta,_x & \zeta,_y & \zeta,_z \end{bmatrix} . \tag{6.34}$$

If we knew conditions at boundary of an element, we could find a solution for one element e, that is, a solution in domain Ω^e, by solving equations (6.23). Because the conditions include interaction between the element and all neighboring elements, we have to assemble systems of equations (6.23) for all the elements into one global system of equations and find a solution for the whole domain $\bar{\Omega}$. The global system can be written in the form

$$\begin{bmatrix} \mathbf{M^1} & 0 & 0 & \dots \\ 0 & \mathbf{M^2} & 0 & \dots \\ 0 & 0 & \mathbf{M^3} & \dots \\ \vdots & \vdots & \vdots & \ddots \end{bmatrix} \begin{bmatrix} \ddot{\mathbf{u}}^1 \\ \ddot{\mathbf{u}}^2 \\ \ddot{\mathbf{u}}^3 \\ \vdots \end{bmatrix} + \begin{bmatrix} \mathbf{K^1} & 0 & 0 & \dots \\ 0 & \mathbf{K^2} & 0 & \dots \\ 0 & 0 & \mathbf{K^3} & \dots \\ \vdots & \vdots & \vdots & \ddots \end{bmatrix} \begin{bmatrix} \mathbf{u}^1 \\ \mathbf{u}^2 \\ \mathbf{u}^3 \\ \vdots \end{bmatrix} = \begin{bmatrix} \mathbf{bc}^1 \\ \mathbf{bc}^2 \\ \mathbf{bc}^3 \\ \vdots \end{bmatrix} + \begin{bmatrix} \mathbf{f}^1 \\ \mathbf{f}^2 \\ \mathbf{f}^3 \\ \vdots \end{bmatrix} . \tag{6.35}$$

This system is not directly solvable in this form because the number of equations is much larger then the number of unknown variables.

There are nodes in the mesh which belong to more than one element. At such a node the total (that is, global) nodal force is the sum of forces acting at that node and due to all elements sharing that node. This fact can be used to reduce the number of equations. By summing up all the lines and rows belonging to the same node we will obtain a system of ordinary differential equations for the whole domain $\bar{\Omega}$:

$$\mathbb{M}\,\ddot{\mathbb{u}} + \mathbb{K}\,\mathbb{u} = \mathbb{bc} + \mathbb{f} \, . \tag{6.36}$$

Here $\mathbb{M}$ and $\mathbb{K}$ are the global mass and stiffness matrices, respectively, $\mathbb{bc}$ is the global boundary-condition term, and $\mathbb{f}$ is the global loading-force term. The system of equations (6.36) represents the standard FEM formulation with the global stiffness matrix $\mathbb{K}$.

Using the 2^{nd}-order central-difference approximation for the 2^{nd} time derivative in system (6.36) we obtain the explicit recurrent formula for the unknown variable $\mathbb{u}^{m+1}$ at time $t = (m+1)\,\Delta t$:

$$\mathbb{u}^{m+1} = \Delta^2 t \ \mathbb{M}^{-1} \left(-\mathbb{K}\,\mathbb{u}^m + \mathbb{bc}^m + \mathbb{f}^m\right) + 2\mathbb{u}^m - \mathbb{u}^{m-1} \, . \tag{6.37}$$

Consider boundary conditions at boundaries between neighboring elements, and prescribed boundary conditions at boundary Γ_N in the process of assembling the global system of equations (6.36). The force terms due to tractions acting at boundaries between neighboring elements

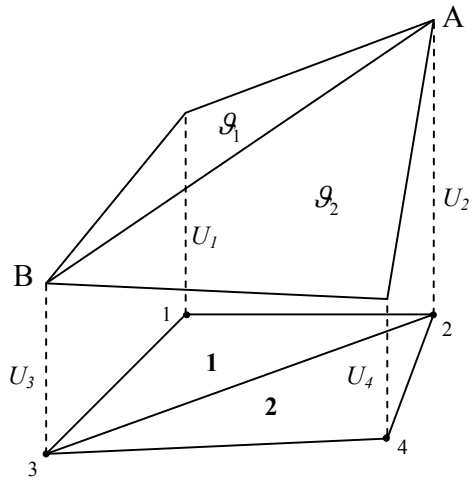

Fig. 6.3. The continuity of the displacement at the connection of two triangular elements.

will not contribute to the boundary term $\mathbb{b}\mathbb{c}$ because they will cancel each other due to the traction continuity at boundaries. Consequently, the boundary term $\mathbb{b}\mathbb{c}$ in system (6.36) will include only those forces which are due to the prescribed traction p_i at boundary Γ_N.

The assembling process itself does not ensure the continuity of displacement. Therefore we have to check the continuity at all possible contacts between neighboring elements, particularly between elements of different shapes or order of approximation. Consider, for example, two triangular elements as shown in Fig. 6.3. The assembling process ensures that the displacements at the nodes shared by elements 1 and 2 are the same for both elements. The solutions in the two elements make planes ϑ_1 and ϑ_2, respectively. The two planes connect along the straight line over the contact of the elements. Because the straight line is uniquely defined by two points, the solution is continuous along the contact.

An analogous consideration can be applied to any contact between elements in which different types of shape functions are used.

In practical applications the order of $\mathbb{M}$ and $\mathbb{K}$ can be quite large $(10^6 - 10^8)$. In some cases the memory requirements can be so large that the problem cannot be solved using the FEM formulation with the global stiffness matrix. In other cases it is crucial to develop an efficient computational algorithm with as small computer time and memory requirements as possible. Consequently, several approaches to reduce memory requirements due to the global matrices have been elaborated.

Matrix $\mathbb{K}$ is a very sparse matrix. Let N^n be the total number of nodes in the mesh. Then the total number of elements in the matrix is $3N^n \times 3N^n$, whereas the number of non-zero elements for the HEX8 element is approximately $3N^n \times 81$. From this, say, relative point of view, the storage of only the non-zero elements means great reduction of the memory requirements. Considering, however, millions to tens of millions of nodes in the relatively modest 3D numerical modeling, we easily realize that even the latter number of the non-zero elements poses a serious

problem.

As it is clear from eq. (6.37), the algorithm requires an inverse matrix $\mathbb{M}^{-1}$. The construction of the inverse matrix is significantly easier, if the global mass matrix is diagonal. Because it is not always possible to obtain strictly diagonal mass matrix, the mass matrix is often approximated by a diagonal mass matrix (lumped mass matrix). The diagonal element of the lumped mass matrix is the sum of all elements in the corresponding row in the original mass matrix.

6.3.2 The FEM Formulation with the Restoring Force

The FEM formulation with the concept of restoring forces at nodes considerably reduces memory requirements compared to the FEM formulation with the global stiffness matrix. Our formulation and implementation is based on the outline of the formulation presented by Ralph. J. Archuleta (Archuleta, 1976, and personal communication) who refers to Frazier and Petersen (1974).

Equation (6.23) in principle represents the FEM formulation with the stiffness matrix for element e. We can use the second term of the l.h.s. of the equation to define the restoring force. Considering eq. (6.30) we define the local vector of the restoring force as

$$\mathbf{r}^e \;=\; \begin{bmatrix} \mathbf{r}_x \\ \mathbf{r}_y \\ \mathbf{r}_z \end{bmatrix} \;=\; -\mathbf{K}^e\,\mathbf{u}^e \;=\; -\begin{bmatrix} \mathbf{K}_{11}\mathbf{u}_x \;+\; \mathbf{K}_{12}\mathbf{u}_y \;+\; \mathbf{K}_{13}\mathbf{u}_z \\ \mathbf{K}_{12}^T\mathbf{u}_x \;+\; \mathbf{K}_{22}\mathbf{u}_y \;+\; \mathbf{K}_{23}\mathbf{u}_z \\ \mathbf{K}_{13}^T\mathbf{u}_x \;+\; \mathbf{K}_{23}^T\mathbf{u}_y \;+\; \mathbf{K}_{33}\mathbf{u}_z \end{bmatrix}. \tag{6.38}$$

Substituting eqs. (6.31) and (6.32) into eq. (6.38), and considering

$$u_{i,j} \;=\; \mathbf{s}_{,j}^T\,\mathbf{u}_i \quad \text{for} \quad i,j \in \{x,y,z\} \tag{6.39}$$

and

$$\mathbf{H}_{ij}\,\mathbf{u}_k \;=\; \int_{\Omega^M} \mathbf{s}_{,i}\,u_{k,j}\,\det\,\mathbf{J}\,\mathrm{d}\Omega \;\;;\quad i,j,k \in \{x,y,z\} \tag{6.40}$$

we obtain

$$\begin{aligned} \mathbf{r}_x \;&=\; -\int_{\Omega^M} (\,\mathbf{s}_{,x}\,\sigma_{xx} \;+\; \mathbf{s}_{,y}\,\sigma_{xy} \;+\; \mathbf{s}_{,z}\,\sigma_{xz})\,\det\,\mathbf{J}\,\mathrm{d}\Omega\,, \\ \mathbf{r}_y \;&=\; -\int_{\Omega^M} (\,\mathbf{s}_{,x}\,\sigma_{xy} \;+\; \mathbf{s}_{,y}\,\sigma_{yy} \;+\; \mathbf{s}_{,z}\,\sigma_{yz})\,\det\,\mathbf{J}\,\mathrm{d}\Omega\,, \\ \mathbf{r}_z \;&=\; -\int_{\Omega^M} (\,\mathbf{s}_{,x}\,\sigma_{xz} \;+\; \mathbf{s}_{,y}\,\sigma_{yz} \;+\; \mathbf{s}_{,z}\,\sigma_{zz})\,\det\,\mathbf{J}\,\mathrm{d}\Omega\,, \end{aligned} \tag{6.41}$$

where

$$\begin{aligned} \sigma_{xx} \;&=\; (\lambda+2\mu)\;\mathbf{s}_{,x}^T\,\mathbf{u}_x \;+\; \lambda\;\mathbf{s}_{,y}^T\,\mathbf{u}_y \;+\; \lambda\;\mathbf{s}_{,z}^T\,\mathbf{u}_z\,, \\ \sigma_{yy} \;&=\; \lambda\;\mathbf{s}_{,x}^T\,\mathbf{u}_x \;+\; (\lambda+2\mu)\;\mathbf{s}_{,y}^T\,\mathbf{u}_y \;+\; \lambda\;\mathbf{s}_{,z}^T\,\mathbf{u}_z\,, \\ \sigma_{zz} \;&=\; \lambda\;\mathbf{s}_{,x}^T\,\mathbf{u}_x \;+\; \lambda\;\mathbf{s}_{,y}^T\,\mathbf{u}_y \;+\; (\lambda+2\mu)\;\mathbf{s}_{,z}^T\,\mathbf{u}_z\,, \\ \sigma_{xy} \;&=\; \mu\;(\,\mathbf{s}_{,y}^T\,\mathbf{u}_x \;+\; \mathbf{s}_{,x}^T\,\mathbf{u}_y\,)\,, \\ \sigma_{xz} \;&=\; \mu\;(\,\mathbf{s}_{,z}^T\,\mathbf{u}_x \;+\; \mathbf{s}_{,x}^T\,\mathbf{u}_z\,)\,, \\ \sigma_{yz} \;&=\; \mu\;(\,\mathbf{s}_{,z}^T\,\mathbf{u}_y \;+\; \mathbf{s}_{,y}^T\,\mathbf{u}_z\,)\,. \end{aligned} \tag{6.42}$$

Substituting eq. (6.38) into eq. (6.23) we obtain a system of ordinary differential equations for one element e:

$$\mathbf{M}^e\,\ddot{\mathbf{u}}^e \;=\; \mathbf{r}^e \;+\; \mathbf{bc}^e \;+\; \mathbf{f}^e. \tag{6.43}$$

Equation (6.43) represents the FEM formulation with the restoring force for one element.

We can assemble systems of equations (6.43) for the all elements into one global system. In principle, we can follow the same procedure as we used for the formulation with the global stiffness matrix. As a result we obtain the global system of differential equations

$$\mathbb{M}\,\ddot{\mathbb{u}} \;=\; \mathbb{r} \;+\; \mathbb{bc} \;+\; \mathbb{f}\,, \tag{6.44}$$

where $\mathbb{r}$ is the global restoring force vector, that is, the global vector of components of the restoring forces at nodes. Approximating again the second time derivative by the central difference formula we obtain the explicit FE scheme

$$\mathbb{u}^{m+1} \;=\; \Delta^2 t\;\mathbb{M}^{-1}(\,\mathbb{r}^m \;+\; \mathbb{bc}^m \;+\; \mathbb{f}^m) \;+\; 2\,\mathbb{u}^m \;-\; \mathbb{u}^{m-1}\,. \tag{6.45}$$

Vector $\mathbb{r}$ contains $3N^n$ values. It is 81 times less than the number of non-zero elements in the global stiffness matrix. As a consequence, the FE scheme (6.45) needs 81 times smaller memory compared to that required by the FE scheme with the global stiffness matrix.

At the same time note that the stiffness matrix was time-independent and thus it is computed once at the beginning of computation. The restoring force is time-dependent and therefore it has to be updated at each time level. This means that the restoring force reduces memory requirements but it may be very time consuming.

For completeness note that the stiffness matrix is time-independent only if material parameters are time-independent. If we considered non-linear behavior of a medium, the stiffness matrix would vary with time, that is, it would have to be updated at each time level. In other words, the stiffness-matrix formulation would loose the advantage of smaller computer time.

6.3.3 The FEM Formulations for Viscoelastic Medium

Here we will describe how the realistic attenuation based on rheology of the generalized Maxwell body (GMB-EK) can be implemented into the two FEM formulations.

The rheology of GMB-EK is described in detail in section 4.4.6. For convenience, recall only the time-domain stress-strain relation for GMB-EK in the displacement formulation, eqs. (4.161) and (4.166):

$$\begin{aligned}\sigma_{ij} \;&=\; \kappa\,\varepsilon_{kk}\,\delta_{ij} \;+\; 2\,\mu\,\left(\varepsilon_{ij} \;-\; \tfrac{1}{3}\,\varepsilon_{kk}\,\delta_{ij}\right)\\ &\quad-\; \sum_{l=1}^{n}\left[\kappa\,Y_l^{\kappa}\zeta_l^{\,kk}\,\delta_{ij} \;+\; 2\,\mu\,Y_l^{\mu}\left(\zeta_l^{\,ij} \;-\; \tfrac{1}{3}\,\zeta_l^{\,kk}\delta_{ij}\right)\right]\end{aligned} \tag{6.46}$$

and

$$\dot{\zeta}_l^{\,ij} \;+\; \omega_l\,\zeta_l^{\,ij} \;=\; \omega_l\,\varepsilon_{ij}\,; \quad l \in \{1,\ldots,n\}\;. \tag{6.47}$$

The anelastic coefficients Y_l^κ and Y_l^μ are defined by relations (4.162), (4.164) and (4.165). Rewrite the stress-strain relation (6.46) in the form more suitable for the FEM implementation,

$$\sigma_{ij} \;=\; \sigma_{ij}^E \;-\; \sum_{l=1}^{n} \sigma_{ij}^{A\,l}\,, \tag{6.48}$$

where σ_{ij}^E is the elastic part given by Hooke's law (6.10), and $\sigma_{ij}^{A\,l}$ are the anelastic parts for the l^{th} relaxation frequency,

$$\begin{bmatrix} \sigma_{xx}^{A\,l} \\ \sigma_{yy}^{A\,l} \\ \sigma_{zz}^{A\,l} \\ \sigma_{xy}^{A\,l} \\ \sigma_{xz}^{A\,l} \\ \sigma_{yz}^{A\,l} \end{bmatrix} \;=\; \begin{bmatrix} Y^+ & Y^- & Y^- & 0 & 0 & 0 \\ Y^- & Y^+ & Y^- & 0 & 0 & 0 \\ Y^- & Y^- & Y^+ & 0 & 0 & 0 \\ 0 & 0 & 0 & \mu Y_l^\mu & 0 & 0 \\ 0 & 0 & 0 & 0 & \mu Y_l^\mu & 0 \\ 0 & 0 & 0 & 0 & 0 & \mu Y_l^\mu \end{bmatrix} \begin{bmatrix} \zeta_l^{xx} \\ \zeta_l^{yy} \\ \zeta_l^{zz} \\ 2\zeta_l^{xy} \\ 2\zeta_l^{xz} \\ 2\zeta_l^{yz} \end{bmatrix}, \tag{6.49}$$

where

$$Y^+ = \kappa\, Y_l^\kappa \;+\; \tfrac{4}{3}\,\mu\, Y_l^\mu \quad \text{and} \quad Y^- = \kappa\, Y_l^\kappa \;-\; \tfrac{2}{3}\,\mu\, Y_l^\mu\,. \tag{6.50}$$

Next, we will use the approach by Kristek and Moczo (2003) to solve eq. (6.47). Because the stress-tensor components in eq. (6.46) are known for time level m, the equation for anelastic functions (6.47) has to be specified for time level m:

$$\dot{\zeta}_l^{ij}(m) \;+\; \omega_l\, \zeta_l^{ij}(m) \;=\; \omega_l\, \varepsilon_{ij}(m)\,; \quad l \in \{1, \ldots, n\}\,. \tag{6.51}$$

Approximating the time derivative using the second order central difference formula and $\zeta_l^{ij}(m)$ by the arithmetic average

$$\zeta_l^{ij}(m) \;=\; \frac{\zeta_l^{ij}(m-\frac{1}{2}) \;+\; \zeta_l^{ij}(m+\frac{1}{2})}{2} \tag{6.52}$$

we obtain a recurrent formula for $\zeta_l^{ij}(m+\frac{1}{2})$,

$$\zeta_l^{ij}(m+\tfrac{1}{2}) \;=\; \frac{2\,\omega_l \Delta t\, \varepsilon_{ij}(m) \;+\; (2-\omega_l \Delta t)\, \zeta_l^{ij}(m-\frac{1}{2})}{2+\omega_l \Delta t}\,. \tag{6.53}$$

Substituting relation (6.53) into (6.52) we obtain $\zeta_l^{ij}(m)$.

The strain-tensor components can be computed using relations (6.39). We get

$$\begin{aligned} \varepsilon_{xx} &= \mathbf{s}_{,x}^T\, \mathbf{u}_x\,, \\ \varepsilon_{yy} &= \mathbf{s}_{,y}^T\, \mathbf{u}_y\,, \\ \varepsilon_{zz} &= \mathbf{s}_{,z}^T\, \mathbf{u}_z\,, \\ \varepsilon_{xy} &= \tfrac{1}{2}(\mathbf{s}_{,y}^T\, \mathbf{u}_x \;+\; \mathbf{s}_{,x}^T\, \mathbf{u}_y)\,, \\ \varepsilon_{xz} &= \tfrac{1}{2}(\mathbf{s}_{,z}^T\, \mathbf{u}_x \;+\; \mathbf{s}_{,x}^T\, \mathbf{u}_z)\,, \\ \varepsilon_{yz} &= \tfrac{1}{2}(\mathbf{s}_{,z}^T\, \mathbf{u}_y \;+\; \mathbf{s}_{,y}^T\, \mathbf{u}_z)\,. \end{aligned} \tag{6.54}$$

The Formulation with the Restoring Force. The restoring force for one element e is given by eq. (6.41). In the case of viscoelastic media we have to adopt the stress-strain relation (6.48). The elastic part of the stress tensor is given by Hooke's law (6.42), the anelastic part is given by relation (6.49). The anelastic functions are updated to the time level m using relations (6.52) and (6.53). The rest of the FEM procedure is the same as for the elastic media.

The restoring force is computed using a numerical quadrature. This requires anelastic functions at all integration points. The integration points are determined by a chosen type of the numerical integration. The update of the anelastic functions to the time-level $m + 1/2$, requires values of the anelastic functions at time time-level $m - 1/2$. Therefore the anelastic functions have to be stored in computer memory. The standard numerical quadratures for element HEX8 use 8 integration points. The memory requirements to store the anelastic functions at 8 integration points can by estimated using the number of the necessary quantities: 8 integration points $\times$ 6 components of the anelastic functions $\times$ 4 relaxation frequencies $\times$ N^e (the number of elements in the mesh). This gives $192N^e$. It is clear that the incorporation of the attenuation dramatically increases the memory requirements: the number of quantities required by the restoring force itself is only $3N^n$. Consequently, computations for vicoelastic media would be impossible in many reasonable problem configurations. (Note: The number of nodes N^n and the number of elements N^e for large models are approximately the same.)

The very large additional memory requirements due to incorporation of the realistic attenuation can be significantly reduced using the coarse spatial distribution of the anelastic functions. The latter will be described in detail in sections 7.2.5 and 8.1.4. If the FEM algorithm is not adjusted specifically for a structured spatial mesh, the FE mesh is in general treated as an unstructured mesh. In such a case we evaluate the anelastic functions only at the center of an element, that is, at one point per element. In other words, for calculation of the anelastic functions using relation (6.53) we consider constant strain within an element. The value of the constant strain is that at the center of the element. In this way we can reduce the number of quantities to store down to $24N^e$.

The Formulation with the Stiffness Matrix. Substituting the stress-strain relation (6.48) into the definition equations for for the restoring force (6.41) we can express the restoring force as the sum of the elastic and anelastic restoring forces:

$$\mathbf{r}_i \;=\; \mathbf{r}_i^E \;-\; \sum_{l=1}^{n} \mathbf{r}_i^{A\,l}\,; \quad i \in \{x, y, z\}\;. \tag{6.55}$$

Here

$$\begin{aligned}
\mathbf{r}_x^E &= -\int_{\Omega^M} (\,\mathbf{s}_{,x}\,\sigma_{xx}^E \;+\; \mathbf{s}_{,y}\,\sigma_{xy}^E \;+\; \mathbf{s}_{,z}\,\sigma_{xz}^E\,)\det\mathbf{J}\,\mathrm{d}\Omega\,,\\
\mathbf{r}_y^E &= -\int_{\Omega^M} (\,\mathbf{s}_{,x}\,\sigma_{xy}^E \;+\; \mathbf{s}_{,y}\,\sigma_{yy}^E \;+\; \mathbf{s}_{,z}\,\sigma_{yz}^E\,)\det\mathbf{J}\,\mathrm{d}\Omega\,,\\
\mathbf{r}_z^E &= -\int_{\Omega^M} (\,\mathbf{s}_{,x}\,\sigma_{xz}^E \;+\; \mathbf{s}_{,y}\,\sigma_{yz}^E \;+\; \mathbf{s}_{,z}\,\sigma_{zz}^E\,)\det\mathbf{J}\,\mathrm{d}\Omega\,,\\
\mathbf{r}_x^{A\,l} &= -\int_{\Omega^M} (\,\mathbf{s}_{,x}\,\sigma_{xx}^{A\,l} \;+\; \mathbf{s}_{,y}\,\sigma_{xy}^{A\,l} \;+\; \mathbf{s}_{,z}\,\sigma_{xz}^{A\,l}\,)\det\mathbf{J}\,\mathrm{d}\Omega\,,
\end{aligned}$$

$$\begin{aligned}\mathbf{r}_y^{A\,l} &= -\int_{\Omega^M} (\,\mathbf{s}_{,x}\,\sigma_{yx}^{A\,l} + \mathbf{s}_{,y}\,\sigma_{yy}^{A\,l} + \mathbf{s}_{,z}\,\sigma_{yz}^{A\,l}\,)\det\mathbf{J}\,\mathrm{d}\Omega\,,\\ \mathbf{r}_z^{A\,l} &= -\int_{\Omega^M} (\,\mathbf{s}_{,x}\,\sigma_{xz}^{A\,l} + \mathbf{s}_{,y}\,\sigma_{yz}^{A\,l} + \mathbf{s}_{,z}\,\sigma_{zz}^{A\,l}\,)\det\mathbf{J}\,\mathrm{d}\Omega\,.\end{aligned} \tag{6.56}$$

Considering eqs. (6.38) and (6.41), and using the fact that σ_{ij}^E is determined by Hooke's law we can write

$$\begin{bmatrix}\mathbf{r}_x^E\\ \mathbf{r}_y^E\\ \mathbf{r}_z^E\end{bmatrix} = -\mathbf{K}^e\,\mathbf{u}^e. \tag{6.57}$$

Substituting eq. (6.57) into eq. (6.55) and then the modified eq. (6.55) into eq. (6.43) we obtain

$$\mathbf{M}^e\,\ddot{\mathbf{u}}^e + \mathbf{K}^e\,\mathbf{u}^e - \mathbf{r}_A^e = \mathbf{bc}^e + \mathbf{f}^e\,, \tag{6.58}$$

where

$$\mathbf{r}_A^e = \begin{bmatrix}\sum_{l=1}^{n}\mathbf{r}_x^{A\,l}\\ \sum_{l=1}^{n}\mathbf{r}_y^{A\,l}\\ \sum_{l=1}^{n}\mathbf{r}_z^{A\,l}\end{bmatrix}. \tag{6.59}$$

Assembling equations for all elements into one system, analogously to the elastic case, we obtain the global system of differential equations

$$\mathbb{M}\,\ddot{\mathrm{u}} + \mathbb{K}\,\mathrm{u} - \mathrm{r}_A = \mathrm{bc} + \mathrm{f}\,, \tag{6.60}$$

and also the recurrent formula for updating the unknown displacements

$$\mathrm{u}^{m+1} = \Delta^2 t\;\mathbb{M}^{-1}(-\mathbb{K}\,\mathrm{u}^m + \mathrm{r}_A^m + \mathrm{bc}^m + \mathrm{f}^m) + 2\,\mathrm{u}^m - \mathrm{u}^{m-1}. \tag{6.61}$$

As we can see, vector r_A is time-dependent and has to be updated at each time-level. For completeness we note that the anelastic functions are updated using the equations (6.52) and (6.53).

It is clear from eq. (6.61) that we have introduced a new global variable - vector r_A with $3N^n$ values. Evaluation of the local vector $\mathbf{r}_A$ using the numerical quadrature requires anelastic functions at all integration points. In the case of the HEX8 element we would need to store $192N^e$ anelastic functions. For comparison we recall that the global stiffness matrix itself has approximately $243N^n$ non-zero values. We see that in this case the memory requirements due the anelastic part (the anelastic functions and vector $\mathbf{r}_A$) and the elastic part (the stiffness matrix) are comparable. From this point of view we can say that in this case there is no need to use a special approach to reduce the memory requirements. At the same time we should point out that the memory requirements due the the stiffness matrix itself are huge. It is possible to apply the same coarse spatial sampling of the anelastic functions as in the case of the restoring-force formulation and reduce the additional memory requirements.

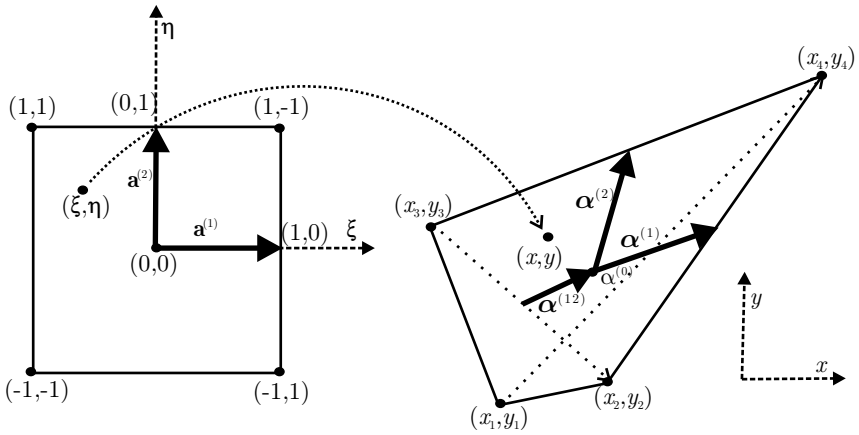

Fig. 6.4. Bilinear transformation.

6.3.4 Efficient Computation of the Restoring Force Using the e-invariants

The e-invariants are new local coordinates for an efficient computation of the local restoring force. The efficiency is due to the fact that e-invariants contain only minimum necessary information for the computation of the local restoring force. The approach was introduced for the 2D quadrilateral element by Balazovjech and Halada (2006). The approach can be used for different types of elements and equations.

The e-invariants for the 2D Quadrilateral Elements. Consider the quadrilateral element with four nodes at the corners. Such element is determined by the positions of its nodes in the global coordinates

$$\mathbf{x} = (x_1, x_2, x_3, x_4)^T, \quad \mathbf{y} = (y_1, y_2, y_3, y_4)^T. \tag{6.62}$$

The first two e-invariants, denote them $x^{(0)}$ and $y^{(0)}$, generate point $\alpha^{(0)}$ in the global coordinates, that is, in the quadrilateral domain. This point corresponds to the $(0,0)$ point in the master element, that is, in the local coordinates, as shown in Fig. 6.4. Coordinates of point $\alpha^{(0)}$ are

$$x^{(0)} = \tfrac{1}{4}(x_1 + x_2 + x_3 + x_4), \quad y^{(0)} = \tfrac{1}{4}(y_1 + y_2 + y_3 + y_4). \tag{6.63}$$

Point $\alpha^{(0)}$ determines the location of the quadrilateral element in the computational domain independently of the rotation and/or change of shape of the element. Therefore the coordinates of point $\alpha^{(0)}$ are not needed for the computation of the restoring force vector.

Next two e-invariants are vectors

$$\boldsymbol{\alpha}^{(1)} = \left(x^{(1)}, y^{(1)}\right), \quad \boldsymbol{\alpha}^{(2)} = \left(x^{(2)}, y^{(2)}\right), \tag{6.64}$$

where

$$\begin{aligned} x^{(1)} &= \tfrac{1}{4}(-x_1 + x_2 - x_3 + x_4), \; y^{(1)} = \tfrac{1}{4}(-y_1 + y_2 - y_3 + y_4), \\ x^{(2)} &= \tfrac{1}{4}(-x_1 - x_2 + x_3 + x_4), \; y^{(2)} = \tfrac{1}{4}(-y_1 - y_2 + y_3 + y_4), \end{aligned} \tag{6.65}$$

or, equivalently,

$$\begin{aligned} x^{(1)} &= \tfrac{1}{2}\,(\,x_2 + x_4\,) - x^{(0)}\,, \quad & y^{(1)} &= \tfrac{1}{2}\,(\,y_2 + y_4\,) - y^{(0)}\,, \\ x^{(2)} &= \tfrac{1}{2}\,(\,x_3 + x_4\,) - x^{(0)}\,, \quad & y^{(2)} &= \tfrac{1}{2}\,(\,y_3 + y_4\,) - y^{(0)}\,. \end{aligned} \tag{6.66}$$

Positions of vectors $\boldsymbol{\alpha}^{(1)}$ and $\boldsymbol{\alpha}^{(2)}$ are shown in Fig. 6.4. Vectors $\boldsymbol{\alpha}^{(1)}$ and $\boldsymbol{\alpha}^{(2)}$ correspond to vectors

$$\mathbf{a}^{(1)} = (\,1, 0\,) \quad \text{and} \quad \mathbf{a}^{(2)} = (\,0, 1\,) \tag{6.67}$$

in the master element, respectively. Both vectors are independent of the position of the quadrilateral element. The magnitudes of the vectors are

$$\left|\,\boldsymbol{\alpha}^{(1)}\,\right| = \sqrt{x^{(1)}x^{(1)} + y^{(1)}y^{(1)}}\,, \qquad \left|\,\boldsymbol{\alpha}^{(2)}\,\right| = \sqrt{x^{(2)}x^{(2)} + y^{(2)}y^{(2)}}\,. \tag{6.68}$$

The angle between the vectors is

$$\beta = \text{Arcos}\left(\frac{x^{(1)}y^{(1)} + x^{(2)}y^{(2)}}{\left|\,\boldsymbol{\alpha}^{(1)}\,\right|\left|\,\boldsymbol{\alpha}^{(2)}\,\right|}\right). \tag{6.69}$$

The magnitudes $\left|\,\boldsymbol{\alpha}^{(1)}\,\right|$ and $\left|\,\boldsymbol{\alpha}^{(2)}\,\right|$ and the angle β are independent of the rotation of the element.

The last e-invariant is vector

$$\boldsymbol{\alpha}^{(12)} = \left(x^{(12)},\, y^{(12)}\right), \tag{6.70}$$

where

$$\begin{aligned} x^{(12)} &= \tfrac{1}{4}\,(\,+ x_1 - x_2 - x_3 + x_4\,)\,, \\ y^{(12)} &= \tfrac{1}{4}\,(\,+ y_1 - y_2 - y_3 + y_4\,)\,, \end{aligned} \tag{6.71}$$

or, equivalently,

$$\begin{aligned} x^{(12)} &= x^{(0)} - \tfrac{1}{2}\,(\,x_2 + x_3\,)\,, \\ y^{(12)} &= y^{(0)} - \tfrac{1}{2}\,(\,y_2 + y_3\,)\,. \end{aligned} \tag{6.72}$$

The magnitude of vector $\boldsymbol{\alpha}^{(12)}$,

$$\left|\,\boldsymbol{\alpha}^{(12)}\,\right| = \sqrt{x^{(12)}x^{(12)} + y^{(12)}y^{(12)}}\,, \tag{6.73}$$

is independent of the element position and its rotation. Vector $\boldsymbol{\alpha}^{(12)}$ can be used as a measure of deformation of an element from the parallelogram because $\boldsymbol{\alpha}^{(12)}$ is zero for the parallelogram and non-zero for other convex quadrilaterals.

The Efficient Computation of the Restoring Force for the 2D Quadrilateral Elements Using the e-invariants in the Elastic Medium. In the case of the quadrilateral element the vector of discretized displacements can be written in the form

$$\mathbf{u}_x \;=\; (\,u_{x1},\,u_{x2},\,u_{x3},\,u_{x4}\,)^{\,T} \;\text{ and }\; \mathbf{u}_y \;=\; (\,u_{y1},\,u_{y2},\,u_{y3},\,u_{y4}\,)^{\,T}\,. \tag{6.74}$$

Considering transformation (6.19) between the element and the master element, and approximation (6.21) we can define vector $\mathbf{c}$:

$$\mathbf{c} \;=\; \begin{bmatrix} x \\ y \\ u_x \\ u_y \end{bmatrix} \;=\; \begin{bmatrix} x_1 & x_2 & x_3 & x_4 \\ y_1 & y_2 & y_3 & y_4 \\ u_{x1} & u_{x2} & u_{x3} & u_{x4} \\ u_{y1} & u_{y2} & u_{y3} & u_{y4} \end{bmatrix} \begin{bmatrix} s_1 \\ s_2 \\ s_3 \\ s_4 \end{bmatrix} \;=\; \mathbf{V}\mathbf{s}\,. \tag{6.75}$$

The components of the vector of the shape functions, see eq. (6.18),

$$\mathbf{s} \;=\; \begin{bmatrix} s_1 \\ s_2 \\ s_3 \\ s_4 \end{bmatrix} \;=\; \frac{1}{4} \begin{bmatrix} (1\,-\,\xi)\,(1\,-\,\eta) \\ (1\,+\,\xi)\,(1\,-\,\eta) \\ (1\,-\,\xi)\,(1\,+\,\eta) \\ (1\,+\,\xi)\,(1\,+\,\eta) \end{bmatrix}\,, \tag{6.76}$$

are Lagrange-family interpolation polynomials defined in $\langle -1,1\rangle \times \langle -1,1\rangle$, that is, in the master element. Omitting the z-coordinate in the eqs. (6.41) and (6.42) we obtain

$$\begin{aligned} \mathbf{r}_x \;&=\; -\int_{-1}^{1}\int_{-1}^{1} (\,\mathbf{s}_{,x}\,\sigma_{xx} \;+\; \mathbf{s}_{,y}\,\sigma_{xy})\,\det\mathbf{J}\,\mathrm{d}\eta\,\mathrm{d}\xi\,, \\ \mathbf{r}_y \;&=\; -\int_{-1}^{1}\int_{-1}^{1} (\,\mathbf{s}_{,x}\,\sigma_{xy} \;+\; \mathbf{s}_{,y}\,\sigma_{yy})\,\det\mathbf{J}\,\mathrm{d}\eta\,\mathrm{d}\xi\,, \end{aligned} \tag{6.77}$$

and

$$\begin{aligned} \sigma_{xx} \;&=\; (\lambda+2\mu)\;\; \mathbf{s}_{,x}^{T}\,\mathbf{u}_x \;\;+\;\;\; \lambda \;\;\; \mathbf{s}_{,y}^{T}\,\mathbf{u}_y\,, \\ \sigma_{yy} \;&=\; \lambda \;\;\; \mathbf{s}_{,x}^{T}\,\mathbf{u}_x \;\;+\;\; (\lambda+2\mu)\;\; \mathbf{s}_{,y}^{T}\,\mathbf{u}_y\,, \\ \sigma_{xy} \;&=\; \mu \;\;\; (\,\mathbf{s}_{,y}^{T}\,\mathbf{u}_x \;\;+\;\; \mathbf{s}_{,x}^{T}\,\mathbf{u}_y\,)\,. \end{aligned} \tag{6.78}$$

Let $\mathbf{s}^{(inv)}$ be a vector of the new shape functions for the master element, that is, in the unit square,

$$\mathbf{s}^{(inv)} \;=\; \big[\,1,\,\xi,\,\eta,\,\xi\eta\,\big]^{T}\,, \tag{6.79}$$

where ξ and η are the local coordinates in the master element. We define a transformation matrix

$$\mathbf{T} = \begin{bmatrix} +1 & +1 & +1 & +1 \\ -1 & +1 & -1 & +1 \\ -1 & -1 & +1 & +1 \\ +1 & -1 & -1 & +1 \end{bmatrix} \tag{6.80}$$

with properties

$$\mathbf{s}^{(inv)} \;=\; \mathbf{T}\mathbf{s} \quad \text{and} \quad \tfrac{1}{4}\,\mathbf{T}\,\mathbf{T}^{T} \;=\; \mathbf{I}\,, \tag{6.81}$$

where $\mathbf{I}$ is the unit matrix. As we will see later, these properties are very important. Vector $\mathbf{c}$, eq. (6.75), can be expressed using the new shape functions:

$$\mathbf{c} \;=\; \mathbf{V}\mathbf{s} \;=\; \mathbf{V}\mathbf{I}\,\mathbf{s} \;=\; \mathbf{V}\left(\tfrac{1}{4}\,\mathbf{T}^{T}\mathbf{T}\right)\mathbf{s} \;=\; \left(\mathbf{V}\,\tfrac{1}{4}\,\mathbf{T}^{T}\right)\left(\mathbf{T}\mathbf{s}\right) \;=\; \mathbf{V}^{(inv)}\,\mathbf{s}^{(inv)}\,. \tag{6.82}$$

In the matrix form

$$\mathbf{c} \;=\; \begin{bmatrix} x \\ y \\ u_x \\ u_y \end{bmatrix} \;=\; \begin{bmatrix} x^{(0)} & x^{(1)} & x^{(2)} & x^{(12)} \\ y^{(0)} & y^{(1)} & y^{(2)} & y^{(12)} \\ u_x^{(0)} & u_x^{(1)} & u_x^{(2)} & u_x^{(12)} \\ u_y^{(0)} & u_y^{(1)} & u_y^{(2)} & u_y^{(12)} \end{bmatrix} \begin{bmatrix} 1 \\ \xi \\ \eta \\ \xi\eta \end{bmatrix}, \tag{6.83}$$

where $x^{(k)}$, $y^{(k)}$; $k \in \{\,0, 1, 2, 12\,\}$ are the e-invariants, see eqs. (6.63), (6.66), and (6.72), and $u_x^{(k)}$, $u_y^{(k)}$; $k \in \{\,0, 1, 2, 12\,\}$ are the time-dependent interpolation coefficients of approximation to solution using the new shape functions $\mathbf{s}^{(inv)}$.

Let us note that the relation between vector $\mathbf{c}$, eq. (6.75), and product of matrix of the e-invariants and vector of the new shape functions makes the basis of the new way of computation of the local restoring force.

The spatial derivatives of displacement can be written in the form

$$u_{x,x} \;=\; \mathbf{s}_{,x}^{T}\,\mathbf{u}_x \;=\; \mathbf{s}_{,x}^{T}\left(\tfrac{1}{4}\,\mathbf{T}^{T}\mathbf{T}\right)\mathbf{u}_x \;=\; \left(\mathbf{s}_{,x}^{T}\,\mathbf{T}^{T}\right)\left(\tfrac{1}{4}\,\mathbf{T}\,\mathbf{u}_x\right) \;=\; \mathbf{s}_{,x}^{(inv)T}\,\mathbf{u}_x^{(inv)}\,. \tag{6.84}$$

Analogously we obtain

$$\begin{aligned} u_{x,y} \;&=\; \mathbf{s}_{,x}^{T}\,\mathbf{u}_x \;=\; \mathbf{s}_{,y}^{(inv)T}\,\mathbf{u}_x^{(inv)}\,, \\ u_{y,x} \;&=\; \mathbf{s}_{,x}^{T}\,\mathbf{u}_y \;=\; \mathbf{s}_{,x}^{(inv)T}\,\mathbf{u}_y^{(inv)}\,, \\ u_{y,y} \;&=\; \mathbf{s}_{,y}^{T}\,\mathbf{u}_y \;=\; \mathbf{s}_{,y}^{(inv)T}\,\mathbf{u}_y^{(inv)}\,. \end{aligned} \tag{6.85}$$

Substituting relations (6.84) and (6.85) into eq. (6.78) we can compute stress at the quadrature points:

$$\begin{aligned} \sigma_{xx} \;&=\; (\lambda + 2\mu)\;\mathbf{s}_{,x}^{(inv)\,T}\,\mathbf{u}_x^{(inv)} \;+\; \lambda \;\mathbf{s}_{,y}^{(inv)\,T}\,\mathbf{u}_y^{(inv)}\,, \\ \sigma_{yy} \;&=\; \lambda \;\mathbf{s}_{,x}^{(inv)\,T}\,\mathbf{u}_x^{(inv)} \;+\; (\lambda + 2\mu)\;\mathbf{s}_{,y}^{(inv)\,T}\,\mathbf{u}_y^{(inv)}\,, \\ \sigma_{xy} \;&=\; \mu \;\mathbf{s}_{,y}^{(inv)\,T}\,\mathbf{u}_x^{(inv)} \;+\; \mu \;\mathbf{s}_{,x}^{(inv)\,T}\,\mathbf{u}_y^{(inv)}\,. \end{aligned} \tag{6.86}$$

The spatial derivatives of the shape functions $\mathbf{s}_{,x}$ and $\mathbf{s}_{,y}$ in definitions (6.77) can be expressed using properties (6.81) as

$$\begin{aligned} \mathbf{s}_{,x} \;&=\; \mathbf{T}^{-1}\mathbf{s}_{,x}^{(inv)} \;=\; \tfrac{1}{4}\,\mathbf{T}^{T}\mathbf{s}_{,x}^{(inv)}\,, \\ \mathbf{s}_{,y} \;&=\; \mathbf{T}^{-1}\mathbf{s}_{,y}^{(inv)} \;=\; \tfrac{1}{4}\,\mathbf{T}^{T}\mathbf{s}_{,y}^{(inv)}\,. \end{aligned} \tag{6.87}$$

Substituting these expressions into eq. (6.77) we obtain

$$\begin{aligned} \mathbf{r}_x &= -\tfrac{1}{4}\,\mathbf{T}^T \int_{-1}^{1}\int_{-1}^{1} \left(\mathbf{s}_{,x}^{(inv)}\,\sigma_{xx} + \mathbf{s}_{,y}^{(inv)}\,\sigma_{xy} \right) \det \mathbf{J}\,\mathrm{d}\eta\,\mathrm{d}\xi\,, \\ \mathbf{r}_y &= -\tfrac{1}{4}\,\mathbf{T}^T \int_{-1}^{1}\int_{-1}^{1} \left(\mathbf{s}_{,x}^{(inv)}\,\sigma_{xy} + \mathbf{s}_{,y}^{(inv)}\,\sigma_{yy} \right) \det \mathbf{J}\,\mathrm{d}\eta\,\mathrm{d}\xi\,. \end{aligned} \tag{6.88}$$

The derivatives of the shape functions $\mathbf{s}^{(inv)}$ with respect to the global coordinates, that is, $\mathbf{s}_{,x}^{(inv)}$ and $\mathbf{s}_{,y}^{(inv)}$, are

$$\mathbf{s}_{,x}^{(inv)} = \begin{bmatrix} 0 \\ \xi_{,x} \\ \eta_{,x} \\ \xi_{,x}\,\eta + \xi\,\eta_{,x} \end{bmatrix}, \qquad \mathbf{s}_{,y}^{(inv)} = \begin{bmatrix} 0 \\ \xi_{,y} \\ \eta_{,y} \\ \xi_{,y}\,\eta + \xi\,\eta_{,y} \end{bmatrix}, \tag{6.89}$$

where the derivatives of the local coordinates with respect to the global coordinates are the components of the inverse Jacobian of transformation (6.19). From relation (6.34) we obtain for our 2D problem

$$\mathbf{J}^{-1} = \begin{bmatrix} \xi_{,x} & \xi_{,y} \\ \eta_{,x} & \eta_{,y} \end{bmatrix}. \tag{6.90}$$

We will illustrate the implementation of the presented approach on the example of the square element. Transformation of the local coordinates in the master element into the global coordinates in the physical element is given by

$$\begin{aligned} x &= \tfrac{1}{4}\,(\,x_1 + x_2 + x_3 + x_4\,) + \xi = x^{(0)} + \xi\,, \\ y &= \tfrac{1}{4}\,(\,y_1 + y_2 + y_3 + y_4\,) + \eta = y^{(0)} + \eta\,. \end{aligned} \tag{6.91}$$

It is easy to see that

$$\mathbf{J} = \begin{bmatrix} x_{,\xi} & x_{,\eta} \\ y_{,\xi} & y_{,\eta} \end{bmatrix} = \begin{bmatrix} 1 & 0 \\ 0 & 1 \end{bmatrix}, \qquad \det \mathbf{J} = 1\,, \tag{6.92}$$

and the derivatives of vector $\mathbf{s}^{(inv)}$ with respect to x and y have a very simple form

$$\mathbf{s}_{,x}^{(inv)} = \begin{bmatrix} 0 \\ \xi_{,x} \\ \eta_{,x} \\ (\xi\eta)_{,x} \end{bmatrix} = \begin{bmatrix} 0 \\ 1 \\ 0 \\ \eta \end{bmatrix}, \quad \mathbf{s}_{,y}^{(inv)} = \begin{bmatrix} 0 \\ \eta_{,y} \\ \xi_{,y} \\ (\xi\eta)_{,y} \end{bmatrix} = \begin{bmatrix} 0 \\ 0 \\ 1 \\ \xi \end{bmatrix}. \tag{6.93}$$

Using the relations (6.93) in (6.84) and (6.85) we can compute derivatives of displacement:

$$\begin{aligned} u_{x,x} &= u_x^{(1)} + \eta\,u_x^{(12)}\,, \qquad u_{x,y} = u_x^{(2)} + \xi\,u_x^{(12)}\,, \\ u_{y,x} &= u_y^{(1)} + \eta\,u_y^{(12)}\,, \qquad u_{y,y} = u_y^{(2)} + \xi\,u_y^{(12)}\,. \end{aligned} \tag{6.94}$$

Tab. 6.1. Comparison of the numbers of operations in different algorithms for computation of the restoring force.

Algorithm	dividing	multiplying	add/substr.	assigning
standard for the Q4 element	4	236	236	196
e-invariants for the Q4 element	4	169	150	127
e-invariants for the square element	0	11	32	29

The stress-tensor components then take form

$$\begin{aligned}
\sigma_{xx} &= (\lambda+2\mu)\left(u_x^{(1)} + \eta\, u_x^{(12)}\right) + \lambda\left(u_y^{(2)} + \xi\, u_y^{(12)}\right), \\
\sigma_{yy} &= (\lambda+2\mu)\left(u_y^{(2)} + \xi\, u_y^{(12)}\right) + \lambda\left(u_x^{(1)} + \eta\, u_x^{(12)}\right), \\
\sigma_{xy} &= \mu\left[\left(u_x^{(2)} + \xi\, u_x^{(12)}\right) + \left(u_y^{(1)} + \eta\, u_y^{(12)}\right)\right].
\end{aligned} \tag{6.95}$$

The local restoring force vector is obtained by exact evaluation of integrals (6.88) and the result is very simple:

$$\begin{aligned}
\mathbf{r}_x &= \tfrac{1}{4}\,\mathbf{T}^T \begin{bmatrix} 0 \\ (\lambda+2\mu)\, u_x^{(1)} + \lambda\, u_y^{(2)} \\ \mu\,(u_x^{(1)} + u_y^{(2)}) \\ \frac{4}{3}[(\lambda+2\mu) + \mu]\, u_x^{(12)} \end{bmatrix}, \\
\mathbf{r}_y &= \tfrac{1}{4}\,\mathbf{T}^T \begin{bmatrix} 0 \\ \mu\,(u_x^{(1)} + u_y^{(2)}) \\ (\lambda+2\mu)\, u_y^{(2)} + \lambda\, u_x^{(1)} \\ \frac{4}{3}\,[(\lambda+2\mu) + \mu]\, u_y^{(12)} \end{bmatrix}.
\end{aligned} \tag{6.96}$$

To compare the efficiency of the different approaches, Balazovjech and Halada (2006) developed an algorithm for computation of the restoring force using the e-invariants for the quadrilateral element and analogous algorithm for the square element. They compared the number of algebraic operations in the two algorithms with the number of operations in the standard algorithm for computation of the restoring force. The comparison is shown in Tab. 6.1.

It is clear that the algorithm for the quadrilateral (Q4) element based on the e-invariants reduces the number of operations by approximately 30%. In the case of the square element, the number of operations is reduced by one order. Given the fact that in many practical applications square elements cover major part of the computational domain, the reduction is significant. It is likely that considerable-to-significant reduction can be expected also in the 3D problem we are about to complete.

The Efficient Computation of the Restoring Force for the 2D Quadrilateral Elements Using the e-invariants in the Viscoelastic Medium. The stress-tensor components in relations for

the restoring-force components (6.88) will be given by eq. (6.48) in the viscoelastic medium. The elastic part σ_{ij}^{E} for the 2D problem is determined by the relations (6.78), (6.84) and (6.85). The anelastic part can be written in the form

$$\begin{bmatrix} \sigma_{xx}^{A\,l} \\ \sigma_{yy}^{A\,l} \\ \sigma_{xy}^{A\,l} \end{bmatrix} = \begin{bmatrix} Y^+ & Y^- & 0 \\ Y^- & Y^+ & 0 \\ 0 & 0 & \mu Y_l^{\mu} \end{bmatrix} \begin{bmatrix} \zeta_l^{xx} \\ \zeta_l^{yy} \\ 2\,\zeta_l^{xy} \end{bmatrix}, \tag{6.97}$$

where

$$Y^+ \;=\; \kappa\, Y_l^{\kappa} \;+\; \tfrac{4}{3}\,\mu\, Y_l^{\mu} \quad \text{and} \quad Y^- \;=\; \kappa\, Y_l^{\kappa} \;-\; \tfrac{2}{3}\,\mu\, Y_l^{\mu}\,. \tag{6.98}$$

The anelastic functions ζ_l^{ij} can be computed using relations (6.52) and (6.53), where the strain-tensor components can be efficiently computed using the e-invariants:

$$\begin{aligned} \varepsilon_{xx} &= \mathbf{s}_{,x}^{(inv)\,T}\, \mathbf{u}_x^{(inv)}\,, \\ \varepsilon_{yy} &= \mathbf{s}_{,y}^{(inv)\,T}\, \mathbf{u}_y^{(inv)}\,, \\ \varepsilon_{xy} &= \tfrac{1}{2}\left(\mathbf{s}_{,y}^{(inv)\,T}\, \mathbf{u}_x^{(inv)} \;+\; \mathbf{s}_{,x}^{(inv)\,T}\, \mathbf{u}_y^{(inv)} \right). \end{aligned} \tag{6.99}$$

The rest of the procedure is the same as that for the FEM formulation with the restoring force for the viscoelastic medium. Note that the e-invariants do not reduce additional memory requirements due to incorporation of the attenuation. The coarse spatial distribution of the anelastic functions can be applied.

7 Finite-difference Schemes for Grid Points in a Smooth Medium

Although we focus in this chapter on schemes applicable to smooth medium and do not discuss the presence of a material interface (discontinuity), we start presentation of each type of the FD schemes with a general brief historic introduction that relates to a particular type of scheme and makes no distinction between schemes for a smooth medium or medium with material interfaces.

7.1 Conventional Schemes

Brief Historic Introduction. In the early days of application of the FD method to earthquake seismology and seismic exploration, the displacement formulation of the equation of motion and conventional grid were used. Representative studies include papers by Alterman and Karal (1968), Alterman and Rotenberg (1969), Alterman and Loewenthal (1970), Boore (1970, 1972), Alford et al. (1974), Ilan et al. (1975), Kelly et al. (1976), and Marfurt (1984). Although Virieux (1984) introduced staggered-grid schemes into modeling of seismic wave propagation and staggered-grid schemes became the most popular, some seismologists tried to improve the conventional displacement schemes even in the staggered-grid era. We can mention, for example, schemes by Kummer et al. (1987), Zahradník (1995), Zahradník and Priolo (1995), and Moczo et al. (1999).

The conventional displacement FD schemes approximated eq. (5.4),

$$\rho\,\ddot{u}_i \;=\; [(\kappa - \tfrac{2}{3}\mu)\,u_{k,k}]_{,i} \;+ (\mu\,u_{i,j})_{,j} \;+ (\mu\,u_{j,i})_{,j} \;+ f_i \tag{7.1}$$

or the alternative form

$$\rho\,\ddot{u}_i \;=\; (\lambda\,u_{k,k})_{,i} \;+ (\mu\,u_{i,j})_{,j} \;+ (\mu\,u_{j,i})_{,j} \;+ f_i\;. \tag{7.2}$$

The first papers addressed 1D and 2D (SH and P-SV) problems, later schemes for the full 3D problem appeared.

The 2$^{\mathrm{nd}}$-order Displacement Conventional Scheme. Here we restrict to the scheme presented by Moczo et al. (1999). It is clear from eqs. (7.1) and (7.2) that we need to find proper approximations for, say, non-mixed and mixed spatial derivatives. Define, for example, an auxiliary function ϕ,

$$\phi \;=\; \mu\,u_{,x}\;. \tag{7.3}$$

We need FD approximations to non-mixed derivative $\phi_{,x}$ and mixed derivative $\phi_{,z}$.

A 2$^{\mathrm{nd}}$-order approximation to $\phi_{,x}$ is

$$\phi_{,x}\,|_{I,J,K} \;\doteq\; \frac{1}{h}(\,\phi_{I+1/2,J,K} \;-\; \phi_{I-1/2,J,K}\,)\;. \tag{7.4}$$

Find now approximations to $\phi_{I+1/2,J,K}$ and $\phi_{I-1/2,J,K}$. From eq. (7.3) we have

$$\frac{\phi}{\mu} \;=\; u_{,x}\;. \tag{7.5}$$

Integrate eq. (7.5) along the grid line between points I, J, K and $I+1, J, K$:

$$\int_{x_{I,J,K}}^{x_{I+1,J,K}} \frac{\phi}{\mu}\,\mathrm{d}x \;=\; \int_{x_{I,J,K}}^{x_{I+1,J,K}} u_{,x}\;\mathrm{d}x\;. \tag{7.6}$$

Applying the mean-value theorem to the left-hand side integral and approximating the mean value by $\phi_{I+1/2,J,K}$, we obtain

$$\phi_{I+1/2,J,K}\int_{x_{I,J,K}}^{x_{I+1,J,K}} \frac{1}{\mu}\,\mathrm{d}x \;\doteq\; U_{I+1,J,K} \;-\; U_{I,J,K}\;. \tag{7.7}$$

Define an effective material grid parameter as an integral harmonic average

$$\mu^{xH}_{I+1/2,J,K} \;=\; \left[\frac{1}{h}\int_{x_{I,J,K}}^{x_{I+1,J,K}} \frac{1}{\mu}\,\mathrm{d}x\right]^{-1}\;. \tag{7.8}$$

Then we get from eq. (7.7) the following approximation at time level *m*:

$$\phi_{I+1/2,J,K} \;\doteq\; \frac{1}{h}\,\mu^{xH}_{I+1/2,J,K}\;(\,U_{I+1,J,K} \;-\; U_{I,J,K}\,)\;. \tag{7.9}$$

Finally we get for the non-mixed derivative

$$\left.\frac{\partial}{\partial x}\left(\mu\frac{\partial u}{\partial x}\right)\right|_{I,J,K} \doteq \frac{1}{h^2}\Big[\ \mu^{xH}_{I+1/2,J,K}\ (\ U_{I+1,J,K}\ -\ U_{I,J,K}\ ) - \mu^{xH}_{I-1/2,J,K}\ (\ U_{I,J,K}\ -\ U_{I-1,J,K}\ )\Big]. \tag{7.10}$$

It is obvious that the two key points in obtaining the approximation were the integration of eq. (7.5) and definition of the harmonic average (7.8) as the effective material grid parameter. Note that the integration leading to the integral harmonic averaging of the elastic modulus $C(x)$ was originally suggested by Tikhonov and Samarskii (see, e.g. Boore, 1972; Mitchell, 1969, p. 23) as a mathematical tool to avoid the derivative of modulus μ. The trick was used then by some authors in 2D and 3D modeling because they recognized good numerical results obtained with the schemes obtained using the harmonic averaging.

It is more difficult to approximate the mixed-derivative term $\phi_{,z}$. Probably the most accurate displacement schemes based on the trick were developed by Zahradník (1995), and Zahradník and Priolo (1995) for the 2D case. Moczo et al. (1999) generalized Zahradník's approach in the 3D case.

A 2$^{\rm nd}$-order approximation to $\phi_{,z}$ is

$$\phi_{,z}\,|_{I,J,K} \doteq \frac{1}{h}\,(\ \phi_{I,J,K+1/2}\ -\ \phi_{I,J,K-1/2}\ ). \tag{7.11}$$

Find approximations to $\phi_{I,J,K+1/2}$ and $\phi_{I,J,K-1/2}$. From eq. (7.3) we have again

$$\frac{\phi}{\mu}\ =\ u_{,x}\,. \tag{7.12}$$

Integrate eq. (7.12) along the grid line between points I,J,K and $I,J,K+1$:

$$\int_{z_{I,J,K}}^{z_{I,J,K+1}} \frac{\phi}{\mu}\,{\rm d}z\ =\ \int_{z_{I,J,K}}^{z_{I,J,K+1}} u_{,x}\ {\rm d}z\,. \tag{7.13}$$

Approximate both integrals:

$$\frac{h}{\mu^{zH}_{I,J,K+1/2}}\ \phi_{I,J,K+1/2}\ \doteq\ h\ u_{,x}\,|_{\,I,J,K+1/2}\ . \tag{7.14}$$

Approximating the right-hand side,

$$h\ u_{,x}\,|_{\,I,J,K+1/2}\ \doteq\ \tfrac{1}{4}\ (\ U_{I+1,J,K+1} - U_{I-1,J,K+1} + U_{I+1,J,K} - U_{I-1,J,K}\ )\,, \tag{7.15}$$

we get

$$\phi_{I,J,K+1/2}\ \doteq\ \frac{1}{4h}\,\mu^{zH}_{I,J,K+1/2}\,\big(\ U_{I+1,J,K+1}\ - U_{I-1,J,K+1} + \ U_{I+1,J,K}\ \ - U_{I-1,J,K}\ \ \big)\,. \tag{7.16}$$

Finally,

$$\begin{aligned}\left.\frac{\partial}{\partial z}\left(\mu\frac{\partial u}{\partial x}\right)\right|_{I,J,K} \doteq \frac{1}{4h^2}\Big[\ \mu^{zH}_{I,J,K+1/2}\ (\ U_{I+1,J,K+1}\ -U_{I-1,J,K+1}\\ +U_{I+1,J,K}\ -U_{I-1,J,K}\ )\\ -\mu^{zH}_{I,J,K-1/2}\ (\ U_{I+1,J,K}\ -U_{I-1,J,K}\\ +U_{I+1,J,K-1}\ -U_{I-1,J,K-1})\Big]\,.\end{aligned} \tag{7.17}$$

The full FD scheme for the U, V and W components of the displacement vector can be written in a concise form:

$$\begin{aligned}U^{m+1}_{I,J,K} &= 2U^{m}_{I,J,K} - U^{m-1}_{I,J,K}\\ &+\frac{\Delta^2 t}{\rho_{I,J,K}}\big[\ L_{xx}(\lambda,U) + 2L_{xx}(\mu,U) + L_{yy}(\mu,U) + L_{zz}(\mu,U)\\ &\qquad L_{yx}(\lambda,V) + L_{zx}(\lambda,W) + L_{xy}(\mu,V) + L_{xz}(\mu,W)\big] + F^{x,m}_{I,J,K}\,,\end{aligned} \tag{7.18}$$

$$\begin{aligned}V^{m+1}_{I,J,K} &= 2V^{m}_{I,J,K} - V^{m-1}_{I,J,K}\\ &+\frac{\Delta^2 t}{\rho_{I,J,K}}\big[\ L_{xx}(\mu,V) + L_{yy}(\lambda,V) + 2L_{yy}(\mu,V) + L_{zz}(\mu,V)\\ &\qquad L_{yx}(\mu,U) + L_{zx}(\lambda,U) + L_{zy}(\lambda,W) + L_{yz}(\mu,W)\big] + F^{y,m}_{I,J,K}\,,\end{aligned} \tag{7.19}$$

$$\begin{aligned}W^{m+1}_{I,J,K} &= 2W^{m}_{I,J,K} - W^{m-1}_{I,J,K}\\ &+\frac{\Delta^2 t}{\rho_{I,J,K}}\big[\ L_{xx}(\mu,W) + L_{yy}(\mu,W) + L_{zz}(\lambda,W) + 2L_{zz}(\mu,W)\\ &\qquad L_{zx}(\mu,U) + L_{zy}(\mu,V) + L_{xz}(\lambda,U) + L_{yz}(\lambda,V)\big] + F^{z,m}_{I,J,K}\,,\end{aligned} \tag{7.20}$$

where we used the $2^{\rm nd}$-order approximation (6.4) for the time derivative, subscript m denotes a time level, operator $L_{\gamma\gamma}(a,\phi)\,;\ \ \gamma\in\{x,y,z\}\,,\ a\in\{\lambda,\mu\}\,,\ \phi\in\{U,V,W\}$ has the form

$$L_{\gamma\gamma}(a,\phi) = \frac{1}{h^2}\left[\ a^{\gamma+}\left(\phi^m_+-\phi^m\right) - a^{\gamma-}\left(\phi^m-\phi^m_-\right)\ \right] \tag{7.21}$$

and subscripts $\pm$ stand for $I\pm1,J,K$, $I,J\pm1,K$ or $I,J,K\pm1$ if $\gamma = x$, y or z, respectively. No subscript means I,J,K. The effective parameters $a^{\gamma+}$ and $a^{\gamma-}$ are defined as

$$a^{\gamma+} = \left[\frac{1}{h}\int_{\gamma_n}^{\gamma_{n+1}}\frac{1}{a}\,{\rm d}\gamma\right]^{-1}\quad,\quad a^{\gamma-} = \left[\frac{1}{h}\int_{\gamma_{n-1}}^{\gamma_n}\frac{1}{a}\,{\rm d}\gamma\right]^{-1}\,, \tag{7.22}$$

where n stands for I, J, K, and $n \pm 1$ stands for $I \pm 1, J, K$, $I, J \pm 1, K$ or $I, J, K \pm 1$ if $\gamma = x, y$ or z, respectively. Operator $L_{\gamma\eta}$; $\gamma \neq \eta$ and $\gamma, \eta \in \{x, y, z\}$ has the form

$$\begin{aligned} L_{\gamma\eta}(a,\phi) \;=\; \frac{1}{4h^2}\big[\; & a^{\eta+}(\,\phi^m_{2+} + \phi^m_{3+} - \phi^m_{2-} - \phi^m_{3-}) \\ & - a^{\eta-}(\,\phi^m_{1+} + \phi^m_{2+} - \phi^m_{1-} - \phi^m_{2-})\,\big] \end{aligned} \tag{7.23}$$

where subscripts $1_\pm$, $2_\pm$ and $3_\pm$ stand for

	xz	xy	yz
$1_\pm$	$I \pm 1, J, K-1$	$I \pm 1, J-1, K$	$I, J \pm 1, K-1$
$2_\pm$	$I \pm 1, J, K$	$I \pm 1, J \quad , K$	$I, J \pm 1, K$
$3_\pm$	$I \pm 1, J, K+1$	$I \pm 1, J+1, K$	$I, J \pm 1, K+1$
	zx	yx	zy
$1_\pm$	$I-1, J, K \pm 1$	$I-1, J \pm 1, K$	$I, J-1, K \pm 1$
$2_\pm$	$I \quad , J, K \pm 1$	$I \quad , J \pm 1, K$	$I, J \quad , K \pm 1$
$3_\pm$	$I+1, J, K \pm 1$	$I+1, J \pm 1, K$	$I, J+1, K \pm 1$

(7.24)

Determination of the effective density $\rho_{I,J,K}$ is not clear from the derivation of the scheme itself. Intuitively, an arithmetic average for the grid cell can be considered appropriate. Another important aspect is that in the mentioned papers still the fundamental and true reason for the harmonic averaging in heterogeneous media was not recognized. We will clarify this in the next chapter.

The scheme is applicable to smooth heterogeneous elastic medium. If it is applied to homogeneous medium, the scheme is 2^{nd}-order accurate in time and space.

Aboudi (1971) found sufficient stability condition for the displacement scheme in a homogeneous medium:

$$\Delta t \;\leq\; h/\sqrt{2\,(\alpha^2 + 2\beta^2)}\,. \tag{7.25}$$

Here α and β are the P- and S-wave velocities. Numerical tests of several seismologists show that less restrictive condition,

$$\Delta t \;\leq\; h/\sqrt{\alpha^2 + \beta^2}, \tag{7.26}$$

that is, the stability condition for the 2D P-SV displacement scheme (Alterman and Loewenthal, 1970) can be used.

Many modelers adopted a rough estimate, based on visual evaluation of the grid-dispersion curves, that taking 10-12 grid spacing per minimum wavelength is a reasonable and sufficient spatial sampling. Such sampling criterion was widely used in earthquake motion simulations. Effect of the grid dispersion obviously is cumulative. Therefore one has to determine a proper spatial sampling according to the length of travel path and a desired/necessary level of accuracy.

Moczo et al. (1999) performed numerical tests of the scheme against the semianalytical discrete-wavenumber method of Bouchon (1981). The scheme was shown to be sufficiently accurate in the heterogeneous media if the P-to-S wave velocity ratio was smaller than approximately 2.2.

In principle, a 4^{th}-order accurate scheme (in the homogeneous medium) is possible to find. As far as we know, however, the 4^{th}-order conventional displacement schemes have not been used in seismology.

7.2 Staggered-grid Schemes

7.2.1 Brief Historic Introduction

As indicated above, the conventional displacement schemes have some limitations. Problems with instabilities in models with high-velocity contrasts and with grid dispersion in media with high Poisson's ratio,

$$\sigma \;=\; \frac{2-\alpha^2/\beta^2}{2\;(1-\alpha^2/\beta^2\,)}\;, \tag{7.27}$$

that is with large P-to-S wave velocity ratio, led Virieux (1984, 1986) to introduce the staggered-grid velocity-stress FD schemes for modeling seismic wave propagation. Virieux followed Madariaga (1976) who introduced the staggered-grid formulation to seismology by his dynamic modeling of the earthquake rupture. In order to decrease spatial sampling ratio (the number of grid points per minimum wavelength that is to be propagated with a desired accuracy) and thus increase computational efficiency, Levander (1988) introduced the $4^{\rm th}$-order staggered-grid FD schemes which in 2D and 3D need at least four and eight times less memory, respectively, compared to the $2^{\rm nd}$-order schemes. In terms of CPU the improvement is 5-8 times in 2D and 10-16 in 3D (Moczo et al., 2007). This is related to the grid dispersion.

The staggered-grid FD schemes have become the dominant type of schemes in the FD modeling of seismic wave propagation and earthquake motion. In order to further reduce the memory requirements, Luo and Schuster (1990) suggested a staggered-grid displacement-stress 2D P-SV FD scheme which they called a parsimonious scheme. Because the scheme does not integrate stress in time, the stress-tensor components are only temporary quantities. Thus, the displacement-stress scheme in 3D needs only 75% of the memory needed by the velocity-stress scheme. Rodrigues (1993), and Yomogida and Etgen (1993) used the $8^{\rm th}$-order 3D displacement-stress FD schemes, Ohminato and Chouet (1997) applied the $2^{\rm nd}$-order while Moczo et al. (2000a, 2002) the $4^{\rm th}$-order approximations. Moczo et al. (2000a) analyzed the grid dispersion of the displacement-stress schemes ($4^{\rm th}$ and $2^{\rm nd}$ order) and pointed out that the stability and grid dispersion of the displacement-stress, displacement-velocity stress and velocity-stress schemes are the same. The advantage of the displacement-velocity-stress scheme is that both displacement and particle-velocity are calculated at no extra cost. At the same time, most FD modelers use the velocity-stress formulation.

Graves (1996) was the first who properly described how effective material grid parameters are determined in his $4^{\rm th}$-order velocity-stress staggered-grid scheme. In order to increase computational efficiency Pitarka (1999) used a spatial grid with a varying size of the grid spacing for the same type of scheme. Moczo et al. (2002) presented a $4^{\rm th}$-order staggered-grid scheme based on a heterogeneous formulation of the equation of motion and numerically demonstrated superior accuracy of their scheme compared to previous staggered-grid schemes. The improvement in accuracy was achieved by a proper treatment of the effective material grid parameters. The treatment was due to analysis of consistency of the scheme with a boundary conditions on material interface.

7.2.2 The 4$^{\mathrm{th}}$-order Velocity-stress Staggered-grid Scheme

If we do not pay a special attention to the question of determination of the effective material grid parameters, it is relatively very easy to obtain, for example, a 4$^{\mathrm{th}}$-order velocity-stress staggered-grid scheme by simple application of the 4$^{\mathrm{th}}$-order FD approximation (6.5) to the first spatial derivatives appearing in the velocity-stress formulation of the equation of motion (5.3). The first time derivative is approximated by the 2$^{\mathrm{nd}}$-order central-difference formula. We obtain

$$
\begin{aligned}
U^{m+1/2}_{I,J+1/2,K+1/2} \;=\; & U^{m-1/2}_{I,J+1/2,K+1/2} + \frac{\Delta t}{\rho^A_{I,J+1/2,K+1/2}}\, F^{x,m}_{I,J+1/2,K+1/2} + \\
& + \frac{\Delta t}{h}\frac{1}{\rho^A_{I,J+1/2,K+1/2}}\Big[\quad a\,\big(\, T^{xx,m}_{I+3/2,J+1/2,K+1/2} - T^{xx,m}_{I-3/2,J+1/2,K+1/2} \,\big) \\
& \qquad\qquad + b\,\big(\, T^{xx,m}_{I+1/2,J+1/2,K+1/2} - T^{xx,m}_{I-1/2,J+1/2,K+1/2} \,\big) \\
& \qquad\qquad + a\,\big(\, T^{xy,m}_{I,J+2,K+1/2} - T^{xy,m}_{I,J-1,K+1/2} \,\big) \\
& \qquad\qquad + b\,\big(\, T^{xy,m}_{I,J+1,K+1/2} - T^{xy,m}_{I,J,K+1/2} \,\big) \\
& \qquad\qquad + a\,\big(\, T^{zx,m}_{I,J+1/2,K+2} - T^{zx,m}_{I,J+1/2,K-1} \,\big) \\
& \qquad\qquad + b\,\big(\, T^{zx,m}_{I,J+1/2,K+1} - T^{zx,m}_{I,J+1/2,K} \,\big)\Big],
\end{aligned}
\tag{7.28}
$$

$$
\begin{aligned}
V^{m+1/2}_{I+1/2,J,K+1/2} \;=\; & V^{m-1/2}_{I+1/2,J,K+1/2} + \frac{\Delta t}{\rho^A_{I+1/2,J,K+1/2}}\, F^{y,m}_{I+1/2,J,K+1/2} + \\
& + \frac{\Delta t}{h}\frac{1}{\rho^A_{I+1/2,J,K+1/2}}\Big[\quad a\,\big(\, T^{yy,m}_{I+1/2,J+3/2,K+1/2} - T^{yy,m}_{I+1/2,J-3/2,K+1/2} \,\big) \\
& \qquad\qquad + b\,\big(\, T^{yy,m}_{I+1/2,J+1/2,K+1/2} - T^{yy,m}_{I+1/2,J-1/2,K+1/2} \,\big) \\
& \qquad\qquad + a\,\big(\, T^{xy,m}_{I+2,J,K+1/2} - T^{xy,m}_{I-1,J,K+1/2} \,\big) \\
& \qquad\qquad + b\,\big(\, T^{xy,m}_{I+1,J,K+1/2} - T^{xy,m}_{I,J,K+1/2} \,\big) \\
& \qquad\qquad + a\,\big(\, T^{yz,m}_{I+1/2,J,K+2} - T^{yz,m}_{I+1/2,J,K-1} \,\big) \\
& \qquad\qquad + b\,\big(\, T^{yz,m}_{I+1/2,J,K+1} - T^{yz,m}_{I+1/2,J,K} \,\big)\Big],
\end{aligned}
\tag{7.29}
$$

$$
\begin{aligned}
W^{m+1/2}_{I+1/2,J+1/2,K} \;=\; & W^{m-1/2}_{I+1/2,J+1/2,K} + \frac{\Delta t}{\rho^A_{I+1/2,J+1/2,K}}\, F^{z,m}_{I+1/2,J+1/2,K} + \\
& + \frac{\Delta t}{h}\frac{1}{\rho^A_{I+1/2,J+1/2,K}}\Big[\quad a\,\big(\, T^{zz,m}_{I+1/2,J+1/2,K+3/2} - T^{zz,m}_{I+1/2,J+1/2,K-3/2} \,\big) \\
& \qquad\qquad + b\,\big(\, T^{zz,m}_{I+1/2,J+1/2,K+1/2} - T^{zz,m}_{I+1/2,J+1/2,K-1/2} \,\big) \\
& \qquad\qquad + a\,\big(\, T^{zx,m}_{I+2,J+1/2,K} - T^{zx,m}_{I-1,J+1/2,K} \,\big) \\
& \qquad\qquad + b\,\big(\, T^{zx,m}_{I+1,J+1/2,K} - T^{zx,m}_{I,J+1/2,K} \,\big) \\
& \qquad\qquad + a\,\big(\, T^{yz,m}_{I+1/2,J+2,K} - T^{yz,m}_{I+1/2,J-1,K} \,\big) \\
& \qquad\qquad + b\,\big(\, T^{yz,m}_{I+1/2,J+1,K} - T^{yz,m}_{I+1/2,J,K} \,\big)\Big],
\end{aligned}
\tag{7.30}
$$

$$
\begin{aligned}
T^{xx,m+1}_{I+1/2,J+1/2,K+1/2} \;=\; & T^{xx,m}_{I+1/2,J+1/2,K+1/2} + \\
& + \frac{\Delta t}{h}\Big\{\big(\kappa^H_{I+1/2,J+1/2,K+1/2} + \tfrac{4}{3}\mu^H_{I+1/2,J+1/2,K+1/2}\big)\times \\
& \qquad \big[\, a\,(\; U^{m+1/2}_{I+2,J+1/2,K+1/2} \;-\; U^{m+1/2}_{I-1,J+1/2,K+1/2}\;) \\
& \qquad\; + b\,(\; U^{m+1/2}_{I+1,J+1/2,K+1/2} \;-\; U^{m+1/2}_{I,J+1/2,K+1/2}\;)\big] \\
& \quad + \big(\kappa^H_{I+1/2,J+1/2,K+1/2} - \tfrac{2}{3}\mu^H_{I+1/2,J+1/2,K+1/2}\big)\times \\
& \qquad \big[\, a\,(\; V^{m+1/2}_{I+1/2,J+2,K+1/2} \;-\; V^{m+1/2}_{I+1/2,J-1,K+1/2}\;) \\
& \qquad\; + b\,(\; V^{m+1/2}_{I+1/2,J+1,K+1/2} \;-\; V^{m+1/2}_{I+1/2,J,K+1/2}\;) \\
& \qquad\; + a\,(\; W^{m+1/2}_{I+1/2,J+1/2,K+2} \;-\; W^{m+1/2}_{I+1/2,J+1/2,K-1}\;) \\
& \qquad\; + b\,(\; W^{m+1/2}_{I+1/2,J+1/2,K+1} \;-\; W^{m+1/2}_{I+1/2,J+1/2,K}\;)\big]\Big\},
\end{aligned}
\tag{7.31}
$$

$$
\begin{aligned}
T^{yy,m+1}_{I+1/2,J+1/2,K+1/2} \;=\; & T^{yy,m}_{I+1/2,J+1/2,K+1/2} + \\
& + \frac{\Delta t}{h}\Big\{\big(\kappa^H_{I+1/2,J+1/2,K+1/2} + \tfrac{4}{3}\mu^H_{I+1/2,J+1/2,K+1/2}\big)\times \\
& \qquad \big[\, a\,(\; V^{m+1/2}_{I+1/2,J+2,K+1/2} \;-\; V^{m+1/2}_{I+1/2,J-1,K+1/2}\;) \\
& \qquad\; + b\,(\; V^{m+1/2}_{I+1/2,J+1,K+1/2} \;-\; V^{m+1/2}_{I+1/2,J,K+1/2}\;)\big] \\
& \quad + \big(\kappa^H_{I+1/2,J+1/2,K+1/2} - \tfrac{2}{3}\mu^H_{I+1/2,J+1/2,K+1/2}\big)\times \\
& \qquad \big[\, a\,(\; U^{m+1/2}_{I+2,J+1/2,K+1/2} \;-\; U^{m+1/2}_{I-1,J+1/2,K+1/2}\;) \\
& \qquad\; + b\,(\; U^{m+1/2}_{I+1,J+1/2,K+1/2} \;-\; U^{m+1/2}_{I,J+1/2,K+1/2}\;) \\
& \qquad\; + a\,(\; W^{m+1/2}_{I+1/2,J+1/2,K+2} \;-\; W^{m+1/2}_{I+1/2,J+1/2,K-1}\;) \\
& \qquad\; + b\,(\; W^{m+1/2}_{I+1/2,J+1/2,K+1} \;-\; W^{m+1/2}_{I+1/2,J+1/2,K}\;)\big]\Big\},
\end{aligned}
\tag{7.32}
$$

$$
\begin{aligned}
T^{xy,m+1}_{I,J,K+1/2} \;=\; & T^{xy,m}_{I,J,K+1/2} + \\
& + \frac{\Delta t}{h}\,\mu^H_{I,J,K+1/2}\Big[\, a\,(\; U^{m+1/2}_{I,J+3/2,K+1/2} - U^{m+1/2}_{I,J-3/2,K+1/2}\;) \\
& \qquad\qquad + b\,(\; U^{m+1/2}_{I,J+1/2,K+1/2} - U^{m+1/2}_{I,J-1/2,K+1/2}\;) \\
& \qquad\qquad + a\,(\; V^{m+1/2}_{I+3/2,J,K+1/2} - V^{m+1/2}_{I-3/2,J,K+1/2}\;) \\
& \qquad\qquad + b\,(\; V^{m+1/2}_{I+1/2,J,K+1/2} - V^{m+1/2}_{I-1/2,J,K+1/2}\;)\Big],
\end{aligned}
\tag{7.33}
$$

$$
\begin{aligned}
T^{zz,m+1}_{I+1/2,J+1/2,K+1/2} \;=\; & T^{zz,m}_{I+1/2,J+1/2,K+1/2} + \\
& + \frac{\Delta t}{h}\Big\{ \big(\kappa^H_{I+1/2,J+1/2,K+1/2} + \tfrac{4}{3}\mu^H_{I+1/2,J+1/2,K+1/2}\big) \times \\
& \quad \big[\, a\,\big(\, W^{m+1/2}_{I+1/2,J+1/2,K+2} - W^{m+1/2}_{I+1/2,J+1/2,K-1}\,\big) \\
& \quad + b\,\big(\, W^{m+1/2}_{I+1/2,J+1/2,K+1} - W^{m+1/2}_{I+1/2,J+1/2,K}\,\big)\big] \\
& + \big(\kappa^H_{I+1/2,J+1/2,K+1/2} - \tfrac{2}{3}\mu^H_{I+1/2,J+1/2,K+1/2}\big) \times \\
& \quad \big[\, a\,\big(\, U^{m+1/2}_{I+2,J+1/2,K+1/2} - U^{m+1/2}_{I-1,J+1/2,K+1/2}\,\big) \\
& \quad + b\,\big(\, U^{m+1/2}_{I+1,J+1/2,K+1/2} - U^{m+1/2}_{I,J+1/2,K+1/2}\,\big) \\
& \quad + a\,\big(\, V^{m+1/2}_{I+1/2,J+2,K+1/2} - V^{m+1/2}_{I+1/2,J-1,K+1/2}\,\big) \\
& \quad + b\,\big(\, V^{m+1/2}_{I+1/2,J+1,K+1/2} - V^{m+1/2}_{I+1/2,J,K+1/2}\,\big)\big]\Big\},
\end{aligned}
\tag{7.34}
$$

$$
\begin{aligned}
T^{zx,m+1}_{I,J+1/2,K} \;=\; & T^{zx,m}_{I,J+1/2,K} + \\
& + \frac{\Delta t}{h}\,\mu^H_{I,J+1/2,K}\Big[\, a\,\big(\, U^{m+1/2}_{I,J+1/2,K+3/2} - U^{m+1/2}_{I,J+1/2,K-3/2}\,\big) \\
& \quad + b\,\big(\, U^{m+1/2}_{I,J+1/2,K+1/2} - U^{m+1/2}_{I,J+1/2,K-1/2}\,\big) \\
& \quad + a\,\big(\, W^{m+1/2}_{I+3/2,J+1/2,K} - W^{m+1/2}_{I-3/2,J+1/2,K}\,\big) \\
& \quad + b\,\big(\, W^{m+1/2}_{I+1/2,J+1/2,K} - W^{m+1/2}_{I-1/2,J+1/2,K}\,\big)\Big],
\end{aligned}
\tag{7.35}
$$

$$
\begin{aligned}
T^{yz,m+1}_{I+1/2,J,K} \;=\; & T^{yz,m}_{I+1/2,J,K} + \\
& + \frac{\Delta t}{h}\,\mu^H_{I+1/2,J,K}\Big[\, a\,\big(\, V^{m+1/2}_{I+1/2,J,K+3/2} - V^{m+1/2}_{I+1/2,J,K-3/2}\,\big) \\
& \quad + b\,\big(\, V^{m+1/2}_{I+1/2,J,K+1/2} - V^{m+1/2}_{I+1/2,J,K-1/2}\,\big) \\
& \quad + a\,\big(\, W^{m+1/2}_{I+1/2,J+3/2,K} - W^{m+1/2}_{I+1/2,J-3/2,K}\,\big) \\
& \quad + b\,\big(\, W^{m+1/2}_{I+1/2,J+1/2,K} - W^{m+1/2}_{I+1/2,J-1/2,K}\,\big)\Big].
\end{aligned}
\tag{7.36}
$$

Here U, V and W denote components of the particle velocity vector, and $a = -1/24$ and $b = 9/8$. Moczo et al. (2002) defined effective grid moduli as integral volume harmonic averages and effective grid densities as integral volume arithmetic averages, for example,

$$
\kappa^H_{I+1/2,\,\mathrm{J}+1/2,\,\mathrm{K}+1/2} \;=\; \left[\frac{1}{h^3}\int_{x_I}^{x_{I+1}}\int_{y_J}^{y_{J+1}}\int_{z_K}^{z_{K+1}} \frac{1}{\kappa}\,\mathrm{d}x\,\mathrm{d}y\,\mathrm{d}z\right]^{-1}, \tag{7.37}
$$

$$
\mu^H_{I+1/2,\,\mathrm{J}+1/2,\,\mathrm{K}+1/2} \;=\; \left[\frac{1}{h^3}\int_{x_I}^{x_{I+1}}\int_{y_J}^{y_{J+1}}\int_{z_K}^{z_{K+1}} \frac{1}{\mu}\,\mathrm{d}x\,\mathrm{d}y\,\mathrm{d}z\right]^{-1} \tag{7.38}
$$

and

$$\rho^{A}_{I,\ \mathrm{J+1/2},\ \mathrm{K+1/2}} \;=\; \frac{1}{h^3}\int_{x_{I-\frac{1}{2}}}^{x_{I+\frac{1}{2}}}\int_{y_J}^{y_{J+1}}\int_{z_K}^{z_{K+1}} \rho\,\mathrm{d}x\,\mathrm{d}y\,\mathrm{d}z\,. \tag{7.39}$$

These definitions will be discussed in the next chapter.

Stability and grid dispersion of the 4^{th}-order staggered-grid schemes were analyzed and numerically demonstrated in detail by Moczo et al. (2000a). A similar investigation for the 2D P-SV staggered-grid schemes can be found in Moczo et al. (2000b). The stability condition for the scheme for homogeneous medium is

$$\Delta t \;\le\; \frac{6}{7\sqrt{3}}\,\frac{h}{\alpha}\,. \tag{7.40}$$

An interesting feature of the scheme is the anisotropy of the grid dispersion. Grid dispersion is strongest for a wave propagating along a coordinate axis and weakest for a wave propagating along a body diagonal; see Fig. 7.1.

7.2.3 Incorporation of the Attenuation

As explained in section 4.4.7 the attenuation corresponding to rheology of the generalized Maxwell body (GMB-EK) can be incorporated if the stress-strain relation for the perfectly elastic medium is replaced by the stress-strain relation for the GMB-EK medium. In the case of the velocity-stress scheme we can apply the stress-strain relation in the form (4.167) with the additional system of ordinary differential equations for the anelastic functions (memory variables) (4.168).

With the 2^{nd}-order accuracy we can write for the anelastic functions in eqs. (4.168)

$$\xi_l^{ij}(t_{m+1/2}) \;\doteq\; \frac{1}{2}\,\left[\,\xi_l^{ij}(t_{m+1}) + \xi_l^{ij}(t_m)\,\right] \tag{7.41}$$

and

$$\dot{\xi}_l^{ij}(t_{m+1/2}) \;\doteq\; \frac{1}{\Delta\,t}\,\left[\,\xi_l^{ij}(t_{m+1}) - \xi_l^{ij}(t_m)\,\right]\,. \tag{7.42}$$

Substituting eqs. (7.41) and (7.42) into eq. (4.168) we obtain

$$\xi_l^{ij}(t_{m+1}) \;=\; \frac{2\,\omega_l\,\Delta t}{2+\omega_l\Delta t}\;\dot{\varepsilon}_{ij}\,(t_{m+1/2}) \;+\; \frac{2-\omega_l\,\Delta t}{2+\omega_l\,\Delta t}\;\xi_l^{ij}(t_m)\,;\quad l=1,\,\ldots,\,n\,. \tag{7.43}$$

Then value of $\xi_l^{ij}(t_{m+1/2})$ needed in the stress-strain relation (4.167) can be obtained from eq. (7.41). Equation (7.41) however means that two values, $\xi_l^{ij}(t_m)$ and $\xi_l^{ij}(t_{m+1})$, have to be kept in memory for each spatial grid position at one time. Kristek and Moczo (2003) therefore modified this procedure. Substituting eq. (7.41) into eq. (7.43) it is easy to eliminate $\xi_l^{ij}(t_m)$ and obtain

$$\xi_l^{ij}(t_{m+1/2}) \;=\; -\frac{\omega_l\,\Delta t}{2-\omega_l\,\Delta t}\;\dot{\varepsilon}_{ij}\,(t_{m+1/2}) \;+\; \frac{2}{2-\omega_l\,\Delta t}\;\xi_l^{ij}(t_{m+1})\,. \tag{7.44}$$

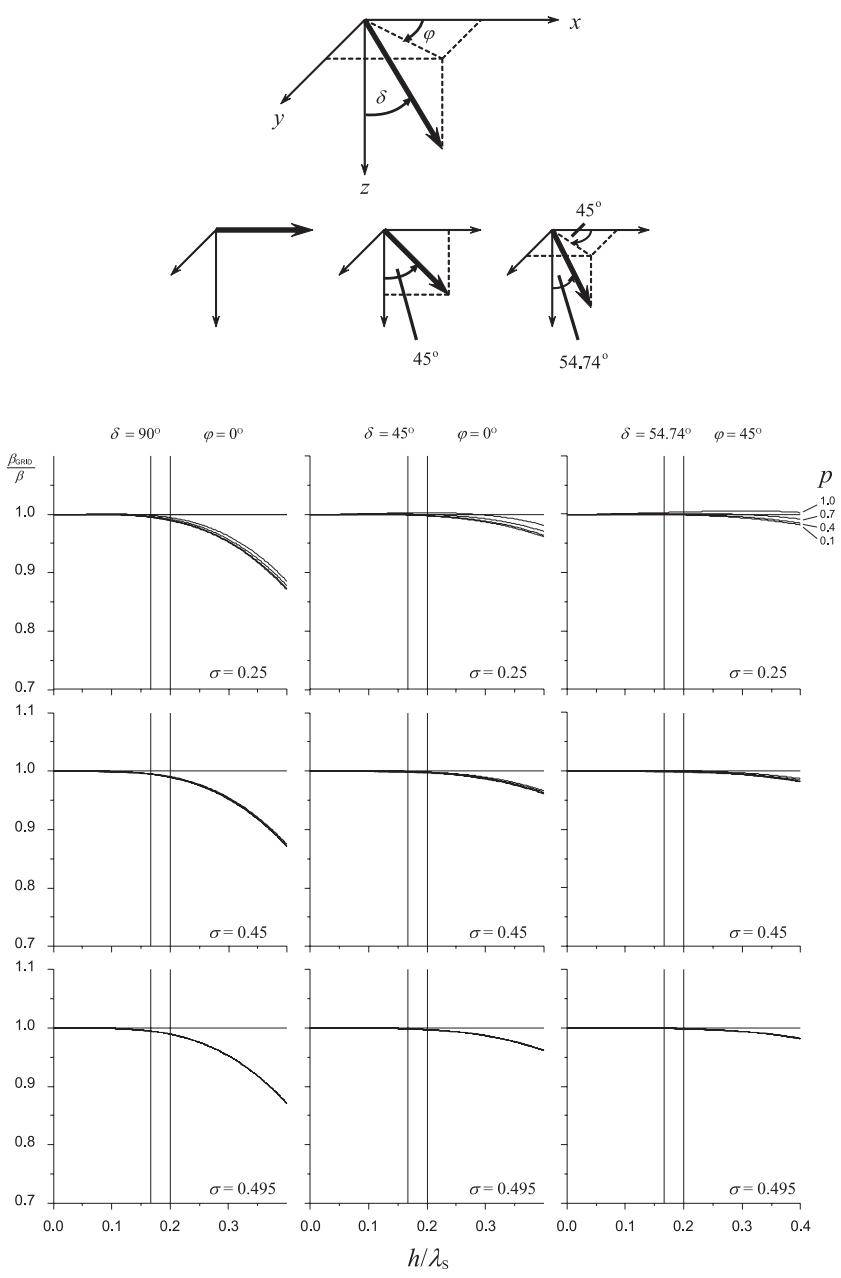

Fig. 7.1. Grid dispersion of the S-wave phase velocity in the 4^{th}-order velocity-stress staggered-grid scheme for three directions of wave propagation – x-axis ($\delta = 90^\circ$, $\varphi = 0^\circ$), the xz-plane diagonal ($\delta = 45^\circ$, $\varphi = 0^\circ$), and body diagonal ($\delta = 54.74^\circ$, $\varphi = 45^\circ$). β_{GRID} is the phase velocity in the grid, β true phase velocity in the medium, h grid spacing, λ_S wavelength of the S-wave, and p the stability ratio.

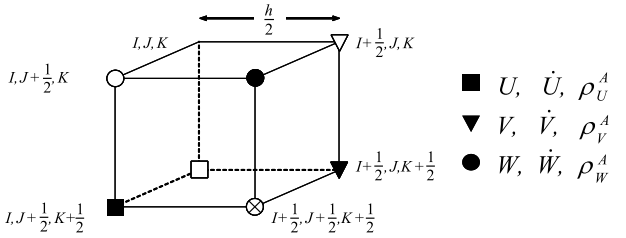

Fig. 7.2. A staggered-grid FD cell with positions of the wavefield variables (displacement and/or velocity vector components $U, V, W; \dot{U}, \dot{V}, \dot{W}$, stress-tensor components $T^{xy}, T^{yz}, T^{zx}, T^{xx}, T^{yy}, T^{zz}$, and anelastic functions $\xi_l^{xy}, \xi_l^{yz}, \xi_l^{zx}, \xi_l^{xx}, \xi_l^{yy}, \xi_l^{zz}$), and effective material parameters (elastic bulk and shear moduli $\kappa^H, \mu^H, \mu_{xy}^H, \mu_{yz}^H, \mu_{zx}^H$, and anelastic coefficients $Y_l^\mu, Y_l^\kappa, Y_l^{\mu\,xy}, Y_l^{\mu\,yz}, Y_l^{\mu\,zx}$). Indices A and H indicate integral volume arithmetic and harmonic averages.

Substitution of $\xi_l^{ij}(t_{m+1/2})$ from eq. (7.44) into the stress-strain relation (4.167) yields

$$\begin{aligned}\dot{\sigma}_{ij}\left(t_{m+1/2}\right) \;=\; & \tilde{\kappa}\,\dot{\varepsilon}_{kk}\left(t_{m+1/2}\right)\,\delta_{ij} \;+\; 2\,\tilde{\mu}\;\left[\,\dot{\varepsilon}_{ij}\left(t_{m+1/2}\right) - \tfrac{1}{3}\dot{\varepsilon}_{kk}\left(t_{m+1/2}\right)\,\delta_{ij}\right] - \\ & - \sum_{l=1}^{n}\left\{\,\tilde{Y}_l^{\kappa}\,\xi_l^{kk}\left(t_{m+1}\right)\,\delta_{ij} \;+\; 2\,\tilde{Y}_l^{\mu}\,\left[\,\xi_l^{ij}\left(t_{m+1}\right) \;-\; \tfrac{1}{3}\,\xi_l^{kk}\left(t_{m+1}\right)\,\delta_{ij}\right]\,\right\}\,,\end{aligned} \tag{7.45}$$

where

$$\begin{aligned}\tilde{\kappa} \;&=\; \kappa\,\left(1+\sum_{l=1}^{n} G_{1l}\,Y_l^{\kappa}\right)\,, \qquad \tilde{\mu} \;=\; \mu\,\left(1+\sum_{l=1}^{n} G_{1l}\,Y_l^{\mu}\right)\,, \\ \tilde{Y}_l^{\kappa} \;&=\; G_{2l}\,\kappa\,Y_l^{\kappa} \qquad\qquad , \quad \tilde{Y}_l^{\mu} \;=\; G_{2l}\,\mu\,Y_l^{\mu}\,, \\ G_{1l} \;&=\; \frac{\omega_l\,\Delta t}{2-\omega_l\,\Delta t} \qquad , \quad G_{2l} \;=\; \frac{2}{2-\omega_l\,\Delta t}\;.\end{aligned} \tag{7.46}$$

Thus $\xi_l^{ij}(t_{m+1})$ are updated using scheme (7.43) and the updated values are then used in eq. (7.45).

7.2.4 The 4$^{\rm th}$-order Velocity-stress Staggered-grid Scheme for the Viscoelastic Medium

Considering relations (7.45) and (7.46) we can easily generalize the 4$^{\rm th}$-order velocity-stress staggered-grid scheme for the elastic medium, eqs. (7.28) - (7.36), for the case of the viscoelastic medium. Positions of the particle-velocity components, stress-tensor components, anelastic functions, density, and elastic and anelastic material parameters are illustrated in Fig. 7.2. The

scheme reads

$$
\begin{aligned}
U^{m+1/2}_{I,J+1/2,K+1/2} \;=\; & U^{m-1/2}_{I,J+1/2,K+1/2} + \frac{\Delta t}{\rho^A_{I,J+1/2,K+1/2}} F^{x,m}_{I,J+1/2,K+1/2} + \\
& + \frac{\Delta t}{h} \frac{1}{\rho^A_{I,J+1/2,K+1/2}} \Big[\quad a \left(T^{xx,m}_{I+3/2,J+1/2,K+1/2} - T^{xx,m}_{I-3/2,J+1/2,K+1/2} \right) \\
& \qquad + b \left(T^{xx,m}_{I+1/2,J+1/2,K+1/2} - T^{xx,m}_{I-1/2,J+1/2,K+1/2} \right) \\
& \qquad + a \left(T^{xy,m}_{I\quad,J+2\quad,K+1/2} - T^{xy,m}_{I\quad,J-1\quad,K+1/2} \right) \\
& \qquad + b \left(T^{xy,m}_{I\quad,J+1\quad,K+1/2} - T^{xy,m}_{I\quad,J\quad,K+1/2} \right) \\
& \qquad + a \left(T^{zx,m}_{I\quad,J+1/2,K+2} - T^{zx,m}_{I\quad,J+1/2,K-1} \right) \\
& \qquad + b \left(T^{zx,m}_{I\quad,J+1/2,K+1} - T^{zx,m}_{I\quad,J+1/2,K} \right) \Big] ,
\end{aligned}
\tag{7.47}
$$

$$
\begin{aligned}
V^{m+1/2}_{I+1/2,J,K+1/2} \;=\; & V^{m-1/2}_{I+1/2,J,K+1/2} + \frac{\Delta t}{\rho^A_{I+1/2,J,K+1/2}} F^{y,m}_{I+1/2,J,K+1/2} + \\
& + \frac{\Delta t}{h} \frac{1}{\rho^A_{I+1/2,J,K+1/2}} \Big[\quad a \left(T^{yy,m}_{I+1/2,J+3/2,K+1/2} - T^{yy,m}_{I+1/2,J-3/2,K+1/2} \right) \\
& \qquad + b \left(T^{yy,m}_{I+1/2,J+1/2,K+1/2} - T^{yy,m}_{I+1/2,J-1/2,K+1/2} \right) \\
& \qquad + a \left(T^{xy,m}_{I+2,J,K+1/2} - T^{xy,m}_{I-1,J,K+1/2} \right) \\
& \qquad + b \left(T^{xy,m}_{I+1,J,K+1/2} - T^{xy,m}_{I,J,K+1/2} \right) \\
& \qquad + a \left(T^{yz,m}_{I+1/2,J,K+2} - T^{yz,m}_{I+1/2,J,K-1} \right) \\
& \qquad + b \left(T^{yz,m}_{I+1/2,J,K+1} - T^{yz,m}_{I+1/2,J,K} \right) \Big] ,
\end{aligned}
\tag{7.48}
$$

$$
\begin{aligned}
W^{m+1/2}_{I+1/2,J+1/2,K} \;=\; & W^{m-1/2}_{I+1/2,J+1/2,K} + \frac{\Delta t}{\rho^A_{I+1/2,J+1/2,K}} F^{z,m}_{I+1/2,J+1/2,K} + \\
& + \frac{\Delta t}{h} \frac{1}{\rho^A_{I+1/2,J+1/2,K}} \Big[\quad a \left(T^{zz,m}_{I+1/2,J+1/2,K+3/2} - T^{zz,m}_{I+1/2,J+1/2,K-3/2} \right) \\
& \qquad + b \left(T^{zz,m}_{I+1/2,J+1/2,K+1/2} - T^{zz,m}_{I+1/2,J+1/2,K-1/2} \right) \\
& \qquad + a \left(T^{zx,m}_{I+2,J+1/2,K} - T^{zx,m}_{I-1,J+1/2,K} \right) \\
& \qquad + b \left(T^{zx,m}_{I+1,J+1/2,K} - T^{zx,m}_{I,J+1/2,K} \right) \\
& \qquad + a \left(T^{yz,m}_{I+1/2,J+2,K} - T^{yz,m}_{I+1/2,J-1,K} \right) \\
& \qquad + b \left(T^{yz,m}_{I+1/2,J+1,K} - T^{yz,m}_{I+1/2,J,K} \right) \Big] ,
\end{aligned}
\tag{7.49}
$$

$$
\begin{aligned}
T^{xx,m+1}_{I+1/2,J+1/2,K+1/2} \;=\; & T^{xx,m}_{I+1/2,J+1/2,K+1/2} + \\
& + \frac{\Delta t}{h}\Big\{\big(\tilde{\kappa}^{H}_{I+1/2,J+1/2,K+1/2} + \tfrac{4}{3}\tilde{\mu}^{H}_{I+1/2,J+1/2,K+1/2}\big)\times \\
& \quad \Big[\;\; a\,\big(\; U^{m+1/2}_{I+2,J+1/2,K+1/2} - U^{m+1/2}_{I-1,J+1/2,K+1/2}\;\big) \\
& \quad\;\; + b\,\big(\; U^{m+1/2}_{I+1,J+1/2,K+1/2} - U^{m+1/2}_{I,J+1/2,K+1/2}\;\big)\Big] \\
& \quad + \big(\tilde{\kappa}^{H}_{I+1/2,J+1/2,K+1/2} - \tfrac{2}{3}\tilde{\mu}^{H}_{I+1/2,J+1/2,K+1/2}\big)\times \\
& \quad \Big[\;\; a\,\big(\; V^{m+1/2}_{I+1/2,J+2,K+1/2} - V^{m+1/2}_{I+1/2,J-1,K+1/2}\;\big) \\
& \quad\;\; + b\,\big(\; V^{m+1/2}_{I+1/2,J+1,K+1/2} - V^{m+1/2}_{I+1/2,J,K+1/2}\;\big) \\
& \quad\;\; + a\,\big(\; W^{m+1/2}_{I+1/2,J+1/2,K+2} - W^{m+1/2}_{I+1/2,J+1/2,K-1}\;\big) \\
& \quad\;\; + b\,\big(\; W^{m+1/2}_{I+1/2,J+1/2,K+1} - W^{m+1/2}_{I+1/2,J+1/2,K}\;\big)\Big]\Big\} - \\
& - \Delta t \sum_{l=1}^{n}\Big\{\big(\tilde{Y}^{(\kappa^H)}_{l\;I+1/2,J+1/2,K+1/2} + \tfrac{4}{3}\tilde{Y}^{(\mu^H)}_{l\;I+1/2,J+1/2,K+1/2}\big)\times \\
& \qquad \xi^{xx,m+1}_{l\;I+1/2,J+1/2,K+1/2} \\
& \qquad + \big(\tilde{Y}^{(\kappa^H)}_{l\;I+1/2,J+1/2,K+1/2} - \tfrac{2}{3}\tilde{Y}^{(\mu^H)}_{l\;I+1/2,J+1/2,K+1/2}\big)\times \\
& \qquad \big[\,\xi^{yy,m+1}_{l\;I+1/2,J+1/2,K+1/2} + \xi^{zz,m+1}_{l\;I+1/2,J+1/2,K+1/2}\big]\Big\}\,,
\end{aligned}
\tag{7.50}
$$

$$
\begin{aligned}
T^{xy,m+1}_{I,J,K+1/2} \;=\; & T^{xy,m}_{I,J,K+1/2} + \\
& + \frac{\Delta t}{h}\,\tilde{\mu}^{H}_{I,J,K+1/2}\Big[\;\; a\,\big(\; U^{m+1/2}_{I,J+3/2,K+1/2} - U^{m+1/2}_{I,J-3/2,K+1/2}\;\big) \\
& \qquad\qquad + b\,\big(\; U^{m+1/2}_{I,J+1/2,K+1/2} - U^{m+1/2}_{I,J-1/2,K+1/2}\;\big) \\
& \qquad\qquad + a\,\big(\; V^{m+1/2}_{I+3/2,J,K+1/2} - V^{m+1/2}_{I-3/2,J,K+1/2}\;\big) \\
& \qquad\qquad + b\,\big(\; V^{m+1/2}_{I+1/2,J,K+1/2} - V^{m+1/2}_{I-1/2,J,K+1/2}\;\big)\Big] - \\
& - \Delta t \sum_{l=1}^{n} 2\,Y^{(\mu^H)}_{l\;I,J,K+1/2}\,\xi^{xy,m+1}_{l\;I,J,K+1/2}\,,
\end{aligned}
\tag{7.51}
$$

$$
\begin{aligned}
T^{yy,m+1}_{I+1/2,J+1/2,K+1/2} \;=\; & T^{yy,m}_{I+1/2,J+1/2,K+1/2} + \\
& + \frac{\Delta t}{h} \Big\{ \big(\tilde{\kappa}^{H}_{I+1/2,J+1/2,K+1/2} + \tfrac{4}{3} \tilde{\mu}^{H}_{I+1/2,J+1/2,K+1/2} \big) \times \\
& \quad \Big[\;\; a \, \big(\; V^{m+1/2}_{I+1/2,J+2,K+1/2} \; - \; V^{m+1/2}_{I+1/2,J-1,K+1/2} \; \big) \\
& \quad \;\; + b \, \big(\; V^{m+1/2}_{I+1/2,J+1,K+1/2} \; - \; V^{m+1/2}_{I+1/2,J,K+1/2} \quad \big) \Big] \\
& \quad + \big(\tilde{\kappa}^{H}_{I+1/2,J+1/2,K+1/2} - \tfrac{2}{3} \tilde{\mu}^{H}_{I+1/2,J+1/2,K+1/2} \big) \times \\
& \quad \Big[\;\; a \, \big(\; U^{m+1/2}_{I+2,J+1/2,K+1/2} \; - \; U^{m+1/2}_{I-1,J+1/2,K+1/2} \; \big) \\
& \quad \;\; + b \, \big(\; U^{m+1/2}_{I+1,J+1/2,K+1/2} \; - \; U^{m+1/2}_{I,J+1/2,K+1/2} \quad \big) \\
& \quad \;\; + a \, \big(\; W^{m+1/2}_{I+1/2,J+1/2,K+2} \; - \; W^{m+1/2}_{I+1/2,J+1/2,K-1} \; \big) \\
& \quad \;\; + b \, \big(\; W^{m+1/2}_{I+1/2,J+1/2,K+1} \; - \; W^{m+1/2}_{I+1/2,J+1/2,K} \quad \big) \Big] \Big\} - \\
& - \Delta t \, \sum_{l=1}^{n} \Big\{ \big(\tilde{Y}^{(\kappa^H)}_{l \; I+1/2,J+1/2,K+1/2} + \tfrac{4}{3} \tilde{Y}^{(\mu^H)}_{l \; I+1/2,J+1/2,K+1/2} \big) \times \\
& \qquad \xi^{yy,m+1}_{l \; I+1/2,J+1/2,K+1/2} \\
& \qquad + \big(\tilde{Y}^{(\kappa^H)}_{l \; I+1/2,J+1/2,K+1/2} - \tfrac{2}{3} \tilde{Y}^{(\mu^H)}_{l \; I+1/2,J+1/2,K+1/2} \big) \times \\
& \qquad \big[\, \xi^{xx,m+1}_{l \; I+1/2,J+1/2,K+1/2} + \xi^{zz,m+1}_{l \; I+1/2,J+1/2,K+1/2} \big] \Big\} ,
\end{aligned}
\tag{7.52}
$$

$$
\begin{aligned}
T^{zx,m+1}_{I,J+1/2,K} \;=\; & T^{zx,m}_{I,J+1/2,K} + \\
& + \frac{\Delta t}{h} \, \tilde{\mu}^{H}_{I,J+1/2,K} \Big[\quad a \, \big(\; U^{m+1/2}_{I,J+1/2,K+3/2} - U^{m+1/2}_{I,J+1/2,K-3/2} \; \big) \\
& \qquad\qquad + b \, \big(\; U^{m+1/2}_{I,J+1/2,K+1/2} - U^{m+1/2}_{I,J+1/2,K-1/2} \; \big) \\
& \qquad\qquad + a \, \big(\; W^{m+1/2}_{I+3/2,J+1/2,K} - W^{m+1/2}_{I-3/2,J+1/2,K} \; \big) \\
& \qquad\qquad + b \, \big(\; W^{m+1/2}_{I+1/2,J+1/2,K} - W^{m+1/2}_{I-1/2,J+1/2,K} \; \big) \Big] - \\
& - \Delta t \sum_{l=1}^{n} 2 \, Y^{(\mu^H)}_{l \; I,J+1/2,K} \, \xi^{zx,m+1}_{l \; I,J+1/2,K} \, ,
\end{aligned}
\tag{7.53}
$$

$$
\begin{aligned}
T^{zz,m+1}_{I+1/2,J+1/2,K+1/2} \;=\; & T^{zz,m}_{I+1/2,J+1/2,K+1/2} + \\
& + \frac{\Delta t}{h}\Big\{ \big(\tilde{\kappa}^H_{I+1/2,J+1/2,K+1/2} + \tfrac{4}{3}\tilde{\mu}^H_{I+1/2,J+1/2,K+1/2}\big) \times \\
& \qquad \big[\;\; a\,\big(\; W^{m+1/2}_{I+1/2,J+1/2,K+2} \;-\; W^{m+1/2}_{I+1/2,J+1/2,K-1}\;\big) \\
& \qquad\quad + b\,\big(\; W^{m+1/2}_{I+1/2,J+1/2,K+1} \;-\; W^{m+1/2}_{I+1/2,J+1/2,K}\;\big)\big] \\
& \quad + \big(\tilde{\kappa}^H_{I+1/2,J+1/2,K+1/2} - \tfrac{2}{3}\tilde{\mu}^H_{I+1/2,J+1/2,K+1/2}\big) \times \\
& \qquad \big[\;\; a\,\big(\; U^{m+1/2}_{I+2,J+1/2,K+1/2} \;-\; U^{m+1/2}_{I-1,J+1/2,K+1/2}\;\big) \\
& \qquad\quad + b\,\big(\; U^{m+1/2}_{I+1,J+1/2,K+1/2} \;-\; U^{m+1/2}_{I,J+1/2,K+1/2}\;\big) \\
& \qquad\quad + a\,\big(\; V^{m+1/2}_{I+1/2,J+2,K+1/2} \;-\; V^{m+1/2}_{I+1/2,J-1,K+1/2}\;\big) \\
& \qquad\quad + b\,\big(\; V^{m+1/2}_{I+1/2,J+1,K+1/2} \;-\; V^{m+1/2}_{I+1/2,J,K+1/2}\;\big)\big]\Big\} - \\
& - \Delta t \sum_{l=1}^{n}\Big\{ \big(\tilde{Y}^{(\kappa^H)}_{l\;I+1/2,J+1/2,K+1/2} + \tfrac{4}{3}\tilde{Y}^{(\mu^H)}_{l\;I+1/2,J+1/2,K+1/2}\big)\times \\
& \qquad \xi^{zz,m+1}_{l\;I+1/2,J+1/2,K+1/2} \\
& \qquad + \big(\tilde{Y}^{(\kappa^H)}_{l\;I+1/2,J+1/2,K+1/2} - \tfrac{2}{3}\tilde{Y}^{(\mu^H)}_{l\;I+1/2,J+1/2,K+1/2}\big) \times \\
& \qquad \big[\,\xi^{xx,m+1}_{l\;I+1/2,J+1/2,K+1/2} + \xi^{yy,m+1}_{l\;I+1/2,J+1/2,K+1/2}\big]\Big\},
\end{aligned}
\tag{7.54}
$$

$$
\begin{aligned}
T^{yz,m+1}_{I+1/2,J,K} \;=\; & T^{yz,m}_{I+1/2,J,K} + \\
& + \frac{\Delta t}{h}\,\tilde{\mu}^H_{I+1/2,J,K}\Big[\;\; a\,\big(\;\; V^{m+1/2}_{I+1/2,J,K+3/2} - V^{m+1/2}_{I+1/2,J,K-3/2}\;\big) \\
& \qquad\qquad + b\,\big(\;\; V^{m+1/2}_{I+1/2,J,K+1/2} - V^{m+1/2}_{I+1/2,J,K-1/2}\;\big) \\
& \qquad\qquad + a\,\big(\; W^{m+1/2}_{I+1/2,J+3/2,K} - W^{m+1/2}_{I+1/2,J-3/2,K}\;\big) \\
& \qquad\qquad + b\,\big(\; W^{m+1/2}_{I+1/2,J+1/2,K} - W^{m+1/2}_{I+1/2,J-1/2,K}\;\big)\Big] - \\
& - \Delta t \sum_{l=1}^{n} 2\,Y^{(\mu^H)}_{l\;I+1/2,J,K}\;\xi^{yz,m+1}_{l\;I+1/2,J,K}\,,
\end{aligned}
\tag{7.55}
$$

where

$$
\begin{aligned}
\tilde{\kappa}^H \;&=\; \kappa^H\,\left(1 + \sum_{l=1}^{n} G_{1l}\,Y^{(\kappa^H)}_l\right), \quad
\tilde{\mu}^H \;=\; \mu^H\,\left(1 + \sum_{l=1}^{n} G_{1l}\,Y^{(\mu^H)}_l\right), \\
\tilde{Y}^{(\kappa^H)}_l \;&=\; G_{2l}\,\kappa^H\,Y^{(\kappa^H)}_l \qquad\qquad , \quad
\tilde{Y}^{(\mu^H)}_l \;=\; G_{2l}\,\mu^H\,Y^{(\mu^H)}_l\,, \\
G_{1l} \;&=\; \frac{\omega_l\,\Delta t}{2 - \omega_l\,\Delta t} \qquad\qquad , \quad
G_{2l} \;=\; \frac{2}{2 - \omega_l\,\Delta t}\,.
\end{aligned}
\tag{7.56}
$$

7.2.5 Coarse Spatial Distribution of the Anelastic Functions

While the GMB-EK rheology (recall its exact equivalence with the GZB rheology) enables much more realistic model of attenuation than simplified approaches, it is obvious that its incorporation considerably increases the number of operations and variables/parameters. Zeng (1996), and independently Day (1998) and Day and Bradley (2001) introduced coarse spatial sampling of the anelastic functions and coefficients in order to reduce the increased memory requirements and also computational time. In Day's (1998) approach, one anelastic function ξ_l^{ij} for one relaxation frequency ω_l is distributed with a spatial period of $2h$. Then the number of relaxation frequencies is $n = 8$. Considering, for example, location of the stress-tensor component T^{zx} at 8 corners of a grid cube $h \times h \times h$, only one of the $8\xi_l^{zx}$ anelastic functions is assigned to one of the 8 corners (ξ_1^{zx} is assigned to one position, ξ_2^{zx} to other position, and so on). Then the total number of the anelastic functions $\xi_l^{zx};\ l = 1, 2, \ldots, 8$ in the whole grid is $\frac{MX}{2} \cdot \frac{MY}{2} \cdot \frac{MZ}{2} \cdot 8 = MX \cdot MY \cdot MZ$, where MX, MY and MZ are the numbers of the grid cells in the three Cartesian directions, respectively. Because there are 6 independent stress-tensor components, the total number of all the anelastic functions in the whole grid is $MX \cdot MY \cdot MZ \cdot 6$. Since the anelastic coefficients Y_l^{κ} and Y_l^{μ} at the grid positions of the normal stress-tensor components, and $Y_l^{\mu\,xy}$, $Y_l^{\mu\,yz}$ and $Y_l^{\mu\,zx}$ at the grid positions of the shear stress-tensor components are distributed in the same coarse manner, the total number of the anelastic coefficients in the grid is $MX \cdot MY \cdot MZ \cdot 5$. This means that the additional memory with the coarse distribution and 8 relaxation frequencies is equivalent to the additional memory required by just one relaxation mechanism (that is, one relaxation frequency) without coarse sampling. Such reduction of the memory requirements is significant. Graves and Day (2003) analyzed stability and accuracy of the scheme with the coarse spatial sampling and defined the effective modulus and the quality factor necessary to achieve sufficient accuracy especially in the case of very low Q.

In a structurally complex model there are material interfaces going through grid cells in different orientations with respect to the coordinate system. In such a case and with the originally suggested spatial sampling it may happen that the medium from one side of the material interface is characterized over one half of the whole considered frequency range while the medium from the other side of the interface is characterized over the other half of the considered frequency range. This means that the behaviors of the two media in contact are described in two disjunctive frequency sub-intervals. Consequently, the two media cannot physically interact.

The geometry of the coarse spatial sampling shown in the papers by Day (1998) and Day and Bradley (2001) is only one of several possible. Keeping the same spatial periodicity of the anelastic quantities, it is possible to choose such distribution that division of a grid cell into two parts characterized in two disjunctive frequency sub-intervals is always avoided. However, with any type of geometric distribution the best possible situation would be characterization of one medium in contact using, for example, relaxation frequencies ω_1, ω_3, ω_5, ω_7 and characterization of the other medium in contact using ω_2, ω_4, ω_6, ω_8. This is much better than two disjunctive frequency subintervals but still not really satisfactory.

It follows from eq. (4.167) or (7.45) that the sum in the anelastic term needs anelastic functions and coefficients at all relaxation frequencies. In the coarse sampling, however, at one grid position we only have anelastic function only at one relaxation frequency. Still it is possible to account for all the anelastic functions and coefficients: the anelastic functions and coefficients

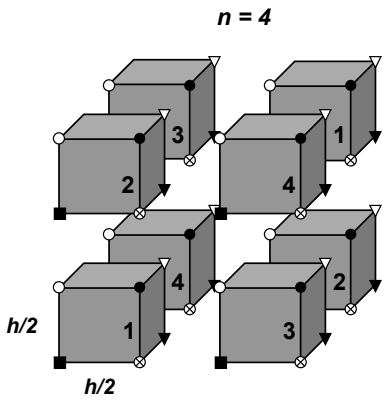

Fig. 7.3. Coarse spatial distribution of grid cells and anelastic functions. The number on a cell face indicates the relaxation frequency of the anelastic functions localized in the cell. For example, grid cell 1 contains $\xi_1^{xx}, \xi_1^{yy}, \xi_1^{zz}, \xi_1^{xy}, \xi_1^{yz}, \xi_1^{zx}$. Reproduced from Kristek and Moczo (2003).

from the neighboring positions are taken with properly weighting coefficients and averaged together at the grid point where the stress-tensor component is to be evaluated.

Such averaging is with material-independent anelastic functions introduced by Kristek and Moczo (2003), see section 4.4.7. This is because averaging of the material-independent anelastic functions does not introduce additional false averaging of the material properties. Note that this would be the case with the material-dependent anelastic functions introduced by Day and Minster (1984), Emmerich and Korn (1987), Carcione et al. (1988a,b) and Robertsson et al. (1994).

Kristek and Moczo (2003) also suggested an alternative coarse spatial distribution of the anelastic functions which only requires $n = 4$ relaxation frequencies, keeping the same memory requirements as in Day (1998), and Day and Bradley (2001). The distribution is shown in Fig. 7.3. Kristek and Moczo (2003) numerically demonstrated accuracy of their FD scheme with the material-independent anelastic functions and new coarse distribution of the anelastic functions.

7.3 Partly-staggered-grid Schemes

The partly-staggered grid, see Fig. 6.1, is something in-between the conventional and staggered grids. Its first-sight advantage compared to the staggered grid relates to incorporation anisotropy - all stress-tensor components are located at the same grid position. Thus no interpolation of particle velocities or strains is necessary. This was the reason why Magnier et al. (1994) used the partly-staggered grid to incorporate anisotropy. However, the partly-staggered grid was applied in seismology sooner. Andrews (1973) applied it in modeling the fault rupture propagation using his traction-at-split-node (TSN) method. Independently, Day (1977, 1982) also used this type of grid for his implementation of the TSN method (discrete fault method, DFM, in terminology of Day). Zhang (1997) used the partly-staggered grid in his 2D velocity-stress FD modeling. However, the developed schemes have not attracted much attention in seismic wave propagation

modeling.

Recently, the use of the partly-staggered grid was promoted by Saenger et al. (2000); see also Saenger and Bohlen (2004), Kruger et al. (2005), Saenger et al. (2005), Bohlen and Saenger (2006). They called the grid rotated staggered grid since they obtained the spatial FD operator by the rotation of the standard staggered-grid operator. The term 'rotated staggered grid' is somewhat unfortunate: assuming one spatial grid position for the stress tensor and another position for the displacement vector, it is easy to find a variety of FD schemes, in general several for a desired order of approximation. Only in one particular case can the spatial FD operator be obtained by the rotation of the standard staggered-grid operator. However, it is very easy to obtain the same scheme without explicit consideration of the rotation. In fact, the particular scheme used by Saenger et al. (2000) is a simple consequence of requirement of the same truncation error with respect to all coordinate axes.

As far as we know, the application of the partly-staggered grid to account for the material heterogeneity still has not been sufficiently analyzed. The schemes based on the partly-staggered grid also have specific numerical problems as, for example, presence of the hour-glass modes. While the schemes can be viewed as robust tool for complex anisotropic media, so far we cannot say that they are in general, say, better, than the staggered-grid schemes.

7.4 Optimally-accurate Schemes

7.4.1 Brief Historic Introduction

In the "staggered-grid schemes era" in seismology, Geller and Takeuchi (1995, 1998) and Takeuchi and Geller (2000) made a fundamental contribution to the theory of the FD schemes and developed their optimally accurate FD schemes in application to the Galerkin-type weak form of Strang and Fix (1973) and Geller and Ohminato (1994). In their schemes displacement is the sole dependent variable, as opposed to the staggered-grid schemes. The clever idea of Geller and Takeuchi (1995) was to minimize the error of the numerical solution first of all at eigenfrequencies (or resonant frequencies), that is at frequencies at which oscillatory motion of a linear mechanical system or finite volume of elastic continuum is naturally most amplified. Geller and Takeuchi (1995) used first-order Born theory and a normal mode expansion to obtain formal estimates of the relative error of the numerical solution and a general criterion for what they named optimally accurate operators. The criterion requires that the inner product of an eigenfunction and the net error of the discretized equation of motion should be approximately equal to zero when the operand is the eigenfunction and the frequency is equal to the corresponding eigenfrequency. The criterion can be used to derive optimally accurate operators without knowing the actual values of the eigenfrequencies and eigenfunctions. Geller and Takeuchi (1995) showed that in the case of a heterogeneous medium the criterion is the logical extension of the criterion to minimize grid dispersion of phase velocity for a homogeneous medium. Geller and Takeuchi (1998) used the criterion to develop optimally accurate 2^{nd}-order FDTD scheme for the elastic 1D case. Takeuchi and Geller (2000) then developed optimally accurate FDTD operators for the 2D and 3D cases. Mizutani (2002) developed a scheme capable to account for an arbitrary position of the material discontinuity in the grid.

The optimization yields implicit schemes. Geller and Takeuchi (1998) applied the predictor-corrector algorithm in order to avoid solving large systems of algebraic equations. Thus the

actual computational schemes are explicit.

Whereas optimally accurate FDTD schemes require at least twice the CPU time per grid point and time step compared to 2^{nd}-order staggered-grid FD schemes, they yield accuracy improvements on the order of 10 (for 1-D), 50 (for 2-D), or 100 (for 3-D). From this point of view they are cost-effective.

The optimally accurate schemes have not yet been widely used in practical FD modeling. The likely reasons are a) the theory might appear relatively complicated compared to that of the standard staggered-grid schemes, b) the fact that quantification and minimization of computational error have not heretofore been widely viewed as high priorities, c) inertia with respect to traditional approaches and the lack of user-friendly codes for optimally accurate schemes.

One (or the only one?) exception is study by Kristek and Moczo (2006) who numerically compared 2^{nd}-order conventional scheme, 4^{th}-order staggered-grid scheme and 2^{nd}-order optimally-accurate scheme. The comparison was restricted to 1D problem. Despite the simplicity of the problem and absence of phenomena arising in 2D or 3D problems, the results clearly indicated serious level of inaccuracy of the staggered-grid schemes compared to the optimally-accurate schemes.

We think that wider application of the optimally-accurate FD schemes in the future is very likely.

7.4.2 General Criterion for Optimally-accurate FD Operators

Here we very closely follow the exposition by Moczo et al. (2007) that is based on the work by Geller and his colleagues. Assume the equation of motion in the form

$$\left(\omega^2\, T - H\right)\vec{c} \;=\; -\vec{g}\,, \tag{7.57}$$

where ω is the angular frequency, T mass matrix, H stiffness matrix, $\vec{c}$ vector of expansion coefficients for the trial functions, $\vec{g}$ force vector,

$$\begin{aligned} T_{rs} \;&=\; \textstyle\int_V \left[\phi_i^{(r)}\right]^* \rho\, \phi_i^{(s)} \mathrm{d}V\,, \qquad H_{rs} \;=\; \textstyle\int_V \left[\phi_{i,j}^{(r)}\right]^* c_{ijkl}\, \phi_{k,l}^{(s)}\, \mathrm{d}V\,, \\ g_r \;&=\; \textstyle\int_V \left[\phi_i^{(r)}\right]^* f_i\, \mathrm{d}V\,, \end{aligned} \tag{7.58}$$

$\phi_i^{(r)}$ is the i^{th} component of the r^{th} trial function, and $*$ means complex conjugate quantity. The displacement is given by

$$u_i = \sum_r c_r\, \phi_i^{(r)}. \tag{7.59}$$

If an infinite trial function expansion were used, eq. (7.57) would yield exact solutions. The trial function expansion in practical computations will be finite. Consequently there will be some numerical error. The exact equation of motion can be formally written as

$$\left(\omega^2\, T^e - H^e\right)\vec{c}^{\,e} \;=\; -\vec{g}\,. \tag{7.60}$$

Assume the following relations between the numerical and exact quantities:

$$T \;=\; T^e + \delta T\,, \quad H \;=\; H^e + \delta H\,, \quad \vec{c} \;=\; \vec{c}^{\,e} + \vec{\delta c}\,, \tag{7.61}$$

Here δT, δH and $\vec{\delta c}$ are errors of the numerical operators and solution, respectively.

Consider normal modes. They satisfy equation

$$\left(\omega_p^2 \, T^e - H^e \right) \vec{c}_p \; = \; 0 \; , \tag{7.62}$$

where ω_p is an eigenfrequency of the p-th mode and $\vec{c}_p$ is the eigenvector. Assume orthonormalization in the form

$$\vec{c}_p^{\,*} \, H^e \, \vec{c}_q \; = \; \omega_p^2 \, \vec{c}_p^{\,*} \, T^e \, \vec{c}_q \; = \; \omega_p^2 \, \delta_{pq} \; . \tag{7.63}$$

Substituting eqs. (7.61) into the l.h.s. of eq. (7.57), replacing the r.h.s. of eq. (7.57) by the l.h.s. of eq. (7.60), and neglecting terms with products of errors (the first-order Born approximation) leads to

$$\left(\omega^2 \, T^e - H^e \right) \; \vec{\delta c} \; = \; - \left(\omega^2 \, \delta T - \delta H \right) \; \vec{c}^{\,e} . \tag{7.64}$$

Equation (7.64) enables to determine the error of the numerical solution, $\vec{\delta c}$, if the exact solution and errors of the operators, i.e., $\vec{c}^{\,e}$, δT and δH are known.

The solution of eq. (7.60) can be represented in terms of an eigenfunction expansion

$$\vec{c}^{\,e} \; = \; \sum_p \, d_p^e \, \vec{c}_p \; . \tag{7.65}$$

Substituting eq. (7.65) into eq. (7.60), and using eq. (7.63) leads to

$$d_p^e \; = \; \vec{c}_p^{\,*} \, \vec{g} \, / \, \left(\omega^2 - \omega_p^2 \right) . \tag{7.66}$$

The expansion coefficient d_p^e will be large, when ω is close to ω_p. Otherwise, it will be negligible.

The solution of eq. (7.64) can also be represented in terms of an eigenfunction expansion

$$\vec{\delta c} \; = \; \sum_p \, \delta d_p \, \vec{c}_p \; . \tag{7.67}$$

Substituting expansions (7.65) and (7.67) into eq. (7.64), and using eqs. (7.63) leads to

$$\delta d_p \; = \; - \sum_q \, \frac{\left(\omega^2 \, \vec{c}_p^{\,*} \, \delta T \, \vec{c}_q - \vec{c}_p^{\,*} \, \delta H \, \vec{c}_q \right) \, d_q^e}{\left(\omega^2 - \omega_p^2 \right)} \; . \tag{7.68}$$

The expansion coefficient δd_p will be large only when ω is close to ω_p. In such a case obviously only d_p^e will be large. Therefore, in the vicinity of $\omega = \omega_p$, the $q \neq p$ terms in eq. (7.68) can be neglected, i.e., the relative error of the numerical solution in the vicinity of ω_p will approximately be

$$\frac{\delta d_p}{d_p^e} \; = \; - \, \frac{\omega^2 \, \vec{c}_p^{\,*} \, \delta T \, \vec{c}_p - \vec{c}_p^{\,*} \, \delta H \, \vec{c}_p}{\omega^2 - \omega_p^2} \; . \tag{7.69}$$

It follows from eq. (7.69) that the relative error will in general greatly increase with $\omega \to \omega_p$. However, if the numerator of eq. (7.69) is also proportional to $\omega - \omega_p$, the relative error will remain approximately constant as $\omega \to \omega_p$. Such proportionality can be achieved if and only if

$$\omega_p^2 \, \vec{c}_p^{\,*} \, \delta T \, \vec{c}_p \; - \; \vec{c}_p^{\,*} \, \delta H \, \vec{c}_p \;\; \doteq \;\; 0 \tag{7.70}$$

for each mode. If eq. (7.70) is approximately satisfied, then eq. (7.69) can be simplified:

$$\left| \frac{\delta d_p}{d_p^e} \right| \;\approx\; \vec{c}_p^{\,*} \, \delta T \, \vec{c}_p \; . \tag{7.71}$$

This means that the relative error for a given grid can be reliably estimated in advance of calculation.

Geller and Takeuchi (1995) defined optimally accurate operators, say T' and H', as operators that satisfy eq. (7.70):

$$\vec{c}_p^{\,*} \, \left(\omega_p^2 \, \delta T' - \delta H' \right) \, \vec{c}_p \;\doteq\; 0 \; . \tag{7.72}$$

Substituting first two of eqs. (7.61) for operators T' and H' into eq. (7.72) and using eq. (7.62) leads to equivalent equation

$$\vec{c}_p^{\,*} \, (\, \omega_p^2 \, T' - H' \,) \, \vec{c}_p \;\doteq\; 0 \; . \tag{7.73}$$

Equation (7.72) will be satisfied if the leading term of the truncation error of the discretized equation is zero when the operand is an eigenfunction and the frequency is equal to the corresponding eigenfrequency, in other words if

$$(\, \omega_p^2 \, \delta T' - \delta H' \,) \, \vec{c}_p \;\doteq\; 0 \; . \tag{7.74}$$

On the other hand, however, it is not necessary for eq. (7.74) to be satisfied in order for eq. (7.72) to be satisfied, because even if the quantity on the l.h.s. of eq. (7.74) is non-zero, its inner product with $\vec{c}_p$ can still be approximately zero.

Consider equation

$$exact \; LHS \, (\omega, \, u) \;=\; \vec{f} \tag{7.75}$$

and such its discretization which gives

$$discretized \; LHS \, (\omega, \, u) \;=\; exact \; LHS \, (\omega, \, u) + \frac{h^2}{a} \, [\, exact \; LHS \, (\omega, \, u)]'' + \ldots \; , \tag{7.76}$$

where the primes denote spatial differentiation. The normal modes satisfy equation

$$exact \; LHS \, (\omega_p, \, u_p) \;=\; 0, \tag{7.77}$$

which implies

$$[\, exact \; LHS \, (\omega_p, \, u_p) \,]'' \;=\; 0 \; . \tag{7.78}$$

Considering normal modes in eq. (7.76), and substituting eqs. (7.77) and (7.78) into eq. (7.76) leads to

$$discretized\, LHS\,(\omega_p,\, u_p) \;\doteq\; 0\,. \tag{7.79}$$

Equation (7.79) corresponds to condition (7.73). The leading term of the truncation error of each FD approximation used to discretize the l.h.s. of eq. (7.75) has the same coefficient, h^2/a, and the displacement 2 times more differentiated than in the approximated term. Thus, we have an indication for constructing optimally accurate discretization.

7.4.3 Optimally-accurate Scheme for the 1D Equation of Motion

Consider for simplicity 1D equation of motion without a body-force term,

$$E \;=\; \rho\,\ddot{u} \;-C\,u_{,zz} \;=\; 0\,. \tag{7.80}$$

The conventional $2^{\rm nd}$-order (both in time and space) approximation to the equation is

$$\begin{aligned} FDE \;&=\; \rho\frac{1}{\Delta^2 t}\,[\,u(t+\Delta t,z)-2u(t,z)+u(t-\Delta t,z)\,] \\ &-\; C\,\frac{1}{h^2}\,[\,u(t,z+h)-2u(t,z)+u(t,z-h)\,] \;\doteq\; 0\,. \end{aligned} \tag{7.81}$$

The truncation error of the approximation is

$$\begin{aligned} \text{TrunError}\,\{FDE\} \;&=\; \text{TaylorExpansion}\,\{FDE\} \;-\; E \\ &=\; \frac{1}{12}\,\Delta^2 t\;\partial^{(2,0)}\left\{\rho u^{(2,0)}\right\} \\ &+\; \frac{1}{12}\;\;h^2\;\;\partial^{(0,2)}\left\{-C u^{(0,2)}\right\} \\ &+\; O\left(\Delta^4 t\right) \;+\; O\left(h^4\right), \end{aligned} \tag{7.82}$$

where

$$\partial^{(m,n)} \;=\; \frac{\partial^{m+n}}{\partial t^m\,\partial z^n}\,, \qquad u^{(m,n)} \;=\; \frac{\partial^{m+n}}{\partial t^m\,\partial z^n}\,u\,. \tag{7.83}$$

The structure of the leading term of the truncation error suggests that it might be possible to find such an approximation, say, OAFDE, for which the leading term of the truncation error would be identically equal to zero in the case of the normal modes:

$$\begin{aligned} \text{TrunError}\,\{OAFDE\} \;&=\; \text{TaylorExpansion}\,\{OAFDE\} \;-\; E \\ &=\; \frac{1}{12}\,\Delta^2 t\;\partial^{(2,0)}\left\{\rho u^{(2,0)}-C u^{(0,2)}\right\} \\ &+\; \frac{1}{12}\;\;h^2\;\;\partial^{(0,2)}\left\{\rho u^{(2,0)}-C u^{(0,2)}\right\} \\ &+\; O\left(\Delta^4 t\right) \;+\; O\left(h^4\right). \end{aligned} \tag{7.84}$$

Expressions in braces are the l.h.s. of the equation of motion for the normal modes in the homogeneous medium. The desired structure of the truncation error can be achieved only if grid

positions shifted in both time and space from the centered position are involved. As the simplest possible approach, relative to the standard centered approximation, is to try to approximate e.g. time derivative as some weighted average of the centered time derivatives at three spatial positions, $z_I - h$, z_I and $z_I + h$. Similarly, the spatial derivative should be the same weighted average of centered spatial derivatives at three time levels, $t_m - \Delta t$, t_m and $t_m + \Delta t$. This means that the desired operator should involve the following displacement values:

$$u_I^m(p,q) \;=\; u\,[\,t_m + (2-p)\Delta t,\; z_I + (q-2)h\,]\,; \quad p\,,q \;\in \{1,2,3\}\,, \tag{7.85}$$

or, in the matrix form,

$$\mathbf{u}_I^m \;=\; \begin{bmatrix} u(t_m+\Delta t\;,z_I-h) & u(t_m+\Delta t\;,z_I) & u(t_m+\Delta t\;,z_I+h) \\ u(t_m\qquad\;\;,z_I-h) & u(t_m\qquad\;\;,z_I) & u(t_m\qquad\;\;,z_I+h) \\ u(t_m-\Delta t\;,z_I-h) & u(t_m-\Delta t\;,z_I) & u(t_m-\Delta t\;,z_I+h) \end{bmatrix}. \tag{7.86}$$

For brevity we will use grid indices. Then eq. (7.86) can be written as

$$\mathbf{u}_I^m \;=\; \begin{bmatrix} u_{I-1}^{m+1} & u_I^{m+1} & u_{I+1}^{m+1} \\ u_{I-1}^{m} & u_I^{m} & u_{I+1}^{m} \\ u_{I-1}^{m-1} & u_I^{m-1} & u_{I+1}^{m-1} \end{bmatrix}. \tag{7.87}$$

Define time and spatial FD operators $\mathbf{A}_I^m$ and $\mathbf{K}_I^m$ which can be written in the matrix form as

$$\mathbf{A}_I^m \;=\; \frac{\rho}{\Delta^2 t} \begin{bmatrix} a_{I-1}^{m+1} & a_I^{m+1} & a_{I+1}^{m+1} \\ a_{I-1}^{m} & a_I^{m} & a_{I+1}^{m} \\ a_{I-1}^{m-1} & a_I^{m-1} & a_{I+1}^{m-1} \end{bmatrix} \tag{7.88}$$

and

$$\mathbf{K}_I^m \;=\; \frac{C}{h^2} \begin{bmatrix} k_{I-1}^{m+1} & k_I^{m+1} & k_{I+1}^{m+1} \\ k_{I-1}^{m} & k_I^{m} & k_{I+1}^{m} \\ k_{I-1}^{m-1} & k_I^{m-1} & k_{I+1}^{m-1} \end{bmatrix}. \tag{7.89}$$

Then the FD approximation to the equation of motion at time level m and spatial position I can be written in the form

$$OAFDE \;=\; [\,A_I^m(p,q) - K_I^m(p,q)\,]\;u_I^m(p,q) \;\doteq\; 0\,; \quad p,\; q \in \{1,2,3\}\,, \tag{7.90}$$

where p is the time summation index and q the spatial summation index. The summation convention is assumed in eq. (7.90), that is, no matrix multiplication is applied. Equation (7.90) means that we have to determine 18 unknown elements of operators $\mathbf{A}_I^m$ and $\mathbf{K}_I^m$ in order to find the desired FD approximation to the equation of motion.

It can be shown that the structure of the Taylor expansion of $OAFDE$ is such that only 9 coefficients are independent. This is due to the fact that we use 9 space-time positions in approximation (7.90). Because we have freedom in choosing for which 9 coefficients we impose

conditions, in our problem we naturally take independent coefficients at $u^{(j,\,l)}$; $j \in \{0,1,2\}$, $l \in \{0,1,2\}$. In

$$\text{TaylorExpansion}\{OAFDE\} - E \tag{7.91}$$

additional terms appear in coefficients at $u^{(2,\,0)}$ and $u^{(0,\,2)}$ due to inclusion of E. Because, however, they are known, being proportional to density ρ and modulus C, the structure of independence of the expansion coefficients does not change.

The desired structure of the truncation error, see eq. (7.84), implies conditions also for coefficients at $u^{(4,\,0)}$, $u^{(2,\,2)}$ and $u^{(0,\,4)}$. Given the explained structure of coefficients we, however, do not need to impose conditions for coefficients at $u^{(4,\,0)}$ and $u^{(0,\,4)}$. Thus we have the 18 following conditions, that is, equations for determination of the 18 unknown elements of operators $\mathbf{A}_I^m$ and $\mathbf{K}_I^m$:

$$\begin{aligned} coef\text{TE\_}u^{(j,\,l)} &= 0\,;\; j \in \{0,1,2\}\,,\; l \in \{0,1,2\}\,,\; (j,l) \neq (2,2)\;, \\ coef\text{TE\_}u^{(2,\,2)} &= \frac{h^2}{12}\;\rho - \frac{\Delta^2 t}{12}\;C\,, \\ \frac{\Delta^2 t}{\rho}\;\mathbf{A}_I^m &= \left[\frac{h^2}{C}\;\mathbf{K}_I^m\right]^T\;. \end{aligned} \tag{7.92}$$

Here we used abbreviation TE for the Taylor expansion. The last condition means that matrix on the l.h.s. is the transpose matrix to matrix at the r.h.s., see eqs. (7.88) and (7.89). The latter is due to our assumption that the time derivative in approximation (7.90) is averaged over time derivatives at three spatial positions in the same way as is the spatial derivative averaged over spatial derivatives at three time levels.

Solving system of algebraic equations (7.92) we obtain

$$\mathbf{A}_I^m = \frac{\rho}{12\,\Delta^2 t}\begin{bmatrix} 1 & 10 & 1 \\ -2 & -20 & -2 \\ 1 & 10 & 1 \end{bmatrix} \tag{7.93}$$

and

$$\mathbf{K}_I^m = \frac{C}{12\,h^2}\begin{bmatrix} 1 & -2 & 1 \\ 10 & -20 & 10 \\ 1 & -2 & 1 \end{bmatrix}\;. \tag{7.94}$$

It is easy to check that approximation (7.90) with operators $\mathbf{A}_I^m$ and $\mathbf{K}_I^m$ defined by eqs. (7.93) and (7.94) has the desired truncation error defined by eq. (7.84). As a consequence, approximation (7.90) becomes in fact 4^{th}-order accurate in the case of normal modes. The approximation satisfies Geller and Takeuchi's criterion for the optimally-accurate operators. In this sense we can call approximation (7.90) with operators (7.93) and (7.94) the optimally-accurate FD approximation.

If we replace true displacement values $u(p,q)$, eq. (7.87), by the corresponding discrete displacement values $U(p,q)$ in eq. (7.90) we obtain the optimally-accurate FD scheme. Then

the optimally-accurate scheme can be written in a, say, full form,

$$\begin{aligned}
&\frac{\rho}{12\,\Delta^2 t}\,\Big[\quad U_{I-1}^{m+1}-2\,U_{I-1}^{m}\;+U_{I-1}^{m-1}\\
&\qquad +10\big(\;U_{I}^{m+1}-2\,U_{I}^{m}\quad+U_{I}^{m-1}\;\big)\\
&\qquad +\quad U_{I+1}^{m+1}-2\,U_{I+1}^{m}\;+U_{I+1}^{m-1}\;\Big]\\
&-\frac{C}{12\,h^2}\,\Big[\quad U_{I-1}^{m+1}-2\,U_{I}^{m+1}+U_{I+1}^{m+1}\\
&\qquad +10\big(\;U_{I-1}^{m}\;-2\,U_{I}^{m}\quad+U_{I+1}^{m}\;\big)\\
&\qquad +\quad U_{I-1}^{m-1}-2\,U_{I}^{m-1}+U_{I+1}^{m-1}\;\Big]\;=\;0\,.
\end{aligned}\tag{7.95}$$

For a comparison, operators of the conventional FD scheme written in the form of eq. (7.90) are

$$\mathbf{convA}_I^m\;=\;\frac{\rho}{\Delta^2 t}\begin{bmatrix}0&1&0\\0&-2&0\\0&1&0\end{bmatrix}\tag{7.96}$$

and

$$\mathbf{convK}_I^m\;=\;\frac{C}{h^2}\begin{bmatrix}0&0&0\\1&-2&1\\0&0&0\end{bmatrix}\,.\tag{7.97}$$

The comparison of the optimally-accurate scheme (7.95) with the conventional scheme is clear – only displacement values in parentheses (in the $2^{\rm nd}$ and $5^{\rm th}$ rows) of the optimally-accurate scheme appear in the conventional scheme.

It is worth to note one interesting aspect of the relation between the conventional and optimally accurate operator. Consider, e.g., displacement $u(t,z)$. Formally we can approximate its value with the $2^{\rm nd}$-order accuracy:

$$\begin{aligned}
u(t,z)\;&=\;\frac{1}{12}\,[\,u(t,z+h)+10\,u(t,z)+u(t,z-h)\,]\\
&\quad+\;\frac{h^2}{12}\;u^{(0,2)}(t,z)\;+\;O(h^4)\,.
\end{aligned}\tag{7.98}$$

The r.h.s. of the first row of eq. (7.98) can be called the identity-operator approximation. Then the first row in the optimally-accurate operator $\mathbf{A}_I^m$, eq. (7.93), can be viewed as the identity-operator approximation to a single displacement value $u(t+\Delta t,z)$ in the conventional scheme, see eq. (7.96). Similarly, the $2^{\rm nd}$ and $3^{\rm rd}$ rows in the optimally-accurate operator $\mathbf{A}_I^m$ correspond to the identity-operator approximations to displacement values $u(t,z)$ and $u(t-\Delta t,z)$, respectively.

It is obvious that the optimally-accurate scheme is implicit. Geller and Takeuchi (1998) used a predictor-corrector scheme based on the first-order Born approximation in order to avoid solving a large system of linear equations at each time step.

7.4.4 Predictor-corrector Algorithm for Solving Optimally-accurate Scheme for the 1D Equation of Motion

Consider equation

$$(\mathbf{convA}_I^m - \mathbf{convK}_I^m) \cdot \mathbf{convU}_I^m \;=\; 0\,, \tag{7.99}$$

where dot means inner product, $\mathbf{convA}_I^m$ and $\mathbf{convK}_I^m$ are defined by eqs. (7.88) and (7.89), and $\mathbf{convU}_I^m$ has the same structure as $\mathbf{u}_I^m$ defined by eq. (7.87).

System of equations, see eq. (7.90), we want to solve is

$$(\mathbf{A}_I^m - \mathbf{K}_I^m) \cdot \mathbf{U}_I^m \;=\; 0\,. \tag{7.100}$$

Define

$$\begin{aligned} \delta\mathbf{A}_I^m &= \mathbf{A}_I^m - \mathbf{convA}_I^m\,, \\ \delta\mathbf{K}_I^m &= \mathbf{K}_I^m - \mathbf{convK}_I^m\,, \\ \delta\mathbf{U}_I^m &= \mathbf{U}_I^m - \mathbf{convU}_I^m\,. \end{aligned} \tag{7.101}$$

Substituting eqs. (7.101) into eq. (7.100) and using the first-order Born approximation we obtain

$$(\mathbf{convA}_I^m - \mathbf{convK}_I^m) \cdot \delta\mathbf{U}_I^m \;=\; -\,(\delta\mathbf{A}_I^m - \delta\mathbf{K}_I^m) \cdot \mathbf{convU}_I^m\,. \tag{7.102}$$

Then the predictor-corrector algorithm for solving optimally-accurate scheme (7.100) for time level $m+1$ is as follows:

1. Find solution $convU_I^{m+1}$ from the conventional scheme (7.99), that is, find displacement at time level $m+1$ at spatial position I. Apply at all spatial positions.

At each spatial position:

2. Evaluate the r.h.s. of eq. (7.102).

3. Because at two previous time steps corrected displacement values were calculated, the elements of $\delta\mathbf{U}_I^m$ corresponding to time levels $m-1$ and m are assumed equal to zero. Then it is easy to obtain δU_I^{m+1}, that is the element of matrix $\delta\mathbf{U}_I^m$ corresponding to time level $m+1$ and spatial position I.

4. $U_I^{m+1} \;=\; convU_I^{m+1} + \delta U_I^{m+1}$

5. The value of U_I^{m+1} is assigned to $convU_I^{m+1}$: $U_I^{m+1} \;\rightarrow\; convU_I^{m+1}$

6. $m+1 \;\rightarrow\; m$, $\;m \;\rightarrow\; m-1$, continue with step 1.

7.4.5 Optimally-accurate Scheme - the 3D Problem

For simplicity we consider here the 3D homogeneous isotropic medium. From eq. (5.4) for the heterogeneous isotropic medium we specify the following equation of motion for the homogeneous medium:

$$\rho\, \ddot{u}_i \;-\; (\lambda+\mu)\, u_{k,ki} \;-\mu\, u_{i,kk} \;-\, f_i \;=\; 0\;, \qquad i,k \in \{x,y,z\}\,. \tag{7.103}$$

Normal modes are solutions of the equation without the body-force term,

$$\rho\, \ddot{u}_i \;-\; (\lambda+\mu)\, u_{k,ki} \;-\mu\, u_{i,kk} \;=\; 0\;, \qquad i,k \in \{x,y,z\}\,. \tag{7.104}$$

Define

$$E_x = \\ \left[\rho\partial_t^2 - (\lambda+2\mu)\partial_x^2 - \mu\partial_y^2 - \mu\partial_z^2\right] u_x - (\lambda+\mu)\partial_y\partial_x\, u_y - (\lambda+\mu)\partial_z\partial_x\, u_z\,, \tag{7.105}$$

$$E_y = \\ -(\lambda+\mu)\partial_y\partial_x\, u_x + \left[\rho\partial_t^2 - \mu\partial_x^2 - (\lambda+2\mu)\partial_y^2 - \mu\partial_z^2\right] u_y - (\lambda+\mu)\partial_z\partial_y\, u_z\,, \tag{7.106}$$

$$E_z = \\ -(\lambda+\mu)\partial_z\partial_x\, u_x - (\lambda+\mu)\partial_y\partial_z\, u_y + \left[\rho\partial_t^2 - \mu\partial_x^2 - \mu\partial_y^2 - (\lambda+2\mu)\partial_z^2\right] u_z\,. \tag{7.107}$$

Then the vectorial eq. (7.104) can be written in the form of three equations:

$$E_i \;=\; 0\;, \qquad i \in \{x,y,z\}\,. \tag{7.108}$$

As in the case of the 1D problem we want to define a desired structure of the truncation error. While the desired structure in the 1D case was relatively easy to see and understand, the 3D problem is more complicated. Therefore it can be useful to look closely at the structure of $E_i\,,\; i \in \{x,y,z\}$. It is easy to see that E_x, E_y and E_z have a common structure:

$$E_x \;=\; X_2\, u_x \;+\; X_{xy}\, u_y \;+\; X_{xz}\, u_z\;, \tag{7.109}$$

$$E_y \;=\; Y_{yx}\, u_x \;+\; Y_2 \;\; u_y \;+\; Y_{yz}\, u_z\;, \tag{7.110}$$

$$E_z \;=\; Z_{zx}\, u_x \;+\; Z_{zy}\, u_y \;+\; Z_2 \;\; u_z\;, \tag{7.111}$$

where subscript '2' stands for a linear combination of the non-mixed second derivatives and the other subscripts directly indicate spatial mixed derivatives. The common structure means that we can first find optimally accurate approximation to, e.g., E_x, and approximations to E_y and E_z will be then derived analogously.

Therefore, focus now at E_x. Each of its operators X_2, X_{xy} and X_{xz} acts only on one component of the displacement vector. Consequently, each of the operators will be FD approximated separately. In the 1D problem we approximated 2^{nd} non-mixed derivatives. Here we have to find approximation also to the 2^{nd} mixed derivatives.

A FD approximation to E_x can written in the form

$$FDE_x \;=\; FDX_2\, u_x \;+\; FDX_{xy}\, u_y \;+\; FDX_{xz}\, u_z\,. \tag{7.112}$$

As in the 1D case, the truncation error is then

$$\text{TrunError}\{FDE_x\} \;=\; \text{TaylorExpansion}\{FDE_x\} \;-\; E_x \tag{7.113}$$

and also

$$\begin{aligned}\text{TrunError}\{FDE_x\} \;&=\; \text{TaylorExpansion}\{FDX_2\;u_x\} \;-\; X_2\;u_x \;+\\ &+\; \text{TaylorExpansion}\{FDX_{xy}\,u_y\} \;-\; X_{xy}\,u_y \;+\\ &+\; \text{TaylorExpansion}\{FDX_{xz}\,u_z\} \;-\; X_{xz}\,u_z \;=\\ &=\; \text{TrunError}\{FDX_2\;u_x\} \;+\\ &+\; \text{TrunError}\{FDX_{xy}\,u_y\} \;+\\ &+\; \text{TrunError}\{FDX_{xz}\,u_z\}\,.\end{aligned} \tag{7.114}$$

In analogy with the 1D problem we can assume

$$\begin{aligned}\text{TrunError}\{FDX_2u_x\} \;&=\; \tfrac{1}{12}\left[\,\Delta^2 t\,\partial_t^2 \;+\; h^2\left(\,\partial_x^2 \;+\; \partial_y^2 \;+\; \partial_z^2\,\right)\right]\;X_2u_x \;+\\ &+\; O(\Delta^p t\cdot h^q)\,;\; p+q\geq 4\,.\end{aligned} \tag{7.115}$$

If we now assume

$$\begin{aligned}\text{TrunError}\{FDX_{xy}\,u_y\} \;&=\; \tfrac{1}{12}\left[\,\Delta^2 t\,\partial_t^2 \;+\; h^2\left(\,\partial_x^2 \;+\; \partial_y^2 \;+\; \partial_z^2\,\right)\right]\;X_{xy}\,u_y \;+\\ &+\; O(\Delta^p t\cdot h^q)\,;\; p+q\geq 4\end{aligned} \tag{7.116}$$

and

$$\begin{aligned}\text{TrunError}\{FDX_{xz}\,u_z\} \;&=\; \tfrac{1}{12}\left[\,\Delta^2 t\,\partial_t^2 \;+\; h^2\left(\,\partial_x^2 \;+\; \partial_y^2 \;+\; \partial_z^2\,\right)\right]\;X_{xz}\,u_z \;+\\ &+\; O(\Delta^p t\cdot h^q)\,;\; p+q\geq 4\,,\end{aligned} \tag{7.117}$$

then the total truncation error will be

$$\begin{aligned}\text{TrunError}\{FDE_x\} \;&=\; \tfrac{1}{12}\left[\,\Delta^2 t\,\partial_t^2 \;+\; h^2\left(\,\partial_x^2 \;+\; \partial_y^2 \;+\; \partial_z^2\,\right)\right]\;E_x \;+\\ &+\; O(\Delta^p t\cdot h^q)\,;\; p+q\geq 4\,,\end{aligned} \tag{7.118}$$

which, in fact, is what we could intuitively assume from the very beginning: vanishing of the lowest terms in the truncation error in the case of normal modes. This is the condition we applied for the 1D optimally-accurate operator.

We will now find an approximation to $X_2\;u_x$, that is $FDX_2\;u_x$. A natural choice for the space-time positions is analogous to the choice in the 1D problem. In such a case, the desired operator should involve the following displacement values:

$$\begin{aligned}&[u_x]^m_{I,J,K}(p,q,r,s) \;=\\ &\quad u_x\left[\,t_m+(p-2)\Delta t,\; x_I+(q-2)h,\; y_J+(r-2)h,\; z_K+(s-2)h\,\right]\;;\\ &\qquad\qquad\qquad\qquad\qquad\qquad p,q,r,s\in\{1,2,3\}\,.\end{aligned} \tag{7.119}$$

Symmetry of the space-time positions with respect to approximation position $(t_m,\; x_I,\; y_J,\; z_K)$ enables to achieve the desired order of approximation using minimum number of the space-time positions. Then the FD approximation can be written in the form (compare with eq. 7.90)

$$FDX_2\;u_x \;=\; G^m_{I,J,K}(p,q,r,s)\;\;[u_x]^m_{I,J,K}(p,q,r,s)\,. \tag{7.120}$$

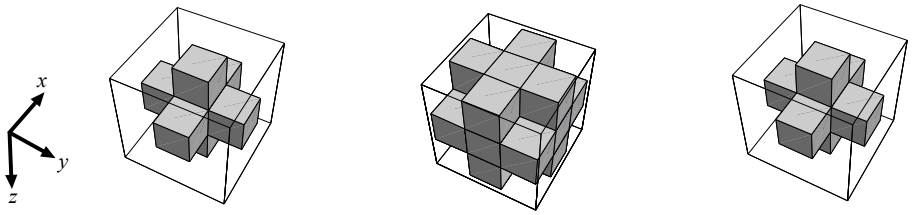

Fig. 7.4. Structure of the nonzero coefficients in $\mathbf{G}^m_{I,J,K}$.

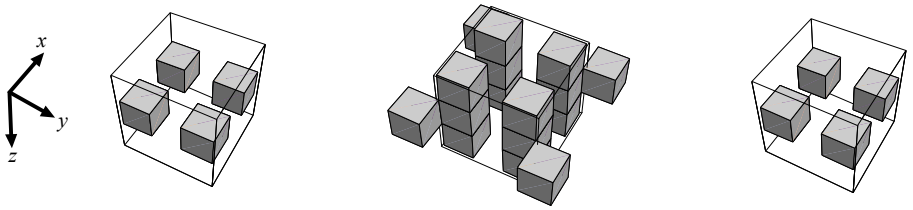

Fig. 7.5. Structure of the nonzero coefficients in $\mathbf{H}^m_{I,J,K}$.

The approximation means that we have to determine 81 unknown coefficients of operator $\mathbf{G}^m_{I,J,K}$. The coefficients can be determined from a system of equations obtained by imposing conditions on coefficients in

$$\text{TaylorExpansion}\left\{FDX_2\, u_x\right\} \;-\; X_2\, u_x \tag{7.121}$$

according to the desired structure of the truncation error, eq. (7.115), compare with the 1D problem. As a result, only 7+19+7 = 33 of the total number of 81 coefficients are found nonzero. The nonzero coefficients are illustrated in Fig. 7.4.

For finding approximation to $X_{xy}\, u_y$, that is $FDX_{xy}\, u_y$, it is not enough to use space-time positions defined by eq. (7.119), if the desired truncation error, eq. (7.116), is to be achieved. We have to use additional space-time positions. The 4+16+4 = 24 nonzero coefficients in a corresponding discrete operator, say, $\mathbf{H}^m_{I,J,K}$, are illustrated in Fig. 7.5.

Approximation to $X_{xz}\, u_z$, that is $FDX_{xz}\, u_z$, can be found analogously to the previous case.

The complete optimally-accurate FD scheme for the considered 3D problem can be written in the concise form:

$$
\begin{aligned}
&\frac{\rho}{12\Delta t^2}\ (6\ L^{\bullet}_{\circ\circ\circ} + L^{\bullet}_{-\circ\circ} + L^{\bullet}_{+\circ\circ} + L^{\bullet}_{\circ-\circ} + L^{\bullet}_{\circ+\circ} + L^{\bullet}_{\circ\circ-} + L^{\bullet}_{\circ\circ+})\ U \\
-&\frac{\lambda+2\mu}{12\Delta x^2}\ (6\ L^{\circ}_{\bullet\circ\circ} + L^{-}_{\bullet\circ\circ} + L^{+}_{\bullet\circ\circ} + L^{\circ}_{\bullet-\circ} + L^{\circ}_{\bullet+\circ} + L^{\circ}_{\bullet\circ-} + L^{\circ}_{\bullet\circ+}\ )\ U \\
-&\frac{\mu}{12\Delta y^2}\ (6\ L^{\circ}_{\circ\bullet\circ} + L^{-}_{\circ\bullet\circ} + L^{+}_{\circ\bullet\circ} + L^{\circ}_{-\bullet\circ} + L^{\circ}_{+\bullet\circ} + L^{\circ}_{\circ\bullet-} + L^{\circ}_{\circ\bullet+}\ )\ U \\
-&\frac{\mu}{12\Delta z^2}\ (6\ L^{\circ}_{\circ\circ\bullet} + L^{-}_{\circ\circ\bullet} + L^{+}_{\circ\circ\bullet} + L^{\circ}_{-\circ\bullet} + L^{\circ}_{+\circ\bullet} + L^{\circ}_{\circ-\bullet} + L^{\circ}_{\circ+\bullet}\ )\ U \\
-&\frac{\lambda+\mu}{96\Delta x\Delta y}\ (10\ L^{\circ}_{\bullet\bullet\circ} - \bar{L}^{\circ}_{\bullet\bullet\circ} + 2\ L^{\circ}_{\bullet\bullet-} + 2\ L^{\circ}_{\bullet\bullet+} - 2\ L^{-}_{\bullet\bullet\circ} - 2\ L^{+}_{\bullet\bullet\circ}\ )\ V \\
-&\frac{\lambda+\mu}{96\Delta x\Delta z}\ (10\ L^{\circ}_{\bullet\circ\bullet} - \bar{L}^{\circ}_{\bullet\circ\bullet} + 2\ L^{\circ}_{\bullet-\bullet} + 2\ L^{\circ}_{\bullet+\bullet} - 2\ L^{-}_{\bullet\circ\bullet} - 2\ L^{+}_{\bullet\circ\bullet}\ )\ W\ =\ F^{x,m}_{J,K,L}\ ,
\end{aligned}
\tag{7.122}
$$

$$
\begin{aligned}
-&\frac{\lambda+\mu}{96\Delta x\Delta y}\ (10\ L^{\circ}_{\bullet\bullet\circ} - \bar{L}^{\circ}_{\bullet\bullet\circ} + 2\ L^{\circ}_{\bullet\bullet-} + 2\ L^{\circ}_{\bullet\bullet+} - 2\ L^{-}_{\bullet\bullet\circ} - 2\ L^{+}_{\bullet\bullet\circ}\ )\ U \\
+&\frac{\rho}{12\Delta t^2}\ (6\ L^{\bullet}_{\circ\circ\circ} + L^{\bullet}_{-\circ\circ} + L^{\bullet}_{+\circ\circ} + L^{\bullet}_{\circ-\circ} + L^{\bullet}_{\circ+\circ} + L^{\bullet}_{\circ\circ-} + L^{\bullet}_{\circ\circ+})\ V \\
-&\frac{\mu}{12\Delta x^2}\ (6\ L^{\circ}_{\bullet\circ\circ} + L^{-}_{\bullet\circ\circ} + L^{+}_{\bullet\circ\circ} + L^{\circ}_{\bullet-\circ} + L^{\circ}_{\bullet+\circ} + L^{\circ}_{\bullet\circ-} + L^{\circ}_{\bullet\circ+}\ )\ V \\
-&\frac{\lambda+2\mu}{12\Delta y^2}\ (6\ L^{\circ}_{\circ\bullet\circ} + L^{-}_{\circ\bullet\circ} + L^{+}_{\circ\bullet\circ} + L^{\circ}_{-\bullet\circ} + L^{\circ}_{+\bullet\circ} + L^{\circ}_{\circ\bullet-} + L^{\circ}_{\circ\bullet+}\ )\ V \\
-&\frac{\mu}{12\Delta z^2}\ (6\ L^{\circ}_{\circ\circ\bullet} + L^{-}_{\circ\circ\bullet} + L^{+}_{\circ\circ\bullet} + L^{\circ}_{-\circ\bullet} + L^{\circ}_{+\circ\bullet} + L^{\circ}_{\circ-\bullet} + L^{\circ}_{\circ+\bullet}\ )\ V \\
-&\frac{\lambda+\mu}{96\Delta x\Delta z}\ (10\ L^{\circ}_{\bullet\circ\bullet} - \bar{L}^{\circ}_{\bullet\circ\bullet} + 2\ L^{\circ}_{\bullet-\bullet} + 2\ L^{\circ}_{\bullet+\bullet} - 2\ L^{-}_{\bullet\circ\bullet} - 2\ L^{+}_{\bullet\circ\bullet}\ )\ W\ =\ F^{y,m}_{J,K,L}\ ,
\end{aligned}
\tag{7.123}
$$

$$
\begin{aligned}
-&\frac{\lambda+\mu}{96\Delta x\Delta y}\ (10\ L^{\circ}_{\bullet\bullet\circ} - \bar{L}^{\circ}_{\bullet\bullet\circ} + 2\ L^{\circ}_{\bullet\bullet-} + 2\ L^{\circ}_{\bullet\bullet+} - 2\ L^{-}_{\bullet\bullet\circ} - 2\ L^{+}_{\bullet\bullet\circ}\ )\ U \\
-&\frac{\lambda+\mu}{96\Delta x\Delta z}\ (10\ L^{\circ}_{\bullet\circ\bullet} - \bar{L}^{\circ}_{\bullet\circ\bullet} + 2\ L^{\circ}_{\bullet-\bullet} + 2\ L^{\circ}_{\bullet+\bullet} - 2\ L^{-}_{\bullet\circ\bullet} - 2\ L^{+}_{\bullet\circ\bullet}\ )\ V \\
+&\frac{\rho}{12\Delta t^2}\ (6\ L^{\bullet}_{\circ\circ\circ} + L^{\bullet}_{-\circ\circ} + L^{\bullet}_{+\circ\circ} + L^{\bullet}_{\circ-\circ} + L^{\bullet}_{\circ+\circ} + L^{\bullet}_{\circ\circ-} + L^{\bullet}_{\circ\circ+})\ W \\
-&\frac{\mu}{12\Delta x^2}\ (6\ L^{\circ}_{\bullet\circ\circ} + L^{-}_{\bullet\circ\circ} + L^{+}_{\bullet\circ\circ} + L^{\circ}_{\bullet-\circ} + L^{\circ}_{\bullet+\circ} + L^{\circ}_{\bullet\circ-} + L^{\circ}_{\bullet\circ+}\ )\ W \\
-&\frac{\mu}{12\Delta y^2}\ (6\ L^{\circ}_{\circ\bullet\circ} + L^{-}_{\circ\bullet\circ} + L^{+}_{\circ\bullet\circ} + L^{\circ}_{-\bullet\circ} + L^{\circ}_{+\bullet\circ} + L^{\circ}_{\circ\bullet-} + L^{\circ}_{\circ\bullet+}\ )\ W \\
-&\frac{\lambda+2\mu}{12\Delta z^2}\ (6\ L^{\circ}_{\circ\circ\bullet} + L^{-}_{\circ\circ\bullet} + L^{+}_{\circ\circ\bullet} + L^{\circ}_{-\circ\bullet} + L^{\circ}_{+\circ\bullet} + L^{\circ}_{\circ-\bullet} + L^{\circ}_{\circ+\bullet}\ )\ W\ =\ F^{z,m}_{J,K,L}\ ,
\end{aligned}
\tag{7.124}
$$

where

$$\circ = 0, \qquad + = +1, \qquad - = -1.$$

Suboperators in eqs. (7.122) – (7.124) are defined by relations (7.125) – (7.127). The full circle indicates type of derivative. The full circle at the left / central / right position in the lower index means second x - derivative / y - derivative / z - derivative, respectively. The full circle in

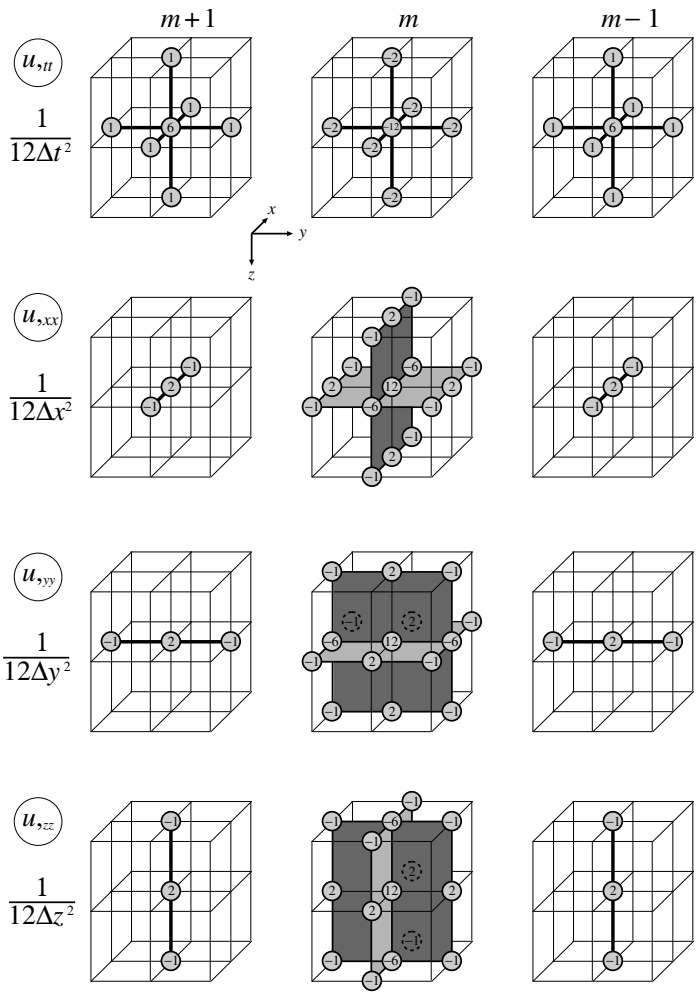

Fig. 7.6. Visualisation of the non-mixed optimally-accurate second derivative operators.

the upper index means second time derivative. Two full circles in the lower index mean second mixed spatial derivatives.

$$
\begin{aligned}
L^p_{\bullet rs}U &= U^{m+p}_{I-1,J+r,K+s} - 2U^{m+p}_{I,J+r,K+s} + U^{m+p}_{I+1,J+r,K+s}\ , \\
L^p_{q\bullet s}U &= U^{m+p}_{I+q,J-1,K+s} - 2U^{m+p}_{I+q,J,K+s} + U^{m+p}_{I+q,J+1,K+s}\ , \\
L^p_{qr\bullet}U &= U^{m+p}_{I+q,J+r,K-1} - 2U^{m+p}_{I+q,J+r,K} + U^{m+p}_{I+q,J+r,K+1}\ , \\
L^\bullet_{qrs}U &= U^{m-1}_{I+q,J+r,K+s} - 2U^{m}_{I+q,J+r,K+s} + U^{m+1}_{I+q,J+r,K+s}\ ,
\end{aligned}
\tag{7.125}
$$

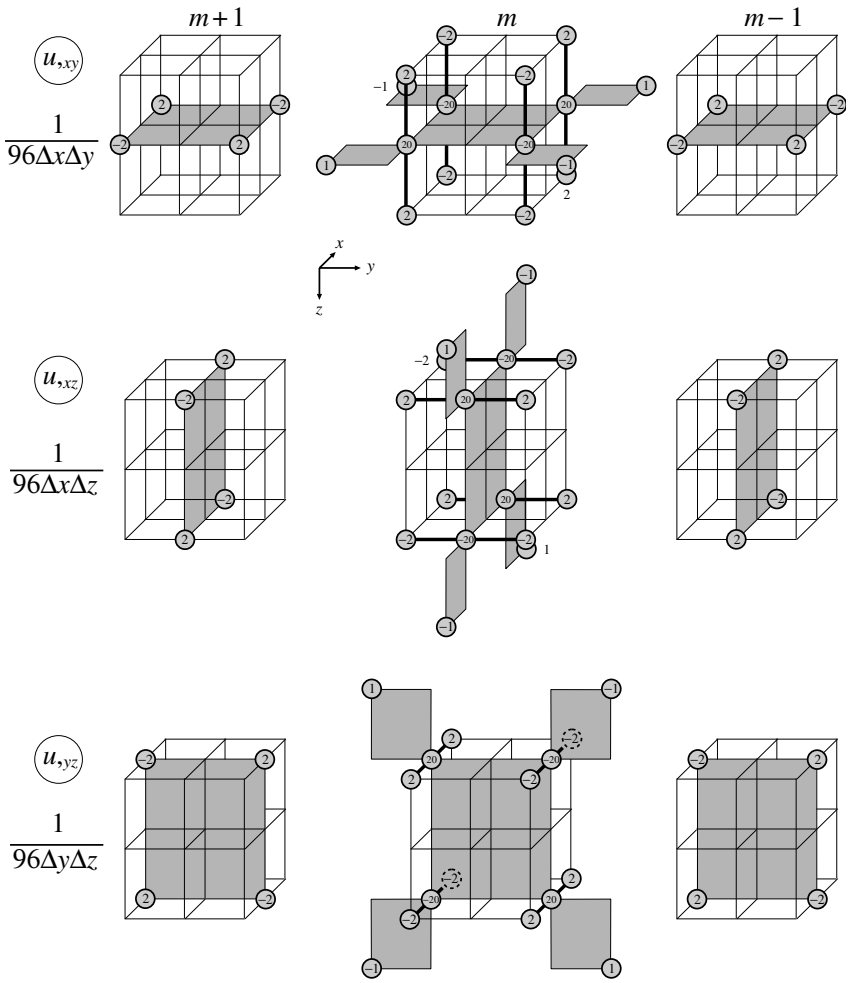

Fig. 7.7. Visualisation of the mixed optimally-accurate second derivative operators.

$$
\begin{aligned}
L^p_{\bullet\bullet s}U &= -U^{m+p}_{I-1,J-1,K+s} + U^{m+p}_{I-1,J+1,K+s} + U^{m+p}_{I+1,J-1,K+s} - U^{m+p}_{I+1,J+1,K+s}\ ,\\
L^p_{\bullet r\bullet}U &= -U^{m+p}_{I-1,J+r,K-1} + U^{m+p}_{I-1,J+r,K+1} + U^{m+p}_{I+1,J+r,K-1} - U^{m+p}_{I+1,J+r,K+1}\ ,\\
L^p_{q\bullet\bullet}U &= -U^{m+p}_{I+q,J-1,K-1} + U^{m+p}_{I+q,J+1,K-1} + U^{m+p}_{I+q,J-1,K+1} - U^{m+p}_{I+q,J+1,K+1}\ ,
\end{aligned}
\tag{7.126}
$$

$$
\begin{aligned}
\bar{L}^p_{\bullet\bullet s}U &= -U^{m+p}_{I-2,J-2,K+s} + U^{m+p}_{I-2,J+2,K+s} + U^{m+p}_{I+2,J-2,K+s} - U^{m+p}_{I+2,J+2,K+s}\ ,\\
\bar{L}^p_{\bullet r\bullet}U &= -U^{m+p}_{I-2,J+r,K-2} + U^{m+p}_{I-2,J+r,K+2} + U^{m+p}_{I+2,J+r,K-2} - U^{m+p}_{I+2,J+r,K+2}\ ,\\
\bar{L}^p_{q\bullet\bullet}U &= -U^{m+p}_{I+q,J-2,K-2} + U^{m+p}_{I+q,J+2,K-2} + U^{m+p}_{I+q,J-2,K+2} - U^{m+p}_{I+q,J+2,K+2}\ .
\end{aligned}
\tag{7.127}
$$

Scheme (7.122) – (7.127) is illustrated in Figs. 7.6 and 7.7. Examination of the stability condition of the scheme yields

$$\Delta t \leq \frac{h}{\sqrt{\alpha^2 + \beta^2}} \,, \tag{7.128}$$

where α and β are the P and S wave velocities, respectively. Condition (7.122) is the same as condition (7.26) for the conventional scheme. This is an important finding: the enlarged stencil does not affect the stability range.

Obviously, the scheme is implicit. As in the 1D problem, the predictor-corrector algorithm can be applied in order to avoid simultaneous solution of a large system of algebraic equations.

Note that the scheme we obtained is different from the scheme presented by Takeuchi and Geller (2000) who applied a different procedure to find a scheme.

8 The FD Targets for the Welded Material Interface and Free Surface

In this chapter we will apply three types of the strong formulations derived in chapter 2 - the strong formulation (SF), integral strong formulation (ISF) and discontinuous strong formulation (DSF) - to the welded material interface in order to obtain objects suitable for the FD approximation, that is, FD targets for the welded interface. We use term FD targets according to Robert J. Geller, who used this term in our personal communication in 2006.

We will then apply, say, the vacuum formalism to the FD targets for the welded interface in order to obtain FD targets for the free surface. We will restrict our analysis to the 1D case. This means that we will treat the planar interface and planar free surface.

Note that we will not apply here the weak formulation (WF). The weak formulation yields a suitable target in the finite-element method, see section 6.3.

8.1 The FD Targets for the Welded Material Interface

In the following we will refer to the formulations given in Tab. 2.1.

8.1.1 The FD Targets Obtained from the Strong Formulation

Define

$$E^{\mp} \;=\; \rho^{\mp}\ddot{u}^{\mp} \;-\; \sigma_{,z}^{\mp} \;-\; f^{\mp} \tag{8.1}$$

to make expressions and equations concise. The strong formulation (SF) is then given by the system of equations

$$\begin{aligned} E^{-} \;=\; 0\,;\;\; 0 \leq z \leq a \quad , \qquad E^{+} \;&=\; 0\,;\;\; a \leq z \leq b\,, \\ u^{-}(a) \;&=\; u^{+}(a)\,, \\ \sigma^{-}(a) \;&=\; \sigma^{+}(a)\,. \end{aligned} \tag{8.2}$$

Clearly the formulation itself directly leads to the homogeneous approach in constructing FD schemes: we find schemes that approximate equations of motion in the two media and other schemes that approximate the boundary conditions. As mentioned previously, the homogeneous approach is tractable in the 1D problem given the geometrical simplicity of the boundary conditions. It is, however, much more difficult to apply it in the 2D and 3D problems in general because each particular geometry of a material interface requires specific discretization. It is much more convenient to apply heterogeneous approach in which presence of the material interface is accounted for only by values of density and (visco)elastic moduli.

Considering strong-form equations of motion evaluated at $z = a$,

$$E^-(a) = 0\,, \tag{8.3}$$

$$E^+(a) = 0\,, \tag{8.4}$$

and combining them together with the displacement-continuity boundary condition in (8.2) we obtain

$$\rho^{PA}(a)\,\ddot{u}(a) \;=\; \frac{1}{2}\left[\,\sigma_{,z}^{-}\,(a) \;+\; \sigma_{,z}^{+}\,(a)\,\right] \;+\; f^{PA}(a)\,, \tag{8.5}$$

with effective density and body force given by

$$\rho^{PA}(a) \;=\; \frac{1}{2}\left[\,\rho^{-}(a) \;+\; \rho^{+}(a)\,\right], \tag{8.6}$$

$$f^{PA}(a) \;=\; \frac{1}{2}\left[\,f^{-}(a) \;+\; f^{+}(a)\,\right]. \tag{8.7}$$

Equations (8.5) - (8.7) together with the traction-continuity boundary condition in (8.2) make the first heterogeneous strong formulation for the material interface. Equations (8.5) - (8.7) correspond to those obtained by Moczo et al. (2002).

Instead of localizing the equations at the interface, we can alternatively integrate them over some small spatial range, for example, over the spatial spacing centered at the interface:

$$E^-(z) = 0\,, \quad \text{in } \left\langle a - \frac{h}{2}\,,\, a \right\rangle, \tag{8.8}$$

$$E^+(z) = 0\,, \quad \text{in } \left\langle a\,,\, a + \frac{h}{2} \right\rangle, \tag{8.9}$$

Assuming $\ddot{u}(a)$ and $\sigma_{,z}^{\mp}\,(a)$ as the integral mean values, keeping integrals of density and body force, and combining the integrated equations we obtain

$$\rho^{IA}(a)\,\ddot{u}(a) \;\doteq\; \frac{1}{2}\left[\,\sigma_{,z}^{-}\,(a) \;+\; \sigma_{,z}^{+}\,(a)\,\right] \;+\; f^{IA}(a), \tag{8.10}$$

with effective density and body force given now as integral arithmetic averages over the considered spatial interval,

$$\rho^{IA}(a) \;=\; \frac{1}{h}\left[\,\int_{a-\frac{h}{2}}^{a} \rho^{-}(z)\,\mathrm{d}z \;+\; \int_{a}^{a+\frac{h}{2}} \rho^{+}(z)\,\mathrm{d}z\,\right], \tag{8.11}$$

$$f^{IA}(a) \;=\; \frac{1}{h}\left[\,\int_{a-\frac{h}{2}}^{a} f^{-}(z)\,\mathrm{d}z \;+\; \int_{a}^{a+\frac{h}{2}} f^{+}(z)\,\mathrm{d}z\,\right]. \tag{8.12}$$

Equations (8.10) - (8.12) together with the traction-continuity boundary condition in (8.2) make the second heterogeneous strong formulation for the material interface.

Note that evaluation of the effective values of density and body force does not pose a problem because we always know the spatial distribution of density and body forces in the forward modeling.

We can realize that the only difference between eqs. (8.5) and (8.10) is in the definition of the effective density and body force. Obviously this can be related to the heterogeneity of the media in the halfspaces close to the interface.

8.1.2 The FD Targets Obtained from the Integral Strong Formulation

In the application of the integral strong form we have to choose the weight function. Our first choice is

$$w(z) \;=\; \delta(z-a)\,. \tag{8.13}$$

This yields

$$\frac{1}{2}\left[\,E^{-}(a)+\;E^{+}(a)\,\right] \;=\; \left[\,\sigma^{+}(a)-\;\sigma^{-}(a)\,\right]\delta(0)\,. \tag{8.14}$$

If we approximate $\delta(0)$ by $\frac{1}{h}$ and consider eq. (8.1) we obtain

$$\rho^{PA}(a)\,\ddot{u}(a) \;\doteq\; \frac{1}{2}\left[\,\sigma_{,z}^{-}\,(a)\;+\;\sigma_{,z}^{+}\,(a)\,\right] \;+\; f^{PA}(a) \;+\; \frac{1}{h}\left[\,\sigma^{+}(a)-\;\sigma^{-}(a)\,\right], \tag{8.15}$$

with effective density $\rho^{PA}(a)$ and body force $f^{PA}(a)$ defined as local averages by eqs. (8.6) and (8.7), respectively.

If we choose the weight function in the form

$$\begin{aligned} w(z) \;&=\; 1\,;\;\; z\in\left\langle a-\frac{h}{2}\,,\,a+\frac{h}{2}\right\rangle, \\ &=\; 0 \quad \text{elsewhere,} \end{aligned} \tag{8.16}$$

we obtain

$$\int_{a-\frac{h}{2}}^{a} E^{-}(z)\,\mathrm{d}z \;+\; \int_{a}^{a+\frac{h}{2}} E^{+}(z)\,\mathrm{d}z \;=\; \sigma^{+}(a)\;-\;\sigma^{-}(a)\,. \tag{8.17}$$

Assuming again $\ddot{u}(a)$ and $\sigma_{,z}^{\mp}\,(a)$ as the integral mean values, and keeping integrals of density and body force we obtain

$$\rho^{IA}(a)\,\ddot{u}(a) \;\doteq\; \frac{1}{2}\left[\,\sigma_{,z}^{-}\,(a)\;+\;\sigma_{,z}^{+}\,(a)\,\right] \;+\; f^{IA}(a) \;+\; \frac{1}{h}\left[\,\sigma^{+}(a)-\;\sigma^{-}(a)\,\right] \tag{8.18}$$

with, as expected, effective density $\rho^{IA}(a)$ and body force $f^{IA}(a)$ defined as integral arithmetic averages by eqs. (8.11) and (8.12), respectively.

Similar to the situation with the application of the strong formulation, the only difference between eqs. (8.15) and (8.18) is in the definition of the effective density and body force.

We can view the two first choices of the weight functions as certain extreme options - one function is localized at one point, the other is uniform over a finite interval. It can be therefore interesting to consider a function that would represent something in-between the two first choices. Consider, for example, the weight function that would be some finite approximation to δ-function, say $\delta_h(z-a)$, symmetric and nonzero in interval $\langle a-\frac{h}{2}\ ,\ a+\frac{h}{2}\rangle$, zero elsewhere, and satisfying the same condition as the two first weight functions,

$$\int_{-\infty}^{\infty} \delta_h(z-a)\,\mathrm{d}z \ = \ 1. \tag{8.19}$$

This choice would give

$$\int_{a-\frac{h}{2}}^{a} E^-(z)\,\delta_h(z-a)\,\mathrm{d}z + \int_{a}^{a+\frac{h}{2}} E^+(z)\,\delta_h(z-a)\,\mathrm{d}z \ = \ \frac{W}{h}\left[\ \sigma^+(a) - \ \sigma^-(a)\ \right]\ . \tag{8.20}$$

Value of W depends on a particular approximating function. For example, in the case of a triangle function $W=2$. Assuming $\ddot{u}(a)$ and $\sigma_{,z}^{\mp}(a)$ as the integral mean values, and keeping integrals of density and body force we obtain

$$\rho^{I\delta_h A}(a)\,\ddot{u}(a) \ \doteq \ \frac{1}{2}\left[\ \sigma_{,z}^{-}(a) \ + \ \sigma_{,z}^{+}(a)\ \right] \ + \ f^{I\delta_h A}(a) \ + \ \frac{W}{h}\left[\ \sigma^+(a) - \ \sigma^-(a)\ \right] \tag{8.21}$$

with effective density $\rho^{I\delta_h A}(a)$ and body force $f^{I\delta_h A}(a)$ defined by

$$\rho^{I\delta_h A}(a) \ = \ \int_{a-\frac{h}{2}}^{a} \rho^-(z)\,\delta_h(z-a)\,\mathrm{d}z \ + \ \int_{a}^{a+\frac{h}{2}} \rho^+(z)\,\delta_h(z-a)\,\mathrm{d}z\,, \tag{8.22}$$

$$f^{I\delta_h A}(a) \ = \ \int_{a-\frac{h}{2}}^{a} f^-(z)\,\delta_h(z-a)\,\mathrm{d}z \ + \ \int_{a}^{a+\frac{h}{2}} f^+(z)\,\delta_h(z-a)\,\mathrm{d}z\,. \tag{8.23}$$

It is obvious that also the average values of density and body force, assigned to position $z=a$, depend on the choice of the approximating function as the weight function.

8.1.3 The FD Targets Obtained from the Discontinuous Strong Formulation

Evaluation of the DSF equation directly at the interface, that is at $z=a$, gives

$$\frac{1}{2}\left[\ E^-(a) + \ E^+(a)\ \right] \ = \ \left[\ \sigma^+(a) - \ \sigma^-(a)\ \right]\delta(0)\,. \tag{8.24}$$

This is the same as the equation obtained from the ISF equation for the weight function $w(z) = \delta(z-a)$, see eq. (8.14). Consequently we can obtain

$$\rho^{PA}(a)\,\ddot{u}(a) \ \doteq \ \frac{1}{2}\left[\ \sigma_{,z}^{-}(a) \ + \ \sigma_{,z}^{+}(a)\ \right] \ + \ f^{PA}(a) \ + \ \frac{1}{h}\left[\ \sigma^+(a) - \ \sigma^-(a)\ \right], \tag{8.25}$$

with effective density $\rho^{PA}(a)$ and body force $f^{PA}(a)$ defined by eqs. (8.6) and (8.7), respectively.

Integration of the DSF equation in interval $\langle a - \frac{h}{2}\,,\, a + \frac{h}{2}\rangle$ gives

$$\int_{a-\frac{h}{2}}^{a} E^{-}(z)\,\mathrm{d}z \;+\; \int_{a}^{a+\frac{h}{2}} E^{+}(z)\,\mathrm{d}z \;=\; \sigma^{+}(a) - \sigma^{-}(a)\,. \tag{8.26}$$

This is the same equation as the equation obtained from the ISF equation for the 2^{nd} choice of the weight function (equal to 1 in the integration interval and zero elsewhere), see eq. (8.17). Consequently, we can obtain

$$\rho^{IA}(a)\,\ddot{u}(a) \;\doteq\; \frac{1}{2}\left[\,\sigma_{,z}^{-}(a) \;+\; \sigma_{,z}^{+}(a)\,\right] \;+\; f^{IA}(a) \;+\; \frac{1}{h}\left[\,\sigma^{+}(a) - \sigma^{-}(a)\,\right] \tag{8.27}$$

with effective density $\rho^{IA}(a)$ and body force $f^{IA}(a)$ defined by eqs. (8.11) and (8.12), respectively.

To make the obtained results more convenient for considerations and comparison, we will summarize the all obtained FD targets for the welded material interface in a concise presentation. For convenience, we summarize results of applications of the alternative formulations to the welded material interface.

FD targets obtained from the strong formulation:

SF-WI-a

$$\begin{aligned} E^{-} \;=\; 0\,;\;\; 0 \le z \le a \quad,\qquad E^{+} \;=\; 0\,;\;\; a \le z \le b\,,\\ u^{-}(a) \;=\; u^{+}(a)\,,\\ \sigma^{-}(a) \;=\; \sigma^{+}(a)\,. \end{aligned} \tag{8.28}$$

SF-WI-b

Evaluation at $z = a$ and combination of equations,

$$\begin{aligned} \rho^{PA}(a)\,\ddot{u}(a) \;&=\; \frac{1}{2}\left[\,\sigma_{,z}^{-}(a) \;+\; \sigma_{,z}^{+}(a)\,\right] \;+\; f^{PA}(a)\,,\\ \sigma^{-}(a) \;&=\; \sigma^{+}(a)\,. \end{aligned} \tag{8.29}$$

SF-WI-c

Integration of $E^{-}(z) = 0$ in $\langle a - \frac{h}{2}\,,\, a\rangle$ and $E^{+}(z) = 0$ in $\langle a\,,\, a + \frac{h}{2}\rangle$, assumption of $\ddot{u}(a)$ and $\sigma_{,z}^{\mp}(a)$ as mean values, combination of the integrated equations,

$$\begin{aligned} \rho^{IA}(a)\,\ddot{u}(a) \;&\doteq\; \frac{1}{2}\left[\,\sigma_{,z}^{-}(a) \;+\; \sigma_{,z}^{+}(a)\,\right] \;+\; f^{IA}(a)\,,\\ \sigma^{-}(a) \;&=\; \sigma^{+}(a)\,. \end{aligned} \tag{8.30}$$

FD targets obtained from the integral strong formulation:

ISF-WI-a

$w(z) = \delta(z-a)$, approximation of $\delta(0)$ by $\frac{1}{h}$ in $\langle a-\frac{h}{2}\,,\, a+\frac{h}{2}\rangle$,

$$\rho^{PA}(a)\,\ddot{u}(a) \doteq \frac{1}{2}\left[\,\sigma_{,z}^{-}(a) + \sigma_{,z}^{+}(a)\,\right] + f^{PA}(a) + \frac{1}{h}\left[\,\sigma^{+}(a) - \sigma^{-}(a)\,\right]. \quad (8.31)$$

ISF-WI-b

$w(z) = \delta_h(z-a)$, symmetric and nonzero in interval $\langle a-\frac{h}{2}\,,\, a+\frac{h}{2}\rangle$, zero elsewhere, satisfying condition $\int_{-\infty}^{\infty}\delta_h(z-a)\,\mathrm{d}z = 1$; assumption of $\ddot{u}(a)$ and $\sigma_{,z}^{\mp}(a)$ as mean values,

$$\rho^{I\delta_h A}(a)\,\ddot{u}(a) \doteq \frac{1}{2}\left[\,\sigma_{,z}^{-}(a) + \sigma_{,z}^{+}(a)\,\right] + f^{I\delta_h A}(a) + \frac{W}{h}\left[\,\sigma^{+}(a) - \sigma^{-}(a)\,\right]. \quad (8.32)$$

ISF-WI-c

$w(z) = 1$ in $\langle a-\frac{h}{2}\,,\, a+\frac{h}{2}\rangle$, $w(z) = 0$ elsewhere; assumption of $\ddot{u}(a)$ and $\sigma_{,z}^{\mp}(a)$ as mean values,

$$\rho^{IA}(a)\,\ddot{u}(a) \doteq \frac{1}{2}\left[\,\sigma_{,z}^{-}(a) + \sigma_{,z}^{+}(a)\,\right] + f^{IA}(a) + \frac{1}{h}\left[\,\sigma^{+}(a) - \sigma^{-}(a)\,\right]. \quad (8.33)$$

FD targets obtained from the discontinuous strong formulation:

DSF-WI-a

Evaluation at $z=a$ and approximation of $\delta(0)$ by $\frac{1}{h}$ in $\langle a-\frac{h}{2}\,,\, a+\frac{h}{2}\rangle$ leads to case ISF-a.

DSF-WI-b

Integration in $\langle a-\frac{h}{2}\,,\, a+\frac{h}{2}\rangle$ leads to case ISF-c.

8.1.4 Heterogeneous Formulation

1D Problem. The application of the strong formulation to the welded interface led to three FD targets. The first one, SF-WI-a, eqs. (8.2) or (8.28), simply was made of two equations of motion and equations for the displacement- and traction-continuity conditions. This formulation, as already noted, directly leads to the homogeneous approach in constructing FD schemes.

The two other obtained FD targets, SF-WI-B, eqs. (8.5) – (8.7) or (8.29), and SF-WI-c, eqs. (8.10) – (8.12) or (8.30), were originally obtained by Moczo et al. (2002) who called them the heterogeneous formulations of the equation of motion. The reason for this term is the fact that eqs. (8.5) and (8.10) have the same form as the strong-form equation of motion but they are valid also for a point directly at the interface. The heterogeneous formulation thus provides basis for a heterogeneous FD scheme: depending on how we approximate the average of stress derivatives, we can have the same FD scheme for the grid points away from the material interface and for the grid point directly at the material interface; presence of the material interface is accounted for only by values of the effective material grid parameters.

In the displacement-stress, eqs. (5.1), displacement-velocity-stress, eqs. (5.2), and velocity-stress, eqs. (5.3), formulations stress tensor is an additional dependent variable. A FD scheme for calculating stress from a FD approximation to the stress-strain relation or its time derivative is therefore necessary. It was relatively easy to find, for example, velocity-stress FD scheme for a smooth continuum, eqs. (7.28) – (7.36). It is, however, not so obvious how to obtain a FD scheme for the stress-tensor component directly at the material interface, if the scheme is to be consistent with the traction-continuity boundary condition at the interface.

Here we follow Moczo et al. (2002) and consider equation

$$\varphi^{\pm}(z) \;=\; c^{\pm}(z)\, g^{\pm}(z) \tag{8.34}$$

where $\varphi^{\pm}(z)$, $c^{\pm}(z)$ and $g^{\pm}(z)$ are real functions of a real argument z . Functions $\varphi^{\pm}$ satisfy boundary (continuity) condition

$$\varphi^{-}(0) \;=\; \varphi^{+}(0) \tag{8.35}$$

whereas functions $c^{\pm}(z)$ and $g^{\pm}(z)$ may have discontinuities of the first order at , say, interface $z = 0$. If we define

$$\bar{g}(0) \;=\; \tfrac{1}{2}\left[\, g^{-}(0) \;+\; g^{+}(0) \,\right]. \tag{8.36}$$

then it follows from eqs. (8.34) and boundary condition that

$$\varphi^{-}\,(0) \;=\; \varphi^{+}(0) \;=\; \bar{c}(0)\, \bar{g}(0)\;, \tag{8.37}$$

where

$$\bar{c}\,(0) \;=\; \frac{2}{\left[\; \dfrac{1}{c^{-}(0)} + \dfrac{1}{c^{+}(0)} \right]}\;. \tag{8.38}$$

Equation (8.37) has the same form as eq. (8.34) and, at the same time, it is valid at $z = 0$. In other words, we found a heterogeneous formulation valid at both $z \neq 0$ (away from the interface) and $z = 0$ (directly at the interface) with $\bar{g}(0)$ given by the arithmetic average of $g^{+}(0)$ and $g^{-}(0)$, eq. (8.36), and $\bar{c}$ given as the harmonic average of $c^{+}(0)$ and $c^{-}\,(0)$, eq. (8.38).

Consider now functions $c^{\pm}(z)$ in the form

$$c^{\pm}(z) \;=\; \frac{1}{r^{\pm}(z)}\;. \tag{8.39}$$

Then we obtain

$$\varphi^{-}(0) \;=\; \varphi^{+}(0) \;=\; \frac{1}{\bar{r}\,(0)}\;\bar{g}\,(0)\;, \tag{8.40}$$

where

$$\bar{r}\,(0) \;=\; \tfrac{1}{2}\left[\, r^{-}(0) + r^{+}\,(0) \,\right]\;. \tag{8.41}$$

Recall now equation of motion (without the body-force term, for brevity) and Hooke's law for the 1D problem:

$$\rho^{\pm}\, \ddot{u}^{\pm} \;=\; \sigma_{,z} \;, \tag{8.42}$$

$$\sigma^{\pm} \;=\; C^{\pm}\, u_{,z} \;. \tag{8.43}$$

Consider further displacement- and traction-continuity boundary conditions at $z = 0$,

$$u^{-}(0) \;=\; u^{+}(0) \tag{8.44}$$

and

$$\sigma^{-}(0) \;=\; \sigma^{+}(0) \,. \tag{8.45}$$

Clearly we can apply eqs. (8.34) to (8.41) to the equation of motion, Hooke's law, and the boundary conditions. We easily obtain for the interface

$$\bar{\rho}(0)\, \ddot{u}(0) \;=\; \overline{\sigma_{,z}}\,(0) \tag{8.46}$$

and

$$\sigma(0) \;=\; \overline{C}(0)\; \overline{u_{,z}}(0) \,, \tag{8.47}$$

where density at the interface is equal to the arithmetic average of the densities in the two halfspaces, and elastic modulus at the interface is equal to the harmonic average of the moduli in the two halfspaces:

$$\bar{\rho}(0) \;=\; \tfrac{1}{2}\,\big[\, \rho^{-}(0) + \rho^{+}(0) \,\big] \;, \quad \overline{C}(0) \;=\; \frac{2}{\left[\dfrac{1}{C^{-}(0)} + \dfrac{1}{C^{+}(0)}\right]} \,. \tag{8.48}$$

The average spatial derivatives of the displacement and stress are

$$\begin{aligned} \overline{u_{,z}}\,(0) \;&=\; \tfrac{1}{2}\,\big[\, u^{-}{}_{,z}(0) \;+\; u^{+}{}_{,z}(0) \,\big] \;, \\ \overline{\sigma_{,z}}(0) \;&=\; \tfrac{1}{2}\,\big[\, \sigma^{-}{}_{,z}(0) \;+\; \sigma^{+}{}_{,z}(0) \,\big] \;. \end{aligned} \tag{8.49}$$

It is obvious that eqs. (8.46) and (8.47) for a point at the interface have the same form as the equation of motion and Hooke's law, eqs. (8.42) and (8.43) at a point away from the interface.

In the displacement formulation, the heterogeneous equation of motion takes the form

$$\bar{\rho}(0)\, \ddot{u}(0) \;=\; \overline{(Cu_{,z}\,)_{,z}}\Big|_{z=0} \,. \tag{8.50}$$

The term on the r.h.s. of the equation means average

$$\overline{(Cu_{,z}\,)_{,z}}\Big|_{z=0} \;=\; \tfrac{1}{2}\Big[\; (Cu_{,z}\,)^{-}{}_{,z}\,\Big|_{z=0} \;+\; \;(Cu_{,z}\,)^{+}{}_{,z}\,\Big|_{z=0}\Big] \,. \tag{8.51}$$

Recall here the mathematical trick of Tikhonov and Samarski (e.g., Mitchell, 1969, p. 23), see section 7.1, who obtained the harmonic averaging of the coefficients (here elastic moduli $C^{\pm}$) in an effort to avoid spatial derivatives of the coefficients in the $2^{\rm nd}$-order displacement formulation. Now we see that the harmonic average in the heterogeneous formulation (8.47) is due to the traction-continuity condition at the welded material interface.

Moczo et al. (2002) also showed simple physical model of the contact of two elastic media. Consider two Hooke's elements (elastic springs), eq. (4.1),

$$\sigma^- \;=\; M^- \, \varepsilon^- \quad , \quad \sigma^+ \;=\; M^+ \, \varepsilon^+ \tag{8.52}$$

If they are connected in series, then, see Tab. 4.1, the stresses acting on the springs are equal,

$$\sigma \;=\; \sigma^- \;=\; \sigma^+ \, , \tag{8.53}$$

and strains are additive,

$$\varepsilon \;=\; \varepsilon^- + \varepsilon^+ \, . \tag{8.54}$$

We can think about finding an averaged Hooke's element,

$$\sigma \;=\; \overline{M} \, \bar{\varepsilon} \, , \tag{8.55}$$

such that two averaged elements connected in series make a system equivalent to the two elements defined by eqs. (8.52) connected in parallel. Because the resultant strain ε in the system of two averaged elements connected in series is

$$\varepsilon \;=\; 2 \, \bar{\varepsilon} \, , \tag{8.56}$$

we easily obtain

$$2 \, \bar{\varepsilon} \;=\; \frac{\sigma}{M^-} + \frac{\sigma}{M^+} \tag{8.57}$$

and

$$\sigma \;=\; \overline{M} \, \bar{\varepsilon} \, ; \quad \bar{\varepsilon} \;=\; \tfrac{1}{2} \, \left(\, \varepsilon^- + \varepsilon^+ \, \right) \, , \quad \overline{M} \;=\; \frac{2}{\left[\, \dfrac{1}{M^-} + \dfrac{1}{M^+} \, \right]} \, . \tag{8.58}$$

This means that the elastic modulus of the averaged Hooke's element is the harmonic average of the elastic moduli of the two, '$-$' and '$+$', elements connected in series.

Similarly we could consider a system of two connected particles with masses m^- and m^+. If the particles move together (which may correspond to the displacement continuity), the equivalent system can be made of two identical particles with mass equal to the arithmetic average of masses m^- and m^+.

3D Problem. Consider surface S with normal vector $\vec{n}$ defining the geometry of the material interface at which elastic moduli κ and μ have a discontinuity of the first order. The welded-interface boundary conditions are continuity of displacement $\vec{u}\,(\vec{\eta})$ and traction $\vec{T}\,(\vec{\eta},\vec{n})$ across the surface:

$$\vec{u}^{-}\,(\vec{\eta}) \;=\; \vec{u}^{+}\,(\vec{\eta}) \quad , \quad \vec{T}^{-}\,(\vec{\eta},\vec{n}) \;=\; \vec{T}^{+}\,(\vec{\eta},\vec{n}) \;. \tag{8.59}$$

In a much simpler configuration we can consider first the planar surface S parallel to the xy-coordinate plane with a normal vector $\vec{n} = (0,\, 0,\, 1)$. The boundary conditions (8.59) then imply

$$\begin{aligned} &\sigma_{zx}^{-} = \sigma_{zx}^{+}\,,\;\; \sigma_{zy}^{-} = \sigma_{zy}^{+}\,,\;\; \sigma_{zz}^{-} = \sigma_{zz}^{+}\,, \\ &\varepsilon_{xx}^{-} = \varepsilon_{xx}^{+}\,,\;\; \varepsilon_{yy}^{-} = \varepsilon_{yy}^{+}\,,\;\; \varepsilon_{xy}^{-} = \varepsilon_{xy}^{+}\,. \end{aligned} \tag{8.60}$$

At the same time, components $\sigma_{xx}, \sigma_{yy}, \sigma_{xy}, \varepsilon_{zx}, \varepsilon_{zy}$ and ε_{zz} may be discontinuous across the interface.

As in the 1D problem we will find Hooke's law for a point at the material interface in the form of Hooke's law in a smooth medium.

Hooke's law in a smooth isotropic medium, eq. (4.10), can be written in the matrix form. If we define stress and strain vectors as

$$\vec{\sigma} \;=\; \left[\sigma_{xx}, \sigma_{yy}, \sigma_{zz}, \sigma_{xy}, \sigma_{yz}, \sigma_{zx}\right]^{T}, \quad \vec{\varepsilon} \;=\; \left[\varepsilon_{xx}, \varepsilon_{yy}, \varepsilon_{zz}, \varepsilon_{xy}, \varepsilon_{yz}, \varepsilon_{zx}\right]^{T}, \tag{8.61}$$

Hooke's law for an isotropic medium can be written as

$$\vec{\sigma} \;=\; E\,\vec{\varepsilon} \tag{8.62}$$

where matrix E,

$$E \;=\; \begin{bmatrix} \kappa+\frac{4}{3}\mu & \kappa-\frac{2}{3}\mu & \kappa-\frac{2}{3}\mu & 0 & 0 & 0 \\ \kappa-\frac{2}{3}\mu & \kappa+\frac{4}{3}\mu & \kappa-\frac{2}{3}\mu & 0 & 0 & 0 \\ \kappa-\frac{2}{3}\mu & \kappa-\frac{2}{3}\mu & \kappa+\frac{4}{3}\mu & 0 & 0 & 0 \\ 0 & 0 & 0 & 2\mu & 0 & 0 \\ 0 & 0 & 0 & 0 & 2\mu & 0 \\ 0 & 0 & 0 & 0 & 0 & 2\mu \end{bmatrix}, \tag{8.63}$$

is the so-called elasticity matrix. We will now try to obtain Hooke's law for a point at the interface in the form of eq. (8.62).

Define averaged stress and strain vectors at the interface:

$$\vec{\sigma}^{A} \;=\; \tfrac{1}{2}\left(\vec{\sigma}^{-} + \vec{\sigma}^{+}\right) \quad , \quad \vec{\varepsilon}^{A} \;=\; \tfrac{1}{2}\left(\vec{\varepsilon}^{-} + \vec{\varepsilon}^{+}\right) \;. \tag{8.64}$$

Accounting for the boundary conditions (8.60) in definitions (8.64) we obtain

$$\begin{aligned} \vec{\sigma}^{A} \;&=\; \left[\,\sigma_{xx}^{A},\; \sigma_{yy}^{A},\; \sigma_{zz},\; \sigma_{xy}^{A},\; \sigma_{yz},\; \sigma_{zx}\,\right]^{T}, \\ \vec{\varepsilon}^{A} \;&=\; \left[\,\varepsilon_{xx},\; \varepsilon_{yy},\; \varepsilon_{zz}^{A},\; \varepsilon_{xy},\; \varepsilon_{yz}^{A},\; \varepsilon_{zx}^{A}\,\right]^{T}. \end{aligned} \tag{8.65}$$

Omitting a little bit longer derivation (see Moczo et al., 2002, for details) we can obtain Hooke's law for a point at the interface in the form

$$\vec{\sigma}^{A} \;=\; \widetilde{E}\;\vec{\varepsilon}^{A}\;, \tag{8.66}$$

where the averaged elasticity matrix is defined by

$$\widetilde{E} \;=\; \begin{bmatrix} \Lambda+2\mu^{A} & \Lambda & \Psi & 0 & 0 & 0 \\ \Lambda & \Lambda+2\mu^{A} & \Psi & 0 & 0 & 0 \\ \Psi & \Psi & \left[\kappa+\frac{4}{3}\mu\right]^{H} & 0 & 0 & 0 \\ 0 & 0 & 0 & 2\mu^{A} & 0 & 0 \\ 0 & 0 & 0 & 0 & 2\mu^{H} & 0 \\ 0 & 0 & 0 & 0 & 0 & 2\mu^{H} \end{bmatrix} \tag{8.67}$$

with effective elastic moduli defined by

$$\begin{aligned} \Lambda \;&=\; \left(\left[\frac{\kappa-\frac{2}{3}\mu}{\kappa+\frac{4}{3}\mu}\right]^{A}\right)^{2}\cdot\left[\kappa+\tfrac{4}{3}\mu\right]^{H}+2\left[\frac{\left(\kappa-\frac{2}{3}\mu\right)\mu}{\kappa+\frac{4}{3}\mu}\right]^{A}, \\ \Psi \;&=\; \left[\frac{\kappa-\frac{2}{3}\mu}{\kappa+\frac{4}{3}\mu}\right]^{A}\cdot\left[\kappa+\tfrac{4}{3}\mu\right]^{H}. \end{aligned} \tag{8.68}$$

Superscripts A and H denote arithmetic and harmonic averages, respectively.

Hooke's law (8.66) for a point at the material interface can be viewed as Hooke's law for a point in a smooth medium. Averaged or effective elasticity matrix $\widetilde{E}$ assures consistency with the traction-continuity condition at the interface.

An important difference between matrices E and $\widetilde{E}$, or, in other words, difference between any of the two original smooth media and the averaged medium is that matrix $\widetilde{E}$ has 5 independent nonzero elements and the averaged medium is transversely isotropic. Matrix E for any of the two isotropic media in contact has only 2 independent nonzero elements. This means that the exact heterogeneous formulation for a planar welded material interface parallel with a coordinate plane increases the number of elastic coefficients necessary to describe the medium.

Consider now a more complicated configuration. Let the planar material interface be in a general position in the Cartesian coordinate system. The normal vector to the interface, $\vec{n} = (n_x, n_y, n_z)$, has then all components non-zero. Find a Cartesian coordinate system $x'y'z'$ in which $\vec{n}$ is parallel to the z'-axis. Then we can find matrix $\widetilde{E}'$ with 5 independent non-zero elements. If we then transform matrix $\widetilde{E}'$ into matrix $\widetilde{E}$ in the original coordinate system xyz, we obtain a symmetric elasticity matrix $\widetilde{E}$ which obviously may have all elements non-zero though only 5 of them are independent.

All nonzero elements of the averaged elasticity matrix mean nothing less than the following complication: all strain-tensor components are necessary to calculate each stress-tensor component at a point of the interface, and 21 non-zero elastic coefficients are necessary at the point. Recalling the configuration of the staggered grid we clearly realize that we do not have all strain-tensor components defined at each grid position of the stress-tensor components. From this point of view, the staggered grid is not really well suited for incorporation of the traction-continuity condition at the material interface.

If the geometry of the interface is defined by a non-planar smooth surface S, the surface may be locally approximated by a planar surface tangential to surface S at a given point.

We see that incorporation of the traction-continuity condition at the material interface in the 3D problem is much more complicated compared to the 1D problem.

Note that the above analysis is equivalent to the application of the Schoenberg and Muir (1989) calculus applied to the special case of one interface between two homogeneous isotropic media. See also Muir et al. (1992).

The above analysis and, at the same time, a pragmatical desire to keep the structure, number of operations and memory requirements of the standard 4^{th}-order staggered-grid scheme led Moczo et al. (2002) to an approximate approach. They evaluated an effective grid elastic modulus (κ or μ) at each grid position of the stress-tensor components as a volume integral harmonic average of the modulus within a volume of the grid cell centered at the grid position. They evaluated an effective density at each position of the displacement or particle-velocity component as a volume integral arithmetic average of the density within a volume of the grid cell centered at the grid position. Such intuitive approach was motivated by the exact averaging in the 1D problem and by the presence of such averaging in the elasticity matrix in the 3D problem.

The averaging applies to both smoothly and discontinuously heterogeneous media. The averages are evaluated by numerical integration.

The corresponding 4^{th}-order velocity-stress staggered-grid scheme is given in section 7.2, eqs. (7.28) – (7.39). Moczo et al. (2002) performed detailed numerical test that confirmed that the scheme is more accurate than previously published staggered-grid schemes. We refer here especially to Fig. 6 of their article. The figure illustrates that the scheme is capable to sense (surprisingly accurately) a position of the material interface anywhere in-between the two grid points. In other words, the length of the grid spacing cannot be considered as an 'atom of resolution' within which the FD scheme cannot see differences, for example, in the position of the interface.

For a review of incorporation of the material interface in the FD schemes see Moczo et al. (2007). Here we explicitly mention an interesting approach to incorporate curved material interface by Zhang and Symes (1998).

Interface Between Two Viscoelastic Media. So far we do not know a heterogeneous formulation if the stress-strain relation has the form (4.161). In such situation we have to apply an approximate approach. Here we follow the approach suggested by Kristek and Moczo (2003), see also Moczo et al. (2004b, 2007), which has been shown sufficiently accurate using numerical tests against the discrete wavenumber method (Bouchon, 1981; Coutant, 1989).

Consider a contact of two viscoelastic media with the GMB-EK rheology. Each of the two media is described by a real density, elastic (unrelaxed) moduli κ_U and μ_U, and complex frequency-dependent moduli $\kappa(\omega)$ and $\mu(\omega)$. We want to determine density, elastic moduli $\bar{\kappa}_U$ and $\bar{\mu}_U$, and anelastic coefficients $Y_l^{\bar{\kappa}}$ and $Y_l^{\bar{\mu}}$; $l = 1, \ldots, n$, for an averaged medium that would represent the contact of two media.

We do not see any reason for other than integral volume arithmetic averaging of density using eq. (7.39).

Average viscoelastic moduli $\bar{\kappa}(\omega)$ and $\bar{\mu}(\omega)$ can be determined by numerical integration of the viscoelastic moduli in the frequency domain as integral volume harmonic averages. From the

averaged viscoelastic moduli, quality factors corresponding to these moduli can be determined at frequencies $\tilde{\omega}_k$; $k = 1, ..., 2n-1$, using

$$Q_{\bar{M}}(\tilde{\omega}_k) = \frac{Re\ \bar{M}(\tilde{\omega}_k)}{Im\ \bar{M}(\tilde{\omega}_k)} \ ; \quad k = 1, 2, \ldots, 2n-1 \ , \tag{8.69}$$

where $\bar{M}$ stands for $\bar{\kappa}$ or $\bar{\mu}$. Having values $Q_{\bar{M}}(\tilde{\omega}_k)$, $k = 1, 2, \ldots, 2n-1$, and assuming the GMB-EK rheology of the averaged medium, we can apply the least-square method to equations

$$Q_{\bar{M}}^{-1}(\tilde{\omega}_k) = \sum_{l=1}^{n} \frac{\omega_l \tilde{\omega}_k + \omega_l^2 Q_{\bar{M}}^{-1}(\tilde{\omega}_k)}{\omega_l^2 + \tilde{\omega}_k^2} Y_l^{\bar{M}} \ ; \qquad k = 1, \ldots, 2n-1 \ , \quad \bar{M} \in \{\bar{\kappa}, \bar{\mu}\} \ , \tag{8.70}$$

compare with eqs. (4.154) and (4.162), to determine anelastic coefficients $Y_l^{\bar{M}}$; $l = 1, \ldots, n$, for the averaged medium.

What remains to determine are the average unrelaxed (elastic) moduli $\bar{\kappa}_U$ and $\bar{\mu}_U$. It follows from eq. (4.39) that

$$\bar{M}_U = \lim_{\omega \to \infty} \bar{M}(\omega) \ . \tag{8.71}$$

Consequently, the harmonic averaging of the viscoelastic modulus gives in the limit the harmonic averaging of the unrelaxed modulus. This means that the unrelaxed (elastic) moduli $\bar{M}_U$ for the averaged viscoelastic medium can be obtained in the same way as in the perfectly elastic medium, for example, using formulas (7.37) and (7.38).

If we do not know directly viscoelastic moduli $\kappa(\omega)$ and $\mu(\omega)$ for each of the two media in contact but, instead, we know measured or estimated $Q_\alpha(\omega)$ for the P- and $Q_\beta(\omega)$ for the S-waves, we have to proceed as follows.

We will assume the GMB rheology of each medium as well as of the averaged medium. For each of the two media we will first determine Y_l^κ and Y_l^μ following eqs. (4.162) – (4.165). Then, assuming known unrelaxed (elastic) moduli for each medium, we can determine viscoelastic moduli $\kappa(\omega)$ and $\mu(\omega)$ using eq. (4.152) for each modulus. Then we can proceed with the numerical averaging of the moduli in the frequency domain, determination of the corresponding quality factors, and determination of the anelastic coefficients as it was described before.

8.2 The FD Targets for the Free Surface

In the numerical modeling of the seismic wave propagation and earthquake motion in the Earth it is sufficient, in most applications, to replace air by vacuum and the real air/water or air/solid interface, that is, the Earth's surface, by the vacuum/water or vacuum/solid interface, that is, the traction-free surface. The traction-free surface is briefly called the free surface. The free surface was already considered in definition of the canonical model with the material interface but was not explicitly treated.

Consider surface S with normal vector $\vec{n}$. Let $\vec{T}(\vec{u}, \vec{n})$ be the traction vector at surface S corresponding to the displacement vector $\vec{u}$ and normal vector $\vec{n}$. Then the traction-free

condition at surface S is

$$\vec{T}(\vec{u},\vec{n}) \;=\; 0 \tag{8.72}$$

or, equivalently,

$$\sigma_{ji}\, n_j \;=\; 0\,. \tag{8.73}$$

If surface S is planar and perpendicular to the z-axis, the normal vector is $\vec{n} \;=\; (0,0,-1)$ and the traction-free condition implies

$$\sigma_{zi} \;=\; 0\,;\;\; i \in \{x,y,z\}\;. \tag{8.74}$$

In the simplest case, 1D problem, the traction-free condition simply means

$$\sigma \;=\; 0\,. \tag{8.75}$$

Because we consider here the free surface as the vacuum/solid interface, we can consider, for example, the '$-$' medium as vacuum in the above FD targets for the welded interface in order to formally obtain FD targets for the free surface. We can call such approach the vacuum formalism. Note that such consideration has been previously applied by many FD modelers directly to the FD schemes for the interior grid points. Obviously, application of the vacuum formalism to the FD targets is not in general equivalent to the application of the vacuum formalism to the interior FD scheme.

The corresponding FD targets for the free surface are summarized here:

FD targets obtained from the strong formulation:

SF-FS-a

$$\begin{aligned} E^+ \;&=\; 0\,;\;\; a \le z \le b\,, \\ \sigma^+(a) \;&=\; 0\,. \end{aligned} \tag{8.76}$$

SF-FS-b

$$\begin{aligned} \rho^+(a)\,\ddot{u}(a) \;&=\; \sigma^+_{,z}(a) \;+\; f^+(a)\,, \\ \sigma^+(a) \;&=\; 0\,. \end{aligned} \tag{8.77}$$

SF-FS-c

$$\begin{aligned} \rho^{IAFS}(a)\,\ddot{u}(a) \;&\doteq\; \sigma^+_{,z}(a) \;+\; f^{IAFS}(a)\,, \\ \rho^{IAFS}(a) \;=\; \frac{2}{h}\int_a^{a+\frac{h}{2}} \rho^+(z)\,\mathrm{d}z \quad &, \quad f^{IAFS}(a) \;=\; \frac{2}{h}\int_a^{a+\frac{h}{2}} f^+(z)\,\mathrm{d}z\,, \\ \sigma^+(a) \;&=\; 0\,. \end{aligned} \tag{8.78}$$

FD targets obtained from the integral strong formulation:

ISF-FS-a

$$\rho^{+}(a)\,\ddot{u}(a) \doteq \sigma^{+}_{,z}(a) + f^{+}(a) + \frac{2}{h}\,\sigma^{+}(a)\,. \tag{8.79}$$

ISF-FS-b

$$\begin{aligned}
\rho^{I\delta_h AFS}(a)\,\ddot{u}(a) &\doteq \sigma^{+}_{,z}(a) + f^{I\delta_h AFS}(a) + \frac{2W}{h}\,\sigma^{+}(a)\,,\\
\rho^{I\delta_h AFS}(a) &= 2\int_a^{a+\frac{h}{2}} \rho^{+}(z)\,\delta_h(z-a)\,\mathrm{d}z\,,\\
f^{I\delta_h AFS}(a) &= 2\int_a^{a+\frac{h}{2}} f^{+}(z)\,\delta_h(z-a)\,\mathrm{d}z\,.
\end{aligned} \tag{8.80}$$

ISF-FS-c

$$\rho^{IAFS}(a)\,\ddot{u}(a) \doteq \sigma^{+}_{,z}(a) + f^{IAFS}(a) + \frac{2}{h}\,\sigma^{+}(a)\,. \tag{8.81}$$

FD targets obtained from the strong formulation:

DSF-FS-a
The same as case ISF-FS-a .

DSF-FS-a
The same as case ISF-FS-c .

In principle, we recognize two basic types of the FD targets for the welded interface and free surface. In the first one, obtained from SF, we have separate equation of motion and additional equation(s) for the boundary condition(s). In the other type, obtained from ISF and DSF, a boundary term with traction(s) appears directly in the 'modified' equation of motion. This is an interesting finding and unification of the three elaborated alternative formulations for our canonical problem with the welded material interface, SF, ISF and DSF.

9 Finite-difference Schemes for the Free Surface

Here we restrict to the planar free surface either in the 3D or 1D problem. For a recent review of approaches in modeling non-planar free surface, that is so-called free-surface topography, see Moczo et al. (2007).

Two principal approaches to simulate the free surface are quite obvious. In the first approach a FD scheme for the interior grid point is formally applied at the grid point at the free surface (or, depending on the scheme and order of approximation, at the grid points near the free surface) and the field (dependent) variables and material parameters above the free surface are somehow defined to simulate vacuum above the surface or directly zero traction at the surface. This approach leads to the so-called vacuum formalism, medium taper or imaging method. The vacuum formalism applies zero moduli above the free surface. The approach may yield good level of accuracy in the conventional-grid displacement schemes; see, for example, Zahradník and Priolo (1995)

in 2D, Moczo et al. (1999) in 3D. Graves (1996) and other authors did not find the approach satisfactory in the staggered-grid modeling. Frankel and Leith (1992) applied density taper in their conventional-grid displacement FD scheme. Levander (1988) introduced the stress imaging in his 2D P-SV $4^{\rm th}$-order staggered-grid velocity-stress FD scheme. The stress-imaging technique applies explicit boundary conditions to the stress-tensor component(s) located at the grid plane coinciding with the free surface, and uses imaged values of the stress-tensor components above the free surface assuming their antisymmetry about the free surface.

In the second approach such FD scheme is applied at grid points at or near the free surface which does not require any values above the free surface. Such scheme in the 1D problem can be called one-sided scheme. An adjusted scheme may be appropriate term for a scheme in the 3D problem because the scheme combines one-sided approximations in the direction perpendicular to the free surface with, for example, centered approximations in the coordinate directions parallel to the free surface. Kristek et al. (2002) and Moczo et al. (2004a) presented the $4^{\rm th}$-order adjusted staggered-grid scheme and demonstrated its better accuracy compared to the stress imaging.

9.1 Conventional Scheme for the 3D Problem - Application of the Vacuum Formalism

The conventional displacement FD scheme (7.18) - (7.24) can be also applied to the grid points located directly at the planar free surface. If the grid point $(I,\, J,\, K)$ is located at the free surface, operators L_{xx}, L_{yy}, L_{xy} and L_{yx} defined by eqs. (7.21) and (7.23) can be directly applied. The other operators, L_{xz}, L_{yz}, L_{zx}, L_{zy}, and L_{zz} can be obtained by application of the vacuum formalism ($\lambda = 0$ and $\mu = 0$ above the free surface) to the second type of approximation of the mixed spatial derivatives suggested by Zahradník (1995). They are

$$L_{zz}(a,\phi) \;=\; \frac{1}{h^2}\, a^z_{I,J,K} \left(\phi^m_{I,J,K+1} \;-\; \phi^m_{I,J,K} \right) , \tag{9.1}$$

$$\begin{aligned} L_{z\eta}(a,\phi) \;=\; \frac{1}{4h^2}\big[& \; a^{\eta+} \left(\phi^m_{2+} + \phi^m_{3+} - \phi^m_{2} - \phi^m_{3} \right) \\ & - \; a^{\eta-} \left(\phi^m_{1+} + \phi^m_{2+} - \phi^m_{1} - \phi^m_{2} \right) \big] , \end{aligned} \tag{9.2}$$

and

$$\begin{aligned} L_{\eta z}(a,\phi) \;=\; \frac{1}{4h^2}\big[& \; a^{z+} \left(\phi^m_{3} + \phi^m_{3+} - \phi^m_{2} - \phi^m_{2+} \right) \\ & - \; a^{z-} \left(\phi^m_{2} + \phi^m_{2+} - \phi^m_{1} - \phi^m_{1+} \right) \big] , \end{aligned} \tag{9.3}$$

where subscripts 1, 2, 3, 1+, 2+, 3+ stand for indices as follows:

	$\eta = x$	$\eta = y$		$\eta = x$	$\eta = y$
1	$I-1,\, J,\, K$	$I,\, J-1,\, K$	1+	$I-1,\, J,\, K+1$	$I,\, J-1,\, K+1$
2	$I\quad ,\, J,\, K$	$I,\, J\quad ,\, K$	2+	$I\quad ,\, J,\, K+1$	$I,\, J\quad ,\, K+1$
3	$I+1,\, J,\, K$	$I,\, J+1,\, K$	3+	$I+1,\, J,\, K+1$	$I,\, J+1,\, K+1$

(9.4)

Effective parameters are:

$$\begin{array}{lll} \text{if } \eta = x \text{ then} & a^{\eta+} = a^{x}_{I,J,K+1/2}\,, & a^{\eta-} = a^{x}_{I-1,J,K+1/2}\,, \\ & a^{z+} = a^{z}_{I+1/2,J,K}\,, & a^{z-} = a^{z}_{I+1/2,J,K}\,, \\ \text{if } \eta = y \text{ then} & a^{\eta+} = a^{y}_{I,J,K+1/2}\,, & a^{\eta-} = a^{y}_{I,J-1,K+1/2}\,, \\ & a^{z+} = a^{z}_{I,J+1/2,K}\,, & a^{z-} = a^{z}_{I,J-1/2,K}\,. \end{array} \tag{9.5}$$

and

$$a^{x}_{I,J,K+1/2} \;=\; \left[\frac{1}{h}\int_{x_{I,J,K+1/2}}^{x_{I+1,J,K+1/2}} \frac{1}{a}\,\mathrm{d}x\right]^{-1}\,, \tag{9.6}$$

$$a^{y}_{I,J,K+1/2} \;=\; \left[\frac{1}{h}\int_{y_{I,J,K+1/2}}^{y_{I,J+1,K+1/2}} \frac{1}{a}\,\mathrm{d}y\right]^{-1}\,, \tag{9.7}$$

$$a^{z}_{I,J,K} \;=\; \left[\frac{1}{h}\int_{z_{I,J,K}}^{z_{I,J,K+1}} \frac{1}{a}\,\mathrm{d}z\right]^{-1}\,. \tag{9.8}$$

Only half-values of density ρ has to be considered in scheme (7.18) - (7.24) when applied to the grid points on the free surface. Only half-values of parameters a^x and a^y (a being either λ or μ) have to be considered in operators L_{xx} , L_{yy} , L_{xy} and L_{yx} when applied to the grid points on the free surface.

Moczo et al. (1999) numerically demonstrated very good level of accuracy of the scheme for media with P/S wave velocity ratio smaller than 2.

9.2 Staggered-grid Schemes for the 3D Problem

9.2.1 Stress Imaging

In the stress imaging explicit boundary conditions are applied to the stress-tensor component(s) located at the grid plane coinciding with the free surface. Moreover, antisymmetry of the stress-tensor components with respect to the free surface is assumed. Considering the free surface located at $z = 0$, the antisymmetry condition can be written as

$$\sigma_{zi}\,(-z) \;=\; -\sigma_{zi}\,(z)\;; \qquad i \in \{x, y, z\}\;. \tag{9.9}$$

The antisymmetry ensures the traction-free boundary condition (8.72). Robertsson (1996) summarized three possibilities for treating the displacement or particle velocity values at grid positions above the free surface required by the 4^{th}-order staggered-grid FD scheme. 1. The values are calculated using the 2^{nd}-order approximations to the boundary condition and imaged stress-tensor components. Examples of the approach are schemes by Levander (1988), Graves (1996), and Kristek et al. (2002). 2. The values are mirrored as symmetric values with respect to the free surface. Examples are schemes by Crase (1990) and Rodrigues and Mora (1993). The problem with this approach is (Robertsson, 1996) that the symmetric values in fact violate the boundary conditions. 3. Robertsson (1996) assumed zero values.

In the staggered grid we have two natural locations for the free surface. In one, the horizontal displacement or particle-velocity components, and stress-tensor components T_{xx}, T_{yy}, T_{zz} and T_{xy} are located at the free surface. In the other the vertical displacement or particle-velocity component and T_{zx} and T_{zy} are at the free surface. Rodrigues (1993) developed a 3D 8^{th}-order staggered-grid displacement-stress scheme and used the stress-imaging technique for the first location. He found it is necessary to use more than twice the number of grid points compared to inside the medium in order to avoid a significant numerical dispersion. Therefore, he combined the stress-imaging technique with a vertically refined grid near the free surface and achieved good accuracy. Such approach reduces the number of grid spacing per minimum wavelength but needs three times smaller time step (the factor of 3 is due to the most natural refinement of the staggered-grid).

Kristek et al. (2002) numerically tested the stress imaging for both locations of the free surface against the discrete-wavenumber method. They demonstrated that in the 3D case the stress-imaging technique in the 4^{th}-order FD modeling requires at least twice as many grid points per wavelength compared to what is sufficient inside the medium if the Rayleigh waves are to be propagated without significant grid dispersion even in the case of the simple homogeneous half-space. They also tested the 4^{th}-order version of the Rodrigues (1993) approach and found it sufficiently accurate. As already mentioned, the drawback of the approach is the three times smaller time step.

9.2.2 Adjusted FD Approximation

It is obvious that either at least twice denser spatial sampling or three times smaller time step considerably degrade the efficiency of the 4^{th}-order staggered-grid modeling inside the medium. Kristek et al. (2002) and Moczo et al. (2004a) therefore developed the adjusted FD approximation (AFDA) technique.

In their approach zero values of σ_{zz} are prescribed at the free surface in the H formulation or zero values of σ_{zx} and σ_{zy} in the W formulation. One-sided FD approximations are used to calculate the z-derivatives at the grid points at the free surface and depths $h/2$ and h. The approximations use only values in the medium, that is, no values are assumed above the free surface. Kristek et al. (2002) showed that while H-AFDA gives slightly better phases, W-AFDA gives better amplitudes. They concluded with the recommendation to use W-AFDA for the earthquake ground motion modeling. The calculation of the stress-tensor and displacement components in W-AFDA can be summarized as follows (if the velocity-stress formulation is considered, displacement components are simply replaced by the particle-velocity components):

Application of the boundary condition:

$$T_{zx}(0) \;=\; 0\;, \qquad T_{zy}(0) \;=\; 0\;. \tag{9.10}$$

Consider the following one-sided approximations to the first derivative with respect to the z

coordinate:

$$\phi'(z_0) = \frac{1}{h}\,[\, -\tfrac{352}{105}\phi(z_0) + \tfrac{35}{8}\phi(z_0+\tfrac{1}{2}h) - \tfrac{35}{24}\phi(z_0+\tfrac{3}{2}h) + \tfrac{21}{40}\phi(z_0+\tfrac{5}{2}h) - \tfrac{5}{56}\phi(z_0+\tfrac{7}{2}h)] + O(h^4)\,, \tag{9.11}$$

$$\phi'(z_0) = \frac{1}{h}\,[\, -\tfrac{11}{12}\phi(z_0-\tfrac{1}{2}h) + \tfrac{17}{24}\phi(z_0+\tfrac{1}{2}h) + \tfrac{3}{8}\,\phi(z_0+\tfrac{3}{2}h) - \tfrac{5}{24}\phi(z_0+\tfrac{5}{2}h) + \tfrac{1}{24}\phi(z_0+\tfrac{7}{2}h)] + O(h^4)\,, \tag{9.12}$$

$$\phi'(z_0) = \frac{1}{h}\,[\, -\tfrac{1}{22}h\;\phi'(z_0-h) - \tfrac{577}{528}\phi(z_0-\tfrac{1}{2}h) + \tfrac{201}{176}\phi(z_0+\tfrac{1}{2}h) - \tfrac{9}{176}\phi(z_0+\tfrac{3}{2}h) + \tfrac{1}{528}\phi(z_0+\tfrac{5}{2}h)] + O(h^4)\,, \tag{9.13}$$

$$\phi'(z_0) = \frac{1}{h}\,[\, \tfrac{16}{105}\phi(z_0-h) - \tfrac{31}{24}\phi(z_0-\tfrac{1}{2}h) + \tfrac{29}{24}\,\phi(z_0+\tfrac{1}{2}h) - \tfrac{3}{40}\phi(z_0+\tfrac{3}{2}h) + \tfrac{1}{168}\phi(z_0+\tfrac{5}{2}h)] + O(h^4)\,. \tag{9.14}$$

Then the stress-tensor components can be calculated using FD schemes defined as follows:

$T_{xx}(h/2)$ is obtained from the 4^{th}-order FD approximation to Hooke's law for σ_{xx}; derivative $u_{z,z}$ is approximated by formula (9.12).

$T_{yy}(h/2)$ and $T_{zz}(h/2)$ – similar to $T_{xx}(h/2)$.

$T_{zx}(h)$ is obtained from the 4^{th}-order FD approximation to Hooke's law for σ_{zx}; derivative $u_{x,z}$ is approximated by formula (9.13) in which $u_{x,z}\,(0)$ is replaced by $u_{z,x}$ due to condition $\sigma_{zx}(0) = 0$.

$T_{zy}(h)$ is obtained from the 4^{th}-order FD approximation to Hooke's law for σ_{zy}; derivative $u_{y,z}$ is approximated by formula (9.13) in which $u_{y,z}\,(0)$ is replaced by $u_{z,y}$ due to condition $\sigma_{zy}(0) = 0$.

Similarly, approximations (9.11) - (9.14) can be used to calculate the displacement-vector components. The corresponding FD schemes are defined as follows:

$W(0)$ is obtained from the 4^{th}-order FD approximation to the equation of motion for u_z; derivative $\sigma_{zz,z}$ is approximated by formula (9.11) in which condition $\sigma_{zz}(0) = 0$ is used.

$U(h/2)$ is obtained from the 4^{th}-order FD approximation to the equation of motion for u_x; derivative $\sigma_{zx,z}$ is approximated by formula (9.12).

$V(h/2)$ is obtained from the 4^{th}-order FD approximation to the equation of motion for u_y; derivative $\sigma_{zy,z}$ is approximated by formula (9.12).

$W(h)$ is obtained from the 4^{th}-order FD approximation to the equation of motion for u_z; derivative $\sigma_{zz,z}$ is approximated by formula (9.14) in which condition $\sigma_{zz}(0) = 0$ is used.

Displacement (or particle-velocity) component W, and stress-tensor components σ_{zx} and σ_{yz} are located at the free surface. The corresponding grid material parameters are evaluated as integral averages in the half grid-cell volumes, that is, the upper half of the volume located above the free surface is not taken into account. For example, density and unrelaxed moduli are

evaluated as

$$\rho^A_W \;=\; \rho^A_{I+1/2,\,J+1/2,\,0} \;=\; \frac{2}{h^3}\int_{x_I}^{x_{I+1}}\int_{y_J}^{y_{J+1}}\int_{z_0}^{z_{1/2}} \rho \,\mathrm{d}x\,\mathrm{d}y\,\mathrm{d}z\;, \tag{9.15}$$

$$\mu^H_{zx} \;=\; \mu^H_{I\quad,\,J+1/2,\,0} \;=\; \left[\frac{2}{h^3}\int_{x_{I-1/2}}^{x_{I+1/2}}\int_{y_J}^{y_{J+1}}\int_{z_0}^{z_{1/2}} \frac{1}{\mu}\,\mathrm{d}x\,\mathrm{d}y\,\mathrm{d}z\right]^{-1}, \tag{9.16}$$

$$\mu^H_{yz} \;=\; \mu^H_{I+1/2,\,J\quad,\,0} \;=\; \left[\frac{2}{h^3}\int_{x_I}^{x_{I+1}}\int_{y_{J-1/2}}^{y_{J+1/2}}\int_{z_0}^{z_{1/2}} \frac{1}{\mu}\,\mathrm{d}x\,\mathrm{d}y\,\mathrm{d}z\right]^{-1}. \tag{9.17}$$

Kristek et al. (2002) performed numerical comparisons of the W-AFDA technique against the discrete-wavenumber method (Bouchon, 1981; Coutant, 1989). The numerical comparison showed that with the W-AFDA technique it is possible to apply the same spatial sampling as inside the medium. Moczo et al. (2004a) tested the accuracy of the W-AFDA technique against the finite-element method for models with near-surface material interfaces. The numerical comparison showed very good level of accuracy of the W-AFDA technique and its capability of the FD scheme to sense the true position of the material interfaces in the spatial grid.

9.3 Conventional Scheme for the 1D Problem - One-sided Approximation

In this section we will return to the FD targets for the free surface and find corresponding 2^{nd}-order (in time and space) conventional-grid displacement FD schemes. Consider for simplicity a homogeneous halfspace. It is clear from the summary of the targets, section 8.2, that we can consider two principal types of targets, FDTarget1,

$$\rho\,\ddot{u} \;-C\,u_{,zz} \;=\; 0\,, \quad C\,u_{,z} \;=\; 0 \quad \text{at} \quad z=a, \tag{9.18}$$

and FDTarget2,

$$\rho\,\ddot{u} \;-C\,u_{,zz} \;-\frac{2W}{h}\,C\,u_{,z} \;=\; 0 \quad \text{at} \quad z=a. \tag{9.19}$$

We took the target with an undetermined weight coefficient W in the boundary term because this coefficient depends on a particular approximation.

Consider first FDTarget1. Because it is reasonable to use a centered FD approximation to the time derivative, we can focus on finding a one-sided FD approximation to term $C\,u_{,zz}$. Assume the following approximation:

$$-C\,u_{,zz}\,(z) \;\doteq\; c_1\,u(t,z) \;+\; c_2\,u(t,z+h) \;+\; c_3\,u(t,z+2h)\,, \tag{9.20}$$

Apply Taylor expansion (TE) to the r.h.s. ot the equation and require that coefficients of the Taylor expansion at u, $u_{,z}$ and $u_{,zz}$ be equal to 0, 0 and $-C$, respectively, that is,

$$coef\mathrm{TE}\_u \;=\; 0\,,\; coef\mathrm{TE}\_u_{,z} \;=\; 0\,,\; coef\mathrm{TE}\_u_{,zz} \;=\; -C\,. \tag{9.21}$$

Solving the obtained system of equations for unknown coefficients c_1, c_2 and c_3, we get

$$\begin{aligned} -\,C\,u_{,zz}\,(t,z) \;&=\; -\frac{1}{h^2}\,C\,[\,u(t,z) \;-\; 2\,u(t,z+h) \;+\; u(t,z+2h)\,] \;+ \\ &+\; C\,u_{,zzz}\,(z)\,h \;+\; O(h^2)\,. \end{aligned} \tag{9.22}$$

Clearly, the use of only three points (z, $z+h$ and $z+2h$) and the above conditions yield only the $1^{\rm st}$-order approximation. In order to increase the order of approximation we could consider an additional point, for example, $(z+3h)$. It is, however, much better to keep the number of points as low as possible. We can have an additional condition by considering the zero traction at the free surface, that is, $C\,u_{,z} = 0$. We can include the boundary condition by allowing $u_{,z}$ to appear in the Taylor expansion of the r.h.s. of eq. (9.20). Accordingly, we modify conditions for coefficients of the Taylor expansion:

$$\begin{aligned} coef\text{TE\_}u \;&=\; 0 \;\;,\;\; coef\text{TE\_}u_{,z} \;=\; d\,, \\ coef\text{TE\_}u_{,zz} \;&=\; -C \;\;,\;\; coef\text{TE\_}u_{,zzz} \;=\; 0\,, \end{aligned} \tag{9.23}$$

where d is unknown. We obtain

$$\begin{aligned} -\,C\,u_{,zz}\,(z) \;&=\; -\frac{1}{h^2}\,C\,\left[\,-\frac{7}{2}u(t,z) \;+\; 4\,u(t,z+h) \;-\; \frac{1}{2}u(t,z+2h)\,\right] \;+ \\ &+\;\; \frac{3}{h}C\,u_{,z}\,(z) \;+\; O(h^2)\,. \end{aligned} \tag{9.24}$$

Because $C\,u_{,z} = 0$ at the free surface, the first line of the r.h.s. of eq. (9.24) can be taken as the one-sided $2^{\rm nd}$-order approximation to $C\,u_{,zz}\,(z)$ at the free surface. Consequently, the one-sided $2^{\rm nd}$-order (in time and space) approximation to the whole FDTarget1, eq. (9.18), can be

$$\begin{aligned} &\frac{1}{\Delta^2 t}\;\; \rho(a)\;[\,u(t+\Delta t,a) \;-\; 2\,u(t,a) \;+\; u(t-\Delta t,a)\,] \;- \\ &-\;\;\; \frac{1}{h^2}\,C(a)\,\left[\,-\frac{7}{2}u(t,a) \;+\; 4\,u(t,a+h) \;\;-\frac{1}{2}u(t,a+2h)\,\right] \;= \\ &=\;\;\; \rho(a)\,\ddot{u}(t,a) \;-\; C(a)\,u_{,zz}\,(t,a) \;+ \\ &+\;\;\; \frac{1}{6}C\,u^{(0,4)}\,h^2 \;+\; \frac{1}{12}\rho\,u^{(4,0)}\,\Delta^2 t \;+\; O(h^3) + \;O(\Delta^4 t)\,, \end{aligned} \tag{9.25}$$

where $u^{(4,0)} = \partial^4 u/\partial t^4$ and $u^{(0,4)} = \partial^4 u/\partial z^4$.

Looking at eq. (9.24) we can realize that if the FD operator on the l.h.s. of eq. (9.25) is applied to a modified target,

$$\rho\,\ddot{u} \;-C\,u_{,zz} \;-\frac{3}{h}\,C\,u_{,z} \;=\; 0 \quad \text{at} \quad z=a, \tag{9.26}$$

the truncation error will be the same - the one in the last line in eq. (9.25). In other words, the presence of term $-\frac{3}{h}\,C\,u_{,z}$ yields a formal $2^{\rm nd}$-order approximation without an additional explicit application of the zero-traction boundary condition. This naturally leads us to proceed with approximating FDTarget2, eq. (9.19).

Assuming again the use of the centered FD approximation to the time derivative, try approximation, compare with eq. (9.20),

$$-C\,u_{,zz}\,(z) \;\;-\;\frac{2W}{h}\,C\,u_{,z} \;\doteq\; c_1\,u(t,z) \;+\; c_2\,u(t,z+h) \;+\; c_3\,u(t,z+2h)\,. \tag{9.27}$$

Application of the Taylor expansion to the r.h.s. of the equation and requirement of

$$\begin{aligned} coef\text{TE\_}u \;&=\; 0 \;\;,\;\; coef\text{TE\_}u_{,z} \;=\; -\frac{2W}{h}\,C\,, \\ coef\text{TE\_}u_{,zz} \;&=\; -C \;\;,\;\; coef\text{TE\_}u_{,zzz} \;=\; 0 \end{aligned} \tag{9.28}$$

yields

$$\begin{aligned} -\,C\,u_{,zz}\,(z) \;-\; \frac{3}{h}C\,u_{,z}\,(z) \;=\; & \\ -\;\frac{1}{h^2}\,C\,\left[\,-\frac{7}{2}u(t,z) \;+\; 4\,u(t,z+h) \;-\; \frac{1}{2}u(t,z+2h)\,\right] & \\ +\;\; O(h^2)\,. & \end{aligned} \tag{9.29}$$

Equation (9.29) is equivalent to eq. (9.24). The approximation to the whole FDTarget2 is

$$\begin{aligned} &\frac{1}{\Delta^2 t}\;\;\rho(a)\;[\;u(t+\Delta t,a)\;-\;2\,u(t,a)\;+\;u(t-\Delta t,a)\;]\;- \\ &-\;\;\frac{1}{h^2}\,C(a)\,\left[\,-\frac{7}{2}u(t,a)\;+\;4\,u(t,a+h)\;-\;\frac{1}{2}u(t,a+2h)\,\right]\;= \\ &=\;\;\rho(a)\,\ddot{u}(t,a)\;-\;C(a)\,u_{,zz}\,(t,a)\;-\;\frac{3}{h}C(a)\,u_{,z}\,(a)\;+ \\ &+\;\;\frac{1}{6}C\,u^{(0,4)}\,h^2\;+\;\frac{1}{12}\rho\,u^{(4,0)}\,\Delta^2 t\;+\;O(h^3)+\;O(\Delta^4 t)\,. \end{aligned} \tag{9.30}$$

The first finding is that the 3-point one-sided 2^{nd}-order approximations to FDTarget1 and FDTarget2 yield the same FD scheme. The second finding is that the approximating of FDTarget2 is straightforward and more elegant: the 2^{nd}-order operator is obtained 'automatically', that is, without an explicit application of the zero-traction boundary condition to the truncation error. This obviously is due to the explicit presence of the boundary term in the ISF-equation of motion. While the difference between the two procedures may seem negligible we have to realize that the approximations were, in fact, trivial. The advantage of manipulating the FD targets with boundary term(s) will become more obvious in more complicated cases.

9.4 Optimally-accurate Scheme for the 1D Problem

Based on the findings in 9.3 here we directly address FD target with the boundary term(s). Our goal is to find an optimally accurate FD approximation. Assume the approximation in the form

$$OAFDE \;=\; [\;A_I^m(p,q) - K_I^m(p,q)\;]\;u_I^m(p,q) \;\doteq\; 0\,; \quad p,\,q \in \{1,2,3\}\,, \tag{9.31}$$

where p is the time summation index and q the spatial summation index. The summation convention is assumed in eq. (9.31), that is, no matrix multiplication is applied. Displacement values involved are

$$u_I^m(p,q) \;=\; u\,[\,t_m + (2-p)\Delta t,\; z_I + (q-1)h\,]\,; \quad p\,,q\;\in\{1,2,3\}\,, \tag{9.32}$$

or, in the matrix form,

$$\mathbf{u}_I^m \;=\; \begin{bmatrix} u(t_m+\Delta t\ ,z_I) & u(t_m+\Delta t\ ,z_I+h) & u(t_m+\Delta t\ ,z_I+2h) \\ u(t_m\qquad\ \ ,z_I) & u(t_m\qquad\ \ ,z_I+h) & u(t_m\qquad\ \ ,z_I+2h) \\ u(t_m-\Delta t\ ,z_I) & u(t_m-\Delta t\ ,z_I+h) & u(t_m-\Delta t\ ,z_I+2h) \end{bmatrix} . \tag{9.33}$$

For brevity we will use grid indices. Then eq. (9.33) can be written as

$$\mathbf{u}_I^m \;=\; \begin{bmatrix} u_I^{m+1} & u_{I+1}^{m+1} & u_{I+2}^{m+1} \\ u_I^m & u_{I+1}^m & u_{I+2}^m \\ u_I^{m-1} & u_{I+1}^{m-1} & u_{I+2}^{m-1} \end{bmatrix} . \tag{9.34}$$

Operators $\mathbf{A}_I^m$ and $\mathbf{K}_I^m$ are

$$\mathbf{A}_I^m \;=\; \frac{\rho}{\Delta^2 t} \begin{bmatrix} a_I^{m+1} & a_{I+1}^{m+1} & a_{I+2}^{m+1} \\ a_I^m & a_{I+1}^m & a_{I+2}^m \\ a_I^{m-1} & a_{I+1}^{m-1} & a_{I+2}^{m-1} \end{bmatrix} \tag{9.35}$$

and

$$\mathbf{K}_I^m \;=\; \frac{C}{h^2} \begin{bmatrix} k_I^{m+1} & k_{I+1}^{m+1} & k_{I+2}^{m+1} \\ k_I^m & k_{I+1}^m & k_{I+2}^m \\ k_I^{m-1} & k_{I+1}^{m-1} & k_{I+2}^{m-1} \end{bmatrix} . \tag{9.36}$$

Equation (9.31) means that we have to determine 18 unknown elements of operators $\mathbf{A}_I^m$ and $\mathbf{K}_I^m$.

We try to approximate the second spatial derivative using three spatial positions over three time levels. Similarly, we want to approximate the time derivative using three time levels over three spatial positions. We saw before that the boundary term in FDTarget2 depended also on a particular FD approximation. Therefore, in this case, we should allow for presence of time derivatives of traction in the target - in addition to the original boundary term with traction itself, see eq. (9.19). Thus, seeking for an optimally accurate approximation we modify FDTarget2:

$$\begin{aligned} EBT \;&=\; \rho\,\ddot{u} \;-\; C\,u_{,zz} \\ &+\; C\,\Big(\, b_1 u^{(0,1)} \;+\; b_2 u^{(1,1)} \;+\; b_3 u^{(2,1)} \;+\; b_4 u^{(3,1)} \;+\; b_5 u^{(4,1)} \,\Big) = 0\,, \end{aligned} \tag{9.37}$$

where $u^{(k,l)} = \partial^k \partial^l u / \partial t^k \partial z^l$. In an optimally accurate approximations we require that the leading term of the truncation error vanishes if the operator is applied to normal modes (which satisfy equation of motion without a body-force term), see Geller and Takeuchi (1995) and Moczo et al. (2007). Let

$$E \;=\; \rho\,\ddot{u} \;-\; C\,u_{,zz}\ . \tag{9.38}$$

In the case of the centered approximation, using $u(t, z-h)$, $u(t,z)$ and $u(t,z+h)$, to the derivative at z, the optimally accurate operator requires presence of $E^{(2,0)}$ and $E^{(0,2)}$ in the

truncation error. If we use $u(t,z)$, $u(t,z+h)$ and $u(t,z+2h)$ for the derivative at z, we should allow for presence of other derivatives of E too. Considering truncation error,

$$\text{TrunError} \;=\; \text{TaylorExpansion}\,\{OAFDE\} \;-\; EBT \;, \tag{9.39}$$

we require

$$\begin{aligned}\text{TrunError} \;=\;& e_1 E^{(2,0)} \;+\; e_2 E^{(0,2)} \;+\; e_3 E^{(1,1)} \;+\; e_4 E^{(0,3)} \;+ \\ &+\; e_5 E^{(1,2)} \;+\; e_6 E^{(2,1)} \;+\; e_7 E^{(3,0)} \;+ \\ &+\; O\left(\,\Delta^k t \cdot h^l\,\right)\;;\; k+l \geq 4\;.\end{aligned} \tag{9.40}$$

Note that $E^{(1,0)}$ and $E^{(0,1)}$ cannot be present if the 2^{nd}-order accuracy in time and space is required. Condition $k+l \geq 4$ for $O\left(\,\Delta^k t \cdot h^l\,\right)$ means that we want the 4^{th}-order accuracy in time and space in the case of normal modes.

Because it is technically easier to work with one matrix, we rewrite eq. (9.31) in the form

$$OAFDE \;=\; G_I^m(p,q)\, u_I^m(p,q) \;\doteq\; 0\,; \quad p,\, q \in \{1,2,3\}\,. \tag{9.41}$$

We find that $G[3,3]$ is a free parameter - any value of $G[3,3]$ will give the desired structure of the truncation error. Having freedom to choose, we require $-C\Delta^2 t\cdot h - 2h^3(\rho - 12\Delta^2 t\cdot G[3,3]) = 0$, which eliminates the lowest-order error term that can be eliminated if operand is not a normal mode. Eventually, in this case it is possible to separate matrix $\mathbf{G}_I^m$ into matrices $\mathbf{A}_I^m$ and $\mathbf{K}_I^m$. We obtain

$$\mathbf{A}_I^m \;=\; \frac{\rho}{24\Delta^2 t}\begin{bmatrix} 38 & -16 & 2 \\ -76 & 32 & -4 \\ 38 & -16 & 2 \end{bmatrix} \tag{9.42}$$

and

$$\mathbf{K}_I^m \;=\; \frac{C}{24h^2}\begin{bmatrix} 7 & -8 & 1 \\ 70 & -80 & 10 \\ 7 & -8 & 1 \end{bmatrix}\;. \tag{9.43}$$

Considering the above approximations also as a preparation for the welded material interface we will continue with looking for approximations for the welded interface.

10 Finite-difference Schemes for the Welded Material Interface

10.1 Conventional Approximation for the Welded Interface

Our main goal is to find a 2^{nd}-order optimally accurate FD approximation for the grid point at the interface, not necessarily approximation, that would lead to a heterogeneous FD scheme (that is, the same FD scheme for all interior grid points). For obvious reason, see section 7.4.4, we will first find a conventional FD scheme. Consider for simplicity a welded interface between

two homogeneous media and omit a body-force term. Our target with the boundary term is, see eq. (8.32),

$$\frac{1}{2}\,(\rho^- + \rho^+)\,\ddot{u} \;-\; \frac{1}{2}\,\big(\,C^- u^-_{,zz} + C^+ u^+_{,zz}\,\big) \\ -\; \frac{W}{h}\,\big(\,C^+ u^+_{,z} - C^- u^-_{,z}\,\big) \;=\; 0 \quad \text{at} \quad z = a. \tag{10.1}$$

Again we will use the centered approximation for the time derivative. If we do not want to neglect the averaging of derivatives of tractions, we have to find 2^{nd}-order one-sided approximations to

$$-\,\frac{1}{2}\,C^- u^-_{,zz} + \frac{W}{h}\,C^- u^-_{,z} \tag{10.2}$$

and

$$-\,\frac{1}{2}\,C^+ u^+_{,zz} - \frac{W}{h}\,C^+ u^+_{,z}\;. \tag{10.3}$$

The approximations are, compare with eqs. (9.26) - (9.29),

$$-\,\frac{1}{2}\,C^- u^-_{,zz}\,(z) \;+\; \frac{3}{2h}\,C^- u^-_{,z}\,(z) \;= \\ =\; -\frac{1}{2h^2}\,C^-\,\left[\,-\frac{7}{2}u(t,z) \;+\; 4\,u(t,z-h) \;-\frac{1}{2}u(t,z-2h)\,\right] \\ +\; O(h^2) \tag{10.4}$$

and

$$-\,\frac{1}{2}\,C^+ u^+_{,zz}\,(z) \;-\; \frac{3}{2h}\,C^+ u^+_{,z}\,(z) \;= \\ =\; -\frac{1}{2h^2}\,C^+\,\left[\,-\frac{7}{2}u(t,z) \;+\; 4\,u(t,z+h) \;-\frac{1}{2}u(t,z+2h)\,\right] \\ +\; O(h^2)\,. \tag{10.5}$$

Application of the centered approximation o the 2^{nd} time derivative, substitution of the l.h.s. of eqs. (10.4) and (10.5), and consideration of the displacement continuity in target (10.1) yields

$$\frac{1}{\Delta^2 t}\;\frac{1}{2}\,(\rho^- + \rho^+)\;[\;u(t+\Delta t,a) \;-\; 2\,u(t,a) \;+\; u(t-\Delta t,a)\;] \;- \\ -\quad \frac{1}{2h^2}\left\{\,-\frac{7}{2}\,\big[\,C^-(a) + C^+(a)\,\big]\,u(t,a) + \right. \\ +\quad C^-(a)\left[4\,u(t,a-h) \;-\; \frac{1}{2}\,u(t,a-2h)\right] \;+ \\ \left. +\quad C^+(a)\left[4\,u(t,a+h) \;-\; \frac{1}{2}\,u(t,a+2h)\right]\right\} \;=$$

$$
\begin{aligned}
&= \frac{1}{2}\,(\rho^- + \rho^+)\;\ddot{u}(t,a) \;-\; \frac{1}{2}\,\big[\, C^- u^-_{,zz}\,(t,a) \;+\; C^+ u^+_{,zz}\,(t,a)\,\big] \\
&- \frac{W}{h}\,\big[\, C^+ u^+_{,z}\,(t,a) \;-\; C^- u^-_{,z}\,(t,a)\,\big] \qquad (10.6)\\
&+ \; O(h^2) + \; O(\Delta^2 t)\,.
\end{aligned}
$$

10.2 Optimally-accurate Approximation for the Welded Interface

Consider FD target with boundary terms,

$$
\begin{aligned}
EBT \;=\; & \frac{1}{2}\,\big(\,\rho^-\,\ddot{u}^- \;-\; C^-\,u^-_{,zz}\,\big) \;+\; \frac{1}{2}\,\big(\,\rho^+\,\ddot{u}^+ \;-\; C^+\,u^+_{,zz}\,\big) \;+ \qquad (10.7)\\
&+\; C^-\,\Big(\, b_1^- u^{-(0,1)} \;+\; b_2^- u^{-(1,1)} \;+\; b_3^- u^{-(2,1)} \;+\; b_4^- u^{-(3,1)} \;+\; b_5^- u^{-(4,1)}\,\Big) \;+ \\
&+\; C^+\,\Big(\, b_1^+ u^{+(0,1)} \;+\; b_2^+ u^{+(1,1)} \;+\; b_3^+ u^{+(2,1)} \;+\; b_4^+ u^{+(3,1)} \;+\; b_5^+ u^{+(4,1)}\,\Big) \;= 0\,,
\end{aligned}
$$

which corresponds to the target considered for the free surface, eq. (9.37). Denote

$$E^- \;=\; \rho^-\,\ddot{u}^- \;-\; C^-\,u^-_{,zz}\;, \qquad (10.8)$$

$$E^+ \;=\; \rho^+\,\ddot{u}^+ \;-\; C^+\,u^+_{,zz}\;. \qquad (10.9)$$

Assume an optimally accurate approximation in the form

$$OAEFD \;=\; G_I^m(p,q)\,u_I^m(p,q) \;\doteq\; 0\,; \quad p \in \{1,2,3\}\,,\;\; q \in \{-1,0,1,2,3\} \qquad (10.10)$$

with

$$u_I^m(p,q) \;=\; [\,t_m + (2-p)\Delta t,\; z_I + (q-1)h\,]\;. \qquad (10.11)$$

We want the $2^{\rm nd}$-order optimally accurate approximations from both sides of the interface. Therefore we consider truncation error

$$
\begin{aligned}
\text{TrunError} \;&=\; \text{TaylorExpansion}\,\{OAFDE\} \;-\; EBT \;= \\
&=\; \text{TrunError}^- \;+\; \text{TrunError}^+ \qquad (10.12)
\end{aligned}
$$

and require, compare with eqs. (9.39) and (9.40),

$$
\begin{aligned}
\text{TrunError}^- \;=\; & e_1^- E^{-(2,0)} \;+\; e_2^- E^{-(0,2)} \;+\; e_3^- E^{-(1,1)} \;+\; e_4^- E^{-(0,3)} \;+ \\
&+\; e_5^- E^{-(1,2)} \;+\; e_6^- E^{-(2,1)} \;+\; e_7^- E^{-(3,0)} \;+ \qquad (10.13)\\
&+\; O\,\big(\,\Delta^k t \cdot h^l\,\big)\;;\; k+l \geq 4
\end{aligned}
$$

and

$$
\begin{aligned}
\text{TrunError}^+ \;=\; & e_1^+ E^{+(2,0)} \;+\; e_2^+ E^{+(0,2)} \;+\; e_3^+ E^{+(1,1)} \;+\; e_4^+ E^{+(0,3)} \;+ \\
&+\; e_5^+ E^{+(1,2)} \;+\; e_6^+ E^{+(2,1)} \;+\; e_7^+ E^{+(3,0)} \;+ \qquad (10.14)\\
&+\; O\,\big(\,\Delta^k t \cdot h^l\,\big)\;;\; k+l \geq 4\,.
\end{aligned}
$$

Requiring antisymmetry of coefficients in the boundary terms,

$$b_i^- = -b_i^+ \; ; \; i \in \{1, 2, ..., 5\} \; , \tag{10.15}$$

and displacement continuity at the interface, we can solve for elements of matrix $\mathbf{G}_I^m$ in eq. (10.10). We obtain

$$\begin{aligned}
\mathbf{G}_I^m \;=\; & \frac{\rho^-}{15\Delta^2 t}\begin{bmatrix} -1 & -1 & 17 & 0 & 0 \\ 2 & -2 & -34 & 0 & 0 \\ -1 & -1 & 17 & 0 & 0 \end{bmatrix} + \frac{\rho^+}{15\Delta^2 t}\begin{bmatrix} 0 & 0 & 17 & -1 & -1 \\ 0 & 0 & -34 & 2 & 2 \\ 0 & 0 & 17 & -1 & -1 \end{bmatrix} + \\
+ \; & \frac{C^-}{24h^2}\begin{bmatrix} 1 & -8 & 7 & 0 & 0 \\ 10 & -80 & 70 & 0 & 0 \\ 1 & -8 & 7 & 0 & 0 \end{bmatrix} + \frac{C^+}{24h^2}\begin{bmatrix} 0 & 0 & 7 & -8 & 1 \\ 0 & 0 & 70 & -80 & 10 \\ 0 & 0 & 7 & -8 & 1 \end{bmatrix} + \\
+ \; & \frac{C^-\rho^+}{10\Delta^2 t C^+}\begin{bmatrix} 1 & -4 & 3 & 0 & 0 \\ -2 & 8 & -6 & 0 & 0 \\ 1 & -4 & 3 & 0 & 0 \end{bmatrix} + \frac{C^+\rho^-}{10\Delta^2 t C^-}\begin{bmatrix} 0 & 0 & 3 & -4 & 1 \\ 0 & 0 & -6 & 8 & -2 \\ 0 & 0 & 3 & -4 & 1 \end{bmatrix} \; .
\end{aligned} \tag{10.16}$$

Because eqs. (10.10) and (10.16) define an implicit scheme, we would like to avoid solving large system of algebraic equations by applying the predictor-corrector algorithm, see section 7.4.4. However, we were unable to find and apply the predictor-corrector algorithm in this case. We see a likely reason in a fact that the structure of matrix $\mathbf{G}_I^m$ is not consistent with the Born approximation which was used to obtain the predictor-corrector scheme.

Therefore we have to find some other optimally accurate approximation to our target (10.7). Assume an optimally accurate approximation in the form

$$OAEFD \;=\; G_I^m(p,q)\, u_I^m(p,q) \doteq 0 \,; \quad p \in \{1,2,3\} \,, \;\; q \in \{-2,-1,0,1,2,3,4\} \tag{10.17}$$

with

$$u_I^m(p,q) \;=\; [\, t_m + (2-p)\Delta t,\; z_I + (q-1)h \,] \; . \tag{10.18}$$

Compared to approximation (10.10) we involve two more spatial grid positions and make the spatial stencil longer. Because we found an optimally accurate approximation even for 5 grid points, the use of two more points yields a problem with an infinite number of solutions. This implies that we have more freedom to choose conditions on the solution. We tried several conditions and eventually we decided for

$$b_1^- = -b_1^+ = \frac{10}{3h} \; , \;\; b_i^- = b_i^+ = 0 \; ; \;\; i \in \{2, ..., 5\} \; . \tag{10.19}$$

With this particular choice the resulting scheme is relative simple and enables application of the

predictor-corrector algorithm. The obtained matrix $\mathbf{G}_I^m$ is

$$\begin{aligned}
\mathbf{G}_I^m &= \frac{\rho^-}{12\Delta^2 t}\begin{bmatrix} 1 & -4 & 5 & 10 & 0 & 0 & 0 \\ -2 & 8 & -10 & -20 & 0 & 0 & 0 \\ 1 & -4 & 5 & 10 & 0 & 0 & 0 \end{bmatrix} + \\
&+ \frac{\rho^+}{12\Delta^2 t}\begin{bmatrix} 0 & 0 & 0 & 10 & 5 & -4 & 1 \\ 0 & 0 & 0 & -20 & -10 & 8 & -2 \\ 0 & 0 & 0 & 10 & 5 & -4 & 1 \end{bmatrix} + \\
&+ \frac{C^-}{12h^2}\begin{bmatrix} 1 & -4 & 5 & -2 & 0 & 0 & 0 \\ -10/3 & 20 & -70 & 160/3 & 0 & 0 & 0 \\ 1 & -4 & 5 & -2 & 0 & 0 & 0 \end{bmatrix} + \\
&+ \frac{C^+}{12h^2}\begin{bmatrix} 0 & 0 & 0 & -2 & 5 & -4 & 1 \\ 0 & 0 & 0 & 160/3 & -70 & 20 & -10/3 \\ 0 & 0 & 0 & -2 & 5 & -4 & 1 \end{bmatrix} .
\end{aligned} \tag{10.20}$$

10.3 Heterogeneous Schemes: DSstag4, Dconv2, Doptm2

In the previous sections we derived conventional and optimally accurate approximations for the welded material interface in the 1D problem. The obtained approximations are 2^{nd}-order accurate in time and space. They can be combined with 2^{nd}-order accurate schemes for interior grid points away from the interface. In such a case, one scheme is applied at the grid point at the interface, other scheme is applied at grid points away from the interface. We will consider such approach in the next section. Here we briefly present heterogeneous schemes – one scheme is applied to all interior grid points no matter what are their positions with respect to the material interface.

Kristek and Moczo (2006) presented three heterogeneous schemes for the 1D heterogeneous formulations (8.46) to (8.50) – DSstag4, Dconv2 and Doptm2.

DSstag4. The displacement-stress (DS), staggered-grid (stag) scheme that is 2^{nd}-order accurate in time and 4^{th}-order accurate in space in the homogeneous medium can be written in the form

$$\begin{aligned}
T_{I+1/2}^m &= C_{I+1/2}^H \frac{1}{h}\left[a\,\left(U_{I+2}^m - U_{I-1}^m\right) \;+\; b\,\left(U_{I+1}^m - U_I^m\right)\right], \\
U_I^{m+1} &= 2U_I^m \;-\; U_I^{m-1} \\
&\quad + \frac{1}{\rho_I^A}\frac{\Delta^2 t}{h}\left[a\,\left(T_{I+3/2}^m - T_{I-3/2}^m\right) \;+\; b\,\left(T_{I+1/2}^m - T_{I-1/2}^m\right)\right],
\end{aligned} \tag{10.21}$$

where $T_{I+1/2}^m$ and U_I^m are discrete approximations to stress and displacement, respectively, and $a = -1/24$, $b = 9/8$. The effective density and elastic modulus are defined by

$$\rho_I^A = \frac{1}{h}\int_{z_{I-1/2}}^{z_{I+1/2}} \rho(z)\;\mathrm{d}z \tag{10.22}$$

and

$$C^H_{I+1/2} \;=\; \left[\frac{1}{h}\int_{z_I}^{z_{I+1}} \frac{1}{C\,(z)}\,dz\right]^{-1} . \tag{10.23}$$

The scheme degenerates to the $1^{\rm st}$-order accuracy at the grid point located directly at the material interface. It can be easily shown that this is due to the averaging of the $1^{\rm st}$-order one-sided approximations to the stress derivatives.

Scheme (10.21) is be applied at all interior grid points. In principle, the interface is not necessarily located at the grid point – it can be anywhere in between two grid points. Still the scheme can sense the position of the interface if the effective material parameters are evaluated using eqs. (10.22) and (10.23).

Dconv2 and Doptm2. Dconv2 means displacement $2^{\rm nd}$-order scheme based on conventional approximation. Doptm2 means displacement $2^{\rm nd}$-order scheme based on the optimally accurate approximation. Both schemes are constructed on the conventional grid.

In a simple approach we approximate single term $(C\,u_{,z}\,)_{,z}$ using the $2^{\rm nd}$-order central difference,

$$(C\,d_{,z}\,)_{,z}\,|_I \;\doteq\; \frac{1}{h}\,\Big(\; C\,u_{,z}\,|_{I+1/2} \;-\; C\,u_{,z}\,|_{I-1/2}\;\Big)\;, \tag{10.24}$$

instead of $2^{\rm nd}$-order approximations to the '$-$' and '$+$' terms in eq. (8.51). Then, we approximate $C\,u_{,z}$ in the same way as we approximated stress in the DS formulation.

As we showed in section 7.4.3, we can use the same form of presentation for both the conventional and optimally accurate schemes,

$$[\;A^m_I\,(p,q) \;-\; K^m_I\,(p,q)\;]\;\; U\,(M,i) \;\;=\;\; 0 \;\;;\quad p,\; q \in \{1,2,3\}\;, \tag{10.25}$$

where m is the time level, at which the equation of motion is approximated, I index of the grid spatial position at which the equation of motion is approximated, p time summation index, q spatial summation index. Discrete displacement values involved can be written in the matrix form as

$$\mathbf{U}^m_I \;=\; \begin{bmatrix} U^{m+1}_{I-1} & U^{m+1}_I & U^{m+1}_{I+1} \\ U^{m}_{I-1} & U^{m}_I & U^{m}_{I+1} \\ U^{m-1}_{I-1} & U^{m-1}_I & U^{m-1}_{I+1} \end{bmatrix} . \tag{10.26}$$

Operators $\mathbf{A}^m_I$ and $\mathbf{K}^m_I$ are

$$\mathbf{A}^m_I \;=\; \begin{bmatrix} a^{m+1}_{I-1}\,\rho_{I-1} & a^{m+1}_I\,\rho_I & a^{m+1}_{I+1}\,\rho_{I+1} \\ a^{m}_{I-1}\,\rho_{I-1} & a^{m}_I\,\rho_I & a^{m}_{I+1}\,\rho_{I+1} \\ a^{m-1}_{I-1}\,\rho_{I-1} & a^{m-1}_I\,\rho_I & a^{m-1}_{I+1}\,\rho_{I+1} \end{bmatrix} \tag{10.27}$$

and

$$\mathbf{K}^m_I \;=\; \begin{bmatrix} k^{m+1}_{I-1}\,C_{I-1} & k^{m+1}_I\,C_I & k^{m+1}_{I+1}\,C_{I+1} \\ k^{m}_{I-1}\,C_{I-1} & k^{m}_I\,C_I & k^{m}_{I+1}\,C_{I+1} \\ k^{m-1}_{I-1}\,C_{I-1} & k^{m-1}_I\,C_I & k^{m-1}_{I+1}\,C_{I+1} \end{bmatrix} . \tag{10.28}$$

For the conventional scheme Dconv2, the operators are specified as

$$\mathbf{A}_I^m = \frac{\rho_I^A}{\Delta^2 t} \begin{bmatrix} 0 & 1 & 0 \\ 0 & -2 & 0 \\ 0 & 1 & 0 \end{bmatrix} \tag{10.29}$$

and

$$\mathbf{K}_I^m = \frac{1}{h^2} \begin{bmatrix} 0 & 0 & 0 \\ 1 & -2 & 1 \\ 0 & 0 & 0 \end{bmatrix} \begin{bmatrix} C_{I-1/2}^H & 0 & 0 \\ 0 & \frac{1}{2}\left(C_{I-1/2}^H + C_{I+1/2}^H\right) & 0 \\ 0 & 0 & C_{I+1/2}^H \end{bmatrix} . \tag{10.30}$$

For the scheme based on the optimally-accurate approximation, Doptm2, the matrices are specified as

$$\mathbf{A}_I^m = \frac{\rho_I^A}{12\ \Delta^2 t} \begin{bmatrix} 1 & 10 & 1 \\ -2 & -20 & -2 \\ 1 & 10 & 1 \end{bmatrix} \tag{10.31}$$

and

$$\mathbf{K}_I^m = \frac{1}{12\ h^2} \begin{bmatrix} 1 & -2 & 1 \\ 10 & -20 & 10 \\ 1 & -2 & 1 \end{bmatrix} \begin{bmatrix} C_{I-1/2}^H & 0 & 0 \\ 0 & \frac{1}{2}\left(C_{I-1/2}^H + C_{I+1/2}^H\right) & 0 \\ 0 & 0 & C_{I+1/2}^H \end{bmatrix} . \tag{10.32}$$

The effective density and elastic modulus are defined by eqs. (10.22) and (10.23), that is, in the same way as in the staggered-grid scheme DSstag4.

Note that in the 1D case, Dconv2 is equivalent to DSstag2, which is the 2^{nd}-order displacement-stress staggered-grid FD scheme.

As scheme DSstag4, also scheme Dconv2 and Doptm2 degenerate to the 1^{st}-order accuracy at the grid point located directly at the material interface.

Kristek and Moczo (2006) performed detailed numerical comparisons of the three schemes using homogeneous space, two halfspaces in contact, and an interior layer with a strong velocity gradient. The model of the unbounded homogeneous space enabled to compare pure effect of the grid dispersion. The simulations for the model with a material interface we designed so that it was possible to separate error due to the interface. The third model enabled to compare capability of the schemes to account for a dramatic change of the velocity inside the layer between two identical halfspaces.

All simulations obtained with the FD schemes were compared against analytical matrix solutions. The level of accuracy of the FD solutions was quantified and characterized using the envelope and phase misfits with respect to the analytical solutions. Here we summarize the conclusions of the numerical investigations closely following Kristek and Moczo (2006):

Error of the FD schemes due to the grid dispersion in a homogeneous medium:

1. The error of Dconv2 (or, equivalently, DSstag2) considerably increases with distance due to the grid dispersion (except for the stability ratio $p = 1$ for which the scheme is accurate); the error can be reduced by drastic increase of the number of grid spacings per wavelength (N) and using the maximum possible stability ratio.
2. The error of DSstag4 grows considerably with distance for small N and large p ; for a chosen N the error can be reduced by using sufficiently small p for which the sum of the envelope and phase misfits, $EM(N,p) + PM(N,p)$, takes the minimum value.
3. The error of Doptm2 is negligible compared to those of Dconv2 and DSstag4.
4. Despite the formal 4^{th}-order accuracy of DSstag4, for $p = 0.95$ the errors of both DSstag4 and Dconv2 as functions of N have the same convergence rate, -2, whereas that of Doptm2 is -4.
5. While adjustment of the stability ratio p value in DSstag4 is possible in the homogeneous medium (at a price of a small fraction of the maximum possible time step), it is not possible in general in the heterogeneous medium.

Error at the interface:

1. The error is primarily controlled by the boundary condition and its numerical approximation.
2. The error weakly grows with the velocity contrast.
3. The 4^{th}-order of DSstag4 does not improve the accuracy compared to the 2^{nd}-order schemes.
4. The arithmetic averaging of elastic moduli yields significantly lower accuracy compared to the harmonic averaging.

Error away from the interface:

1. For a given N the error of DSstag4 can be reduced by using an adjusted small value of the stability ratio p (and consequently small fraction of the maximum possible time step) only in the case of sufficiently small velocity contrast; in the case of moderate or large velocity contrast the error can be reduced only using sufficiently small spatial grid spacing.
2. Despite the formal 4^{th}-order accuracy of DSstag4, the spatial sampling criterion cannot be weaker than that of the formally 2^{nd}-order accurate Doptm2.

Error inside the strong velocity gradient layer:

1. The errors of Dconv2 and Doptm2 are comparable, the error of DSstag4 is larger mainly for small N (i.e., larger grid spacings) likely due to the relative large spatial extent of the operator (large stencil).

The main conclusion of Kristek and Moczo (2006) was that Doptm2, that is the scheme applying Geller and Takeuchi's (1998) 2^{nd}-order optimally accurate operators to the strong heterogeneous formulation of 1D equation of motion of Moczo et al. (2002), is significantly more accurate than the schemes based on the application of the conventional 2^{nd}-order and staggered-grid 4^{th}-order operators.

10.4 Schemes Dconv2i2 and Doptm2i2

Because the order of approximation of schemes Dconv2, Doptm2 and DSstag4 falls from the $2^{\rm nd}$ order in the homogeneous medium down to the $1^{\rm st}$ order at the grid point at the interface, we should investigate whether the $2^{\rm nd}$ order at the interface could improve level of accuracy.

We do not have heterogeneous scheme which would be $2^{\rm nd}$ order at the grid points away from the interface and also at the grid point at the interface. Therefore, for the numerical investigation, we can combine schemes we derived.

Dconv2i2. At grid point I at the material interface we will use scheme based on the approximation (10.6),

$$\begin{aligned} U_I^{m+1} &= 2U_I^m - U_I^{m-1} \\ &+ \frac{2}{(\rho^- + \rho^+)} \frac{\Delta^2 t}{4h^2} \left\{ 7 \left[C^+(U_{I+1}^m - U_I^m) - C^-(U_I^m - U_{I-1}^m) \right] \right. \\ &- \left. \left[C^+(U_{I+2}^m - U_{I+1}^m) - C^-(U_{I-1}^m - U_{I-2}^m) \right] \right\} . \end{aligned} \tag{10.33}$$

At the other grid points we will use scheme Dconv2, eqs. (10.25), (10.26), (10.29), (10.30), with

$$\rho_I^A = \frac{1}{2} \left(\rho^- + \rho^+ \right) \tag{10.34}$$

and

$$C_{I-1/2}^H = C^- , \quad C_{I+1/2}^H = C^+ . \tag{10.35}$$

Doptm2i2. At grid point I at the material interface we will use scheme defined by eqs. (10.17), (10.18) and (10.20). At other grid points we will use scheme Doptm2, eqs. (10.25), (10.26), (10.31), (10.32), with ρ_I^A , $C_{I-1/2}^H$ and $C_{I+1/2}^H$ defined by eqs. (10.34) and (10.35), respectively.

10.5 Effect of the Order of Approximation at the Interface

Having heterogeneous schemes Dconv2 and Doptm2 (only $1^{\rm st}$-order accurate at the interface) as well as combined schemes Dconv2i2 and Doptm2i2 ($2^{\rm nd}$-order accurate also at the interface), we can numerically compare Dconv2 with Dconv2i2 and Doptm2 with Doptm2i2. A reasonable way of numerical comparison is to evaluate envelope and phase misfits between each FD solution and corresponding analytical (exact) solution. We will use the envelope and misfit criteria developed by Kristekova et al. (2006).

Consider contact of two homogeneous halfspaces with c^+ being velocity in the halfspace, where the plane wave is radiated, and c^- velocity in the other halfspace. We considered $c^+ = 3464$ m/s and $c^- \in \{2310.0, 837.3, 346.4\}$ m/s in the simulations. The corresponding velocity contrasts are $c^+/c^- \in \{1.5, 4.1, 10.0\}$. Densities were $\rho^+ = 2700$ kg/m^3 and $\rho^- = 2500$kg/m^3. The interface is located at a grid point with spatial index I.

A wave is radiated in the halfspace with c^+ toward the interface at the distance of 4 grid spacings from the interface. The Alterman and Karal (1968) decomposition is used to prescribe a source-time function corresponding to a displacement. The source-time function is Gabor signal, i.e., a harmonic carrier with a Gaussian envelope,

$$s(t) = \exp\left\{-\left[\omega_p(t-t_s)/\gamma_s\right]^2\right\}\cos\left[\omega_p(t-t_s)+\theta\right] \ . \tag{10.36}$$

Here, $\omega_p = 2\pi f_p$, $t \in < 0, 2t_s >$, $f_p = 0.5$ Hz is predominant frequency, $\gamma_s = 11$ controls the width of the signal, $\theta = \pi/2$ is a phase shift, and $t_s = 0.45\gamma_s/f_p$. The signal has relatively narrow spectrum with a dominant frequency. The amplitude spectrum falls from its maximum at the frequency $f_p = 0.5$ Hz by three orders of magnitude down to a value at $f_{max} = 0.74$ Hz. Given the maximum frequency, we can define the minimum wavelength in the '$-$' halfspace by

$$\lambda_{min} \ = \ \frac{c^-}{f_{max}} \ . \tag{10.37}$$

The number of grid spacings per λ_{min} is

$$N \ = \ \frac{\lambda_{min}}{h} \ . \tag{10.38}$$

The stability condition for Dconv2 and Doptm2 in the homogeneous medium is

$$\Delta t \ \leq \ \frac{h}{c^+} \tag{10.39}$$

and stability ratio, that is, a fraction of the maximum possible time step, is

$$p \ = \ \frac{c^+}{h}\,\Delta t \ . \tag{10.40}$$

Schemes Dconv2 and Dconv2i2 are compared in Figure 10.1 where the envelope and phase misfits between the FD solutions and analytical solutions are shown as functions of $N \in \{10, 11, ..., 30\}$ and $p \in \{0.1, 0.15, ..., 0.95\}$. The solutions are compared directly at the point at the interface. It is clear that the error in general is not large - it is less than 0.5% in all cases. At the same time, the application of the $2^{\rm nd}$-order scheme also at the interface clearly improves the level of accuracy at the interface. The improvement is more pronounced in terms of the envelope misfit. The error weakly decreases with the increasing velocity contrast. A likely explanation is a better spatial sampling in the halfspace with larger velocity.

A similar comparison of schemes Doptm2 and Doptm2i2 is shown in Figure 10.2. Misfits for Doptm2i2 are displayed only for values of the stability ratio up to 0.8. The reason is that the results were unstable for larger values. This indicates that, likely due to relatively larger complexity of Doptm2i2, the stability condition for the scheme is slightly more restrictive compared to the three other schemes. As we expected, the overall level of error is even smaller than in the case of the conventional schemes. Similarly to the conventional schemes, the application of the $2^{\rm nd}$-order scheme also for the grid point at the interface clearly reduces the error.

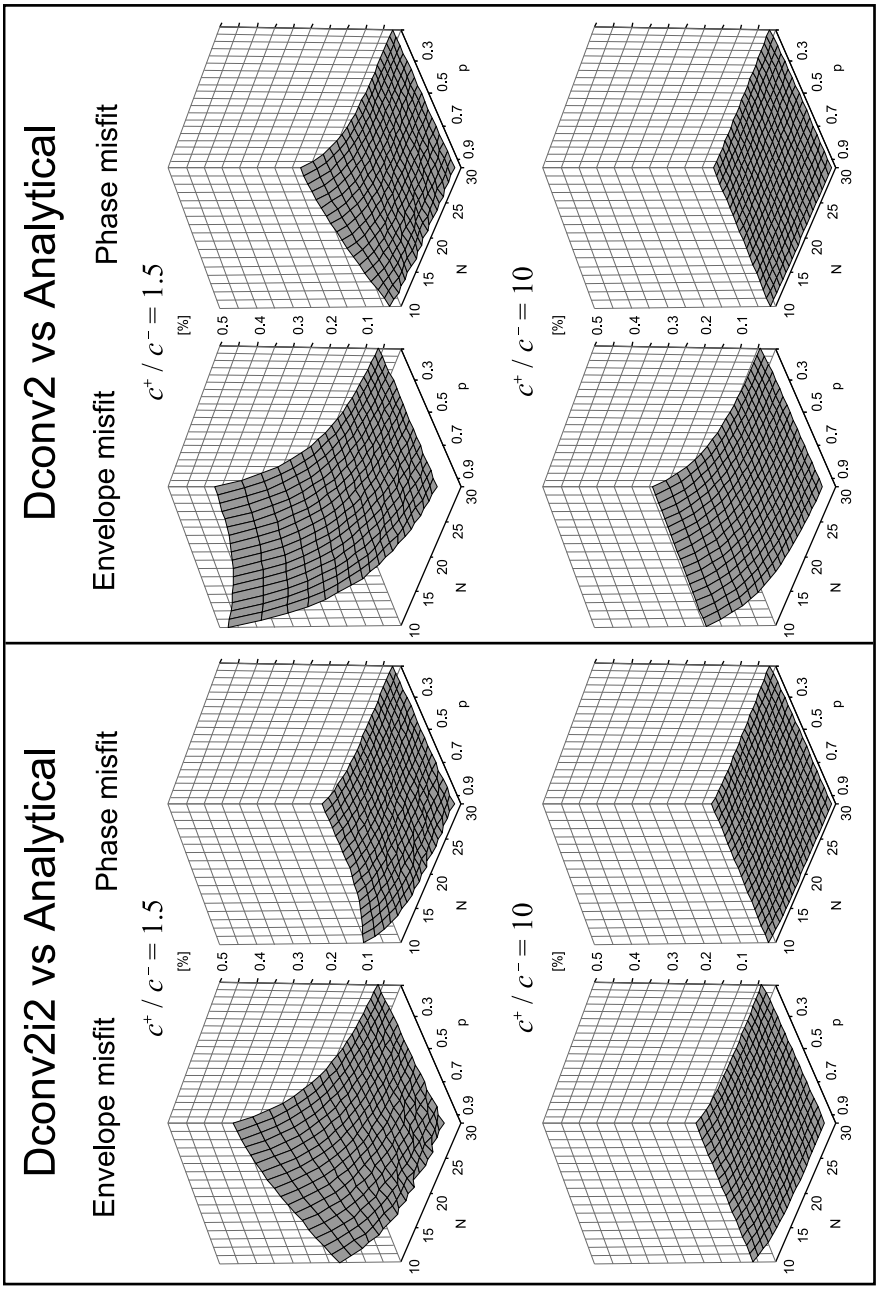

Fig. 10.1. Error at the interface: envelope and phase misfits of the FD schemes Dconv2 and Dconv2i2 as functions of $N \in \{10, 11, ..., 30\}$ and $p \in \{0.1, 0.15, ..., 0.95\}$ at the interface for two values of the velocity contrast. The misfits are evaluated relative to the exact (analytical) solution.

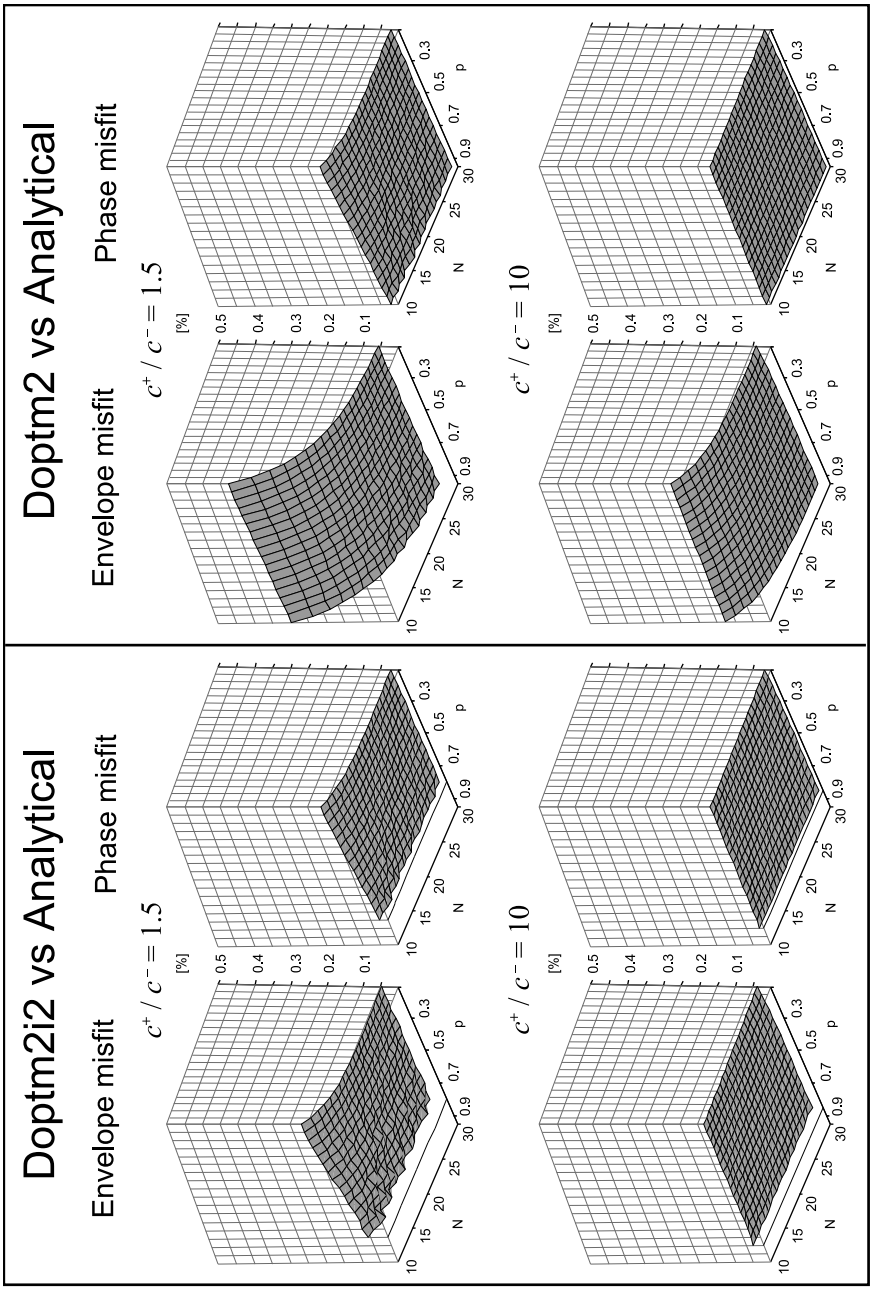

Fig. 10.2. Error at the interface: envelope and phase misfits of the FD schemes Doptm2 and Doptm2i2 as functions of $N \in \{10, 11, ..., 30\}$ and $p \in \{0.1, 0.15, ..., 0.95\}$ at the interface for two values of the velocity contrast. The misfits are evaluated relative to the exact (analytical) solution.

11 Simulation of the Dynamic Rupture Propagation

11.1 Staggered-grid FD Implementation of the TSN Method

The TSN (Traction-at-Split-Nodes) method for simulation of rupture propagation on the earthquake fault was explained in section 3.4. As mentioned there, the method has been developed independently by Andrews (1973, 1999) and Day (1977, 1982). Andrews implemented his TSN formulation in the finite-difference scheme in which spatial differentiation is equivalent to the 2^{nd}-order finite-element method. Day implemented his slightly different formulation of the TSN method in the 2^{nd}-order partly-staggered finite-difference scheme. Both Andrews and Day applied then the TSN method to investigate dynamics of the earthquake rupture propagation.

Recently Day et al. (2005) compared the TSN method with the boundary integral method and found very good level of agreement. Dalguer and Day (2006) compared the TSN method with the thick-fault method of Madariaga et al. (1998) and the stress-glut method presented by Andrews (1999). Using extensive numerical tests they demonstrated superior accuracy of the TSN method compared to the thick-fault and stress-glut methods.

Because the 4^{th}-order velocity-stress staggered-grid FD scheme is at present accepted as the most efficient FD scheme for simulation of the seismic wave propagation and earthquake motion, Dalguer and Day (2007) implemented the TSN method in the scheme. The fault plane is represented by the grid plane of the split nodes for the normal stress-tensor components, the corresponding shear stress-tensor component (σ_{xy}), two fault-parallel components of the particle velocity (v_x and v_y). Dalguer and Day applied the 4^{th}-order centered approximation to spatial derivatives at grid points at distances $3/2$ of the grid spacing ($3\,h/2$) and more from the fault plane. At grid points at distances h and $h/2$ from the fault plane they applied the 2^{nd}-order centered approximation. Finally, at grid points at the fault plane, Dalguer and Day applied the 1^{st}-order one-sided approximation for spatial derivatives in the direction perpendicular to the fault plane and the 2^{nd}-order centered approximation for derivatives in the directions parallel to the fault plane.

Dalguer and Day performed numerical tests of their implementation (they termed it SGSN – Staggered-Grid Split Node) against the partly-staggered implementation of the TSN method (Day, 1977, 1982) and boundary integral method, and found it satisfactorily accurate, with the convergence rates similar to those of the two latter methods.

Kristek et al. (2006) presented three different implementations of the TSN method in the velocity-stress staggered-grid scheme. In the first one they applied the 4^{th}-order approximation to spatial derivatives away from the fault plane, and the 2^{nd}-order approximations at grid positions close to and at the fault plane. In the second implementation they applied the 4^{th}-order approximation to spatial derivatives away from the fault, 2^{nd}-order approximations at grid positions close to the fault, and 4^{th}-order approximations at the fault plane. In the third implementation they applied the 4^{th}-order approximations to the spatial derivatives everywhere.

Here we will describe the first implementation. The geometrical configuration of the horizontal fault plane and spatial staggered grid is shown in Fig. 11.1. Because the fault plane is represented as a contact of the '$-$' and '$+$' fault surfaces, the corresponding horizontal grid plane with spatial index $K^F + \frac{1}{2}$ is split into two grid planes. Assuming a shear faulting, we have to distinguish the '$-$' and '$+$' values of the horizontal components of the particle velocity, $v^{\pm,\,x}$ and $v^{\pm,\,y}$, two normal stress-tensor components, $\sigma^{\pm,\,xx}$ and $\sigma^{\pm,\,yy}$, and one shear

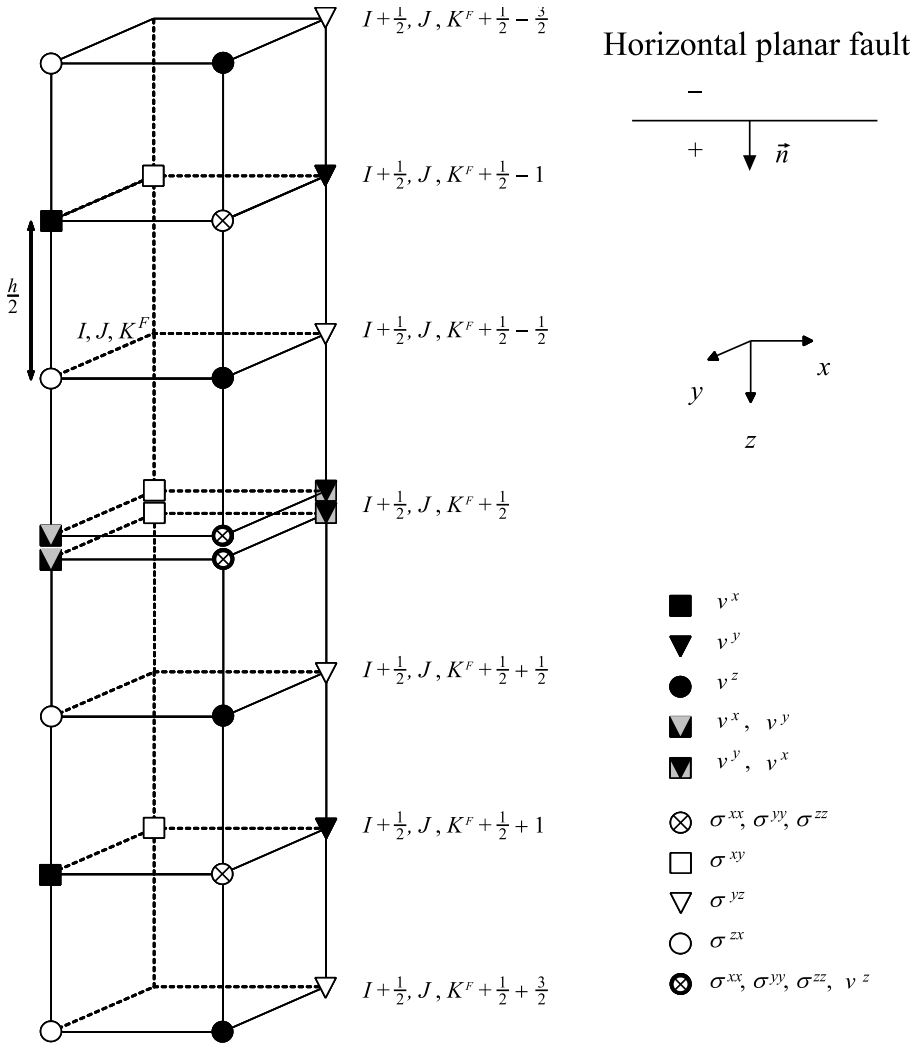

Fig. 11.1. Configuration of the fault plane in the staggered grid. The fault is represented by a horizontal grid plane of split nodes. Indication of the '$-$' and '$+$' sides of the fault.

stress-tensor component, $\sigma^{\pm,xy}$, which become discontinuous when slip on the fault occurs. Note that we use here the upper indices to indicate the '$-$' and '$+$' values and components. This is because we will use lower indices to indicate grid positions. For conciseness, in the following we will partly or fully omit grid indices if the omission cannot cause misunderstanding. Basically, we will show or comment only those parts of the algorithm that are modified or different compared to the 4^{th}-order velocity-stress scheme for interior grid points for medium without the faulting surface. The notation is relatively close to that of Dalguer and Day (2007).

Grid points at distances of $3\,h/2$ from the fault plane Spatial derivatives at $K = K^F + \frac{1}{2} \pm \frac{3}{2}$ in the z-direction (fault-normal) are approximated using the standard $4^{\rm th}$-order formula in which the '$-$' or '$+$' values at the fault are taken:

$$\partial_z\,\phi \doteq h^{-1}\,D_z^{(4)}\phi \;=\; h^{-1}\left[\,\tfrac{9}{8}(\phi_{K+1/2}-\phi_{K-1/2}) - \tfrac{1}{24}(\,\phi^-_{K+3/2}-\phi^+_{K-3/2})\,\right]\,. \quad (11.1)$$

Here, $\phi \in \{\,v^x, v^y, \sigma^{zz}\,\}$ and $+/-$ applies in correspondence to $+/-$ in the grid index K, that is,

$$\text{if}\quad K = K^F + \tfrac{1}{2} - \tfrac{3}{2}\,,\quad \text{the rightmost term is}\quad (\;\phi^-_{K^F+1/2} - \phi_{K^F+1/2-6/2})\,,$$

$$\text{if}\quad K = K^F + \tfrac{1}{2} + \tfrac{3}{2}\,,\quad \text{the rightmost term is}\quad (\;\phi_{K^F+1/2+6/2} - \phi^+_{K^F+1/2})\,.$$

Equation (11.1) also defines spatial operator $D_z^{(4)}$. Later we will also use symbol $D_z^{(2)}$ for the $2^{\rm nd}$-order centered approximation.

Grid points at distances of h from the fault plane All spatial derivatives at grid points at $K = K^F + \frac{1}{2} \pm 1$ are approximated by the $2^{\rm nd}$-order centered FD formula.

Grid points at distances of $h/2$ from the fault plane All spatial derivatives at grid points at $K = K^F + \frac{1}{2} \pm \frac{1}{2}$ are approximated by the $2^{\rm nd}$-order centered FD formula. For derivatives in the $z-$direction appropriate values are taken:

$$\partial_z\,\phi \doteq h^{-1}\,D_z^{(2)}\phi \;=\; h^{-1}\,(\;\phi^-_{K+1/2} \;-\; \phi^+_{K-1/2}\;) \quad (11.2)$$

with $+/-$ applied in correspondence to $+/-$ in the grid index K.

Split nodes on the fault plane The grid index in the $z-$direction for the split nodes is $K = K^F + \frac{1}{2}$. The centered $2^{\rm nd}$-order approximation is used for spatial derivatives of the $+/-$ functions in the $x-$ and $y-$directions. Adjusted $2^{\rm nd}$-order approximation is used for the spatial derivative of the shear stress-tensor components σ^{zx} and σ^{zy} in the $z-$direction:

$$(\partial_z\,\sigma^{z\gamma})^{\pm} \;\doteq\; h^{-1}\;\left[\,\mp\;\tfrac{8}{3}(\;T^{\gamma} - T^{0,\gamma}\;)\;\pm\;3\,\sigma^{z\,\gamma}_{K\pm1/2}\;\mp\;\tfrac{1}{3}\sigma^{z\gamma}_{K\pm3/2}\,\right]\;;\;\gamma\in\{x,y\}\;. \quad (11.3)$$

Here, T^{γ} and $T^{0,\,\gamma}$, $\gamma\in\{x,y\}$, are the components of the constraint traction on the fault. Then approximations to the equations of motion for $v^{\pm,\,x}$ and $v^{\pm,\,y}$ are

$$\begin{aligned}\rho^{\pm}\tfrac{1}{\Delta t}\;\left[\;v^{\pm,\,\gamma,m+1/2} - v^{\pm,\,\gamma,m-1/2}\;\right] \;=\; h^{-1}\left[\;D_x^{(2)}\sigma^{\pm,\,x\gamma,\,m}\;+\;D_y^{(2)}\sigma^{\pm,\,y\,\gamma,m}\;\right]\;+\\ +\;(\partial_z\sigma^{z\,\gamma})^{\pm}\;;\quad\gamma\in\{x,y\}\;,\end{aligned} \quad (11.4)$$

where $(\partial_z\,\sigma^{z\,\gamma})^{\pm}$ is defined by eq. (11.3) and $m+1/2$ is the time index for $t+\Delta t/2$.

Slip rate at time level $m+1/2$ is

$$Dv^{\gamma} \;=\; v^{+,\,\gamma} - v^{-,\,\gamma}\;;\quad \gamma\in\{x,y\}\;. \quad (11.5)$$

Then slip is obtained from

$$Du^{\gamma,\,m+1} \;=\; Du^{\gamma,\,m} + \Delta t \cdot Dv^{\gamma,\,m+1/2}\,; \quad \gamma \in \{x,y\}\,. \tag{11.6}$$

A value of the constraint traction $\vec{T}^{\,c}$ on the fault obtained under condition of $D\vec{v}^{\,m+1/2} \;=\; 0$ defines the trial traction. Let, for simplicity of notation here, $\vec{T}^{\,c\,t}$ denote the shear component of the trial traction. The boundary conditions on the fault are enforced by

$$\begin{aligned} T^{c\,,\gamma} \;&=\; T^{c\,t,\,\gamma} \qquad , \quad \gamma \in \{x,y\}\,; \qquad |\vec{T}^{\,c\,t}| \;\leq\; S \\ &=\; \frac{\vec{T}^{\,c\,t}}{|\vec{T}^{\,c\,t}|}\,S \qquad ; \qquad |\vec{T}^{\,c\,t}| \quad > \quad S\,. \end{aligned} \tag{11.7}$$

In evaluation of the trial traction at grid positions of the particle-velocity components the missing components of the trial traction are obtained by interpolation:

$$\begin{aligned} |\,\vec{T}^{\,c\,t}_{I,\,J+1/2}\,|^2 \;=\; &\left[\; T^{c\,t,\,x}_{I,\,J+1/2} \;\right]^2 \\ &+\; \left[\; \tfrac{1}{4}\,\left(T^{c\,t,\,y}_{I+1/2,\,J} \;+\; T^{c\,t,\,y}_{I-1/2,\,J} \;+\; T^{c\,t,\,y}_{I+1/2,\,J+1} \;+\; T^{c\,t,\,y}_{I-1/2,\,J+1} \right) \;\right]^2 \end{aligned} \tag{11.8}$$

and

$$\begin{aligned} |\,\vec{T}^{\,c\,t}_{I+1/2,\,J}\,|^2 \;=\; &\left[\; \tfrac{1}{4}\,\left(T^{c\,t,\,x}_{I,\,J+1/2} + T^{c\,t,\,x}_{I+1,\,J+1/2} + T^{c\,t,\,x}_{I,\,J-1/2} + T^{c\,t,\,x}_{I+1,\,J-1/2} \right) \;\right]^2 \\ &+\; \left[T^{c\,t,\,y}_{I+1/2,\,J} \right]^2 . \end{aligned} \tag{11.9}$$

Missing components of the slip rate in evaluation of the slip-path length are interpolated analogously.

Finally, the approximations for the stress-tensor components are

$$\dot{\sigma}^{\pm,\,xy} \;\doteq\; \mu\,h^{-1}\left(D^{(2)}_y v^{\pm,x} + D^{(2)}_x v^{\pm,\,y} \right)\,, \tag{11.10}$$

$$\begin{aligned} \dot{\sigma}^{\pm,\gamma\,\gamma} \;\doteq\; &\lambda^{\pm} h^{-1}\,\left[\; D^{(2)}_x v^{\,\pm,\,x} + D^{(2)}_y v^{\pm,\,y} + (\partial_z v^z)^{\pm} \;\right] \\ &+\; 2\,\mu^{\pm} h^{-1}\, D^{(2)}_\gamma v^{\pm,\,\gamma} \;\; ; \quad \gamma \in \{x,y\} \end{aligned} \tag{11.11}$$

and

$$\dot{\sigma}^{\,\pm,\,zz} \;\doteq\; \lambda^{\pm} h^{-1}\,\left[\; D^{(2)}_x v^{\pm,\,x} + D^{(2)}_y v^{\pm,\,y} + (\partial_z v^z)^{\pm} \;\right] + 2\,\mu^{\pm}\,(\partial_z v^z)^{\pm}\,, \tag{11.12}$$

where the adjusted $2^{\rm nd}$-order approximation is used for the $z-$derivative:

$$(\partial_z v^z)^{\pm} \;\doteq\; h^{-1}\,\left[\; \mp\;\tfrac{8}{3} v^z \;\pm\; 3\,v^z_{K\pm 1/2} \;\mp\; \tfrac{1}{3} v^z_{K\pm 3/2} \;\right]\,. \tag{11.13}$$

Values of the continuous $z-$component of the particle velocity on the fault,

$$v^{\,z} \;=\; v^z_{I+1/2,\,J+1/2,\,K^F+1/2}\,, \tag{11.14}$$

are determined from the 2^{nd}-order approximation to the boundary condition

$$\left(\dot{\sigma}^{+,\,zz} \;=\; \dot{\sigma}^{-,\,zz} \right)_{K^F+1/2} . \tag{11.15}$$

The algorithms of the second and third implementations are relatively more complicated and we will not detail them here.

We did not introduce any artificial damping in the FD schemes. Dalguer and Day (2007) introduced viscous damping into the equations of motion in order to suppress short-wavelength oscillations arising from the numerical dispersion characteristic for low-order FD approximations.

11.2 The FEM Implementation of the TSN Method

The FEM formulations with the global stiffness matrix and restoring force, explained in section 6.3, are explicit. This is one of the necessary conditions for the implementation of the TSN method in the FE method. The second condition is that a displacement at a node at a time level be determined by the loading force acting only at that node. For the FE scheme this means that the mass matrix must be diagonal. If the global mass matrix is non-diagonal it must be approximated by a lumped mass matrix.

The computational domain except the fault plane is covered by the 'normal' nodes. Nodes at the fault plane are split. A split node has two partial nodes, $p.n.^+$ and $p.n.^-$. The $+$ node belongs only to halfspace H^+, the $-$ node to H^-. As mentioned in section 3.4, the partial nodes (at one grid position) differ in the 'halfspace' properties/quantities (for example, mass, displacement, particle-velocity, forces, material parameters). At the same time, they share the 'fault' properties/quantities (for example, slip, slip-rate, friction, coefficients of friction). This implies extra conditions on the assembling procedure.

In the assembling procedure we must correctly assemble the local quantities (local mass matrix, local stiffness matrix, local restoring force vector) into the global ones. In particular, we must ensure that the restoring force acting at partial node $p.n.^+$ be only due to the deformation in halfspace H^+. In other words, if we considered no interaction between the partial nodes, no signal from halfspace H^+ would be transfered into halfspace H^-, and vice versa.

The first step of the frictional procedure is computation of the trial traction, $\vec{T}^{c\,t}(m)$, eq. (3.25). Forces $\vec{F}^{\,+}(m)$ and $\vec{F}^{\,-}(m)$ introduced in section 3.4 exactly correspond to the restoring forces acting at the partial nodes.

In the case of the formulation with the global stiffness matrix the restoring force in the elastic medium is obtained from eq. (6.38). In the viscoelastic medium, the anelastic force r_A^e has to be added.

The normal and shear components of the trial traction $\vec{T}^{c\,t}\,(m)$ can be obtained using

$$\begin{aligned} \vec{T}_n^{c\,t}\,(m) \;&=\; \left[\vec{T}^{c\,t}\,(m)\cdot\vec{n}\right]\vec{n}\,, \\ \vec{T}_{sh}^{c\,t}\,(m) \;&=\; \vec{T}^{c\,t}\,(m) \;-\; \vec{T}_n^{c\,t}\,(m)\;. \end{aligned} \tag{11.16}$$

The slip path length l, defined by eq. (3.10), can be approximated by

$$l\,(m) \;=\; l\,(m-1) \;+\; dt\,\left|\,D\vec{v}\left(\,m-\tfrac{1}{2}\right)\right|. \tag{11.17}$$

If, for example, the slip-weakening friction law is applied, the current value of the slip path length $l\,(m)$ can be used to compute the fault strength $S\,(m)$.

The enforcement of the boundary conditions on the fault, as explained in section 3.4, yields

$$D\vec{v}\left(m+\tfrac{1}{2}\right) \;=\; \mathrm{d}t\; B\;\left[\;\vec{T}^{c\,t}_{sh}(m)\;-\;\vec{T}^{c}_{sh}(m)\;\right]. \tag{11.18}$$

The updated slip-rate value is used to obtain the displacements at the partial nodes. The velocity of centroid of two partial nodes is

$$\vec{v}_{cent}\left(m+\tfrac{1}{2}\right) \;=\; \vec{v}_{cent}\left(m-\tfrac{1}{2}\right) \;+\; \Delta t\;\frac{\vec{F}^{\,+}(m)+\vec{F}^{\,-}(m)}{M^{+}+M^{-}}\,. \tag{11.19}$$

The slip-rate, that is, the differential velocity between two partial nodes, is distributed between the partial nodes according to their masses:

$$\vec{v}^{\,\mp}\left(m+\tfrac{1}{2}\right) \;=\; \vec{v}_{cent}\left(m+\tfrac{1}{2}\right) \;\mp\; \Delta t\;\frac{M^{\pm}\,D\vec{v}\left(m+\tfrac{1}{2}\right)}{M^{+}+M^{-}}\,. \tag{11.20}$$

Then the displacements at the partial nodes are

$$\vec{u}^{\,\mp}\,(m+1) \;=\; \vec{u}^{\,\mp}\,(m) \;+\; \Delta t\,\vec{v}^{\,\mp}\left(m+\tfrac{1}{2}\right). \tag{11.21}$$

Recall that a quadrature scheme is used to compute the local restoring force vector, eq. (6.41), or integrals $\mathbf{H}_{ij}$, eq. (6.32), for the local stiffness matrix. Different quadrature scheme can be used in the FE method. A quadrature scheme should be sufficiently accurate and, especially in the case of the restoring force formulation, also computationally efficient. As it is well known, the Gauss quadrature is the most exact quadrature for a chosen number of integration points, if it is applied to the polynomial functions. For a chosen precision it is also the most efficient quadrature because it uses the least possible number of integration points. Therefore, the Gauss quadrature is widely used in the FE method.

We can estimate the required order of the quadrature scheme from eq. (6.41). Consider a master element for which the local coordinates and global coordinates are equivalent. The required order of quadrature is then determined by the that combination of derivatives of the shape functions which requires the highest order. An application of the quadrature of order larger or equal to the required one the exact value of the considered integral can be found (exact here means that the error would be only due the discrete representation of numbers in computer).

In the case of deformed hexahedron, the larger the deformation, the larger the integration error.

However, there are problems that cannot be solved using sufficiently accurate quadrature scheme, see, for example, Belytschko et al. (2000). In some cases elements with the 'exact' quadrature behave more stiffer that they should and they lock. Therefore, the solution may be one order of magnitude smaller than the exact solution. In such cases the application of a lower-order quadrature scheme, also known as the reduced integration, may result in better behavior of the element. Consequently, the reduced integrations may be used to obtain a correct approximate solution. Sometimes, however, such a solution may be polluted by oscillations - hour glass modes (also known as the zero-energy modes or spurious zero-energy modes). If the solution is

not affected by the oscillations, it can be considered a reasonable solution (e.g., Zienkiewicz and Taylor, 1989; Ottosen and Petersson, 1992).

Our numerical tests showed that the 8-point (2 points in one direction) Gauss quadrature for the HEX8 element does not produce correct solution in the TSN implementation. The reduced 1-point Gauss quadrature yields oscillations. The 8-point Lobatto quadrature (of the same order as the 1-point Gauss quadrature but the integration points are located at nodes) applied to the HEX8 elements yields solution close to the reference solution.

11.3 Numerical Test and Comparison

We have four implementations of the TSN method for simulation of the rupture propagation: three implementations in the staggered-grid (SG) velocity-stress FD scheme and one implementation in the FE method.

In all three SG FD implementations 4^{th}-order centered approximations are used for spatial derivatives at grid points at distances equal or larger than $3\,h/2$ from the fault plane. The three implementations differ from one another by approximations used for spatial derivatives at grid points close to the fault plane and grid points directly on the fault plane. These differences are indicated by the acronyms we will use for the implementations:

SG FD 2^{nd}-order:

2^{nd}-order at grid points close to the fault plane and grid points on the fault plane,

SG FD mixed 2^{nd} – 4^{th}-order :

2^{nd}-order at grid points close to the fault plane and 4^{th}-order at grid points on the fault plane,

SG FD 4^{th}-order:

4^{th}-order at all grid points. The FE implementation is the 2^{nd}-order accurate. We will denote it by FE 2^{nd}-order.

We performed a series of numerical simulations of spontaneous rupture propagation on a planar fault in a homogeneous unbounded elastic medium. In order to have a reference solution we followed Dalguer and Day (2007) who used Version 3 of the Southern California Earthquake Center (SCEC) benchmark problem (Harris et al., 2004). The geometrical configuration of the benchmark problem is shown in Fig. 11.2. Material and dynamic stress parameters are given in Tab. 11.1.

The initial shear traction is oriented in the x-direction. Considering the origin of the coordinate system in the center of the fault area and the nucleation zone, the x-axis and y-axis are axes of symmetry or antisymmetry for the slip and traction components. The coordinate xz-plane undergoes pure in-plane motion whereas the coordinate yz-plane undergoes pure anti-plane motion.

The rupture is simultaneously initiated within the nucleation zone due to the initial shear traction slightly larger than the static yielding traction. The spontaneous rupture propagation outside the nucleation zone is then controlled by the linear slip-weakening friction law (3.11).

Table 11.2 provides an overview of the all performed numerical simulations for the defined problem. Simulations differed in values of the used spatial grid spacing h and time steps Δt. We wanted to see an effect of the spatial sampling on the level of accuracy of the simulations. We took the DFM0.05 solution by Day et al. (2005) as the reference solution. DFM means Day's implementation of the TSN method in the partly-staggered grid, 0.05 means 50 m large grid

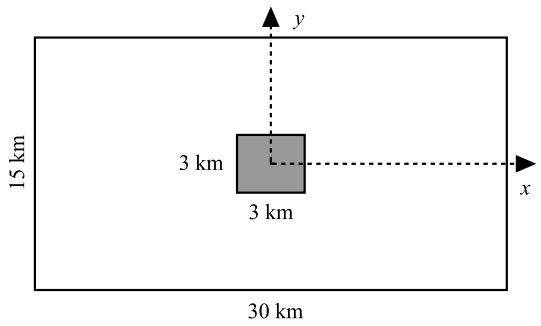

Fig. 11.2. The geometrical configuration of the planar-fault model corresponding to Version 3 of the SCEC benchmark problem (Harris et al., 2004). The fault plane, in correspondence to the theory in section 11.1, is a horizontal plane perpendicular to the z-axis. The shadowed square indicates the nucleation zone.

Tab. 11.1. Material and dynamic stress parameters for the planar-fault model configuration shown in Fig. 11.2.

P-wave velocity: 6000 m/s S-wave velocity: 3464 m/s Density: 2670 kg/m^3 **Parameters**			**Within fault area of 30 km x 15 km**		**Outside fault area**
			Nucleation zone	**Outside nucleation zone**	
Initial shear traction	T_{sh}^0	[MPa]	81.6	70.0	70.0
Initial normal traction	T_n^0	[MPa]	120.0	20.0	120.0
Static coefficient of friction	μ_s		0.677	0.677	infinite
Dynamic coefficient of friction	μ_d		0.525	0.525	0.525
Static yielding stress	T_{sh}^s	[MPa]	81.24	81.24	infinite
Dynamic yielding stress	T_{sh}^d	[MPa]	63.0	63.0	63.0
Dynamic stress drop	$T_{sh}^0 - T_{sh}^d$	[MPa]	18.6	7.0	7.0
Strength excess	$T_{sh}^s - T_{sh}^0$	[MPa]	-0.36	11.24	infinite
Critical slip distance	D_c	[m]	0.40	0.40	0.40

spacing. The rupture propagation is illustrated in Fig. 11.3. Figure 11.3 shows a sequence of snapshots from the simulation by the FE 2$^{\mathrm{nd}}$-order implementation of the TSN method. The area

Tab. 11.2. Values of the spatial grid spacings h and time steps Δt used in the simulations by the four implementations of the TSN method. RMS of the rupture-propagation time misfits evaluated over the whole ruptured area (shown in Fig. 11.2). Maximum values of the rupture-propagation time misfits over the ruptured area.

Grid spacing h [m]	Time step Δt [s]	Rupture Time Misfit for SG FD 2nd-order		Rupture Time Misfit for SG FD mixed 2nd-4th-order		Rupture Time Misfit for SG FD 4th-order		Rupture Time Misfit for FE 2nd-order	
		RMS [%]	MAX [%]	RMS [%]	MAX [%]	RMS [%]	MAX [%]	RMS [%]	MAX [%]
50	0.0033	0.26	1.08	0.29	1.09	0.73	1.81	0.34	0.85
75	0.005	0.36	1.13	0.42	1.30	0.87	2.20	0.62	1.64
100	0.0066	0.44	1.56	0.54	1.84	0.96	2.37	0.84	2.29
150	0.0099	0.58	2.21	0.74	2.79	1.08	2.65	1.24	3.40
250	0.016	0.77	2.92	1.02	4.28	1.25	3.94	2.10	5.22
300	0.02	0.82	2.70	1.07	4.66	1.27	4.39	2.55	5.81

of the fault plane within which the rupture propagation is allowed (the area of the split nodes) is indicated by the bounding rectangle in each snapshot. The interaction of the rupture front with boundaries of the split-node-area produces healing (indicated by white color near the top and bottom boundaries at times of 4.08 s and later). Individual solutions are graphically compared in Figs. 11.4 – 11.9. For each our numerical simulation we evaluated the root-mean-square (RMS) misfit between the rupture-propagation times in our solution and the rupture-propagation times in the DFM0.05 solution over the whole ruptured area. The RMS value as well as the maximum misfit value is shown for each our solution in Tab. 11.2. The comparison of all four implementations is graphically summarized in Fig. 11.10. Figure 11.10 shows the RMS misfits in the rupture-propagation times relative to the reference solution DFM0.05 of Day et al. (2005). Because the width of the cohesive zone varies as the rupture propagates, the cohesive zone resolution is defined as the median value of the number of the grid spacings per width of the cohesive zone measured in the x-direction. The comparison of the RMS misfits for the four implementations of the TSN method shown in Fig. 11.10 leads us to conclusion that the FE 2^{nd}-order implementation of the TSN method has the highest rate of convergence while the rate of convergence of the SG FD 4^{th}-order implementation is the lowest. Let us note that Fig. 11.10 does not really compare the relative accuracy of the individual implementations. This is because we cannot take the reference solution DFM0.05 as the most accurate solution. Figure 11.10 thus only compares the convergence rates for the particular choice of the reference solution. At the same time it is likely that DFM0.05 is a reasonably accurate solution.

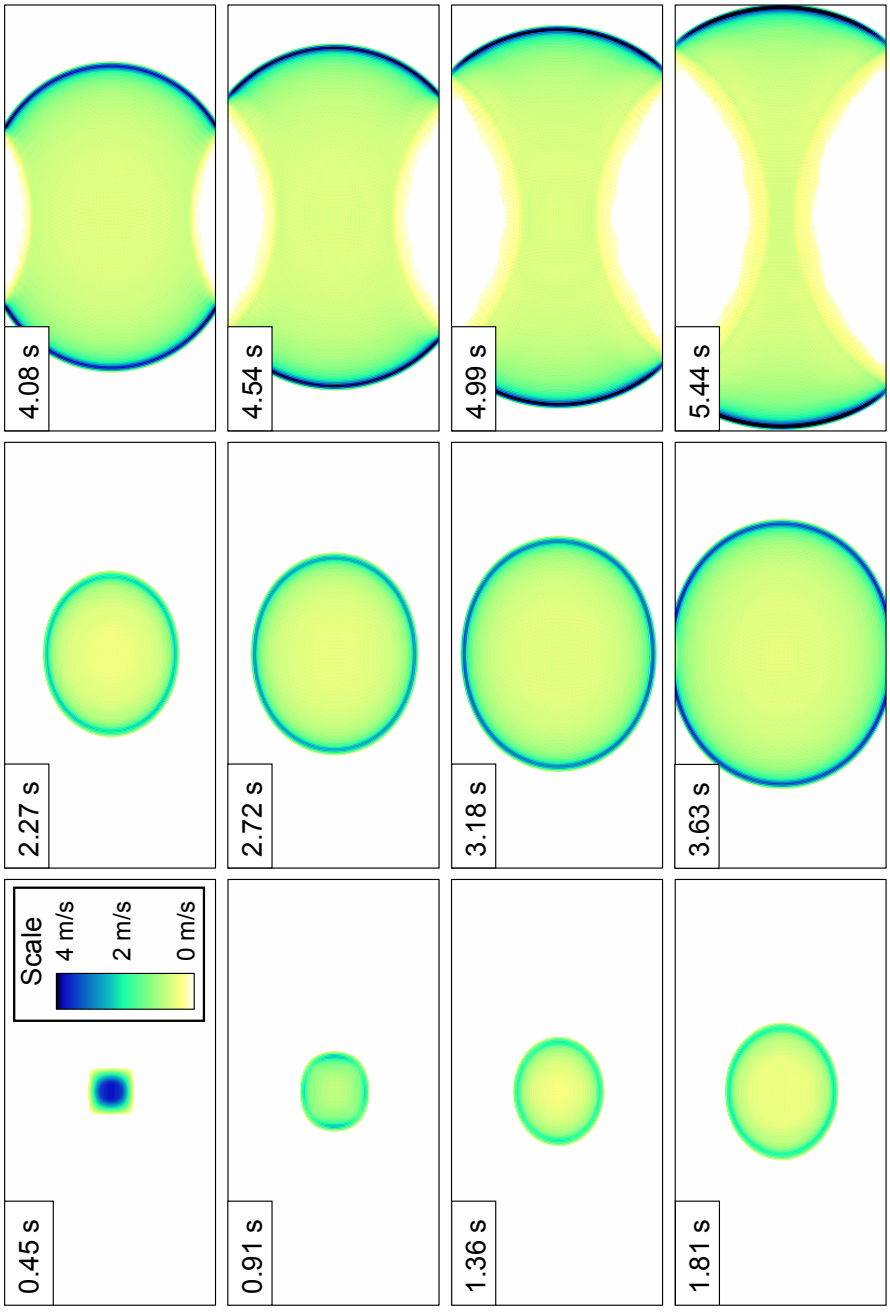

Fig. 11.3. Sequence of the rupture propagation snapshots. Simulation by the FE 2^{nd}-order method.

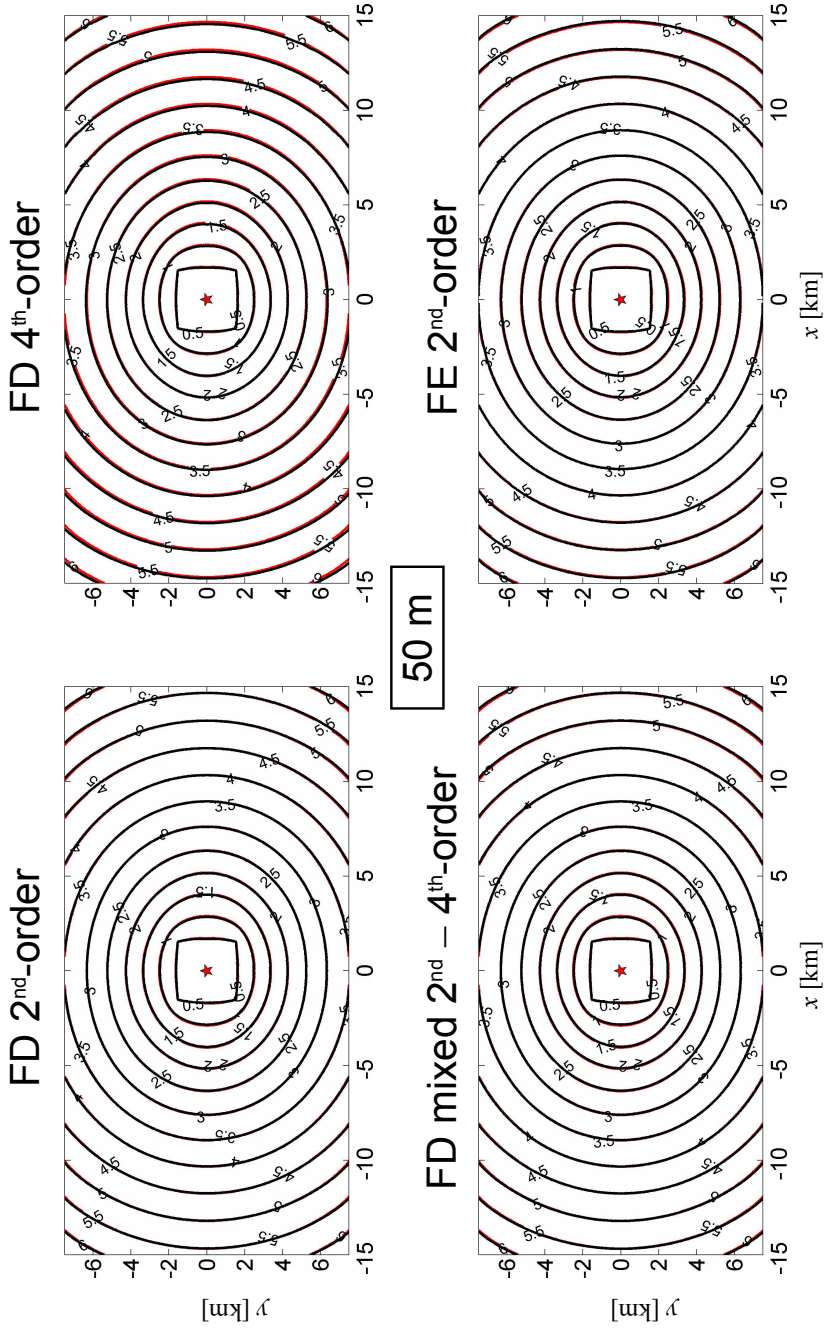

Fig. 11.4. Contour plots of the rupture front for the four numerical simulations. The grid spacing is 50 m.

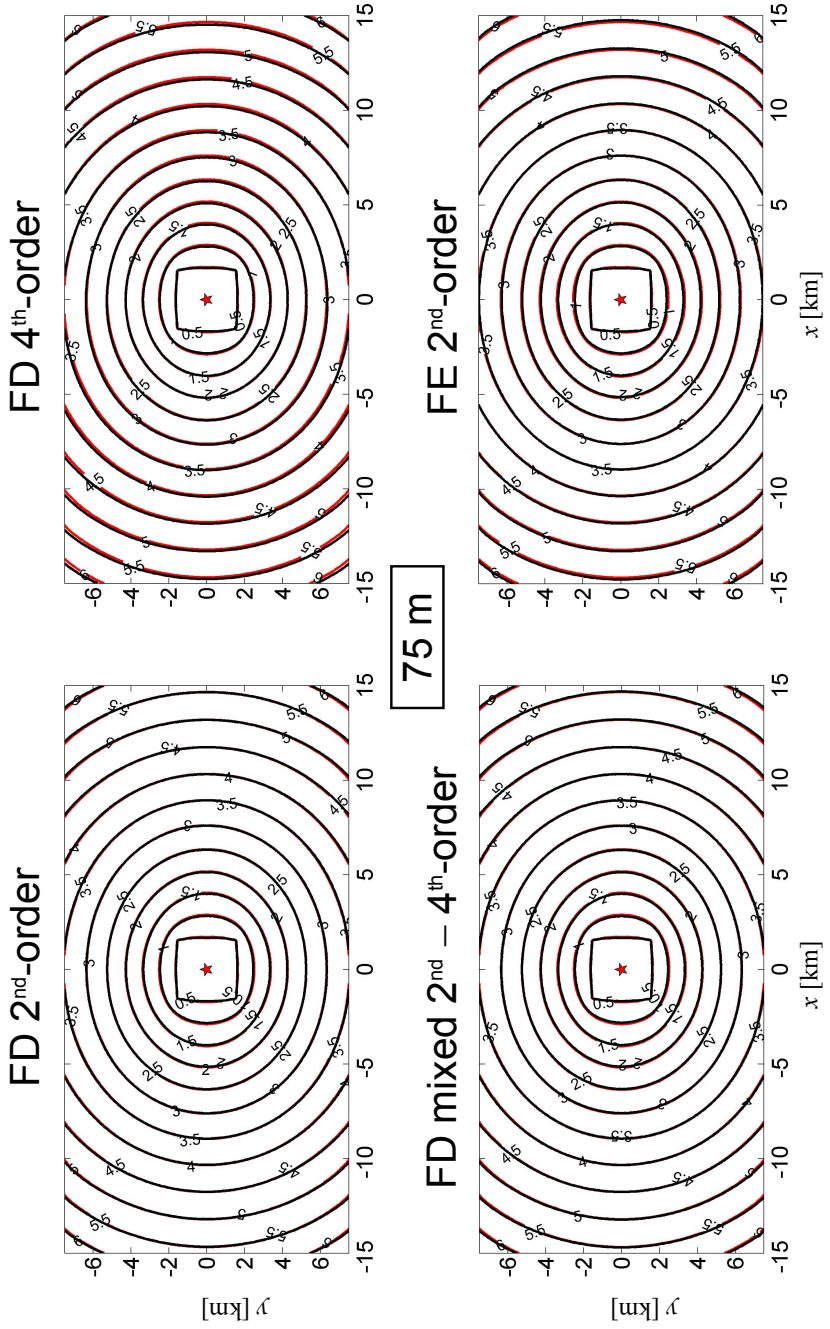

Fig. 11.5. Contour plots of the rupture front for the four numerical simulations. The grid spacing is 75 m.

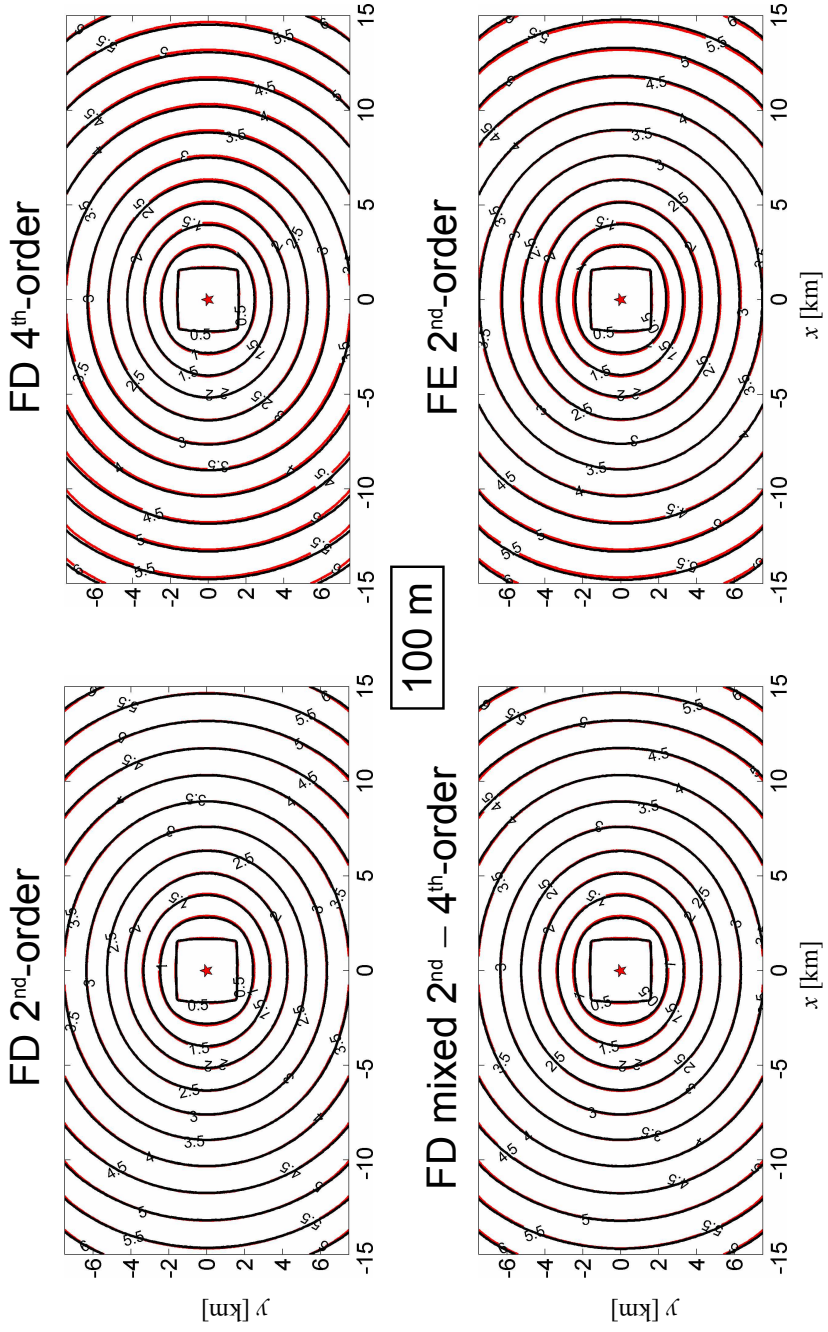

Fig. 11.6. Contour plots of the rupture front for the four numerical simulations. The grid spacing is 100 m.

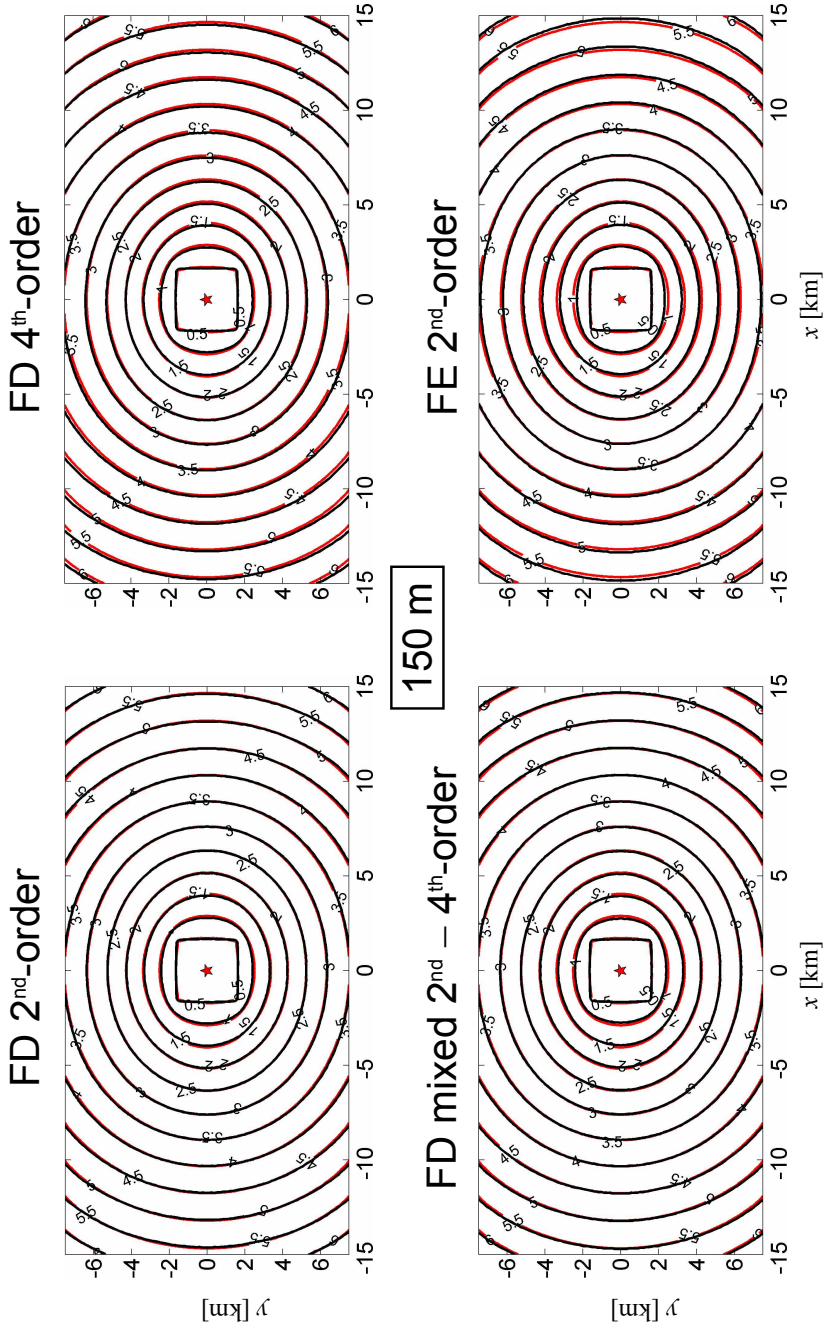

Fig. 11.7. Contour plots of the rupture front for the four numerical simulations. The grid spacing is 150 m.

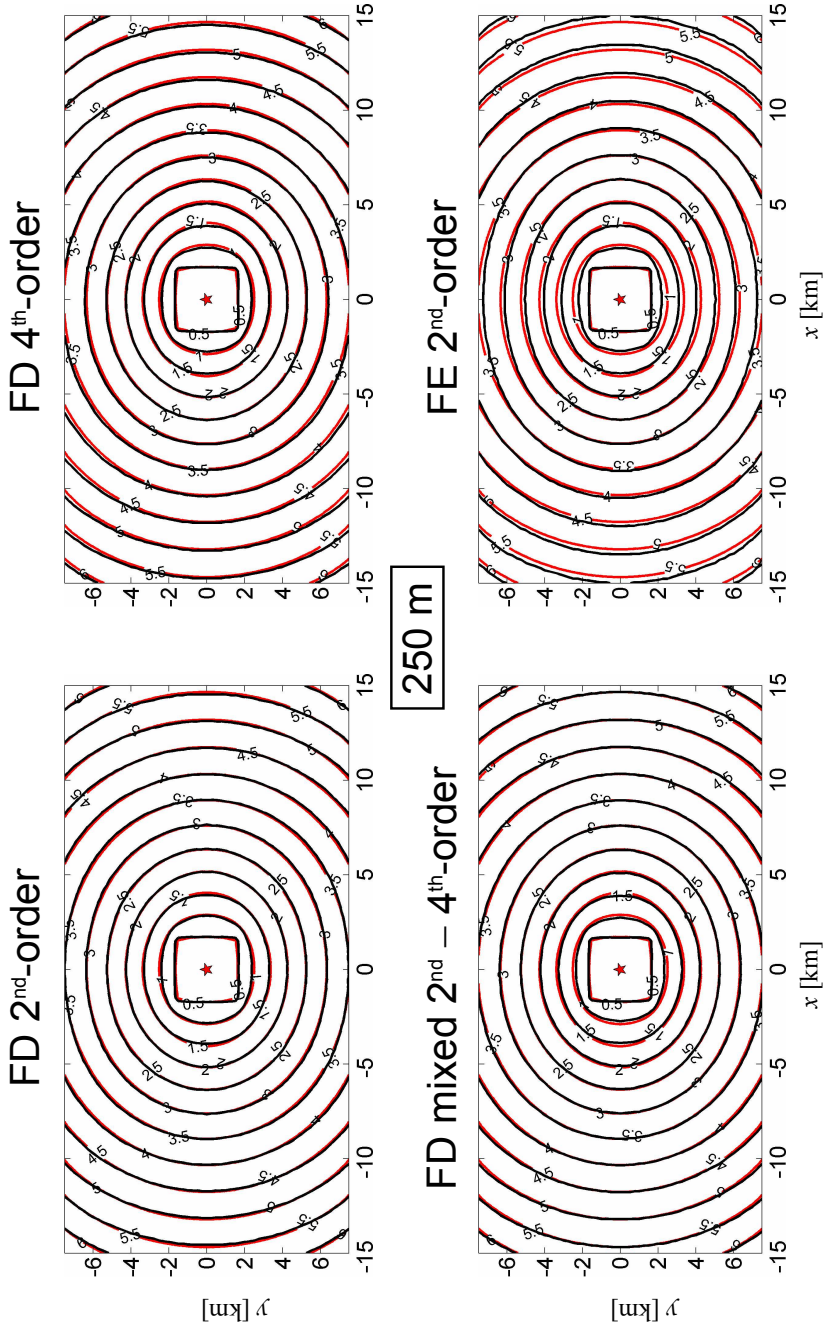

Fig. 11.8. Contour plots of the rupture front for the four numerical simulations. The grid spacing is 250 m.

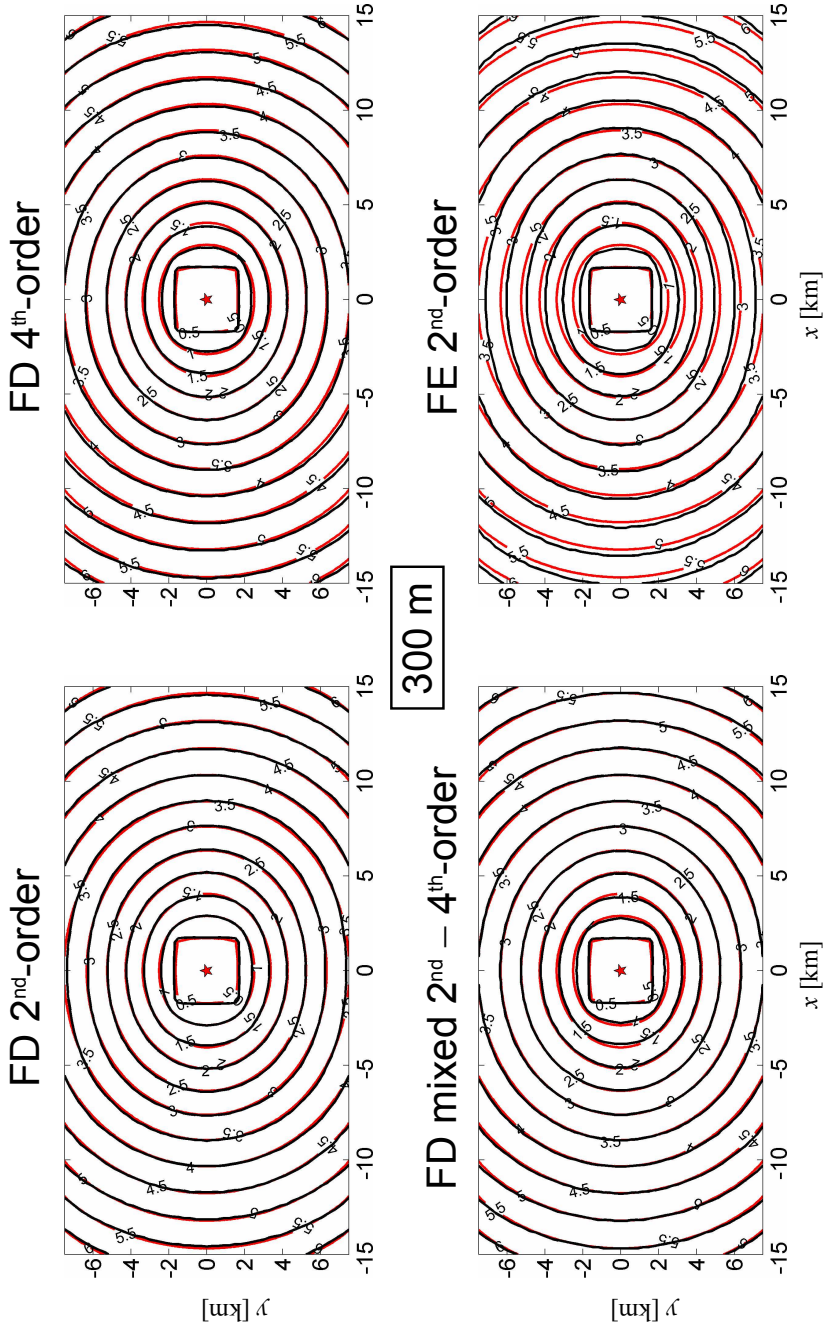

Fig. 11.9. Contour plots of the rupture front for the four numerical simulations. The grid spacing is 300 m.

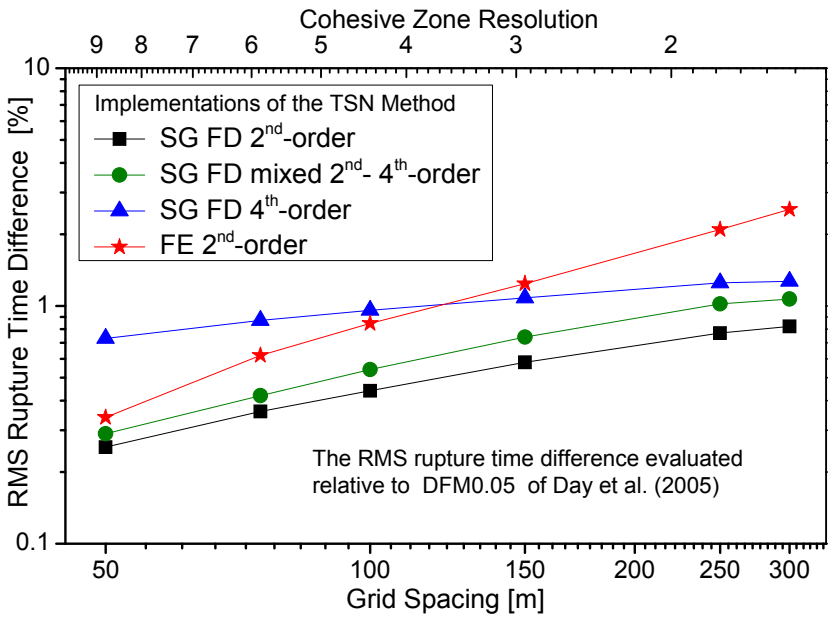

Fig. 11.10. Differences in the rupture-propagation times relative to the reference solution DFM0.05 of Day et al. (2005). The RMS misfit is evaluated over the whole ruptured area. The cohesive zone resolution is defined as the median value of the number of the grid spacings per width of the cohesive zone measured in the x-direction.

12 Simulation of the Kinematic Sources

12.1 Simulation in the Conventional FD Schemes

We want to simulate a point dislocation source in the finite-difference scheme. This means a simulation of a system of the force-couples $(p,\, q\,)$ with a strength M_{pq} acting at a grid point. A body-force term in the equation of motion provides such a possibility. Frankel (1993) proposed such an approach and used it in the displacement formulation on a conventional grid. Graves (1996) adapted the approach in the velocity-stress formulation on a staggered grid.

Consider, e.g., an (y, x) couple acting at the grid point (I_s, J_s, K_s) ; see Fig. 12.1. The body-force term in the equation of motion corresponding to this couple, that is, f_y can be approximated as

$$f_y \doteq \frac{1}{h^3}\frac{1}{2h}\, M_{yx}(t)\, (\, \delta_{II_R}\, \delta_{JJ_R}\, \delta_{KK_R} - \delta_{II_L}\, \delta_{JJ_L}\, \delta_{KK_L}\,)\ , \tag{12.1}$$

where $2h$ is the arm length and $1/h^3$ normalizes the force to the unit volume.

In general, assuming the body-force couples acting at the grid point (I, J, K) in the conven-

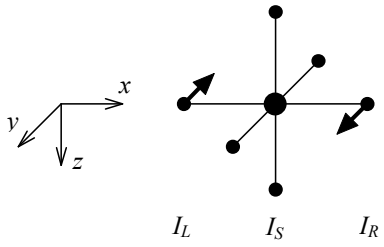

Fig. 12.1. Illustration of simulation of the (y, x) couple acting at the grid point (I_s, J_s, K_s) in the conventional grid.

tional grid, we obtain for the discrete approximations to the body forces

$$
\begin{aligned}
F^x_{I+1,\,J\quad,\,K} &= -F^x_{I-1,\,J\quad,\,K} = \frac{1}{2h^4}\,M_{xx}(t)\,,\\
F^y_{I+1,\,J\quad,\,K} &= -F^y_{I-1,\,J\quad,\,K} = \frac{1}{2h^4}\,M_{yx}(t)\,,\\
F^z_{I+1,\,J\quad,\,K} &= -F^z_{I-1,\,J\quad,\,K} = \frac{1}{2h^4}\,M_{zx}(t)\,,\\
F^x_{I\quad,\,J+1,\,K} &= -F^x_{I\quad,\,J-1,\,K} = \frac{1}{2h^4}\,M_{xy}(t)\,,\\
F^y_{I\quad,\,J+1,\,K} &= -F^y_{I\quad,\,J-1,\,K} = \frac{1}{2h^4}\,M_{yy}(t)\,,\\
F^z_{I\quad,\,J+1,\,K} &= -F^z_{I\quad,\,J-1,\,K} = \frac{1}{2h^4}\,M_{zy}(t)\,,\\
F^x_{I\quad,\,J\quad,\,K+1} &= -F^x_{I\quad,\,J\quad,\,K-1} = \frac{1}{2h^4}\,M_{xz}(t)\,,\\
F^y_{I\quad,\,J\quad,\,K+1} &= -F^y_{I\quad,\,J\quad,\,K-1} = \frac{1}{2h^4}\,M_{yz}(t)\,,\\
F^z_{I\quad,\,J\quad,\,K+1} &= -F^z_{I\quad,\,J\quad,\,K-1} = \frac{1}{2h^4}\,M_{zz}(t)\,.
\end{aligned}
\tag{12.2}
$$

In the case of a tangential slip the moment tensor $M_{pq}(t)$ is given by relation (3.53) or (3.50).

12.2 Simulation in the Staggered FD Schemes

Simulation of the kinematic source in the staggered grid is slightly more complicated. This is because the displacement (or particle-velocity) components are located at different positions in the grid.

Let us illustrate this in the xz plane in the P-SV case. Assume the body-force couples acting at the grid point $(I + 1/2,\ K + 1/2)$, where the normal stress-tensor components T^{xx} and T^{zz} are located. Consider the x-component of the body-force term. Since this term is present in the equation for the x-component of the displacement, we can apply it only at the grid positions, where the discrete approximations to the x-component of the displacement, $U_{I,K+1/2}$, are located.

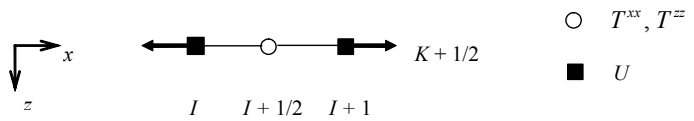

Fig. 12.2. Illustration of simulation of the (x, x) couple acting at the grid point $(I + 1/2,\ K + 1/2)$ in the staggered grid in the 2D P-SV problem.

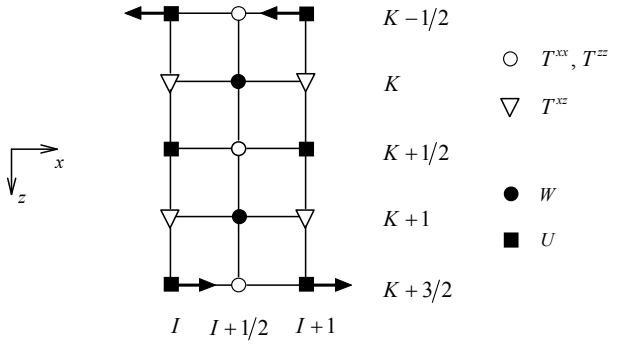

Fig. 12.3. Illustration of simulation of the (x, z) couple acting at the grid point $(I + 1/2,\ K + 1/2)$ in the staggered grid in the 2D P-SV problem.

The force couples having forces in the x-direction contribute to the f_x term. Consider first the (x, x) couple. This can be simulated at the $(I, K + 1/2)$ and $(I + 1, K + 1/2)$ grid points, see Fig. 12.2:

$$F^x_{I+1,\ K+1/2} \ = \ -F^x_{I,\ K+1/2} \ = \ \frac{1}{h^3}\frac{1}{h}\, M_{xx}(t) \ = \ \frac{1}{h^4}\, M_{xx}(t) \tag{12.3}$$

Consider now the (x, z) couple. We cannot simulate it at the $(I + 1/2,\ K + 1)$ and $(I + 1/2,\ K)$ grid points, (that is, analogously to the conventional grid) since discrete displacements U are not located at these grid points. We can consider, however, one couple along the grid line $(I + 1)$ and one couple along the grid line (I), that is,

$$F^x_{I+1,\ K+3/2} \ = \ -F^x_{I+1,\ K-1/2} \ = \ \frac{1}{2}\frac{1}{h^3}\frac{1}{2h}\, M_{xz}(t) \ = \ \frac{1}{4h^4}\, M_{xz}(t) \tag{12.4}$$

and

$$F^x_{I,\ K+3/2} \ = \ -F^x_{I,\ K-1/2} \ = \ \frac{1}{2}\frac{1}{h^3}\frac{1}{2h}\, M_{xz}(t) \ = \ \frac{1}{4h^4}\, M_{xz}(t)\ , \tag{12.5}$$

(see Fig. 12.3), and take the average of the two couples (the reason for $\frac{1}{2}$ in eqs. (12.4) and (12.5)).

Return now to the 3D problem. Assume the body-force couples acting at the grid point $(I + 1/2,\ J + 1/2,\ K + 1/2)$. Then we obtain for the staggered grid with the stress-tensor

components T^{xx}, T^{yy} and T^{zz} located at the grid point $(I+1/2,\ J+1/2,\ K+1/2)$ the following grid body forces:

$$
\begin{aligned}
F^x_{I+1\ ,\ J+1/2,\ K+1/2} &= -F^x_{I\ \ ,\ J+1/2,\ K+1/2} = \frac{1}{h^4}\, M_{xx}(t)\ , \\
F^x_{I+1\ ,\ J+3/2,\ K+1/2} &= -F^x_{I+1\ ,\ J-1/2,\ K+1/2} = \frac{1}{4h^4}\, M_{xy}(t)\ , \\
F^x_{I\ \ \ ,\ J+3/2,\ K+1/2} &= -F^x_{I\ \ ,\ J-1/2,\ K+1/2} = \frac{1}{4h^4}\, M_{xy}(t)\ , \\
F^x_{I+1\ ,\ J+1/2,\ K+3/2} &= -F^x_{I+1\ ,\ J+1/2,\ K-1/2} = \frac{1}{4h^4}\, M_{xz}(t)\ , \\
F^x_{I\ \ \ ,\ J+1/2,\ K+3/2} &= -F^x_{I\ \ ,\ J+1/2,\ K-1/2} = \frac{1}{4h^4}\, M_{xz}(t)\ ,
\end{aligned}
\tag{12.6}
$$

$$
\begin{aligned}
F^y_{I+1/2,\ J+1\ ,\ K+1/2} &= -F^y_{I+1/2,\ J\ \ ,\ K+1/2} = \frac{1}{h^4}\, M_{yy}(t)\ , \\
F^y_{I+3/2,\ J+1\ ,\ K+1/2} &= -F^y_{I-1/2,\ J+1\ ,\ K+1/2} = \frac{1}{4h^4}\, M_{yx}(t)\ , \\
F^y_{I+3/2,\ J\ \ \ ,\ K+1/2} &= -F^y_{I-1/2,\ J\ \ ,\ K+1/2} = \frac{1}{4h^4}\, M_{yx}(t)\ , \\
F^y_{I+1/2,\ J+1\ ,\ K+3/2} &= -F^y_{I+1/2,\ J+1\ ,\ K-1/2} = \frac{1}{4h^4}\, M_{yz}(t)\ , \\
F^y_{I+1/2,\ J\ \ \ ,\ K+3/2} &= -F^y_{I+1/2,\ J\ \ ,\ K-1/2} = \frac{1}{4h^4}\, M_{yz}(t)\ ,
\end{aligned}
\tag{12.7}
$$

$$
\begin{aligned}
F^z_{I+1/2,\ J+1/2,\ K+1} &= -F^z_{I+1/2,\ J+1/2,\ K} = \frac{1}{h^4}\, M_{zz}(t)\ , \\
F^z_{I+3/2,\ J+1/2,\ K+1} &= -F^z_{I-1/2,\ J+1/2,\ K+1} = \frac{1}{4h^4}\, M_{zx}(t)\ , \\
F^z_{I+3/2,\ J+1/2,\ K\ \ } &= -F^z_{I-1/2,\ J+1/2,\ K\ \ } = \frac{1}{4h^4}\, M_{zx}(t)\ , \\
F^z_{I+1/2,\ J+3/2,\ K+1} &= -F^z_{I+1/2,\ J-1/2,\ K+1} = \frac{1}{4h^4}\, M_{zy}(t)\ , \\
F^z_{I+1/2,\ J+3/2,\ K\ \ } &= -F^z_{I+1/2,\ J-1/2,\ K\ \ } = \frac{1}{4h^4}\, M_{zy}(t)\ .
\end{aligned}
\tag{12.8}
$$

In a computer code it is reasonable to consider integer values of the grid indices. Equations (12.6) – (12.8) can be rewritten replacing actual-position indices by indices corresponding to the finite-difference cells. The rule for the re-indexing is simple: 1. an index having an integer value does not change, 2. $1/2$ has to be subtracted from an index which does not have an integer value. (The same reindexing can be applied to all the staggered-grid schemes we showed before.) Equations

(12.6) - (12.8) become

$$
\begin{aligned}
F^x_{I+1,\,J\quad,\,K} &= -F^x_{I\quad,\,J\quad,\,K} = \frac{1}{h^4}\,M_{xx}(t)\,,\\
F^x_{I+1,\,J+1,\,K} &= -F^x_{I+1,\,J-1,\,K} = \frac{1}{4h^4}\,M_{xy}(t)\,,\\
F^x_{I\quad,\,J+1,\,K} &= -F^x_{I\quad,\,J-1,\,K} = \frac{1}{4h^4}\,M_{xy}(t)\,,\\
F^x_{I+1,\,J\quad,\,K+1} &= -F^x_{I+1,\,J\quad,\,K-1} = \frac{1}{4h^4}\,M_{xz}(t)\,,\\
F^x_{I\quad,\,J\quad,\,K+1} &= -F^x_{I\quad,\,J\quad,\,K-1} = \frac{1}{4h^4}\,M_{xz}(t)\,,
\end{aligned}
\tag{12.9}
$$

$$
\begin{aligned}
F^y_{I\quad,\,J+1,\,K} &= -F^y_{I\quad,\,J\quad,\,K} = \frac{1}{h^4}\,M_{yy}(t)\,,\\
F^y_{I+1,\,J+1,\,K} &= -F^y_{I-1,\,J+1,\,K} = \frac{1}{4h^4}\,M_{yx}(t)\,,\\
F^y_{I+1,\,J\quad,\,K} &= -F^y_{I-1,\,J\quad,\,K} = \frac{1}{4h^4}\,M_{yx}(t)\,,\\
F^y_{I\quad,\,J+1,\,K+1} &= -F^y_{I\quad,\,J+1,\,K-1} = \frac{1}{4h^4}\,M_{yz}(t)\,,\\
F^y_{I\quad,\,J\quad,\,K+1} &= -F^y_{I\quad,\,J\quad,\,K-1} = \frac{1}{4h^4}\,M_{yz}(t)\,,
\end{aligned}
\tag{12.10}
$$

$$
\begin{aligned}
F^z_{I\quad,\,J\quad,\,K+1} &= -F^z_{I\quad,\,J\quad,\,K} = \frac{1}{h^4}\,M_{zz}(t)\,,\\
F^z_{I+1,\,J\quad,\,K+1} &= -F^z_{I-1,\,J\quad,\,K+1} = \frac{1}{4h^4}\,M_{zx}(t)\,,\\
F^z_{I+1,\,J\quad,\,K} &= -F^z_{I-1,\,J\quad,\,K} = \frac{1}{4h^4}\,M_{zx}(t)\,,\\
F^z_{I\quad,\,J+1,\,K+1} &= -F^z_{I\quad,\,J-1,\,K+1} = \frac{1}{4h^4}\,M_{zy}(t)\,,\\
F^z_{I\quad,\,J+1,\,K} &= -F^z_{I\quad,\,J-1,\,K} = \frac{1}{4h^4}\,M_{zy}(t)\,.
\end{aligned}
\tag{12.11}
$$

Equations (12.9) - (12.11) with the finite-difference cell indices are ready for programming.

If we want/need to simulate source acting at the grid point (I, J, K) in the staggered grid with the stress-tensor components T^{xx}, T^{yy} and T^{zz} located at the grid point (I, J, K), we

obtain

$$
\begin{aligned}
F^x_{I+1/2,\,J\;\;,\,K} &= -F^x_{I-1/2,\,J\;\;,\,K} = \frac{1}{h^4}\,M_{xx}(t)\,,\\
F^x_{I+1/2,\,J+1\;,\,K} &= -F^x_{I+1/2,\,J-1\;,\,K} = \frac{1}{4h^4}\,M_{xy}(t)\,,\\
F^x_{I-1/2,\,J+1\;,\,K} &= -F^x_{I-1/2,\,J-1\;,\,K-1/2} = \frac{1}{4h^4}\,M_{xy}(t)\,,\\
F^x_{I+1/2,\,J\;\;,\,K+1} &= -F^x_{I+1/2,\,J\;\;,\,K-1} = \frac{1}{4h^4}\,M_{xz}(t)\,,\\
F^x_{I-1/2,\,J\;\;,\,K+1} &= -F^x_{I-1/2,\,J\;\;,\,K-1} = \frac{1}{4h^4}\,M_{xz}(t)\,,
\end{aligned}
\tag{12.12}
$$

$$
\begin{aligned}
F^y_{I\;\;,\,J+1/2,\,K} &= -F^y_{I\;\;,\,J-1/2,\,K} = \frac{1}{h^4}\,M_{yy}(t)\,,\\
F^y_{I+1\;,\,J+1/2,\,K} &= -F^y_{I-1\;,\,J+1/2,\,K} = \frac{1}{4h^4}\,M_{yx}(t)\,,\\
F^y_{I+1\;,\,J-1/2,\,K} &= -F^y_{I-1\;,\,J-1/2,\,K} = \frac{1}{4h^4}\,M_{yx}(t)\,,\\
F^y_{I\;\;,\,J+1/2,\,K+1} &= -F^y_{I\;\;,\,J+1/2,\,K-1} = \frac{1}{4h^4}\,M_{yz}(t)\,,\\
F^y_{I\;\;,\,J-1/2,\,K+1} &= -F^y_{I\;\;,\,J-1/2,\,K-1} = \frac{1}{4h^4}\,M_{yz}(t)\,,
\end{aligned}
\tag{12.13}
$$

$$
\begin{aligned}
F^z_{I\;\;,\,J\;\;,\,K+1/2} &= -F^z_{I\;\;,\,J\;\;,\,K-1/2} = \frac{1}{h^4}\,M_{zz}(t)\,,\\
F^z_{I+1\;,\,J\;\;,\,K+1/2} &= -F^z_{I-1\;,\,J\;\;,\,K+1/2} = \frac{1}{4h^4}\,M_{zx}(t)\,,\\
F^z_{I+1\;,\,J\;\;,\,K-1/2} &= -F^z_{I-1\;,\,J\;\;,\,K-1/2} = \frac{1}{4h^4}\,M_{zx}(t)\,,\\
F^z_{I\;\;,\,J+1\;,\,K+1/2} &= -F^z_{I\;\;,\,J-1\;,\,K+1/2} = \frac{1}{4h^4}\,M_{zy}(t)\,,\\
F^z_{I\;\;,\,J+1\;,\,K-1/2} &= -F^z_{I\;\;,\,J-1\;,\,K-1/2} = \frac{1}{4h^4}\,M_{zy}(t)\,.
\end{aligned}
\tag{12.14}
$$

For the alternative approaches to the implementation of the source see, for example, Yomogida and Etgen (1993), Coutant et al. (1995), and Olsen et al. (1995).

12.3 Simulation in the FE Method

Consider a source located at node S_0 in the conventional grid, see Fig. 12.4. Let h be the grid spacing, that is the distance between two neighboring nodes. The source can be simulated using

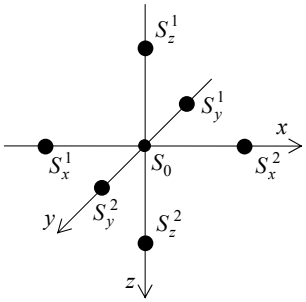

Fig. 12.4. Nodes of the finite-element grid (mesh) used for simulation of the point kinematic source at node S_0.

the following nodal forces - discrete approximations to the body forces:

$$\begin{aligned} F_x\left(S_x^1,t\right) &= -F_x\left(S_x^2,t\right) = \frac{1}{2h}\,M_{xx}\left(t\right), \\ F_y\left(S_x^1,t\right) &= -F_y\left(S_x^2,t\right) = \frac{1}{2h}\,M_{xy}\left(t\right), \\ F_z\left(S_x^1,t\right) &= -F_z\left(S_x^2,t\right) = \frac{1}{2h}\,M_{xz}\left(t\right), \end{aligned} \tag{12.15}$$

$$\begin{aligned} F_x\left(S_y^1,t\right) &= -F_x\left(S_y^2,t\right) = \frac{1}{2h}\,M_{xy}\left(t\right), \\ F_y\left(S_y^1,t\right) &= -F_y\left(S_y^2,t\right) = \frac{1}{2h}\,M_{yy}\left(t\right), \\ F_z\left(S_y^1,t\right) &= -F_z\left(S_y^2,t\right) = \frac{1}{2h}\,M_{yz}\left(t\right), \end{aligned} \tag{12.16}$$

$$\begin{aligned} F_x\left(S_z^1,t\right) &= -F_x\left(S_z^2,t\right) = \frac{1}{2h}\,M_{xz}\left(t\right), \\ F_y\left(S_z^1,t\right) &= -F_y\left(S_z^2,t\right) = \frac{1}{2h}\,M_{yz}\left(t\right), \\ F_z\left(S_z^1,t\right) &= -F_z\left(S_z^2,t\right) = \frac{1}{2h}\,M_{zz}\left(t\right), \end{aligned} \tag{12.17}$$

where $F_i\left(S_j^k,t\right);\ i,j \in \{x,y,z\},\ k \in \{1,2\}$ denotes the force acting in the i-direction at node S_j^k. Note that the the moment-tensor components are scaled here only by the length of the force-couple arm - unlike the scaling in the analogous equations for the simulations in the FD schemes. The reason for the difference is that force here means force acting on a mass of a node. The forces given in eqs. (12.9) – (12.14) were forces per unit volumes, that is, corresponding to the body-force terms in the strong-form equation of motion.

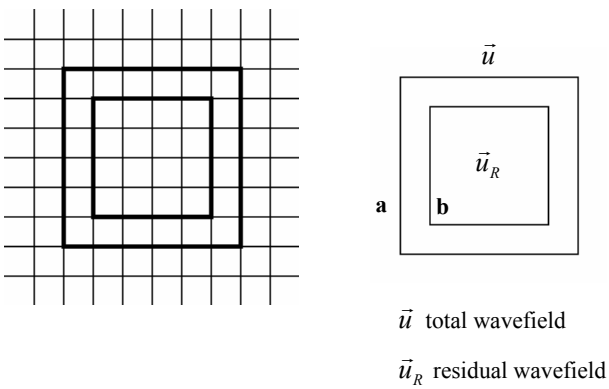

Fig. 12.5. Rectangles **a** and **b**, say, excitation rectangles, used for decomposition of the total displacement into the source and residual (scattered) parts in the conventional grid in the 2^{nd}-order FD schemes.

12.4 Decomposition of the Wavefield

Let $\vec{s}$ be a displacement produced by a source. Then the total displacement $\vec{u}$ can be decomposed in the form

$$\vec{u} \;=\; \vec{s} \;+\; \vec{u}_R \;, \tag{12.18}$$

where $\vec{u}_R$ is the displacement corresponding to the residual (or scattered) wavefield.

Consider now rectangles (or squares) **a** and **b** in the conventional rectangular grid (see Fig. 12.5). Let us assume a source located inside rectangle **b**. Using decomposition (12.18) we can compute the total wavefield outside rectangle **b** without introducing a source (body-force term) in the finite-difference scheme used inside rectangle **b** or prescribing displacements at the grid points inside rectangle **b**. The residual displacement $\vec{u}_R$ inside and directly at rectangle **b** can be computed by the finite-difference scheme (the 2^{nd}-order scheme is assumed). The residual displacement $\vec{u}_R$ at rectangle **a** is computed using

$$\vec{u}_R\,(\mathrm{a}) \;=\; \vec{u}\,(\mathrm{a}) \;-\; \vec{s}\,(\mathrm{a}) \;. \tag{12.19}$$

The total displacement $\vec{u}$ at rectangle **b** is computed using

$$\vec{u}\,(\mathrm{b}) \;=\; \vec{s}\,(\mathrm{b}) \;+\; \vec{u}_R\,(\mathrm{b}) \;. \tag{12.20}$$

The total displacement $\vec{u}$ outside rectangle **b** (i.e., at rectangle **a** and outside rectangle **a**) is computed by the finite-difference scheme.

Note that the 4^{th}-order scheme obviously needs more excitation rectangles.

Such an indirect wavefield excitation was proposed by Alterman and Karal (1968). It is clear that using the source-displacement $\vec{s}$ it is possible to 'inject', e.g., an analytical solution corresponding to a desired source into the FD computation. Alterman and Karal (1968) used the technique to avoid a point-source singularity. The technique was applied by many modelers, e.g., Vidale et al. (1987) in the 4^{th}-order modeling, Moczo (1989), Fäh (1992), Fäh et al. (1993),

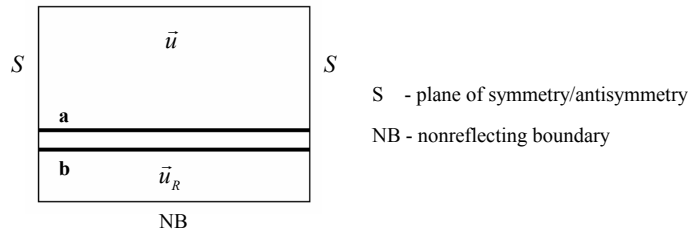

Fig. 12.6. Excitation lines **a** and **b** used for decomposition of the total displacement in simulation of the plane-wave radiation from the grid line **b** in the 2D problem.

Zahradník (1995), Robertson et al. (1996), Zahradník and Moczo (1996), Moczo et al. (1997), Robertson and Chapman (2000), Takeuchi and Geller (2003). For more details see Moczo et al. (2007).

A special case when only two excitation lines are used for a wavefield excitation (e.g., Moczo, 1989) is illustrated in Fig. 12.6. In this case the residual displacement $\vec{u}_R$ at line **b** and below line **b** is computed by the finite-difference scheme. The residual displacement $\vec{u}_R$ at line **a** is computed using eq. (12.19). The total displacement $\vec{u}$ at line **b** is computed using eq. (12.20). The total displacement $\vec{u}$ at line **a** and above line **a** is computed by the finite-difference scheme.

Fäh (1992), Fäh et al. (1993), Zahradník (1995), Robertson et al. (1996), Zahradník and Moczo (1996), Moczo et al. (1997), Robertson and Chapman (2000), Takeuchi and Geller (2003) applied the indirect wavefield excitation as a part of the two-step hybrid computations. Figure 12.7 illustrates the hybrid method of Zahradník (1995) and Zahradník and Moczo (1996).

In the $1^{\rm st}$ step, the wavefield is recorded along lines **a** and **b**. This wavefield, $\vec{u}_K$, consists of the wavefield radiated from the source (incident wavefield) and also of that reflected from the free surface (this is important). In the $2^{\rm nd}$ step

- $\vec{u}_R$ at rectangle **b** and inside the region bounded by rectangle **b**, nonreflecting (NB) boundaries and free surface (including) is computed by the finite-difference scheme,
- $\vec{u}_R$ at rectangle **a** is computed using

$$\vec{u}_R\,(\mathrm{a}) \;=\; \vec{u}\,(\mathrm{a}) \;-\; \vec{u}_K\,(\mathrm{a}), \tag{12.21}$$

- $\vec{u}$ at rectangle **b** is computed using

$$\vec{u}\,(\mathrm{b}) \;=\; \vec{u}_K\,(\mathrm{b}) \;+\; \vec{u}_R\,(\mathrm{b}), \tag{12.22}$$

- $\vec{u}$ at rectangle **a**, and inside the region bounded by **a** and the free surface is computed by the finite-difference scheme.

The use of the discrete-wavenumber method is not necessary - the source radiation and background wave propagation can be computed by any suitable method.

Moczo et al. (1997) generalized the hybrid approach of Zahradník and Moczo (1996) in their hybrid DW-FD-FE method for modeling of the 2D P-SV seismic motion in sedimentary/topographic local structures. The principle of the hybrid approach is illustrated in Fig. 12.8.

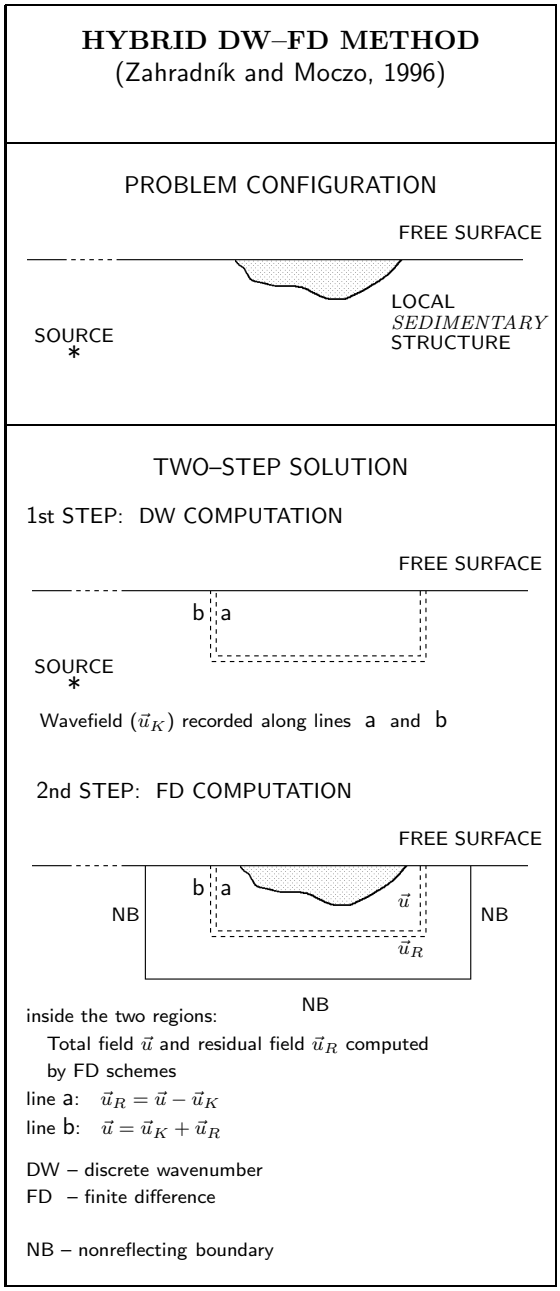

Fig. 12.7. Scheme of the hybrid discrete-wavenumber finite-difference method of Zahradník (1995) and Zahradník and Moczo (1996). DW discrete-wavenumber method, FD finite-difference method.

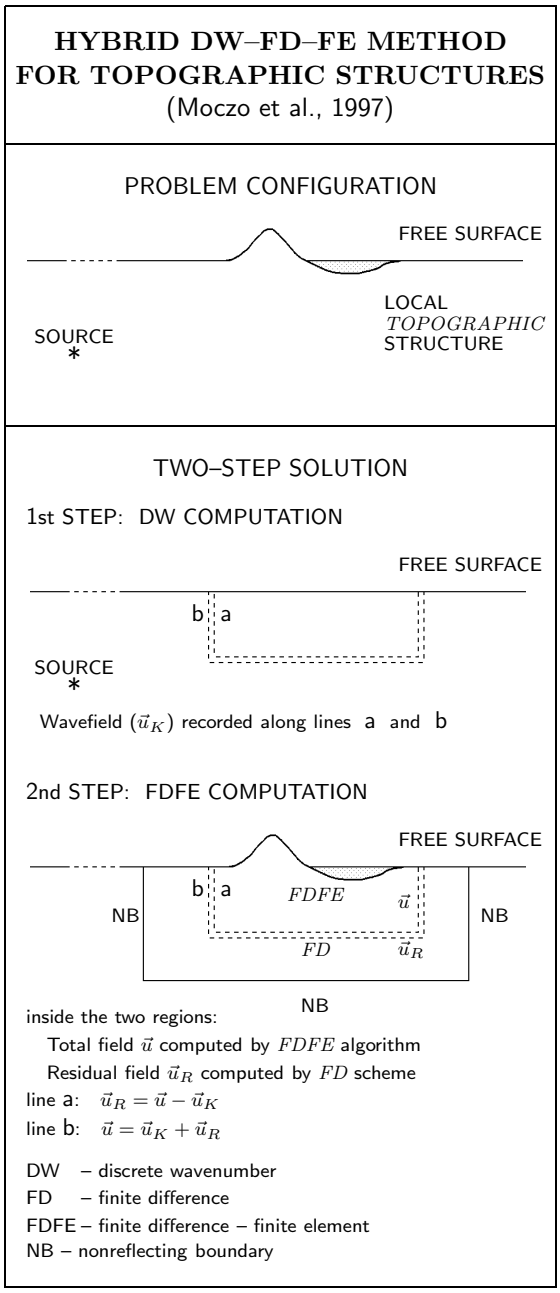

Fig. 12.8. Scheme of the DW-FD-FE (discrete-wavenumber - finite-difference - finite-element) hybrid method for computation of the 2D P-SV seismic motion in local surface structures including sedimentary body and topography of the free surface. Adapted from Moczo et al. (1997).

13 The FD Modeling of Earthquake Motion in Grenoble Basin, France

13.1 The ESG 2006 Grenoble Basin Benchmark

The Third International Symposium on the Effects of Surface Geology on Seismic Motion, ESG2006, was organized by Pierre-Yves Bard and his colleagues in the Laboratoire de Géophysique Interne et de Tectonophysique (LGIT), Université Joseph Fourier in Grenoble, France. The symposium provided an excellent opportunity to focus the traditional blind prediction experiment on numerical modeling of earthquake motion in the Grenoble basin for local weak and moderate earthquakes.

The Grenoble basin is a typical deep sedimentary Alpine basin. The city of Grenoble has considerable population, modern industry, and educational and research institutions. The regional and local earthquake activity imposes non-negligible level of earthquake hazard and risk. The structure of the sedimentary body was a subject of relatively detailed geophysical and seismological investigations. As a consequence, it was possible to define a reasonable structural model as well as possible earthquake sources for the numerical modeling of the earthquake motion.

13.2 Structural Model and Earthquake Sources

The organizers of the benchmark defined a structural model and four earthquake sources. The structural model is based on the map of the bedrock topography constructed by Vallon (1999). The bedrock depth has been obtained by inverting gravimetric measurements.

Geometry of the sediment-bedrock interface is shown in Fig. 13.1. Material parameters in the bedrock are specified in Tab. 13.1. Material parameters in the sediments are defined by relations

$$\alpha = 1450 + 1.2\,d\,, \tag{13.1}$$

$$\beta = 300 + 19.2\,\sqrt{d}\,, \tag{13.2}$$

$$\rho = 2140 + 0.125\,d\,, \tag{13.3}$$

$$Q_\mu = 50\,, \tag{13.4}$$

$$Q_\kappa = \infty\,, \tag{13.5}$$

$$Q_S = 50\,, \tag{13.6}$$

$$Q_P = \frac{3}{4}\,Q_S\,\frac{\alpha^2}{\beta^2}\,, \tag{13.7}$$

where α and β are the P- and S-wave velocities in m/s, ρ is density in kg/m^3, and d is depth in m. The density, P- and S-wave velocities as functions of depth are shown in Fig. 13.2.

The weak event W1 is a $M_w = 2.9$ right-lateral strike-slip earthquake on the Eastern part of the Belledonne border fault. The weak event W2 is a $M_w = 2.8$ left-lateral strike-slip earthquake on the Southern part of the Belledonne border fault. The strong event S1 is a $M_w = 6.0$ right-lateral strike-slip earthquake on the Eastern part of the Belledonne border fault. The kinematic model of the earthquake assumes a Haskell circular crack (with constant final displacement) propagating within a rectangular fault. The strong event S2 is a $M_w = 6.0$ left-lateral strike-slip earthquake on the Southern part of the Belledonne border fault. The kinematics of the event is the same as that of the S1 event. The source parameters of the four earthquakes are

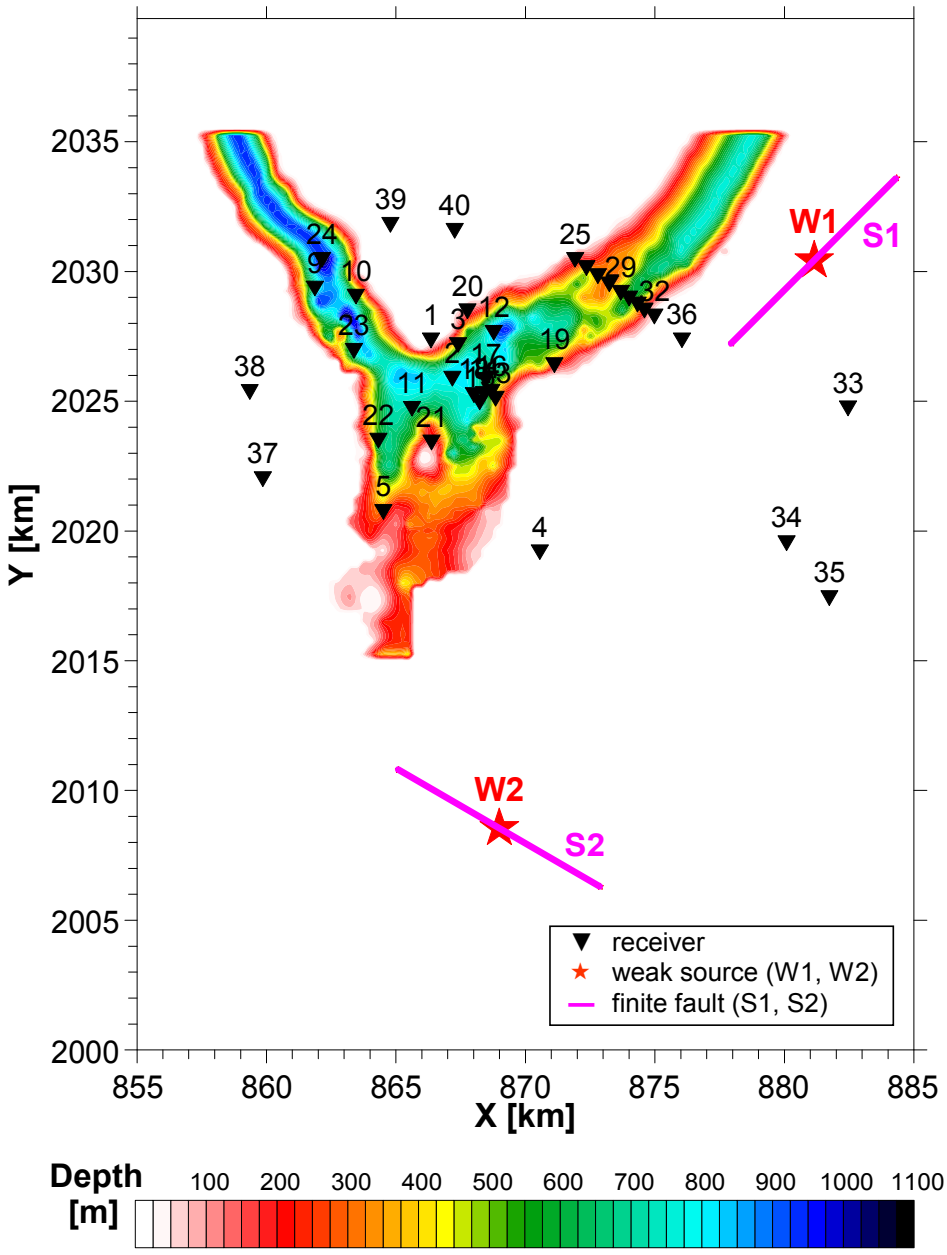

Fig. 13.1. Geometry of the sediment-bedrock interface in the standard geotechnical model provided for the benchmark simulation. Black triangles indicate positions of the receivers. Red stars indicate epicenters of two weak local earthquakes, W1 and W2, lines indicate finite faulting areas of two strong events, S1 and S2.

Tab. 13.1. Density ρ, P-wave velocity α, S-wave velocity β, quality factor for the shear modulus Q_μ, and quality factor for the bulk modulus Q_κ in the 1D model of bedrock.

Depth of the top of the layer [m]	α [m/s]	β [m/s]	ρ [kg/m^3]	Q_μ	Q_κ
0	5 600	3 200	2 720	∞	∞
3 000	5 920	3 430	2 720	∞	∞
27 000	6 600	3 810	2 920	∞	∞
35 000	8 000	4 450	3 320	∞	∞

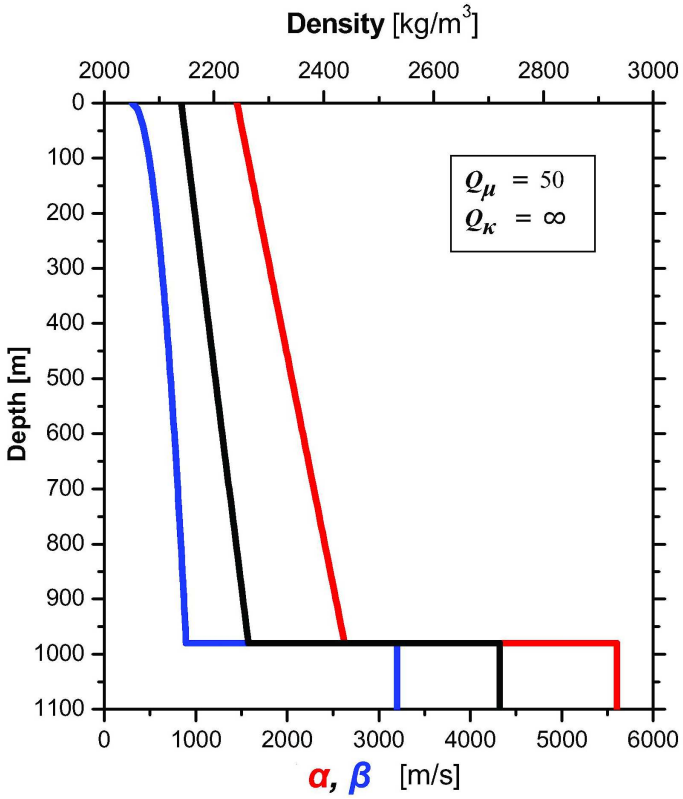

Fig. 13.2. Density ρ, P-wave velocity α and S-wave velocity β as functions of depth in the sediments. The quality factors for the shear and bulk moduli, Q_μ and Q_κ.

Tab. 13.2. The fault-orientation parameters, fault dimensions, hypocentral depth, and moment magnitude for the four considered events.

Source	Fault orientation			Fault dimensions		Hypocentral depth [m]	Moment magnitude M_w
	Strike [°]	Dip [°]	Rake [°]	Length [m]	Width [m]		
W1	45	90	180	n/a	n/a	3 000	2.9
W2	160	90	180	n/a	n/a	3 000	2.8
S1	45	90	180	9 000	4 500	3 000	6.0
S2	120	90	0	9 000	4 500	3 000	6.0

specified in Tab. 13.2. The slip as function of time was specified by

$$s_{tf} \;=\; \frac{1}{2}\left[\,1 \;+\; \mathrm{erf}\left(\; scaling\,\frac{t\;-\;t_0}{t_{dur}}\;\right)\right] \tag{13.8}$$

with $scaling = 2$, $t_{dur} = \tau/2$, and $t_0 = 2\,\tau$. For events W1 and W2 $\tau = 0.03$ s, for events S1 and S2 $\tau = 1.116$ s. These times were chosen to define the slip velocity of (approximately) 1 m/s.

13.3 Arbitrary Discontinuous Staggered Grid and the 4$^{\mathrm{th}}$-order VS SG Scheme

The minimum S-wave velocity in the bedrock is more than three time larger than the maximum S-wave velocity in sediments. The ratio is even much larger for the sediments near the free surface. The hypocentral depth in all four events is 3 km. Therefore, it is very clear that the application of the uniform spatial grid with a constant size of the grid spacing would lead to a considerable oversampling in a major part of the computational domain. This would lead to unnecessary large computer memory and time requirements.

The total number of the grid points/cells and/or the computer memory and time requirements can be reduced using several approaches. Examples are material cell types, core memory optimization, combined memory optimization, spatial discontinuous grid, varying size of the grid spacing, spatially varying time step, discontinuous space-time grids, higher-order approximation in space and/or time, and parallelization. For a review of these approaches we refer to Moczo et al. (2007).

Reduction of the total number of grid points using an irregular spatial grid obviously can be a strong tool in optimizing the numerical simulation. The rectangular grid with a varying size of the grid spacings was first used by Boore (1970) in the 1D problem. Mikumo and Miyatake (1987) applied the varying size of the grid spacing in the 3D case in a homogeneous medium. Moczo (1989) applied the grid with the varying size of the grid spacing to the 2D SH problem in the laterally heterogeneous medium, Pitarka (1999) presented the 3D velocity-stress scheme with a varying size of the grid spacing. Jastram and Behle (1992), Jastram and Tessmer (1994), Falk et al. (1996), Moczo et al. (1996), Kristek et al. (1999), Aoi and Fujiwara (1999), Hayashi et al. (2001), Moczo et al. (2001), and Wang et al. (2001) introduced spatial discontinuous grids.

A spatial discontinuous grid for modeling of seismic motion in near-surface sedimentary structures usually consists of two spatial grids - a finer grid covering the sediments (with smaller S-wave velocity) and a coarser grid covering the stiffer bedrock. In the simplest configuration a horizontal layer of finer grid cells overlies a horizontal layer of larger grid cells. In order to make such combined (or discontinuous) spatial grid efficient, the ratio of the size of a spatial grid spacing in the coarser grid and that in the finer grid should correspond to the ratio of the shear-wave velocities in the stiffer bedrock and softer sediments. Therefore we developed an algorithm that enables to adjust a discontinuous spatial grid accordingly except that, due to the structure of the staggered grid, the ratio of the spatial grid spacings in the coarser and finer grids has to be an odd number. In other words, depending on the model of medium, we can choose a 1:1 (uniform) grid, or 1:3, 1:5, ... discontinuous grid. The grid is illustrated in Fig. 13.3.

The FD scheme used for the benchmark simulations is the 4^{th}-order velocity-stress staggered-grid scheme described in detail in sections 7.2, 8.1.4 and 9.2.

Fig. 13.3 indicates an overlapping of the finer and coarser grids.If the grid points of the finer and coarser grids share the same position, they also share the same values of the particle-velocity and stress-tensor components. At the grid points close to the bottom of the finer grid only the 2^{nd}-order FD scheme is applied. Still there are grid points (shown in yellow in Fig. 13.3) for which the stencil of the 2^{nd}-order scheme is not complete. At these points the required values of the particle-velocity or stress-tensor components are obtained by a bicubic interpolation using values at neighboring grid points at the same horizontal plane.

Note that despite the formal 2^{nd}-order accuracy at the grid points close to the bottom of the finer grid, the effective accuracy of the 4^{th}-order modeling is not affected for a simple reason: the overlapping zone of the two grids is located in the stiffer bedrock, that is in the medium with at least 3 times larger S-wave velocity. Consequently, there is a relative oversampling of the minimum wavelength.

13.4 Simulations and Results

In the benchmark simulation we used the 1:5 discontinuous spatial grid. The PML (Perfectly Matching Layers) with a layer thickness of 10 grid spacings in the coarser and 50 grid spacings in the finer grid were used.

All simulations where performed on the small cluster of Opteron 2.2 GHz machines (6 CPUs, 10 GB RAM in total). The discontinuous grid with finer grid of $1321 \times 1431 \times 45$ grid cells and 25 m grid spacing, and coarser grid of $265 \times 287 \times 65$ grid cells and 125 m grid spacing were used. The time step in all simulations was 0.0022 s. The maximum frequency is around 2.5 Hz. The computational time for the 30 s time window (for the weak events W1 and W2) was 33 hours, for the 80s time window (for the strong events S1 and S2) 88 hours. The peak-ground-velocity maps and the z-component (here positive in the upward vertical direction) of the particle velocity at (theoretical) receiver positions R25 - R32 along the 2D profile are displayed in Figs. 13.4 – 13.7. We do not interpret the results here. The comparison of all submitted solutions is a subject of the complex evaluation of the benchmark simulation experiment by the organizers. Moreover, the structural model defined for the benchmark is, in fact, a little bit modified compared to the true structure. This is because it is easier to perform simulations for laterally bounded sedimentary body. Here we only illustrate our simulation by comparing it with the simulation performed by Emmanuel Chaljub of LGIT, Université Joseph Fourier, Grenoble. Chaljub used the spectral-element method (SPEM) for his simulation. Figure 13.8 shows the z-component of

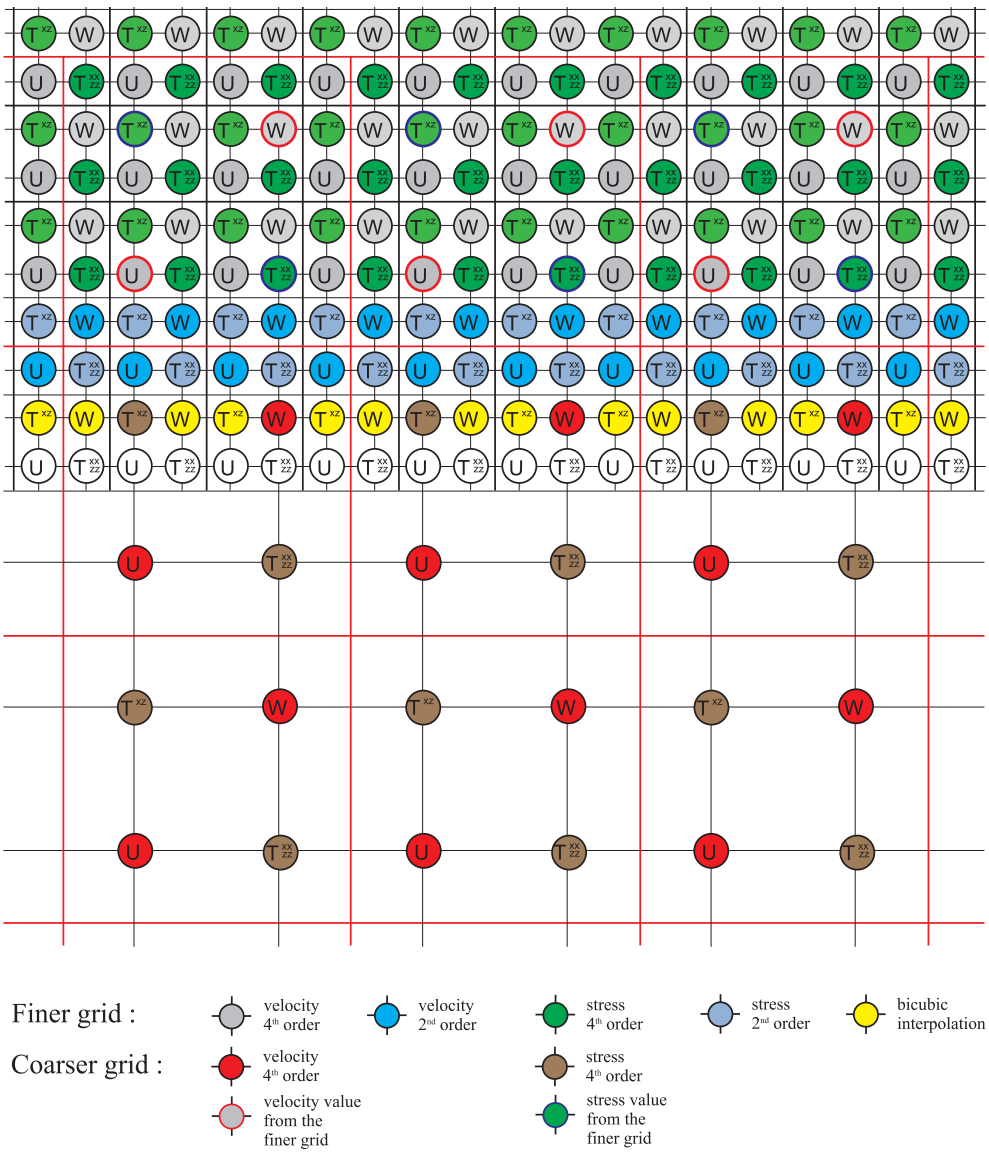

Fig. 13.3. A vertical grid plane in the arbitrary discontinuous spatial grid in the case of the coarser-to-finer spatial grid spacing ratio equal to 3.

the particle velocity at receiver positions R25 - R32 simulated by our FD scheme and spectral-element method. Given the structural complexity of the benchmark model and differences in the two simulation methods, the synthetic velocity seismograms obtained by the two methods can be

considered surprisingly close.

14 Hybrid FD-FE Modeling of Earthquake Motion

14.1 Introduction to the Hybrid Modeling

In many wavefield-medium problem configurations it is advantageous to combine two or even more computational methods in order to solve the problem with a reasonable level of accuracy and computational efficiency. In some cases it is advantageous to solve time dependence of the displacement using one method and spatial dependence using some other method (e.g., Alexeev and Mikhailenko, 1980). In some other cases it is reasonable to split the computational domain into two or more parts and solve each part by the best suited method. Several hybrid methods were developed in an effort to achieve reasonable computational efficiency in applications to relatively complex structural models. They include methods by Ohtsuki and Harumi (1983), Shtivelman (1984, 1985), Van den Berg (1984), Kummer et al. (1987), Stead and Helmberger (1988), Kawase (1988), Gaffet and Bouchon (1989), Emmerich (1989, 1992), Fäh (1992), Fäh et al. (1993), Rovelli et al. (1994), Bouchon and Coutant (1994), Robertsson (1996), Zahradník and Moczo (1996), Moczo et al. (1997), Lecomte (2004), Ma et al. (2004).

14.2 The 4^{th}-order VS SG FD Scheme Combined with the 2^{nd}-order FE Scheme

The FE method more easily incorporates boundary conditions at the free surface and material interfaces compared to the FD method. This is especially true about non-planar surfaces and interfaces. From this point of view the FE method is better suited for simulation of the traction-free condition and rupture propagation. On the other hand, the 4^{th}-order staggered-grid FD scheme is computationally more efficient if the seismic wave produced, e.g., by the dynamically rupturing fault, are to be propagated away from the fault. It is therefore very natural to think of a hybrid combination of the two methods if we want to comprise both the dynamic earthquake source and the wave propagation in the complex heterogeneous medium. Moczo et al. (1997) combined the 2^{nd}-order conventional FD scheme with the 2^{nd}-order FE method for the 2D P-SV modeling of seismic motion in the near-surface sedimentary/topographic structure. Ma et al. (2004) combined the 4^{th}-order velocity-stress staggered-grid scheme with the 2^{nd}-order FE method for the 2D P-SV modeling.

Here we combine the 4^{th}-order velocity-stress staggered-grid scheme with the 2^{nd}-order FE method for the 3D modeling of earthquake motion in the heterogeneous viscoelastic medium with the free-surface topography and with, optionally, kinematic (point or finite) or dynamic earthquake source.

The basic theory was explained in sections 3.4, 6.3, 7.2, 8.1.4, 9.2.2, and 11.2. In the following sections we will focus on particular aspects of the hybrid FD-FE modeling.

14.2.1 Computational Domain

A part of the computational domain with the free-surface topography or dynamically rupturing fault can be covered by the finite elements. In principle the whole computational domain can involve several FE regions. Obviously, the FE region should be as small as possible. The rest

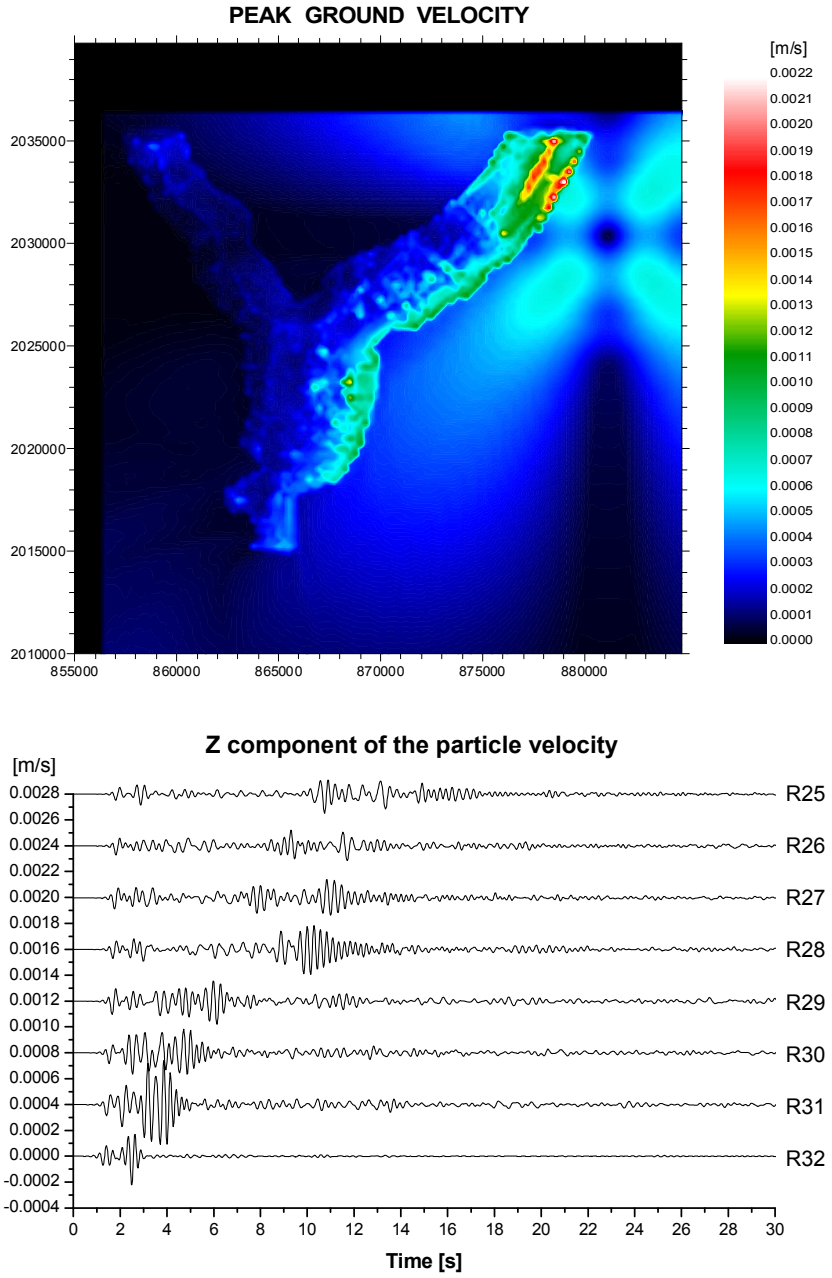

Fig. 13.4. Numerical simulation for the W1 earthquake. Top: The peak-ground velocity map, bottom: vertical component of the particle velocity at receivers No. 25 - No. 32.

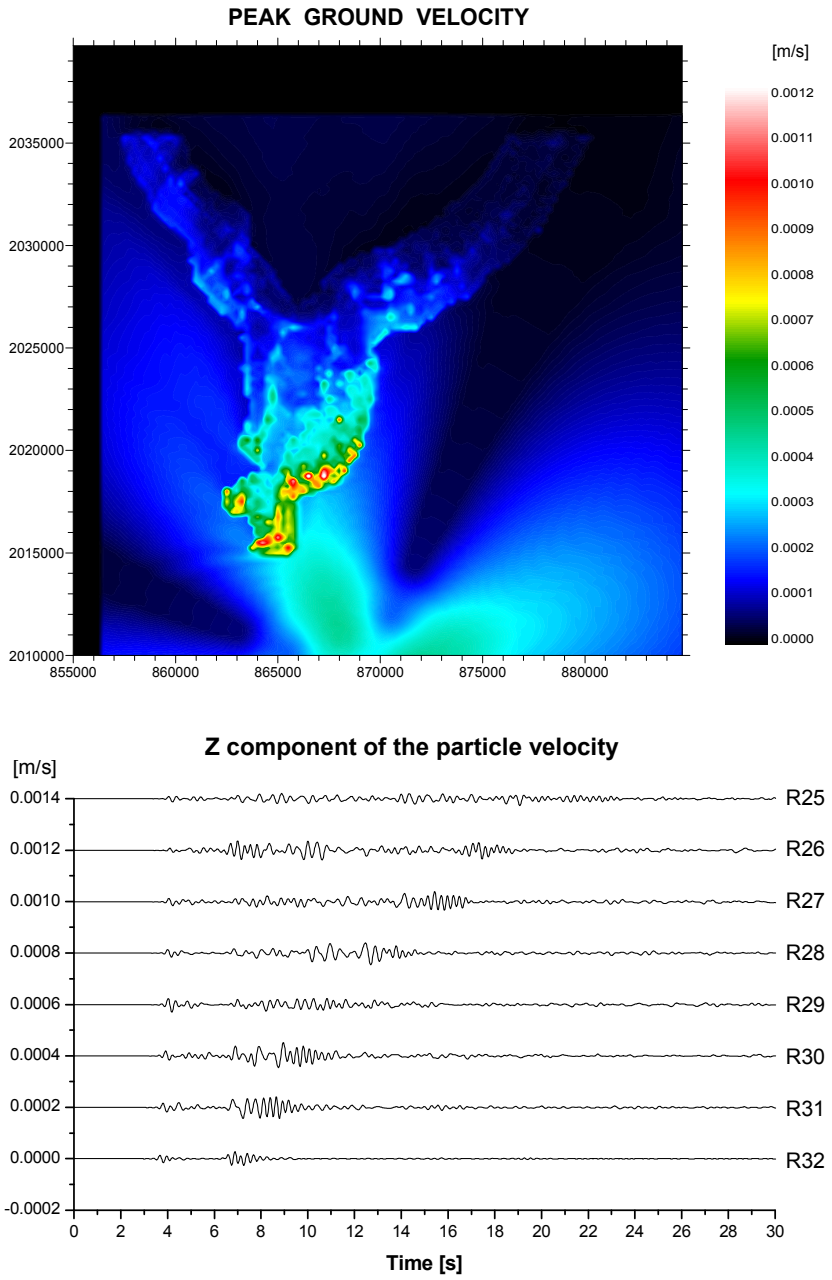

Fig. 13.5. Numerical simulation for the W2 earthquake. Top: The peak-ground velocity map, bottom: vertical component of the particle velocity at receivers No. 25 - No. 32.

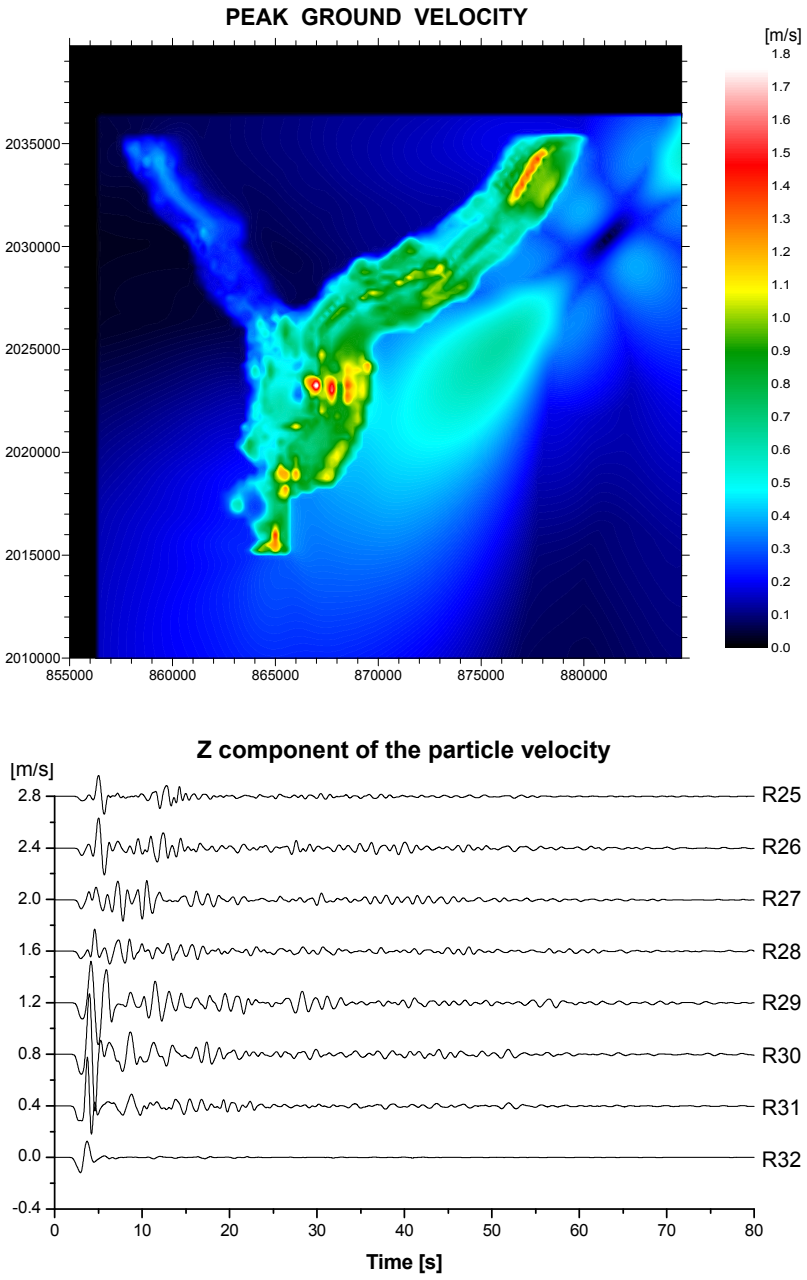

Fig. 13.6. Numerical simulation for the S1 earthquake. Top: The peak-ground velocity map, bottom: vertical component of the particle velocity at receivers No. 25 - No. 32.

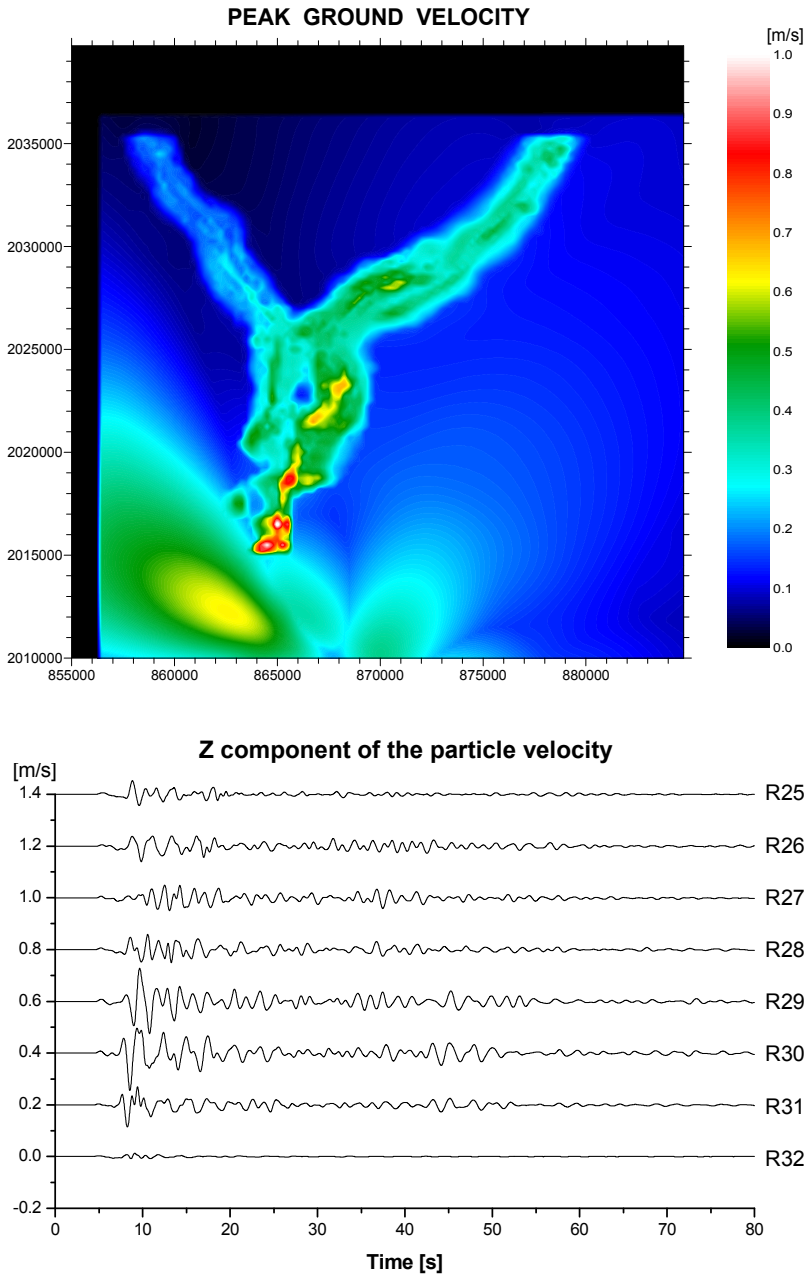

Fig. 13.7. Numerical simulation for the S2 earthquake. Top: The peak-ground velocity map, bottom: vertical component of the particle velocity at receivers No. 25 - No. 32.

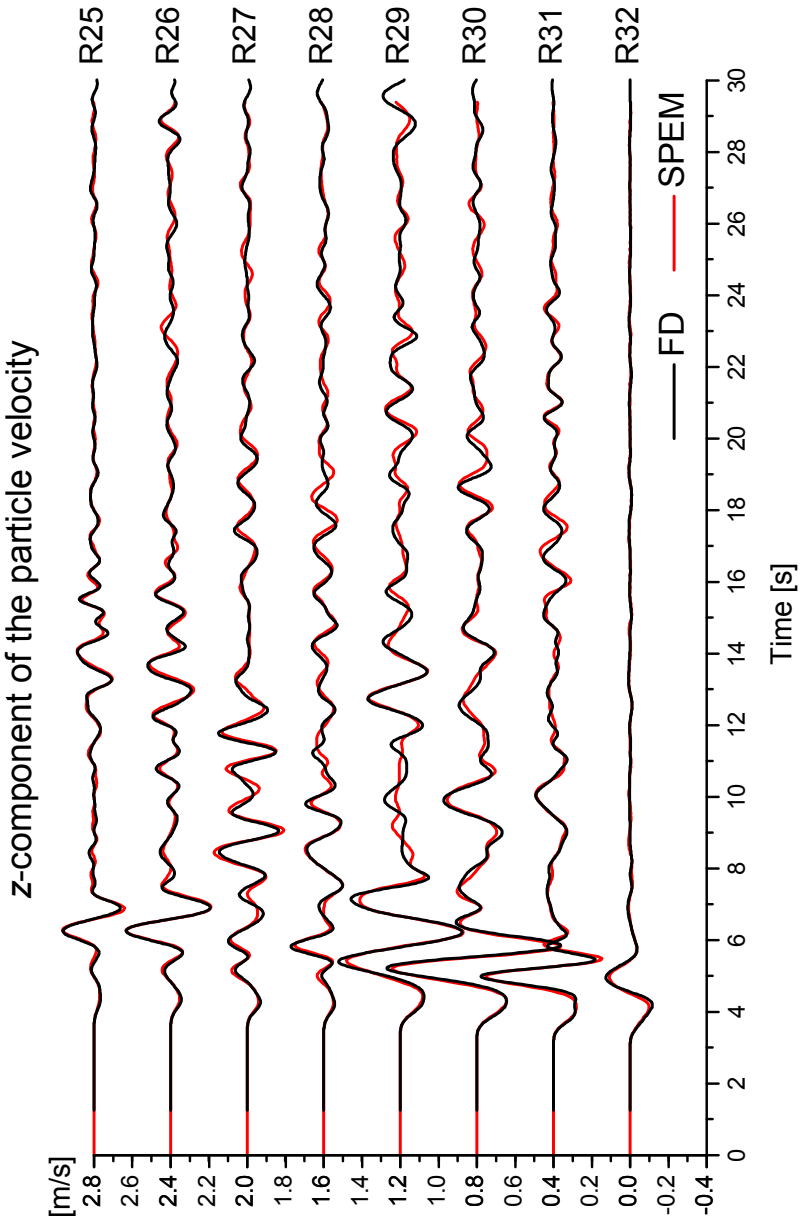

Fig. 13.8. Comparison of the velocity seismograms obtained using the 4^{th}-order velocity-stress staggered-grid FD scheme (FD, in black; our simulation) with the velocity seismograms obtained using the spectral-element method (SPEM, in red; author Emmanuel Chaljub, LGIT, Université Joseph Fourier, Grenoble) for the S1 Grenoble benchmark simulation experiment.

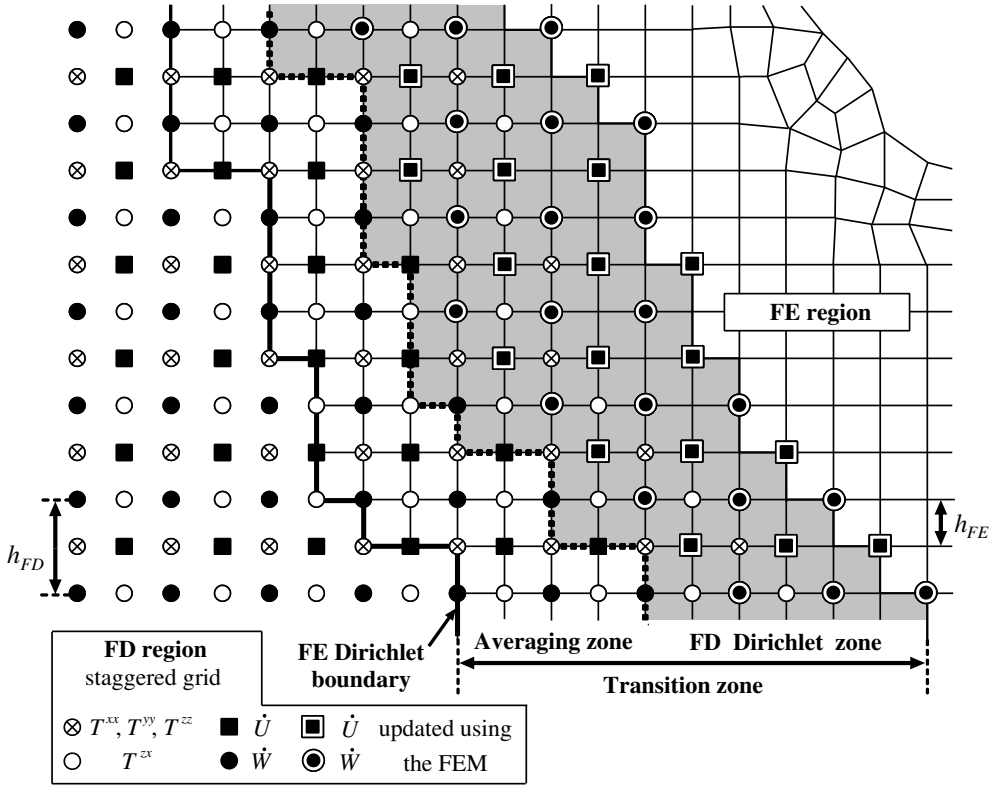

Fig. 14.1. The FD-FE transition zone in the FD-FE hybrid modeling. For simplicity, only the vertical grid plane with the x- and z-components of the particle velocity, $\dot{U}$ and $\dot{W}$, is shown (compare with Fig. 6.1). h_{FD} is the spatial grid spacing in the FD grid, h_{FE} is the spatial grid spacing in the uniform part of the FE grid near the transition zone (the rest of the FE grid can be non-uniform). Note that no special symbol is used to indicate positions of the displacement in the FE grid. Each grid point in the FE region, that is, each intersection of the grid lines in the FE region, is a position of the all components of the displacement vector.

of the computational domain is covered by the FD grid. The interiors of the FE and FD regions are updated independently by the FE and FD schemes, respectively. The FE and FD regions communicate at each time level at the contacts of the regions, that is, in the FD-FE transitions zones.

14.2.2 The FD-FE Transition Zone

The FD and FE schemes communicate with each other at each time level only in the transition zone. The transition zone is the region where the FD and FE grids overlap. A vertical cross-section of the transition zone is shown in Fig. 14.1. The transition zone consists of the FE Dirichlet boundary, averaging zone, and FD Dirichlet zone. The FE Dirichlet boundary is,

in general, a staircase grid surface that has to go through the grid points of the FD staggered grid. The algorithm of the FD-FE communication in fact does not require the weighting zone. However, our numerical tests clearly show that it is significantly better if the averaging zone is defined. Even one FD grid spacing thick averaging zone makes a significant difference in the numerical behavior of the transition zone. The local thickness and (staircase) shape of the FD Dirichlet zone is determined by requirement that the particle-velocity and stress-tensor components located directly at the grid interface between the averaging zone and FD Dirichlet zone be calculated using the $4^{\rm th}$-order VS SG interior-point formula. The FE region near the transition zone has to be uniform because the staggered grid is uniform.

As shown in Fig. 14.1, the size of the grid spacing in the FE grid is twice smaller compared to that in the FD grid. Intuitively, this is a reasonable choice given the $2^{\rm nd}$- and $4^{\rm th}$-order approximations in the FE and FD schemes, respectively. Kristek and Moczo (2006) indicated by their numerical investigations for the 1D problem that the $4^{\rm th}$-order staggered-grid scheme requires denser spatial sampling than that usually considered in the $4^{\rm th}$-order staggered-grid modeling (that is, approximately twice coarser compared to the $2^{\rm nd}$-order conventional schemes). At the same time, the numerical modeling of the rupture propagation and free-surface topography requires denser spatial sampling compared to that usually considered for the wave propagation.

The algorithm of the FD-FE hybrid method can be summarized in the following steps:

- Displacements $U_{FE}(m+1)$ are updated at the grid points of the interior FE region (the FE grid points except the FE Dirichlet boundary).
- Particle velocities $\dot{U}_{FD}(m+\frac{1}{2})$ are updated at the grid points of the interior FD region (that is, including the dashed line between the averaging zone and FD Dirichlet zone in Fig. 14.1).
- Particle velocities within the FD Dirichlet zone (that is at the grid points indicated by the double squares and circles in Fig. 14.1;) are updated using the FE displacement values at the same grid points:

$$\dot{U}_{FD}(m+\tfrac{1}{2}) \;=\; \frac{U_{FE}(m+1)-U_{FE}(m)}{dt}\,. \tag{14.1}$$

- Averaging of the FD particle velocities in the averaging zone (including the dashed line between the averaging zone and FD Dirichlet zone in Fig. 14.1):

$$\dot{U}^{w}_{FD}(m+\tfrac{1}{2}) \;=\; w\,\frac{U_{FE}(m+1)-U_{FE}(m)}{dt} \;+\; (1-w)\,\dot{U}_{FD}(m+\tfrac{1}{2})\,, \tag{14.2}$$

  where $w = 1$ at the dashed line between the averaging zone and FD Dirichlet zone, and $w = 0$ at the FE Dirichlet boundary. The weighting coefficient linearly changes between the two values over the averaging zone.

- Averaging of the FE displacements in the averaging zone (including the dashed line between the averaging zone and FD Dirichlet zone in Fig. 14.1):

$$\dot{U}^{w}_{FE}(m+\tfrac{1}{2}) \;=\; w\,\dot{U}_{FE}(m+\tfrac{1}{2}) \;+\; (1-w)\,\dot{U}_{FD}(m+\tfrac{1}{2})\,, \tag{14.3}$$

$$U^{w}_{FE}(m+1) \;=\; U_{FE}(m) \;+\; dt\,\dot{U}^{w}_{FE}(m+\tfrac{1}{2})\,. \tag{14.4}$$

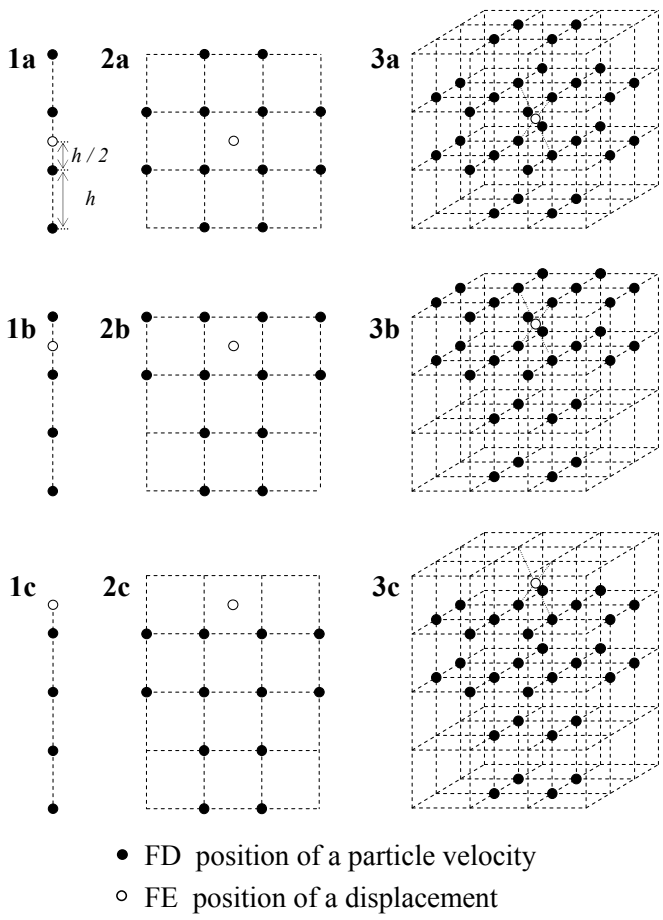

Fig. 14.2. All possible grid positions of the FE displacements at which a missing component of the FD particle velocity has to be interpolated. The boldface letter **a** refers to the interior grid points, **b** to the near-surface, and **c** to the surface grid points.

Because at one grid point in the averaging zone either one or no component of the FD particle velocity is available, it is necessary to calculate the missing components of the FD particle velocity using interpolation from the neighboring grid points. Figure 14.2 shows all possible positions at which a missing component of the particle velocity has to be interpolated. All interpolations are the 4^{th}-order accurate.

- The original FD particle velocities and FE displacements in the averaging zone (that is those updated by the FD and FE schemes) are replaced by the averaged values.

- Update of the FE displacements at FE Dirichlet boundary at time level $m + 1$ from the

FD particle velocities at time level $m + 1/2$:

$$U_{FE}(m+1) \;=\; U_{FE}(m) \;+\; dt\,\dot{U}_{FD}(m+\tfrac{1}{2})\,. \tag{14.5}$$

Because at one grid point at the Dirichlet boundary either one or no component of the FD particle velocity is available, it is necessary to calculate the missing components of the FD particle velocity using interpolation from the neighboring grid points - as in the averaging of the FE displacements.

14.3 Hybrid Modeling of Earthquake Motion in Grenoble Basin

The local earthquake activity near Grenoble is related to several faults; see, e.g., Cotton et al. (1998). With reference to investigations of the historical earthquake activity and tectonic situation by Gamond (1994) and Thouvenot (1996), Cotton et al. (1998) considered two hypothetical earthquakes near Grenoble and performed numerical simulations of the earthquake motion in Grenoble basin. One earthquake was considered as a thrust event beneath Grenoble, the other earthquake was assumed as a strike-slip faulting in the Belledonne Massif. In both cases Cotton et al. (1998) modeled the earthquake sources as kinematic point sources. They used the 4^{th}-order velocity-stress staggered-grid FD scheme.

Here we apply our hybrid FD-FE method for the modeling of the two hypothetical earthquakes. Because it is relatively easy in our method to model dynamically rupturing fault, we consider in both cases a finite size of the ruptured area and spontaneous rupture propagation. Michel Bouchon and Pierre-Yves Bard (both LGIT, Université Joseph Fourier, Grenoble), suggested the following hypothetical dynamic model: initial traction in the horizontal in-plane direction 10 MPa, initial traction in the horizontal anti-plane direction 0 MPa, initial normal traction -17 MPa, static and dynamic coefficients of friction 0.7 and 0.235, respectively, linear slip-weakening friction law. The same dynamic model is assumed for both the thrust and strike-slip earthquakes. The ruptured area was restricted to approximately 4 km $\times$ 2 km by a continuous increase of the values of the static and dynamic coefficients of friction. This restriction was chosen to produce slip equivalent to $M_w = 5.3$ earthquake. The hypocenter was located at the center of the ruptured area. The initialization zone was a circle with the 500 m diameter. The in-plane shear initial traction inside the initialization zone was 2.5 % larger than the static traction.

The geometrical configuration of the Grenoble basin and thrust fault is shown in Fig. 14.3. The rupturing area of the fault is located inside the FE box. As it is clear from the figure, the FE box is relatively small portion of the whole computational domain. The major part of the domain is covered by the FD grid. This hybrid or combined coverage of the computational domain makes the simulation considerably computationally more efficient compared to the simulation with the FE grid covering the whole domain.

Material parameters of the structural model are specified in Fig. 14.4. The computational parameters were chosen such that the simulation should be sufficiently accurate up to (approximately) 7.6 Hz in the bedrock and 0.7 Hz in the sediments near the free surface.

Results of the numerical simulation for the thrust event are illustrated in Figs. 14.5 - 14.7. The figures show sequence of the wavefield snapshots of the simulated earthquake motion at the free surface. Each snapshot shows the spatial distribution of the absolute value of the (total) horizontal component of the particle velocity at the free surface at a chosen time. The sequence

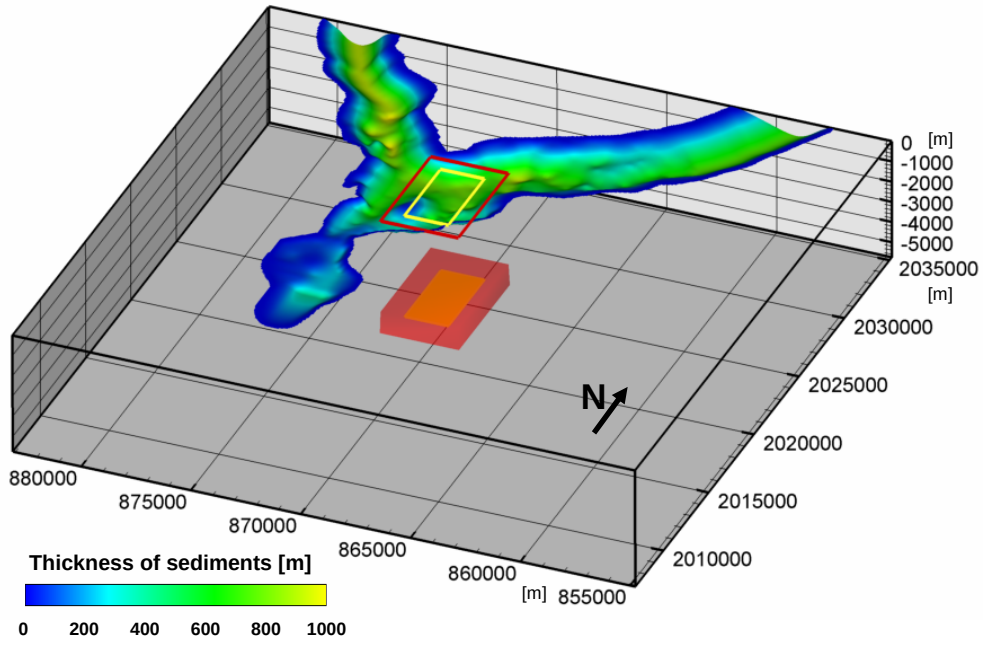

Fig. 14.3. Geometrical configuration of the Grenoble sedimentary basin and dynamically rupturing thrust (horizontal) fault: interface between sediments and bedrock with indication of the sediment thickness, the FE region (red box) covering the ruptured fault area (yellow area inside the red box), projections of the FE region and ruptured fault area onto the flat free surface. The fault is at depth of 5 km.

of snapshots clearly indicates seismic waves radiated from the rupturing fault and the corresponding seismic motion outside the basin as well as the penetration of the seismic waves into the sedimentary body at earlier times of the simulation. Due to relatively large impedance contrast between the sediments and bedrock, the seismic energy is trapped in the sediments at later times. Due to the complex development of the wavefield inside the geometrically complicated sedimentary body (generation of local surface waves in the sediments, constructive/destructive interference of the body and surface waves, multiple reflections of the waves between the free surface and the sediment-bedrock interface, diffraction), clear dominance of the motion inside the basin compared to that outside the basin, and its complex space-time variation, is observed in the snapshots.

Figure 14.8 shows the geometrical configuration of the Grenoble basin and strike-slip fault considered in the simulation of the second hypothetical earthquake. The mechanical parameters of the structural model are the same as in the previous case. Results of the numerical simulation for the strike-slip event are illustrated in Figs. 14.9 - 14.11. Similarly to the first simulation, the figures show sequence of the wavefield snapshots of the simulated earthquake motion at the free surface. Though, qualitatively, we can say almost the same brief characteristics of the development as in the case of the first earthquake, it is very clear from the sequence of snapshots

	Sediments	Halfspace
P-wave velocity [m/s]	Grad.	5400
S-wave velocity [m/s]	Grad.	3200
Density [kg/m^3]	Grad.	2500
P-wave quality factor	40	∞
S-wave quality factor	20	∞

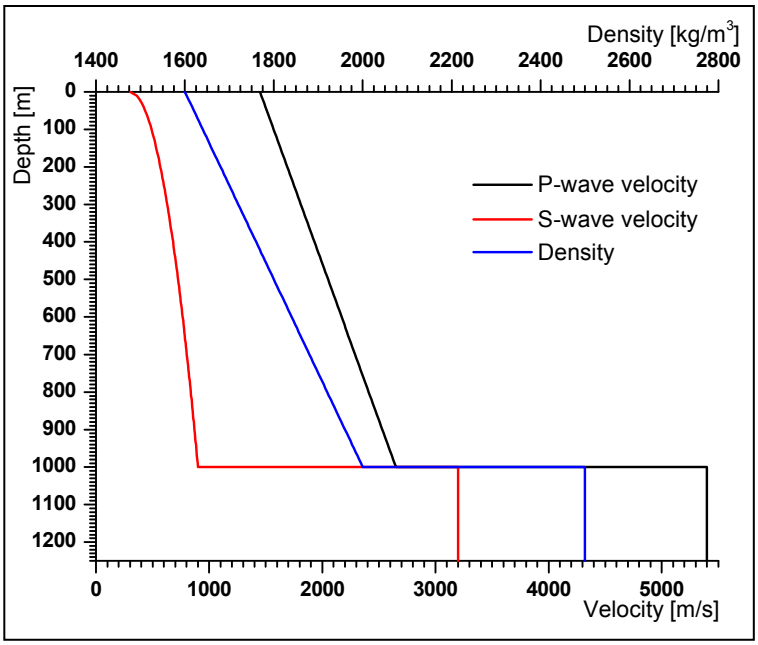

Fig. 14.4. Material parameters in the computational model of the Grenoble basin.

that the space-time variation of the earthquake motion in the basin considerably differs from that in the first earthquake. Obviously, this is a consequence of different geometrical configuration of the basin structure and the rupturing fault.

While a detailed analysis and complex characterization of the seismic motion is necessary and possible in the seismological investigations, it is not commonly applied in the earthquake-engineering practice. Instead of a complex time history of the displacement, particle-velocity or acceleration at each point of the investigated area of the free surface they require at most one scalar quantity representative of the earthquake motion at a given point of the free surface. Several single-valued or integral characteristics of the earthquake motion were defined for this purpose. Here we consider peak horizontal acceleration, PHA, that is the maximum value of the

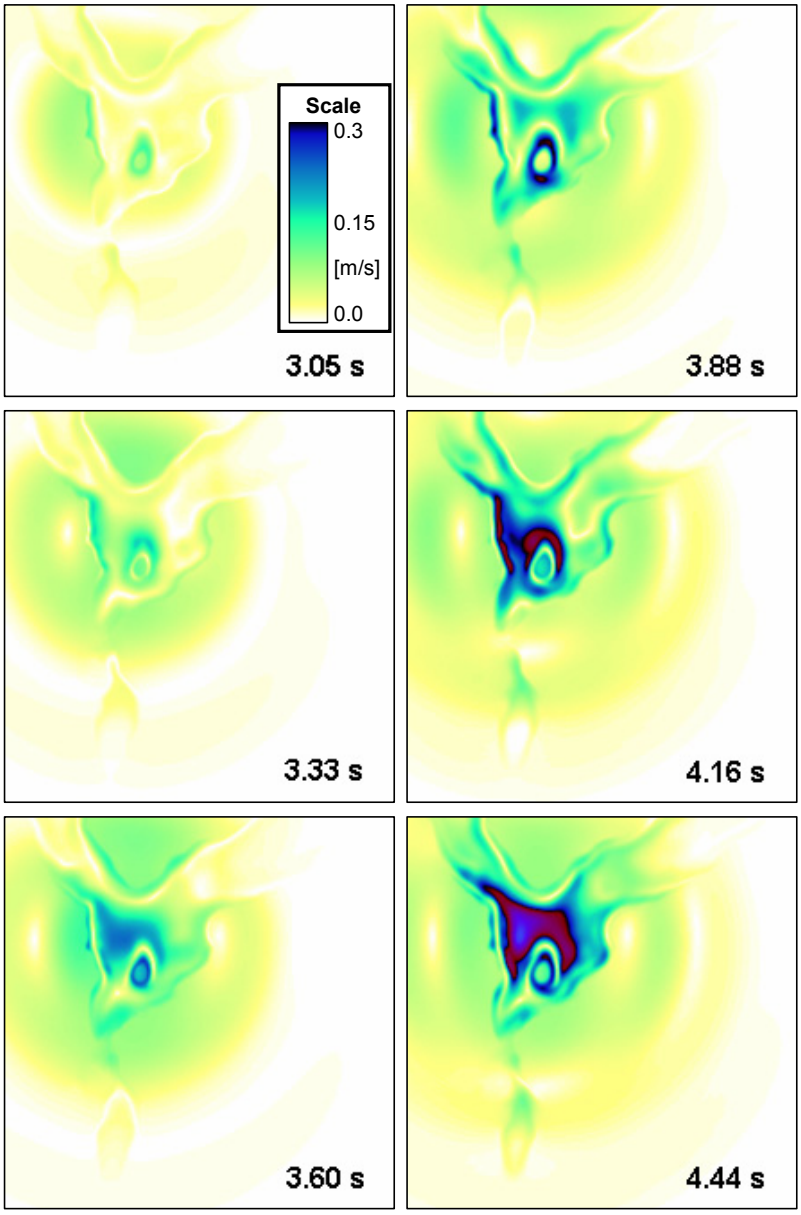

Fig. 14.5. Sequence of the wavefield snapshots for the simulated thrust earthquake beneath the Grenoble basin - the first part. The color scale indicates the absolute value of the horizontal component of the particle velocity at the free surface. For the movie click here.

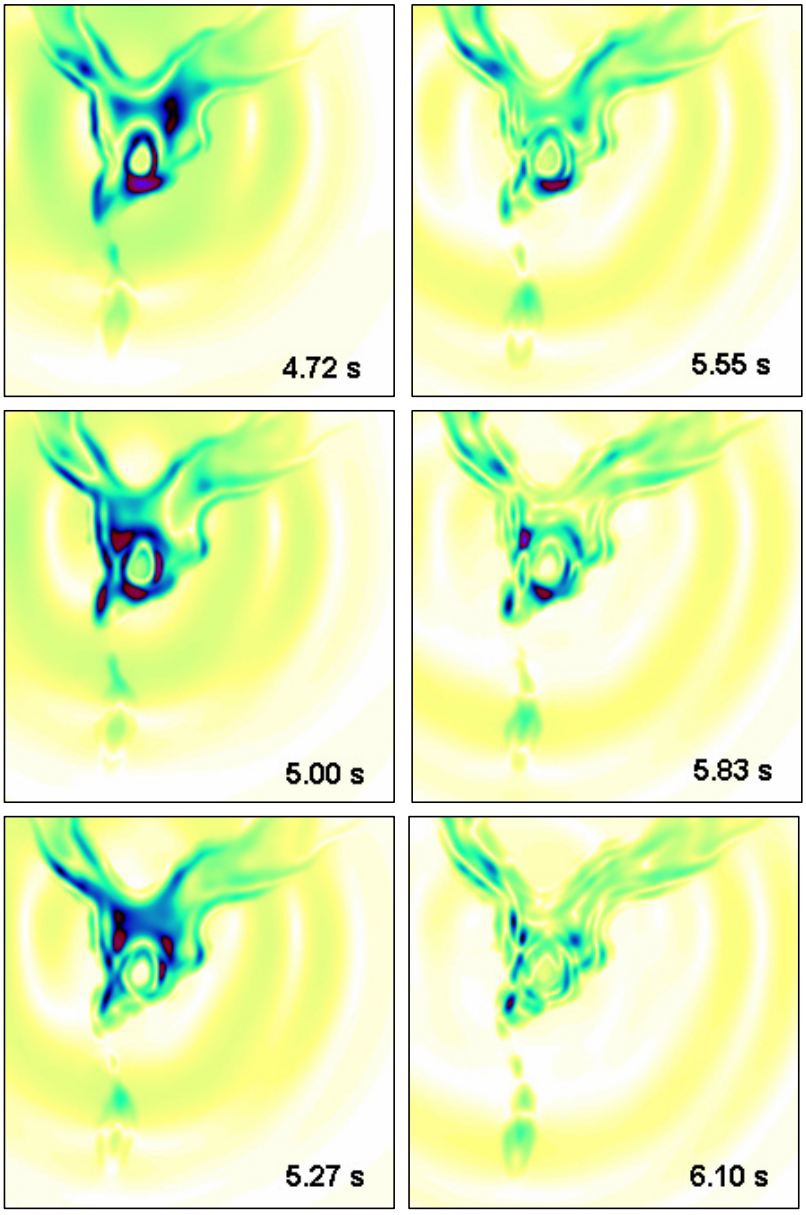

Fig. 14.6. Sequence of the wavefield snapshots for the simulated thrust earthquake beneath the Grenoble basin - the second part. The color scale indicates the absolute value of the horizontal component of the particle velocity at the free surface.

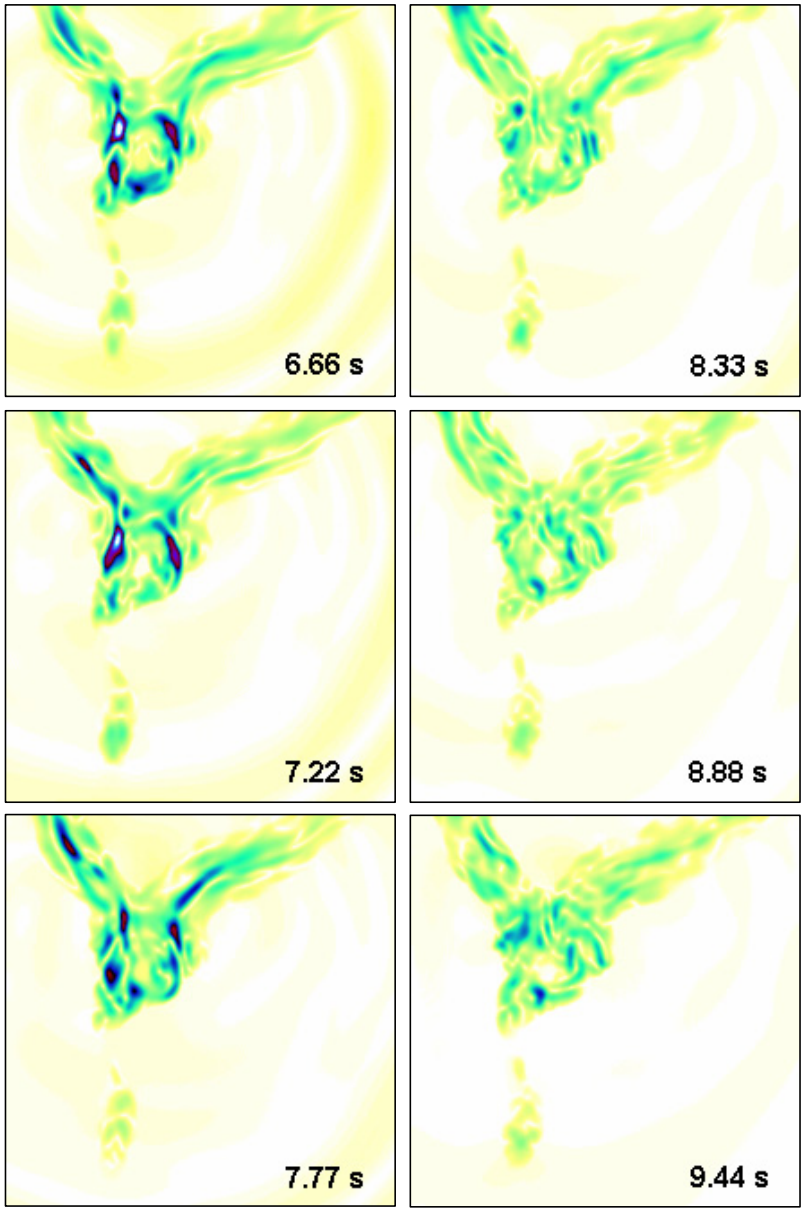

Fig. 14.7. Sequence of the wavefield snapshots for the simulated thrust earthquake beneath the Grenoble basin - the third part. The color scale indicates the absolute value of the horizontal component of the particle velocity at the free surface.

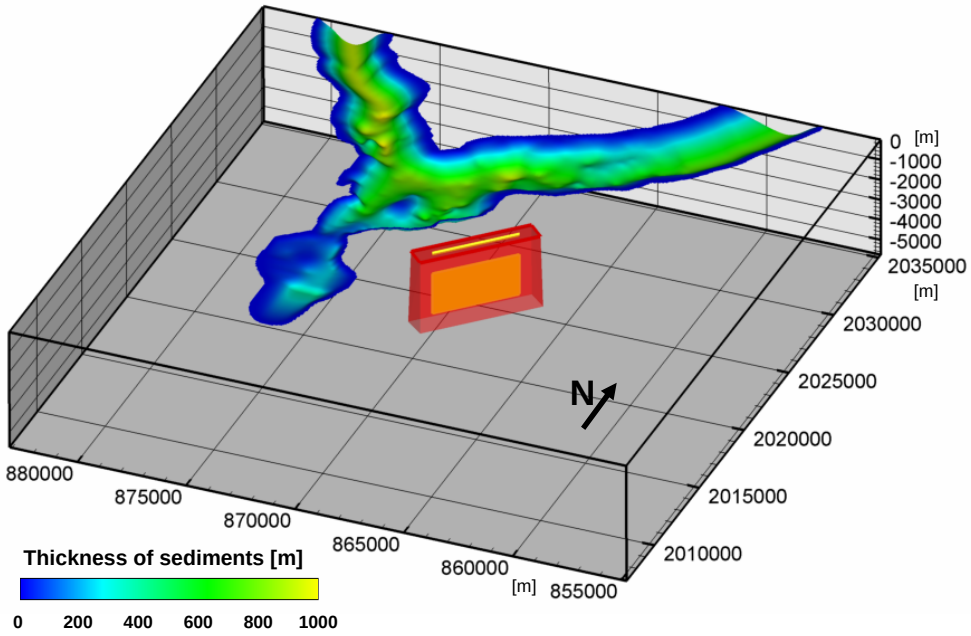

Fig. 14.8. Geometrical configuration of the Grenoble sedimentary basin and dynamically rupturing strike-slip (vertical) fault: interface between sediments and bedrock with indication of the sediment thickness, the FE region (red box) covering the ruptured fault area (yellow area inside the red box), projections of the FE region and ruptured fault area onto the flat free surface. The ruptured fault area reaches depth of 3.5 km.

modulus of the total horizontal component of acceleration, Arias intensity, AI, and cumulative absolute velocity, CAV. The two latter characteristics are defined, e.g., Reiter (1990), as

$$AI = \frac{\pi}{2\,g} \int_0^{t_0} a^2(t)\,\mathrm{d}t\,, \tag{14.6}$$

$$CAV = \int_0^{t_0} |\,a(t)\,|\,\mathrm{d}t\,, \tag{14.7}$$

where t_0 is time when the strong motion ceases and $a(t)$ is the horizontal acceleration (of seismic motion).

Figure 14.12 shows the Arias intensity, peak horizontal acceleration, and cumulative absolute velocity evaluated at the free surface for the two simulated earthquakes.

Summarizing the sequences of snapshots and the three characteristics of the simulated earthquake motions we can conclude that the two earthquakes produce considerably different space-time variations of the surface motion in the Grenoble basin as well as considerably different spatial distributions of the Arias intensity, peak horizontal acceleration, and cumulative absolute velocity. It is very likely that we can take this observation as a strong indication of the very lim-

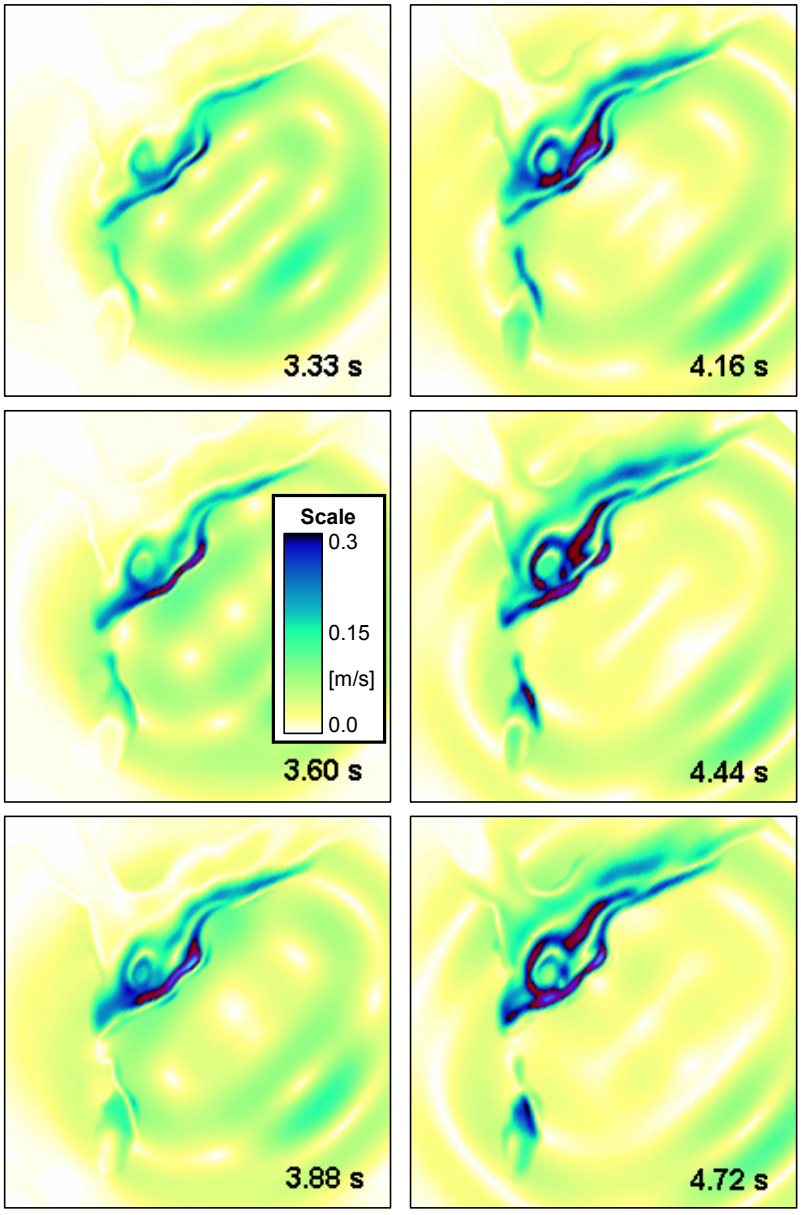

Fig. 14.9. Sequence of the wavefield snapshots for the simulated strike-slip earthquake near the Grenoble basin - the first part. The color scale indicates the absolute value of the horizontal component of the particle velocity at the free surface. For the movie click here.

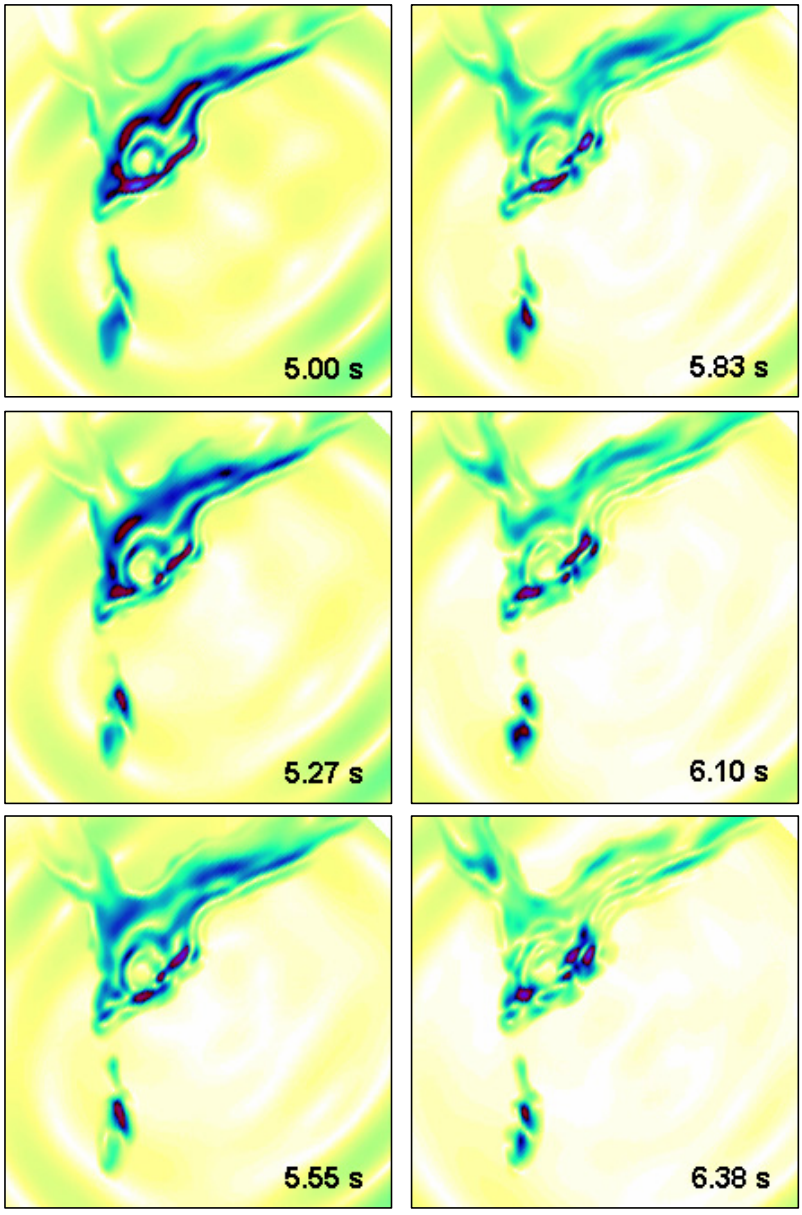

Fig. 14.10. Sequence of the wavefield snapshots for the simulated strike-slip earthquake near the Grenoble basin - the second part. The color scale indicates the absolute value of the horizontal component of the particle velocity at the free surface.

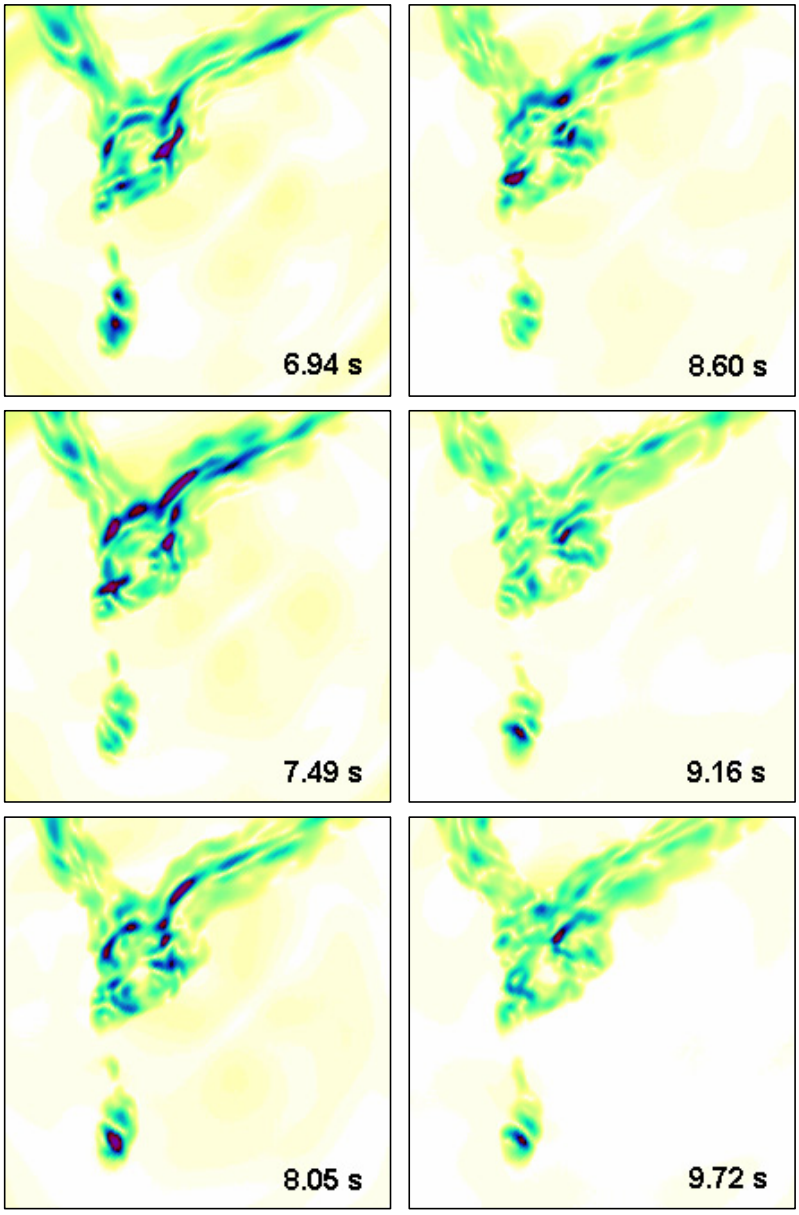

Fig. 14.11. Sequence of the wavefield snapshots for the simulated strike-slip earthquake near the Grenoble basin - the third part. The color scale indicates the absolute value of the horizontal component of the particle velocity at the free surface.

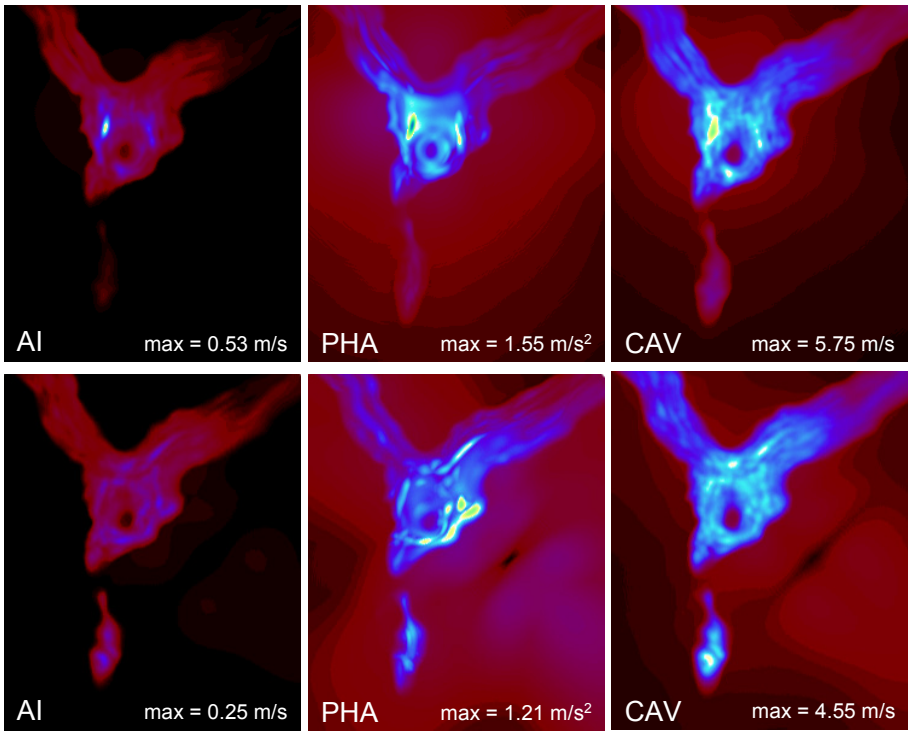

Fig. 14.12. Arias intensity (AI), peak horizontal acceleration (PHA), and cumulative absolute velocity (CAV) for the two simulated earthquakes - top panel for the thrust earthquake, bottom panel for the strike-slip earthquake. The values relate to the free surface.

ited meaning of the estimates of the earthquake motion based on the simulations for the vertical incidence of a plane wave.

We were also interested in comparison of the earthquake motions due to the finite dynamic sources with those due to equivalent point kinematic sources. A point source is defined by its strike, dip, rake, see Fig. 3.3, scalar seismic moment M_0, eq. (3.49), and source-time function $s(t)$, eq. (3.47). Therefore we numerically integrated slip at each time level over the whole ruptured area at that time level. The obtained time function of the slip was then divided by the final size of the ruptured area A, eq. (3.46). This gave the average slip as function of time $\overline{Du}(t)$, eq. (3.46). Its final value defines the final average slip $\overline{Du}$, eq. (3.46). Finally, the source-time function $s(t)$ was then obtained by dividing $\overline{Du}(t)$ by the final average slip $\overline{Du}$. The obtained scalar seismic moment is $M_0 \doteq 8.8$ Nm. The source-time function is shown in Fig. 14.13. Values of strike, dip and rake are 90^o, 0^o and 90^o for the thrust fault, and 45^o, 90^o and 90^o for the strike-slip fault.

In the first comparison of the dynamic and equivalent point sources we considered two hypothetical locations of sources along the Belledonne fault. They are shown in Fig. 14.14 and termed

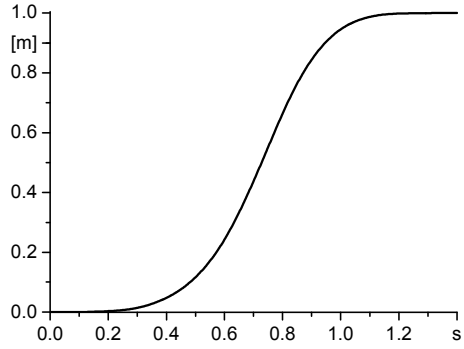

Fig. 14.13. Source-time function of the point source equivalent to the finite dynamic source considered in the simulations.

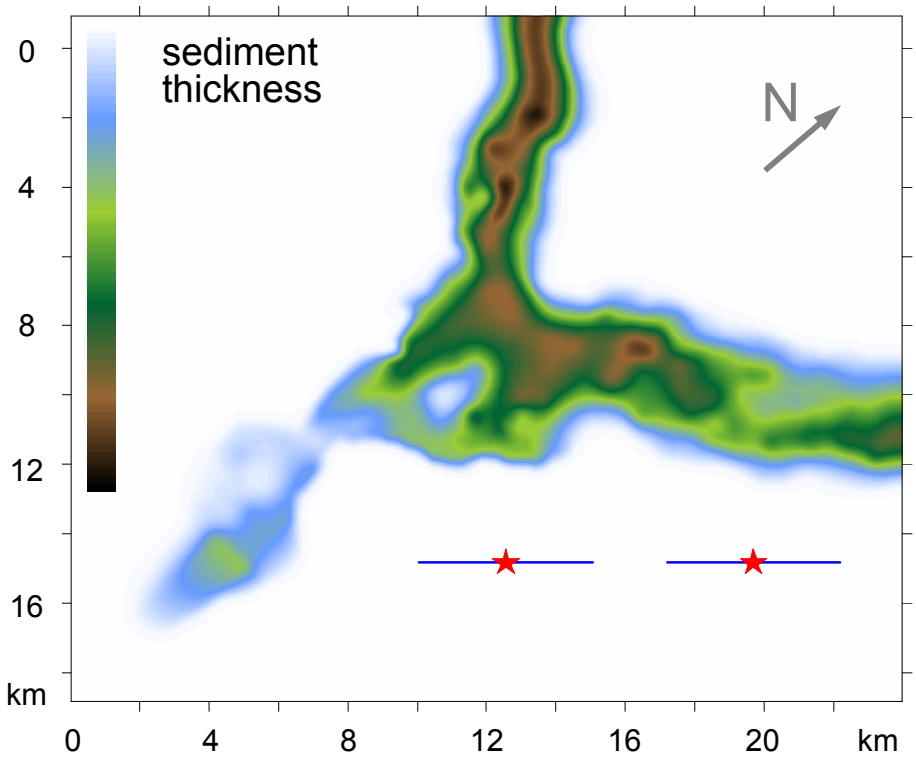

Fig. 14.14. Two locations of the earthquake sources in the Belledonne Massif - 'left' and 'right' The lines indicate dynamic sources on the vertical faults, stars indicate epicenters of the equivalent point sources.

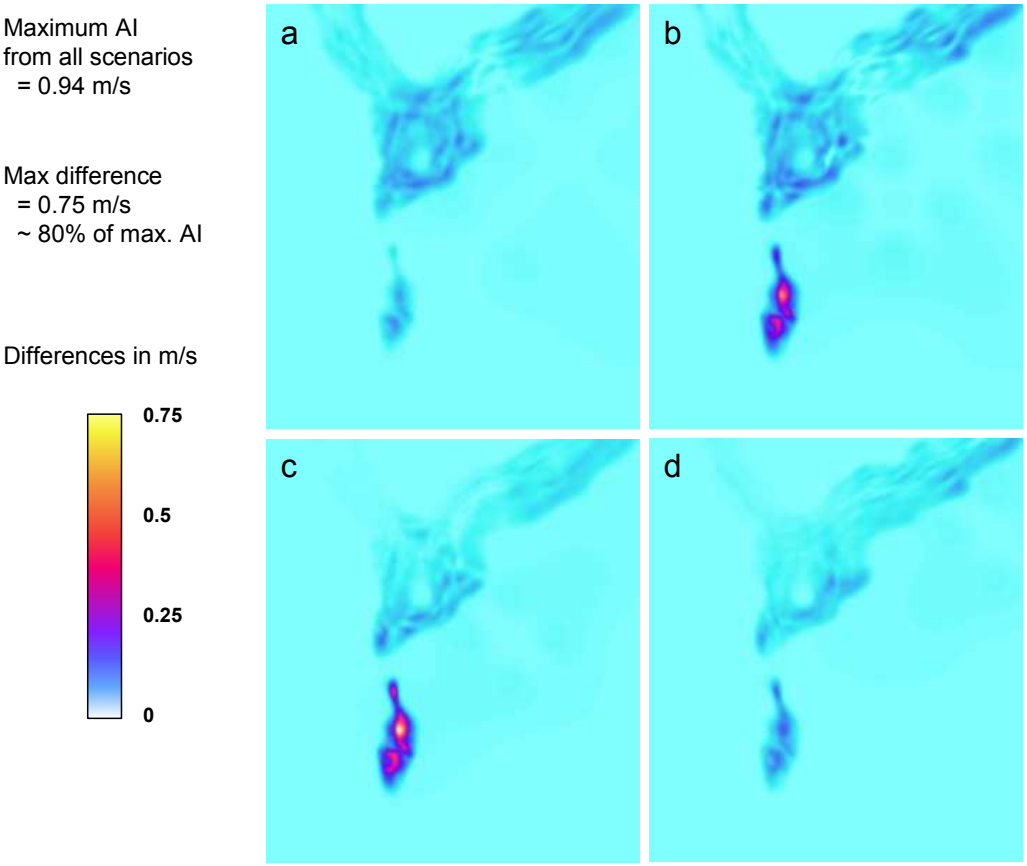

Fig. 14.15. Difference in the Arias intensity a) due to different locations of the dynamic sources, b) due to different locations of the equivalent point sources, c) due to different (dynamic and point) sources at the 'left' location, d) due to different (dynamic and point) sources at the 'right' location.

'left' and 'right' locations. We performed four simulations - for the point source at the 'left' location, dynamic source at the 'left' location, point source at the 'right' location, and dynamic source at the 'right' location. The results are summarized in Figs. 14.15 - 14.17. The figures show differences in the Arias intensity, peak horizontal acceleration, and cumulative absolute velocity due to different locations of the same types of the sources as well as due to different types of the sources at the same locations. The figures indicate that the directivity effect is underestimated when the equivalent point source is used. Apart from the directivity effect, the source location is more important than the type of the source. Note that these conclusions are indicated for relatively small-size earthquakes. We should not a priori assume the latter conclusion for larger events.

In order to compare the earthquake motion due to the hypothetical thrust earthquake beneath

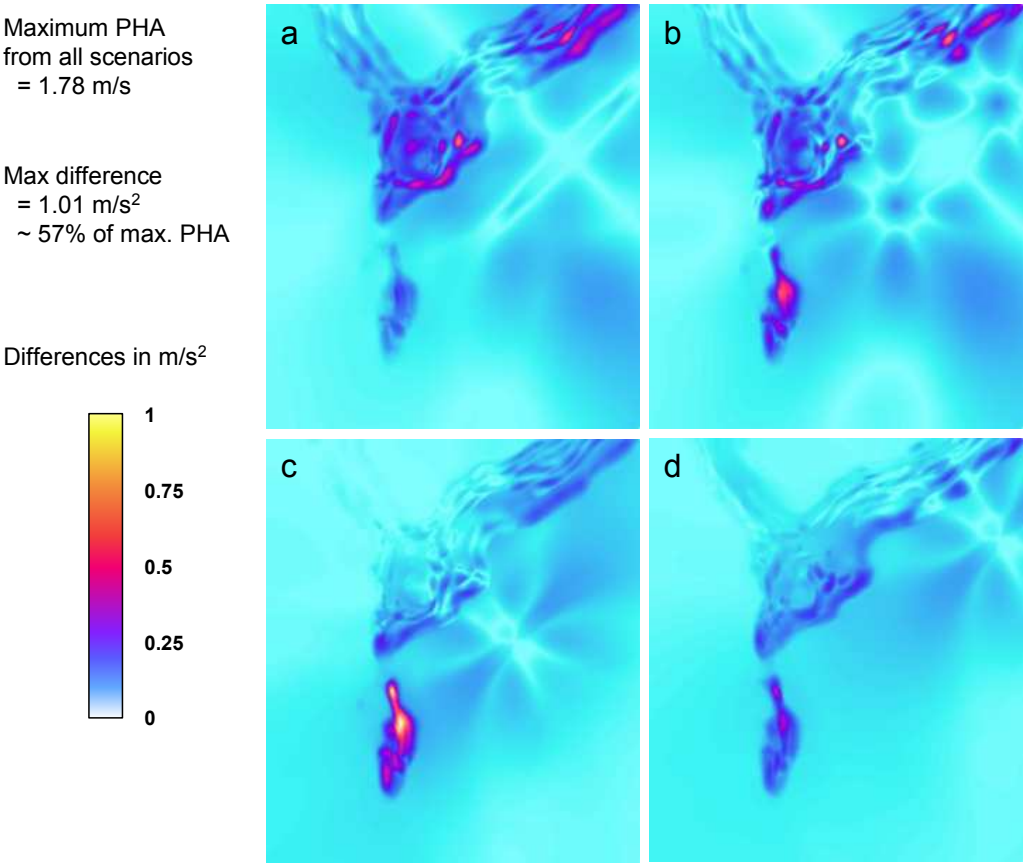

Fig. 14.16. Difference in the peak horizontal acceleration a) due to different locations of the dynamic sources, b) due to different locations of the equivalent point sources, c) due to different (dynamic and point) sources at the 'left' location, d) due to different (dynamic and point) sources at the 'right' location.

Grenoble with motion produced by the equivalent point source located on the horizontal fault, we performed simulation for the latter case. Figure 14.18 shows differences in the Arias intensity, peak horizontal acceleration, and cumulative absolute velocity due to different types of source on the horizontal fault beneath Grenoble. It follows from the figure that maxima of the Arias intensity, peak horizontal acceleration, and cumulative absolute velocity determined from the simulation for the equivalent point source overestimate maxima determined from the dynamic simulation by 20, 20 and 40 %, respectively.

All the comparisons strongly suggest that the dynamically faulting sources, that is, the most realistic sources, should be modeled in the simulations aiming in the earthquake motion predictions.

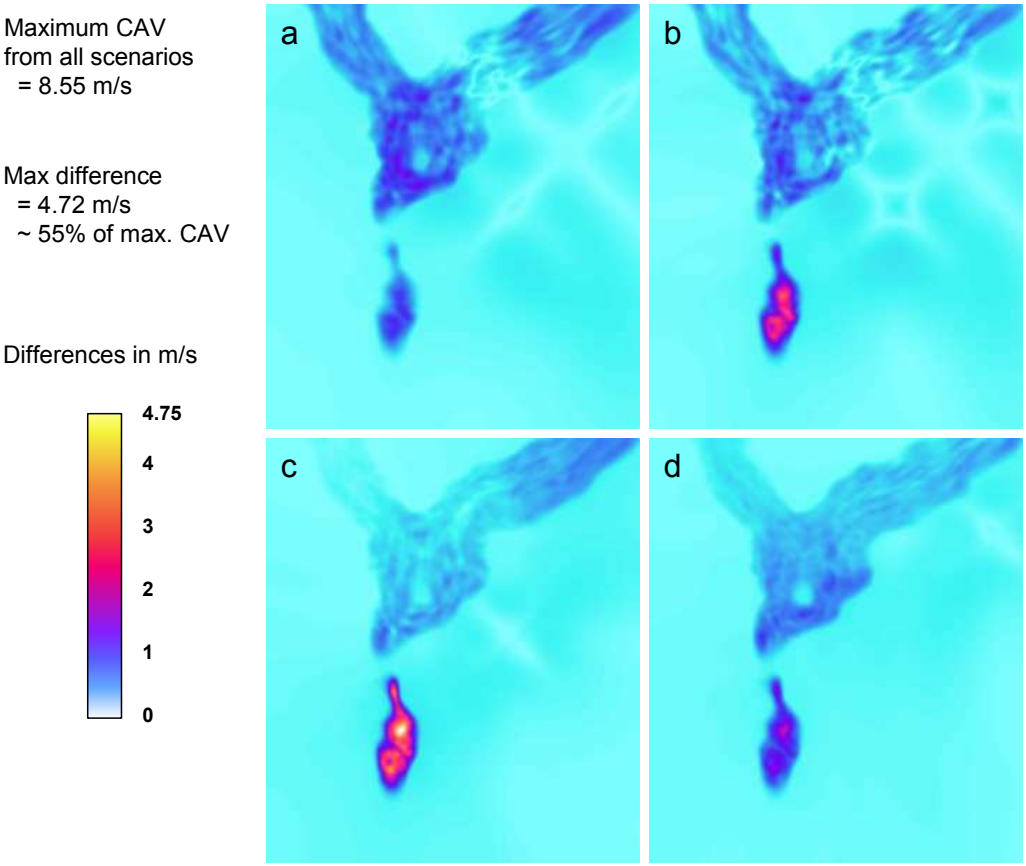

Fig. 14.17. Difference in the cumulative absolute velocity a) due to different locations of the dynamic sources, b) due to different locations of the equivalent point sources, c) due to different (dynamic and point) sources at the 'left' location, d) due to different (dynamic and point) sources at the 'right' location.

15 Concluding Remarks

As we mentioned in the introduction, there are several powerful numerical-modeling methods. It is very likely that none of them is (in its recent elaboration) and can be (in future) better than others in all important aspects and properties. In other words, in our opinion, it is very likely that the finite-difference, finite-element, spectral-element, and arbitrary high-order derivative – discontinuous Galerkin methods will further develop and be widely applied in future. In principle, for solving a problem one should choose the best suited of the available methods - not vice versa. In practice, unfortunately but understandably, one sometime prefers to accommodate (modify) the problem configuration to the particular method developed or in use in the team/lab.

We strongly believe that the best time of the finite-difference method in seismology is in the

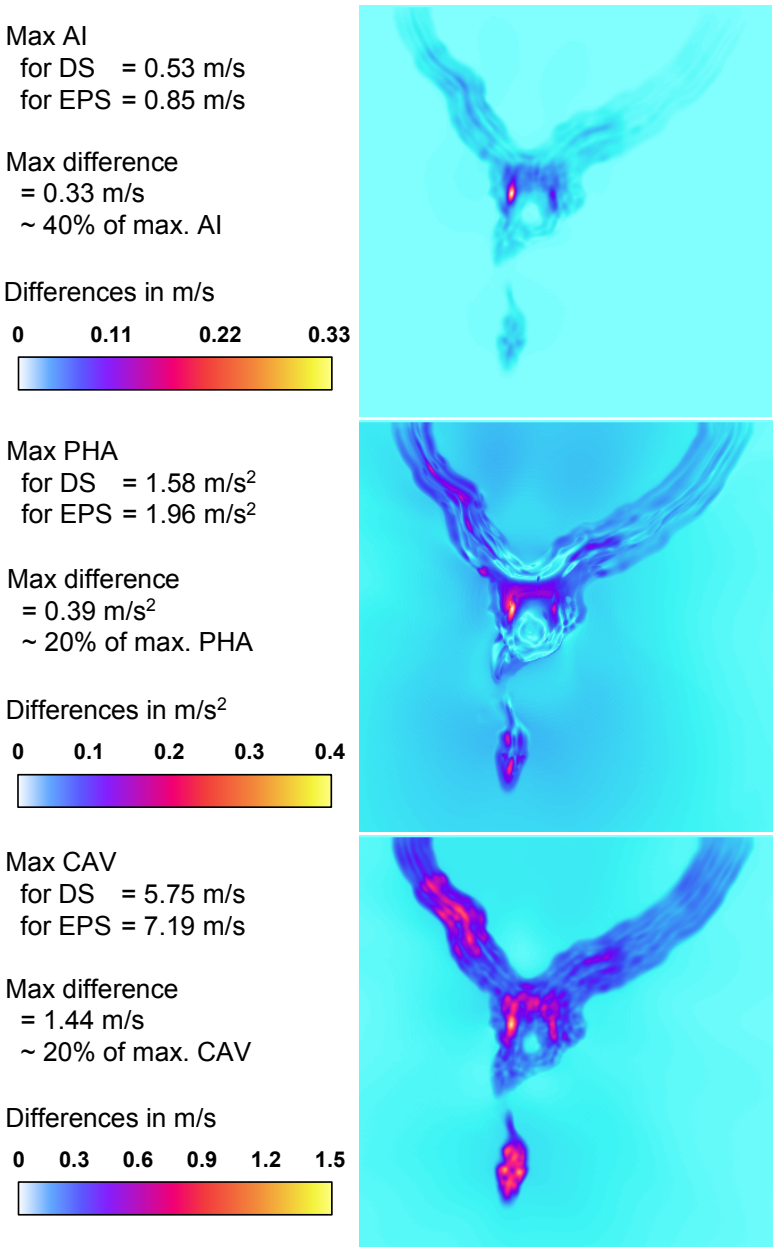

Fig. 14.18. Difference in the Arias intensity, peak horizontal acceleration, and cumulative absolute velocity between the dynamic and equivalent point sources on the thrust fault beneath Grenoble.

future. We hope that our monograph provides a strong indication for this. Better incorporation of the boundary conditions on non-planar surfaces, optimization, and enhancement of the computational efficiency are still ahead of us as well as reasonable hybrid combinations with other numerical methods.

References

Aboudi, J., 1971. The motion excited by an impulsive source in an elastic half-space with a surface obstacle. *Bull. Seism. Soc. Am.* 148, 747-763.

Aki, K. and P. G. Richards, 1980. Quantitative Seismology. Theory and Methods, Vol. I and II. *W. H. Freeman & Co.*, San Francisco.

Aki, K. and P. G. Richards, 2002. Quantitative Seismology. Second Edition. *University Science Books*.

Akin, J. Ed, 1986. Finite Element Analysis for Undergraduates. *Academic Press*.

Alekseev, A. S. and B. G. Mikhailenko, 1980. The solution of dynamic problems of elastic wave propagation in inhomogeneous media by a combination of partial separation of variables and finite-difference methods. *J. Geophys.* 48, 161-172.

Alterman, Z. and F. C. Karal, 1968. Propagation of elastic waves in layered media by finite-difference methods. *Bull. Seism. Soc. Am.* 58, 367-398.

Alford, R. M., K. R. Kelly, and D. M. Boore, 1974. Accuracy of finite difference modeling of the acoustics wave equation. *Geophysics* 39, 834-842.

Alterman, Z. and D. Loewenthal, 1970. Seismic waves in a quarter and three-quarter plane. *Geophys. J. Roy. Astr. Soc.* 20, 101-126.

Alterman, Z. and A. Rotenberg, 1969. Seismic waves in a quarter plane. *Bull. Seism. Soc. Am.* 59, 347-368.

Anderson, D. A., J. C. Tannehill, and R. H. Pletcher, 1984. Computational Fluid Mechanics and Heat Transfer. *Hemisphere Publishing Corporation*.

Andrews, D. J., 1973. A numerical study of tectonic stress release by underground explosions. *Bull. Seism. Soc. Am.* 63, 1375-1391.

Andrews, D. J., 1976a. Rupture propagation with finite stress in antiplane strain. *J. Geophys. Res.* 81, 3575-3582.

Andrews, D. J., 1976b. Rupture velocity of plane strain shear cracks. *J. Geophys. Res.* 81, 5679-5687.

Andrews, D. J., 1999. Test of two methods for faulting in finite-difference calculations. *Bull. Seism. Soc. Am.* 89, 931-937.

Aochi, H. and E. Fukuyama, 2002. Three-dimensional nonplanar simulation of the 1992 Landers earthquake. *J. Geophys. Res.* 107.

Aoi, S. and H. Fujiwara, 1999. 3D finite-difference method using discontinuous grids. *Bull. Seism. Soc. Am.* 89, 918-930.

Archuleta, R. J., 1976. Experimental and numerical three-dimensional simulations of strike-slip earthquakes. PhD. Thesis. *University of California*, San Diego.

Balazovjech, M. and L. Halada, 2006. Effective computation of restoring force vector in FEM. Submitted to *Kybernetika*.

Barenblatt, G. I., 1959. Concerning equilibrium crack forming during brittle fracture. The stability of isolated cracks. Relationship with energetic theories. *Appl. Math. Mech.* 23, 1273-1282.

Beeler, N. M., T. E. Tullis, and J. D. Weeks, 1994. The roles of time and displacement in the evolution effect in rock friction. *Geophys. Res. Lett.* 21, 1987-1990.

Belytschko, T., Liu, W. K., and B. Moran, 2000. Nonlinear Finite Elements for Continua and Structures. *John Wiley & Sons*, New York.

Ben-Menahem, A. and S. J. Singh, 1981. Seismic Waves and Sources. *Springer*.

Bielak, J., K. Loukakis, Y. Hisada, and Ch. Yoshimura, 2003. Domain reduction method for three-dimensional earthquake modeling in localized regions. Part I: Theory. *Bull. Seism. Soc. Am.* 93, 817-824.

Bizzarri, A. and M. Cocco, 2003. Slip-weakening behavior during the propagation of dynamic ruptures obeying to rate- and state-dependent friction laws. *J. Geophys. Res.* 108, 2373.

Bizzarri, A. and M. Cocco, 2005. 3D dynamic simulations of spontaneous rupture propagation governed by different constitutive laws with rake rotation allowed. *Annals of Geophysics* 48, 279-299.

Blanch, J. O., J. O. A. Robertsson, and W. W. Symes, 1995. Modeling of a constant Q: Methodology and algorithm for an efficient and optimally inexpensive viscoelastic technique. *Geophysics* 60, 176-184.

Bohlen, T. and E. H. Saenger, 2006. Accuracy of heterogeneous staggered-grid finite-difference modeling of Rayleigh waves, *Geophysics* 71, T109-T115.

Boore, D. M., 1970. Love waves in nonuniform waveguides: finite difference calculations. *J. Geophys. Res.* 75, 1512-1527.

Boore, D., 1972. Finite-difference methods for seismic wave propagation in heterogeneous materials. In *Methods in Computational Physics*, Vol. 11, B. A. Bolt, ed., *Academic Press*, New York.

Bouchon, M., 1981. A simple method to calculate Green's functions for elastic layered media. *Bull. Seism. Soc. Am.* 71, 959-971.

Bouchon, M. and O. Coutant, 1994. Calculation of synthetic seismograms in a laterally-varying medium by the boundary element - discrete wavenumber method. *Bull. Seism. Soc. Am.* 84, 1869-1881.

Bouchon, M. and F. J. Sánchez-Sesma, 2007. Boundary integral equations and boundary elements methods in elastodynamics. In *Advances in Wave Propagation in Heterogeneous Earth*, 157-189, R.-S. Wu and V. Maupin, eds., in the series *Advances in Geophysics*, Vol. 48, R. Dmowska, ed. *Elsevier - Academic Press*.

Carcione, J. M., 2001. Wave Fields in Real Media: Wave Propagation in Anisotropic, Anelastic and Porous Media. *Pergamon*.

Carcione, J. M. and F. Cavallini, 1994. A rheological model for anelastic anisotropic media with applications to seismic wave propagation. *Geophys. J. Int.* 119, 338-348.

Carcione, J. M., G. C. Herman, and A. P. E. ten Kroode, 2002. Seismic modeling. *Geophysics* 67, 1304-1325.

Carcione, J. M., D. Kosloff, and R. Kosloff, 1988a. Wave propagation simulation in a linear viscoacoustic medium. *Geophys. J.* 93, 393-407.

Carcione, J. M., D. Kosloff, and R. Kosloff, 1988b. Wave propagation simulation in a linear viscoelastic medium. *Geophys. J.* 95, 597-611.

Chaljub, E., Komatitsch, D., Vilotte, J. P., Capdeville, Y., and Festa, G., 2007. Spectral Element Analysis in Seismology. In *Advances in Wave Propagation in Heterogeneous Earth*, 365-420, R.-S. Wu and V. Maupin, eds., in the series *Advances in Geophysics*, Vol. 48, R. Dmowska, ed. *Elsevier - Academic Press*.

Christensen, R. M., 1971. Theory of Viscoelasticity. An Introduction. *Academic Press*.

Cocco, M. and A. Bizzarri, 2002. On the slip-weakening behavior of rate- and state-dependent constitutive laws. *Geophys. Res. Lett.* 29, 10.1029/2001GL013999, 11,1-11,4.

Cohen, G. C., 2002. Higher-order Numerical Methods for Transient Wave Equations. *Springer*.

Cotton, F., C. Berge, F. Lemeille, A. Pitarka, B. Lebrun, and M. Vallon, 1998. Three-dimensional simulation of earthquakes in the Grenoble's basin. In *The Effects of Surface Geology on Seismic Motion*, Vol. 2, 873-878, K. Irikura, K. Kudo, H. Okada, and T. Sasatani, eds., *Balkema*, Rotterdam.

Coutant, O., 1989. Program of numerical simulation AXITRA. Res. Rep. LGIT (in French), *Université Joseph Fourier*, Grenoble.

Coutant, O., J. Virieux, and A. Zollo, 1995. Numerical source implementation in a 2D finite difference scheme for wave propagation. *Bull. Seism. Soc. Am.* 85, 1507-1512.

Crase, E., 1990. High-order (space and time) finite-difference modeling of the elastic wave equation. *60th Ann. Intl. Meeting, Soc. Expl. Geophys., Expanded Abstracts*, 987-991.

Crase, E., Ch. Wideman, M. Noble, and A. Tarantola, 1992. Nonlinear elastic waveform inversion of land seismic reflection data. *J. Geophys. Res.* 97, 4685-4703.

Červený, V., 2001. Seismic Ray Theory. *Cambridge University Press*.

Dablain, M. A., 1986. The application of high-order differencing to the scalar wave equation. *Geophysics* 51, 54-66.

Dahlen, F. A. and J. Tromp, 1998. Theoretical Global Seismology. *Princeton University Press*.

Dalguer, L. A. and S. M. Day, 2006. Comparison of fault representation methods in finite difference simulations of dynamic rupture. *Bull. Seism. Soc. Am.* 96, 1764-1778.

Dalguer, L. A. and S. M. Day, 2007. Staggered-grid split-node method for spontaneous rupture simulation. *J. Geophys. Res.*, in press.

Day, S. M., 1977. Finite element analysis of seismic scattering problems. PhD. Dissertation, *University of California*, San Diego.

Day, S. M., 1982. Three-dimensional simulation of spontaneous rupture: the effect of nonuniform prestress. *Bull. Seism. Soc. Am.* 72, 1881-1902.

Day, S. M., 1998. Efficient simulation of constant Q using coarse-grained memory variables. *Bull. Seism. Soc. Am.* 88, 1051-1062.

Day, S. M., 2005. Personal communication.

Day, S. M. and C. R. Bradley, 2001. Memory-efficient simulation of anelastic wave propagation. *Bull. Seism. Soc. Am.* 91, 520-531.

Day, S. M., L. A. Dalguer, N. Lapusta, and Y. Liu, 2005. Comparison of finite difference and boundary integral solutions to three-dimensional spontaneous rupture. *J. Geophys. Res.* 110, B12307.

Day, S. M. and J. B. Minster, 1984. Numerical simulation of wavefields using a Padé approximant method. *Geophys. J. Roy. astr. Soc.* 78, 105-118.

Dieterich, J. H., 1979. Modeling of rock friction – 1. Experimental results and constitutive equations. *J. Geophys. Res.* 84, 2161-2168.

Dieterich, J. H., 1986. A model for the nucleation of earthquake slip. In *Earthquake Source Mechanics*, 37-47, *Geophysical Monograph* 37, *Maurice Ewing Series* 6, S. Das, J. Boatwright and C. H. Scholz, eds., *Am. Geophys. Union*, Washington D. C.

Durran, D. R., 1999. Numerical Methods for Wave Equations in Geophysical Fluid Dynamics. *Springer*.

Emerman, S. H., W. Schmidt, and R. A. Stephen, 1982. An implicit finite-difference formulation of the elastic wave equation. *Geophysics* 47, 1521-1526.

Emmerich, H., 1989. 2-D wave propagation by a hybrid method. *Geophys. J. Int.* 99, 307-319.

Emmerich, H., 1992. PSV-wave propagation in a medium with local heterogeneities: a hybrid formulation and its application. *Geophys. J. Int.* 109, 54-64.

Emmerich, H. and M. Korn, 1987. Incorporation of attenuation into time-domain computations of seismic wave fields. *Geophysics* 52, 1252-1264.

Falk, J., E. Tessmer, and D. Gajewski, 1996. Tube wave modelling by the finite-differences method with varying grid spacing. *PAGEOPH* 148, 77-93.

Fäh, D., 1992. A hybrid technique for the estimation of strong ground motion in sedimentary basins. Diss. ETH Nr. 9767, *Swiss Federal Institute of Technology*, Zürich.

Fäh, D., P. Suhadolc, and G. F. Panza, 1993. Variability of seismic ground motion in complex media: the case of a sedimentary basin in the Friuli (Italy) area. *J. Applied Geophysics* 30, 131-148.

Felippa, C. A., 2005. Introduction to Finite Element Methods (ASEN 5007). Lecture notes. *University of Colorado*, Boulder.

Fornberg, B., 1988. Generation of finite difference formulas on arbitrary spaced grids. *Math. Computation* 51, 699-706.

Forsythe, G. E. and W. R. Wasow, 1960. Finite Difference Methods for Partial Differential Equations. *J. Wiley & Sons*, New York.

Frankel, A., 1993. Three-dimensional simulations of ground motions in the San Bernardino Valley, California, for hypothetical earthquakes on the San Andreas fault. *Bull. Seism. Soc. Am.* 83, 1020-1041.

Frankel, A. and W. Leith, 1992. Evaluation of topographic effects on P- and S-waves of explosions at the Northern Novaya Zemlya test site using 3-D numerical simulations. *Geophys. Res. Lett.* 19, 1887-1890.

Frazier, G. A. and C. M. Petersen, 1974. 3-D stress wave code for the Illiac IV. *Systems, Science and Software Report SSS-R-74-2103*.

Gaffet, S. and M. Bouchon, 1989. Effects of two-dimensional topographies using the discrete wavenumber-boundary integral equation method in P-SV cases. *J. Acoust. Soc. Am.* 85, 2277-2283.

Gamond, J. F., 1994. Normal faulting and tectonic inversion driven by gravity in a thrusting regime. *J. Struct. Geol.* 16, 1-9.

Geller, R. J. and T. Ohminato, 1994. Computation of synthetic seismograms and their partial derivatives for heterogeneous media with arbitrary natural boundary conditions using the Direct Solution Method. *Geophys. J. Int.* 116, 421-446.

Geller, R. J. and N. Takeuchi, 1995. A new method for computing highly accurate DSM synthetic seismograms. *Geophys. J. Int.* 123, 449-470.

Geller, R. J. and N. Takeuchi, 1998. Optimally accurate second-order time-domain finite difference scheme for the elastic equation of motion: one-dimensional case. *Geophys. J. Int.* 135, 48-62.

Graves, R. W., 1996. Simulating seismic wave propagation in 3D elastic media using staggered-grid finite differences. *Bull. Seism. Soc. Am.* 86, 1091-1106.

Graves, R. W. and S. M. Day, 2003. Stability and accuracy analysis of coarse-grain viscoelastic simulations. *Bull. Seism. Soc. Am.* 93, 283-300.

Gubbins, D., 1990. Seismology and Plate Tectonics. *Cambridge University Press*.

Harris, R.A., R. Archuleta, B. Aagaard, J. P. Ampuero, D.J. Andrews, L. Dalguer, S. Day, E. Dunham, G. Ely, Y. Kase, N. Lapusta, Y. Liu, S. Ma, D. Oglesby, K. Olsen and A. Pitarka, 2004. The Source Physics of Large Earthquakes – Validating Spontaneous Rupture Methods. *Eos Trans. AGU*, 85(47), Fall Meet. Suppl., Abstract S12A-05.

Hayashi, K., D. R. Burns, and M. N. Toksöz, 2001. Discontinuous-grid finite-difference seismic modeling including surface topography. *Bull. Seism. Soc. Am.* 91, 1750-1764.

Hughes, T. J. R., 2000. The Finite Element Method Linear Static and Dynamic Finite Element Method Analysis. *Prentice Hall*.

Ida, Y., 1972. Cohesive force across the tip of a longitudinal-shear crack and Griffith's specific surface energy. *J. Geophys. Res.* 77, 3796-3805.

Igel, H., P. Mora, and B. Riollet, 1995. Anisotropic wave propagation through finite-difference grids. *Geophysics* 60, 1203-1216.

Ilan, A., A. Ungar, and Z. S. Alterman, 1975. An improved representation of boundary conditions in finite difference schemes for seismological problems. *Geophys. J. R. Astr. Soc.* 43, 727-745.

Isaacson, E. and H. B. Keller, 1966. Analysis of Numerical Methods. *J. Wiley & Sons*, New York.

Jastram, C. and A. Behle, 1992. Acoustic modeling on a grid of vertically varying spacing. *Geophys. Prosp.* 40, 157-169.

Jastram, C. and E. Tessmer, 1994. Elastic modelling on a grid with vertically varying spacing. *Geophys. Prosp.* 42, 357-370.

Kawase, H., 1988. Time-domain response of a semi-circular canyon for incident SV, P, and Rayleigh waves calculated by the discrete wavenumber boundary element method. *Bull. Seism. Soc. Am.* 78, 1415-1437.

Käser, M. and M. Dumbser, M., 2006. An arbitrary high-order discontinuous Galerkin method for elastic waves on unstructured meshes - I. The two-dimensional isotropic case with external source terms. *Geophys. J. Int.* 166, 855-877.

Kelly, K. R., R. W. Ward, S. Treitel, and R. M. Alford, 1976. Synthetic seismograms: a finite-difference approach. *Geophysics* 41, 2-27.

Kennett, B. L. N., 2001. The Seismic Wavefield. Vol. I: Introduction and Theoretical Development. *Cambridge University Press*.

Kennett, B. L. N., 2002. The seismic wavefield. Vol. II: Interpretation of Seismograms on Regional and Global Scales. *Cambridge University Press*.

Klimeš, L., 1996. Accuracy of elastic finite differences in smooth media. *PAGEOPH* 148, 39-76.

Komatitsch, D., Q. Liu, J. Tromp, P. Suss, C. Stidham, and J. H. Shaw, 2004. Simulations of ground motion in the Los Angeles basin based upon the spectral element method. *Bull. Seism. Soc. Am.* 94, 187-206

Kostrov, B. V. and S. Das, 1988. Principles of Earthquake Source Mechanics. *Cambridge University Press*.

Kristek, J. and P. Moczo, 2003. Seismic wave propagation in viscoelastic media with material discontinuities – a 3D 4th-order staggered-grid finite-difference modeling. *Bull. Seism. Soc. Am.* 93, 2273-2280.

Kristek, J. and P. Moczo, 2006. On the accuracy of the finite-difference schemes: the 1D elastic problem. *Bull. Seism. Soc. Am.* 96, 2398–2414.

Kristek, J., P. Moczo, and R. J. Archuleta, 2002. Efficient methods to simulate planar free surface in the 3D 4th-order staggered-grid finite-difference schemes. *Studia Geophys. Geod.* 46, 355-381.

Kristek, J., P. Moczo, and M. Galis, 2006. Comparison of the 2nd-order and 4th-order Staggered-Grid Finite-Difference Implementations of the TSN Method for Rupture Propagation. *EoS Trans. AGU*, 87(52), Fall Meet. Suppl., Abstract S41C-1341.

Kristek, J., P. Moczo, I. Irikura, T. Iwata, and H. Sekiguchi, 1999. The 1995 Kobe mainshock simulated by the 3D finite differences. In *The Effects of Surface Geology on Seismic Motion* Vol. 3, 1361-1368, K. Irikura, K. Kudo, H. Okada, and T. Sasatani, eds., *Balkema*, Rotterdam.

Kristekova, M., J. Kristek, P. Moczo, and S. M. Day, 2006. Misfit criteria for quantitative comparison of seismograms. *Bull. Seism. Soc. Am.* 96, 1836-1850.

Kruger, O. S., E. H. Saenger, and S. A. Shapiro, 2005. Scattering and diffraction by a single crack: an accuracy analysis of the rotated staggered grid. *Geophys. J. Int*. 162, 25-31.

Kummer, B. and A. Behle, 1982. Second-order finite-difference modeling of SH-wave propagation in laterally inhomogeneous media. *Bull. Seism. Soc. Am.* 72, 793-808.

Kummer, B., A. Behle, and F. Dorau, 1987. Hybrid modelling of elastic-wave propagation in two-dimensional laterally inhomogeneous media. *Geophysics* 52, 765-771.

Lecomte, I., H. Gjøystdal, F. Maaø, R. Bakke, Å. Drottning, and T.-A. Johansen, 2004. Efficient and flexible seismic modelling of reservoirs: the HybriSeis concept. *The Leading Edge* 23, 432-437.

Levander, A. R., 1988. Fourth-order finite-difference P-SV seismograms. *Geophysics* 53, 1425-1436.

Levander, A. R., 1989. Finite-difference forward modeling in seismology, In *The Encyclopedia of Solid Earth Geophysics*, 410-431, James, D. E., ed., *Van Nostrand Reinhold*.

Liu, H.-P., D. L. Anderson, and H. Kanamori, 1976. Velocity dispersion due to anelasticity; implications for seismology and mantle composition. *Geophys. J. R. Astr. Soc.* 47, 41-58.

Luo, Y. and G. Schuster, 1990. Parsimonious staggered grid finite-differencing of the wave equation. *Geophys. Res. Let*. 17, 155-158.

Ma, S., R. J. Archuleta, and P. Liu, 2004. Hybrid Modeling of Elastic P-SV Wave Motion: A Combined Finite-Element and Staggered-Grid Finite-Difference Approach. *Bull. Seism. Soc. Am.* 94, 1557-1563.

Madariaga, R., 1976. Dynamics of an expanding circular fault. *Bull. Seism. Soc. Am.* 67, 163-182.

Madariaga, R., K. Olsen, and R. J. Archuleta, 1998. Modeling dynamics rupture in a 3D earthquake fault model. *Bull. Seism. Soc. Am.* 88, 1182-1197.

Magnier, S.-A., P. Mora, and A. Tarantola, 1994. Finite differences on minimal grids. *Geophysics* 59, 1435-1443.

Marchuk, G. I., 1982. Methods of Numerical Mathematics. *Springer*.

Marfurt, K. J., 1984. Accuracy of finite-difference and finite-element modeling of the scalar and elastic wave equations. *Geophysics* 49, 533-549.

McDonal, F. J., F. A. Angona, L. R. Mills, R. L. Sengbush, R. G. van Nostrand, and J. E. White, 1958. Attenuation of shear and compressional waves in Pierre shale. *Geophysics* 23, 421-439.

Michlin, S. G., 1970. Variacionnyje metody v matematicceskoj fizike. *Nauka*, Moskva.

Mikumo, T. and T. Miyatake, 1987. Numerical modeling of realistic fault rupture processes. In *Seismic Strong Motion Synthetics*, 91-151, B. A. Bolt, ed., *Academic Press*.

Mitchell, A. R., 1969. Computational Methods in Partial Differential Equations. *J. Wiley & Sons*, London.

Mitchell, A. R. and D. F. Griffiths, 1994. The Finite Difference Method in Partial Differential Equations. *J. Wiley & Sons*, New York.

Mizutani, H., 2002. Accurate and efficient methods for calculating synthetic seismograms when elastic discontinuities do not coincide with the numerical grid. PhD. Thesis. *The University of Tokyo*.

Mizutani, H., R. J. Geller, and N. Takeuchi, 2000. Comparison of accuracy and efficiency of time-domain schemes for calculating synthetic seismograms. *Phys. Earth Planet. Int.* 119, 75-97.

Moczo, P., 1989. Finite-difference technique for SH-waves in 2-D media using irregular grids - application to the seismic response problem. *Geophys. J. Int.* 99, 321-329.

Moczo, P., 1998. Introduction to Modeling Seismic Wave Propagation by the Finite-Difference Method. Lecture Notes. *Kyoto University*. Available in pdf format at ftp://ftp.nuquake.eu/pub/Papers

Moczo, P. and P.-Y. Bard, 1993. Wave diffraction, amplification and differential motion near strong lateral discontinuities. *Bull. Seism. Soc. Am.* 83, 85-106.

Moczo, P., E. Bystrický, J. Kristek, J. M. Carcione, and M. Bouchon, 1997. Hybrid modeling of P-SV seismic motion at inhomogeneous viscoelastic topographic structures. *Bull. Seism. Soc. Am.* 87, 1305-1323.

Moczo, P. and J. Kristek, 2005. On the rheological models used for time-domain methods of seismic wave propagation. *Geophys. Res. Lett.* 32, L01306.

Moczo, P., J. Kristek, and E. Bystrický, 2000b. Stability and grid dispersion of the P-SV 4th-order staggered-grid finite-difference schemes. *Studia Geophys. Geod*. 44, 381-402.

Moczo, P., J. Kristek, and E. Bystrický, 2001. Efficiency and optimization of the 3D finite-difference modeling of seismic ground motion. *J. Comp. Acoustics* 9, 593-609.

Moczo, P., J. Kristek, and M. Gális, M., 2004a. Simulation of planar free surface with near-surface lateral discontinuities in the finite-difference modeling of seismic motion. *Bull. Seism. Soc. Am.* 94, 760-768.

Moczo, P., J. Kristek, and L. Halada, 2000a. 3D 4th-order staggered-grid finite-difference schemes: stability and grid dispersion. *Bull. Seism. Soc. Am.* 90, 587-603.

Moczo, P., J. Kristek, and L. Halada, 2004b. The Finite-Difference Method for Seismologists. An Introduction. *Comenius University*, Bratislava. Available in pdf format at ftp://ftp.nuquake.eu/pub/Papers

Moczo, P., J. Kristek, V. Vavryčuk, R. J. Archuleta, and L. Halada, 2002. 3D heterogeneous staggered-grid finite-difference modeling of seismic motion with volume harmonic and arithmetic averaging of elastic moduli and densities. *Bull. Seism. Soc. Am.* 92, 3042-3066.

Moczo, P., P. Labák, J. Kristek, and F. Hron, 1996. Amplification and differential motion due to an antiplane 2D resonance in the sediment valleys embedded in a layer over the halfspace. *Bull. Seism. Soc. Am.* 86, 1434-1446.

Moczo, P., M. Lucká, J. Kristek, and M. Kristeková, 1999. 3D displacement finite differences and a combined memory optimization. *Bull. Seism. Soc. Am.* 89, 69-79.

Moczo, P., J. O. A. Robertsson, and L. Eisner, 2007. The finite-difference time-domain method for modeling of seismic wave propagation. In *Advances in Wave Propagation in Heterogeneous Earth*, 421-516, R.-S. Wu and V. Maupin, eds., *Advances in Geophysics* Vol. 48, R. Dmowska, ed. *Elsevier - Academic Press*.

Morton, K. W. and D. F. Mayers, 1994. Numerical Solution of Partial Differential Equations. *Cambridge University Press*.

Mufti, I. R., 1985. Seismic modeling in the implicit mode. *Geophys. Prosp.* 33, 619-656.

Muir, F., J. Dellinger, J. Etgen, and D. Nichols, 1992. Modeling elastic fields across irregular boundaries. *Geophysics* 57, 1189-1193.

Murphy, W. F. III, 1982. Effects of partial saturation on attenuation in Massilon sandstone and Vycor porous glass. *J. Acoust. Soc. Am.* 71, 1458-1468.

Okubo, P. G., 1989. Dynamic rupture modeling with laboratory-derived constitutive relations. *J. Geophys. Res.* 94, 12321-12335.

Okubo, P. G. and J. H. Dieterich, 1984. Effects of physical fault properties on frictional instabilities produced on simulated faults. *J. Geophys. Res.* 89, 5817-5827.

Ohminato, T. and B. A. Chouet, 1997. A free-surface boundary condition for including 3D topography in the finite-difference method. *Bull. Seism. Soc. Am*. 87, 494-515.

Ohnaka, M. and T. Yamashita, 1989. A cohesive zone model for dynamic shear faulting based on experimentally inferred constitutive relation and strong motion source parameters. *J. Geophys. Res.* 94, 4089-4104.

Ohtsuki, A. and K. Harumi, 1983. Effects of topography and subsurface inhomogeneities on seismic SV waves. *Earthquake Eng. Struct. Dyn.*, 11, 441-462.

Olsen, K.B., R.J. Archuleta, and J.R. Matarese, 1995. Magnitude 7.75 earthquake on the San Andreas fault: three-dimensional ground motion in Los Angeles. *Science* 270, 1628-1632.

Ottosen, N. S. and H. Petersson, 1992. Introduction to the Finite Element Method. *Prentice Hall*.

Palmer, A. C. and J. R. Rice, 1973. The growth of slip surfaces in the progressive failure of overconsolidated clay. *Proc. Royal Soc. London* A332, 527-548.

Pitarka, A., 1999. 3D elastic finite-difference modeling of seismic motion using staggered grids with nonuniform spacing. *Bull. Seism. Soc. Am.* 89, 54-68.

Pujol, J., 2003. Elastic Wave Propagation and Generation in Seismology. *Cambridge University Press*.

Ranalli, G., 1995. Rheology of the Earth. *Chapman & Hall*.

Reddy, J. N., 2006. An Introduction to the Finite Element Method, *McGraw-Hill*, New York.

Reiter, L., 1990. Earthquake Hazard Analysis. Issues and Insights. *Columbia University Press*, New York.

Richtmyer, R. D. and K. W. Morton, 1967. Difference Methods for Initial Value Problems. *J. Wiley & Sons*, New York; (reprinted by *Kreiger*, New York, 1994).

Robertsson, J. O. A., 1996. A numerical free-surface condition for elastic/viscoelastic finite-difference modeling in the presence of topography. *Geophysics* 61, 1921-1934.

Robertsson, J. O. A., J. O. Blanch, and W. W. Symes, 1994. Viscoelastic finite-difference modeling. *Geophysics* 59, 1444-1456.

Robertsson, J. O. A. and C. H. Chapman, 2000. An efficient method for calculating finite-difference seismograms after model alterations. *Geophysics* 65, 907-918.

Robertsson, J. O. A., A. Levander, and K. Holliger, 1996. A hybrid wave propagation simulation technique or ocean acoustic problems. *J. Geophys. Res.* 101, 11225-11241.

Rodrigues, D., 1993. Large scale modelling of seismic wave propagation. PhD. Thesis, *École Centrale*, Paris.

Rodrigues, D. and P. Mora, 1993. An efficient implementation of the free-surface boundary condition in 2-D and 3-D elastic cases. *63th Ann. Intl. Meeting, Soc. Expl. Geophys., Expanded Abstracts*, 215-217.

Rovelli, A., A. Caserta, L. Malagnini, and F. Marra, 1994. Assessment of potential strong ground motions in the city of Rome. *Annali di Geofisica* 37, 1745-1769.

Ruina, A. L., 1980. Friction laws and instabilities: a quasistatic analysis of some dry frictional behavior. Ph.D. Thesis. *Brown University*, Providence.

Ruina, A. L., 1983. Slip instability and state variable friction laws. *J. Geophys. Res.* 88, 10359-10370.

Saenger, E. H., N. Gold, and S. A. Shapiro, 2000. Modeling the propagation of elastic waves using a modified finite-difference grid. *Wave Motion* 31, 77-92.

Saenger, E. H. and T. Bohlen, 2004. Finite-difference modeling of viscoelastic and anisotropic wave propagation using the rotated staggered grid. *Geophysics* 69, 583-591.

Saenger, E. H., S. A. Shapiro, and Y. Keehm, 2005. Seismic effects of viscous Biot-coupling: Finite difference simulations on micro-scale. *Geophys. Res. Lett.* 32 (14), L14310.

Schoenberg, M. and F. Muir, 1989. A calculus for finely layered anisotropic media. *Geophysics* 54, 581-589.

Shearer, P. M., 1999. Introduction to Seismology. *Cambridge University Press*.

Shtivelman, V., 1984. A hybrid method for wave field computation. *Geophys. Prospect.* 32, 236-257.

Shtivelman, V., 1985. Two-dimensional acoustic modelling by a hybrid method. *Geophysics* 50, 1273-1284.

Slawinski, R. A. and E. S. Krebes, 2002. The homogeneous finite-difference formulation of the P-SV-wave equation of motion. *Studia Geoph. Geod.* 46, 731-751.

Strang, G. and G. J. Fix, 1973. An Analysis of the Finite Element Method. *Prentice-Hall*.

Strang, G. and G. J. Fix, 1988. An Analysis of the Finite Element Method. *Wellesley Cambridge Press*.

Spencer, J. W. Jr., 1981. Stress relaxation at low frequencies in fluid-saturated rocks. *J. Geophys. Res.* 86, 1803-1812.

Stead, R.J. and D. V. Helmberger, 1988. Numerical-analytical interfacing in two dimensions with applications to modeling NTS seismograms. In *Scattering and Attenuation of Seismic Waves*, 157-193, A. Aki and R.-S. Wu, eds. *Birkhauser*, Basel.

Taflove, A. and S. C. Hagness, 2005. Computational Electrodynamics: The Finite-difference Time-domain Method. *Artech House*.

Takenaka, H., T. Furumura, and H. Fujiwara, 1998. Recent developments in numerical methods for ground motion simulation. In *The Effects of Surface Geology on Seismic Motion*, Vol. 2, 91-101, K. Irikura, K. Kudo, H. Okada, and T. Sasatani, eds. *Balkema*, Rotterdam.

Takeuchi, N. and R. J. Geller, 2000. Optimally accurate second order time-domain finite difference scheme for computing synthetic seismograms in 2-D and 3-D media. *Phys. Earth Planet. Int.* 119, 99-131.

Takeuchi, N. and R. J. Geller, 2003. Accurate numerical methods for solving the elastic equation of motion for arbitrary source locations. *Geophys. J. Int.* 154, 852-866.

Thouvenout, F., 1996. Aspects géophysiques et structuraux des Alpes occidentales et de trois autres orogenes (Atlas, Pyrénées, Oural). *Université Joseph Fourier*, Grenoble, pp. 378.

Udías, A., 1999. Principles of Seismology. *Cambridge University Press*.

Vallon, M., 1999. Estimation de l'epaisseur d'alluvions et sediments quaternaires dans la region grenobloise par inversion des anomalies gravimetriques. LGGE, *Université Joseph Fourier*, Grenoble, pp. 33.

Van den Berg, A., 1984. A hybrid solution for wave propagation problems in regular media with bounded irregular inclusions. *Geophys. J. R. Astr. Soc.*, 79, 3-10.

Vidale, J. E. and D.V. Helmberger, 1987. Path effects in strong motion seismology. In *Seismic Strong Motion Synthetics*, 267-319, B. A. Bolt, ed. *Academic Press*.

Virieux, J., 1984. SH-wave propagation in heterogeneous media: velocity-stress finite-difference method. *Geophysics* 49, 1933-1957.

Virieux, J., 1986. P-SV wave propagation in heterogeneous media: velocity-stress finite-difference method. *Geophysics* 51, 889-901.

Wang, Y., J. Xu, and G. T. Schuster, 2001. Viscoelastic wave simulation in basins by a variable-grid finite-difference method. *Bull. Seism. Soc. Am.* 91, 1741-1749.

Wu, R.-S. and V. Maupin, eds., 2007. Advances in Wave Propagation in Heterogeneous Earth. In *Advances in Geophysics* Vol. 48, R. Dmowska, ed. *Elsevier - Academic Press*.

Xu, T. and G. A. McMechan, 1995. Composite memory variables for viscoelastic synthetic seismograms. *Geophys. J. Int.* 121, 634-639.

Xu, T. and G. A. McMechan, 1998. Efficient 3-D viscoelastic modeling with application to near-surface land seismic data. *Geophysics* 63, 601-612.

Yomogida, K. and J. T. Etgen, 1993. 3-D wave propagation in the Los Angeles basin for the Whittier-Narrows earthquake. *Bull. Seism. Soc. Am.* 83, 1325-1344.

Yoshimura, Ch., J. Bielak, Y. Hisada, and A. Fernández, 2003. Domain reduction method for three-dimensional earthquake modeling in localized regions. Part II: Verification and applications. *Bull. Seism. Soc. Am.* 93, 825-840.

Zahradník, J., 1995. Comment on 'A hybrid method for estimation of ground motion in sedimentary basins: Quantitative modeling for Mexico City' by D. Fäh, P. Suhadolc, St. Mueller and G.F. Panza. *Bull. Seism. Soc. Am.* 85, 1268-1270.

Zahradník, J. and P. Moczo, 1996. Hybrid seismic modeling based on discrete-wavenumber and finite-difference methods. *PAGEOPH* 148, 21-38.

Zahradník, J. and E. Priolo, 1995. Heterogeneous formulations of elastodynamic equations and finite-difference schemes. *Geophys. J. Int.* 120, 663-676.

Zeng, X., 1996. Finite difference modeling of viscoelastic wave propagation in a generally heterogeneous medium in the time domain, and a dissection method in the frequency domain. Ph.D. Thesis. *University of Toronto*.

Zhang, J., 1997. Quadrangle-grid velocity-stress finite-difference method for elastic-wave-propagation simulation. *Geophys. J. Int.* 131, 127-134.

Zhang, Ch. and W. W. Symes, 1998. Fourth order, full-stencil immersed interface method for elastic waves with discontinuous coefficients. *1998 SEG Expanded Abstracts*.

Zienkiewicz, O. C. and R. L. Taylor, 1989. The Finite Element Method. 4th edition, Vol. 1, *McGraw-Hill*, New York.